

**Forschungsbericht 2021-26**

**Transition prediction method for  
three-dimensional flows using  
linear stability theory**

Normann Krimmelbein

Deutsches Zentrum für Luft- und Raumfahrt  
Institut für Aerodynamik und  
Strömungstechnik  
Braunschweig



**DLR**

**Deutsches Zentrum  
für Luft- und Raumfahrt**

# **Forschungsbericht 2021-26**

## **Transition prediction method for three-dimensional flows using linear stability theory**

Normann Krimmelbein

Deutsches Zentrum für Luft- und Raumfahrt  
Institut für Aerodynamik und Strömungstechnik  
Braunschweig

135 Seiten  
78 Bilder  
6 Tabellen  
122 Literaturstellen



Deutsches Zentrum  
DLR für Luft- und Raumfahrt



*Herausgeber:*

Deutsches Zentrum  
für Luft- und Raumfahrt e. V.  
Wissenschaftliche Information  
D-51170 Köln  
Porz-Wahnheide  
Linder Höhe  
D-51147 Köln

ISSN 1434-8454



CC-BY-NC-3.0-DE

This work is made available according to the conditions of the  
Creative Commons  
Attribution-NonCommercial 3.0 Germany (CC BY-NC 3.0 DE) li-  
cense

Full details are available at:

<https://creativecommons.org/licenses/by-nc/3.0/de/legalcode>

# Transition prediction method for three-dimensional flows using linear stability theory

Von der Fakultät für Maschinenbau  
der Technischen Universität Carolo-Wilhelmina zu Braunschweig

zur Erlangung der Würde

eines Doktor-Ingenieurs (Dr.-Ing.)

genehmigte Dissertation

von: Normann Krimmelbein  
aus (Geburtsort): Ostfildern-Ruit  
eingereicht am: 31. Mai 2020  
mündliche Prüfung am: 10. Februar 2021  
Gutachter: Prof. Dr.-Ing. Rolf Radespiel  
Prof. Dr.-Ing. Cord-Christian Rossow



## Abstract

In the present work, a methodology to predict the laminar-turbulent transition in Reynolds averaged Navier-Stokes computations for general three-dimensional aerodynamic configurations is presented. The transition prediction methodology consists of a coupled program system and incorporates the DLR RANS solver TAU, a transition prediction module directly implemented into the RANS solver and an external stability code for the solution of the stability equations. Transition prediction is applied based on linear stability theory in combination with the  $e^N$  method together with the  $2N$ -factor strategy for the consideration of streamwise and cross-flow instabilities. The stability analysis is applied along inviscid streamlines derived from surface-projected boundary layer edge velocity vectors and the laminar boundary layer velocity profiles needed for the stability analysis and the transition prediction are directly extracted from the solution of the unstructured computational fluid dynamics solver.

To account for the high computational demand for the computations of flows over complex and fully three-dimensional configurations the transition prediction methodology is adapted to be efficiently applied in parallel computations. Concepts and implementation issues regarding the extraction of boundary layer velocity profiles, the determination of the boundary layer edge and the calculation of inviscid streamlines are presented. With focus on the external stability solver, strategies and their implementation in the transition prediction methodology for an automatic, autonomous and robust application of the linear stability analysis are given. An examination of the computing times required for applying the transition prediction method, in particular for parallel RANS calculations, shows the additional numerical computational effort that is required for transition prediction compared to RANS calculations without transition prediction. To determine the requirements for the resolution of the computational grid in wall normal direction for an sufficiently accurate calculation of three-dimensional boundary layer profiles needed for the application of the linear stability theory, a detailed grid convergence study is carried out.

The transition prediction capability of the presented method for general three-dimensional geometries is demonstrated for the flow around a generic aircraft configuration. Based on several wind tunnel test for flows of varying complexity, the accuracy of the transition prediction method is validated and the capability to determine boundary layer velocity profiles from the RANS solution with appropriate accuracy for linear stability analysis is verified. For the two-dimensional flow around a NLF (1)–0416 airfoil a very good agreement compared to experimental transition locations is achieved for a broad range of flow conditions in terms of angle of attack and Reynolds number. Three-dimensional flows are considered for infinite swept wing flows over wings with NLF (2)–0415 and ONERA D wing sections for which transition is mainly caused by cross-flow instabilities and predicted transition points are again in good agreement with the experiments. The successful application of the transition prediction for these test cases also demonstrates the capability of the RANS solver to compute streamwise and cross-flow velocity profiles with sufficient accuracy for linear stability analysis. The application of the prediction method to fully three-dimensional flows is validated based on the flow around a wing with a NACA 64<sub>2</sub>-A-015 profile and variable sweep angle and the DLR prolate spheroid. For the majority of the flow conditions considered, a good accordance with the experimental transition locations is achieved for these cases as well.



## Übersicht

In der vorliegenden Arbeit wird eine Methode zur Vorhersage des laminar-turbulenten Umschlags in Reynolds-gemittelten Navier-Stokes Rechnungen für allgemeine dreidimensionale aerodynamische Konfigurationen vorgestellt. Die Transitionsvorhersagemethode stellt ein gekoppeltes Programmsystem dar und besteht aus dem DLR RANS Löser TAU, einem direkt in den RANS Löser integrierten Transitionsvorhersagemodul und einem externen Stabilitätscode zur Lösung der Stabilitätsgleichungen. Die Stabilitätsanalyse wird basierend auf der linearen Stabilitätstheorie in Kombination mit der  $e^N$  Methode durchgeführt. Für die Berücksichtigung von Längs- und Querströmungsinstabilitäten wird dabei die  $2N$ -Faktor Strategie angewandt. Die Stabilitätsanalyse wird entlang Grenzschichtrandstromlinien angewendet, welche mit Hilfe von auf die Oberfläche der Geometrie projizierten Geschwindigkeiten am Grenzschichtrand berechnet werden. Die für die Stabilitätsanalyse und die Transitionsvorhersage benötigten Geschwindigkeitsprofile der laminaren Grenzschicht werden direkt aus der Lösung des Strömungslösers extrahiert.

Um dem hohen Rechenaufwand für die Berechnung von Strömungen um komplexe und dreidimensionale Konfigurationen Rechnung zu tragen, wurde die Transitionsvorhersagemethode für eine effiziente Anwendung bei parallelen Berechnungen angepasst. Hinsichtlich der Extraktion von Geschwindigkeitsprofilen, der Bestimmung des Grenzschichtrandes und der Berechnung von Grenzschichtrandstromlinien werden Konzepte und deren Implementierung dargestellt. Bezüglich des externen Stabilitätslösers werden Strategien für eine automatische, autonome und robuste Anwendung der linearen Stabilitätsanalyse und deren Umsetzung in der Transitionsvorhersagemethode erläutert. Eine Untersuchung der benötigten Rechenzeiten für die Anwendung der Transitionsvorhersagemethode, insbesondere für parallele RANS Rechnungen, zeigt den zusätzlichen numerischen Rechenaufwand auf, der für die Transitionsvorhersage im Vergleich zu RANS Rechnungen ohne Transitionsvorhersage erforderlich ist. Zur Bestimmung der Anforderungen an die Rechenauflösung in Wandnormalenrichtung für eine ausreichend genaue Berechnung von dreidimensionalen Grenzschichtprofilen für die Anwendung der linearen Stabilitätstheorie wird eine ausführliche Netzkonvergenzstudie durchgeführt.

Anhand der Umströmung einer generischen Flugzeugkonfiguration wird die prinzipielle Eignung der vorgestellten Methode zur Transitionsvorhersage für dreidimensionale Geometrien demonstriert. Basierend auf mehreren Windkanalversuchen für Strömungen unterschiedlicher Komplexität wird die Genauigkeit der Transitionsvorhersagemethode validiert und zudem die Fähigkeit überprüft, Grenzschichtgeschwindigkeitsprofile aus RANS Lösungen mit genügender Genauigkeit für eine lineare Stabilitätsanalyse zu bestimmen. Für die zweidimensionale Strömung um ein NLF (1)–0416 Profil wird eine sehr gute Übereinstimmung der vorhergesagten Transitionslagen im Vergleich zu experimentellen Transitionslagen für eine Vielzahl von unterschiedlichen Anströmbedingungen basierend auf Anstellwinkel und Reynoldszahl erreicht. Dreidimensionale Strömungen werden anhand der Umströmung von unendlich schiebenden Flügelsegmenten an Flügeln mit NLF (2)–0415 und ONERA D Profilen untersucht, wobei die Transition hier hauptsächlich durch Querströmungsinstabilitäten hervorgerufen wird. Auch für diese Fälle ergibt sich eine gute Übereinstimmung mit den experimentellen Transitionslagen. Insgesamt bestätigt die erfolgreiche Anwendung der Transitionsvorhersagemethode auf diese ersten Testfälle auch die Fähigkeit des Strömungslösers, Längs- und Quergeschwindigkeitsprofile mit ausreichender Genauigkeit für eine lineare Stabilitätsanalyse zu berechnen. Die Anwendung der Vorhersagemethode auf voll dreidimensionale Strömungen wird Anhand der Umströmung eines Flügels mit NACA 64<sub>2</sub>-A-015 Profil und variablem Pfeilwinkel und am DLR Rotationsellipsoiden validiert. Für den Großteil der untersuchten Anströmbedingungen ergeben sich auch für diese Fälle gute Übereinstimmungen mit den experimentellen Transitionslagen.



## Contents

<b>1. Introduction</b>	<b>1</b>
1.1. Three-dimensional boundary layer . . . . .	3
1.2. Transition scenarios . . . . .	4
1.3. Transition prediction methods . . . . .	5
1.4. Objective and structure of the work . . . . .	9
<b>2. Methods</b>	<b>11</b>
2.1. RANS equations and turbulence model . . . . .	11
2.2. Linear stability theory and $e^N$ method . . . . .	13
2.3. Transition prediction methodology . . . . .	16
2.3.1. Coupled program system . . . . .	16
2.3.2. Stability solver . . . . .	18
<b>3. Implementation</b>	<b>21</b>
3.1. Overview of parallelization . . . . .	21
3.2. Geometrical data . . . . .	22
3.3. Boundary layer data . . . . .	23
3.3.1. Boundary layer profiles . . . . .	24
3.3.2. Boundary layer edge . . . . .	25
3.4. Streamlines . . . . .	28
3.4.1. Three-dimensional streamlines . . . . .	28
3.4.2. Two-dimensional and quasi-two-dimensional flows . . . . .	30
3.5. Stability code . . . . .	31
3.5.1. General input and execution of the code . . . . .	31
3.5.2. $N$ -factor integration . . . . .	31
3.5.3. Computation of amplification rates . . . . .	33
3.6. Application of transition criteria . . . . .	34
3.7. Concluding remarks and statistics . . . . .	36
<b>4. Results</b>	<b>39</b>
4.1. Verification . . . . .	39
4.1.1. Code parallelization . . . . .	39
4.1.2. Grid convergence . . . . .	41
4.1.3. Feasibility . . . . .	46
4.2. Validation . . . . .	46
4.2.1. NLF (1)-0416 . . . . .	48
4.2.2. NLF (2)-0415 . . . . .	49
4.2.3. ONERA D . . . . .	51
4.2.4. NACA 64 <sub>2</sub> -A-015 . . . . .	52
4.2.5. DLR prolate spheroid . . . . .	59
4.3. Comparison to transport equation approaches . . . . .	64
<b>5. Conclusion</b>	<b>69</b>
<b>6. Published data</b>	<b>73</b>
<b>7. References</b>	<b>75</b>
<b>8. Figures</b>	<b>83</b>

<b>A. Appendix</b>	<b>127</b>
A.1. Grid generation strategy . . . . .	127
A.2. Reynolds number based scaling of boundary layers . . . . .	128
A.3. NACA 64 <sub>2</sub> -A-015 computation strategy . . . . .	129
A.3.1. General computation strategy . . . . .	129
A.3.2. Scaling for stability analysis . . . . .	131
A.3.3. Attachment line analysis . . . . .	131
<b>B. Appendix figures</b>	<b>135</b>

## Nomenclature

### Latin symbols

$A$	amplitude
$a$	speed of sound
$a_{ij}$	coefficient in Runge-Kutta method
$b$	half span length
$b_i$	coefficient in Runge-Kutta method
$c$	chord length
$c_d$	drag coefficient
$c_f$	skin friction coefficient
$c_l$	lift coefficient
$c_p$	pressure coefficient, specific heat coefficient at constant pressure
$\vec{c}$	vector in cross-flow direction
$d$	diameter
$E$	total energy
$f$	a general factor
$H$	total enthalpy
$h$	step size in Runge-Kutta method, roughness height
$H_{12}$	shape factor
$i_H$	angle of incidence for horizontal tail plane
$K$	Acceleration parameter
$K_2$	Curvature of potential line
$k_i$	intermediate step in Runge-Kutta method
$L$	length
$l_{cell}$	length representative of the surface cell size
$L_p$	sound pressure level
$Ma$	Mach number
$N$	$N$ -factor
$n$	number of streamlines, number of points
$n_{rk}$	number of Runge-Kutta steps
$\vec{n}$	wall-normal vector

$p$	static pressure, number of processes
$Pr$	Prandtl number
$p_t$	total pressure
$\vec{p}$	coordinates of a grid point
$q$	arbitrary flow variable
$q$	stretching factor
$R$	specific gas constant
$Re$	Reynolds number
$\vec{r}$	vector between two points
$s$	arc length, number of Runge-Kutta stages
$s_g$	arc length along group velocity trajectory
$s_{Re}$	Reynolds number based scaling factor
$\vec{s}$	vector in streamwise direction
$T$	temperature, transformation matrix
$t$	time, thickness
$T_s$	Sutherland reference temperature
$\hat{T}_s$	non-dimensional Sutherland reference temperature
$Tu$	turbulence intensity
$u_\tau$	friction velocity
$\vec{u}$	velocity vector
$u, v, w$	velocity components
$\vec{v}_g$	group velocity vector
$x, y, z$	orthogonal coordinates, cartesian or curvilinear
$y$	wall distance
$y_0$	wall distance of the first prism layer
$y^+$	dimensionless wall distance
$z$	wall normal coordinate

**Greek symbols**

$\alpha$	complex spatial wave number, angle of attack
$\alpha_r$	spatial wave number
$\beta$	complex spatial wave number, sideslip angle

$\beta_r$	spatial wave number
$\delta$	boundary layer thickness
$\delta_1$	displacement thickness
$\delta_2$	momentum loss thickness
$\delta_{ij}$	Kronecker delta
$\eta$	non-dimensional wall distance
$\gamma$	isentropic exponent
$\kappa_{nc}$	normal curvature in cross-flow direction
$\Lambda$	sweep angle
$\lambda$	thermal conductivity
$\mu$	dynamic viscosity
$\mu_s$	Sutherland reference viscosity
$\nu$	kinematic viscosity
$\tilde{\nu}$	SA viscosity
$\phi$	angle between to vectors
$\phi$	azimuth angle, rotation angle
$\theta$	angle between line-in-flight cut and inviscid streamline direction
$\rho$	density
$\sigma$	spatial amplification rate
$\tau$	shear stress
$\vec{\tau}_w$	wall shear stress vector
$\tau_w$	wall shear stress
$\omega$	complex circular frequency
$\omega_i$	temporal amplification rate
$\omega_r$	circular frequency
$\Psi$	propagation direction
$\Psi_g$	angle between group velocity direction and inviscid streamline direction

**Superscripts**

'	value in leading edge normal coordinate system, fluctuating velocity
'	disturbed quantity
^	instationary quantity

**Subscripts**

$0$	initial value, stationary quantity
$\infty$	value at infinity, value far away from the geometry
<i>cell</i>	value associated with a grid cell
<i>cone</i>	value of visibility cone method
<i>crit</i>	critical value
<i>db</i>	value from database method
<i>dest</i>	destruction
<i>diff</i>	diffusion
<i>e</i>	value at boundary layer edge
<i>env</i>	envelope
<i>g</i>	group velocity
<i>i</i>	imaginary part
<i>ijk</i>	indices
<i>lam</i>	laminar
<i>lim</i>	limiting value
<i>max</i>	maximum value
<i>min</i>	minimum value
<i>n</i>	value associated with a normal direction, normalized value
<i>nb</i>	value at a neighbour point of a grid point
<i>p</i>	vector parallel to wall, projected value
<i>prod</i>	production
<i>r</i>	real part
<i>rk</i>	value associated with a Runge-Kutta method
<i>rms</i>	root mean square
<i>scn</i>	values in streamline-coordinate system
<i>surf</i>	value at the surface
<i>t</i>	total value
<i>tr</i>	value at the transition point
<i>target</i>	target value
<i>turb</i>	turbulent

$w$	value at the wall
$wave$	parameter associated with a single wave
$xyz$	values in $x, y, z$ -coordinate system

**Acronyms**

2D	two-dimensional
3D	three-dimensional
AL	attachment line
CF	cross-flow
DLR	Deutsches Zentrum für Luft- und Raumfahrt (German Aerospace Center)
FF	farfield
LU-SGS	Lower upper symmetric Gauss-Seidel
I/O	input/output
ISW	infinite swept wing
LILO	stability code
MPI	message passing interface (a communication protocol for parallel programs)
RANS	Reynolds-averaged Navier-Stokes
SA	Spalart-Allmaras
SCF	stationary cross-flow
TAU	compressible unstructured DLR Reynolds-averaged Navier-Stokes code
TCF	travelling cross-flow
THETA	incompressible unstructured DLR Reynolds-averaged Navier-Stokes code
TS	Tollmien-Schlichting
WT	wind tunnel



## List of Figures

1.	Evolution of a transitional boundary layer along a flat plate. . . . .	83
2.	Three-dimensional boundary layer profile. . . . .	83
3.	Development of cross-flow velocity profiles in three-dimensional flow. . . . .	84
4.	Principle of the $e^N$ method. . . . .	84
5.	Coupled program system of RANS solver and transition module. . . . .	85
6.	General structure of the transition module. . . . .	85
7.	Basic steps for transition prediction for three-dimensional flows. . . . .	86
8.	Structure for the determination of wall-normal lines. . . . .	86
9.	Structure for the determination of inviscid streamlines. . . . .	87
10.	Schematic of typical boundary layer velocity profiles in a RANS solution. . . . .	87
11.	$N$ -factors and group velocity direction, NACA 64 <sub>2</sub> -A-015, $\Lambda = 50.0^\circ$ , $\alpha = -1.0^\circ$ , $Re = 5.0 \times 10^6$ . . . . .	88
12.	Nested loops for stability computation. . . . .	88
13.	Extrapolation of $N$ -factors. . . . .	89
14.	Edge streamlines and domain boundaries, 1, 4, 8 and 12 domains, 6:1 prolate spheroid. . . . .	89
15.	Computational time vs number of processes, transition prediction step and execution of stability code, 6, 12 and 24 streamlines. . . . .	90
16.	Computational time vs number of processes, transition prediction step, normalized with time for one multigrid cycle of the TAU solver, 6, 12 and 24 streamlines. . . . .	90
17.	Computational time vs number of streamlines, 6:1 prolate spheroid and generic transport aircraft, 8 domains. . . . .	91
18.	Grid convergence, $N$ -factors, NACA 64 <sub>2</sub> -A-015, $\Lambda = 50.0^\circ$ , $\alpha = -2.5^\circ$ , $Re = 3.0 \times 10^6$ . . . . .	91
19.	Grid convergence, $N$ -factors, NACA 64 <sub>2</sub> -A-015, $\Lambda = 30.0^\circ$ , $\alpha = 0.5^\circ$ , $Re = 1.5 \times 10^7$ . . . . .	92
20.	Grid convergence, $N$ -factors, NACA 64 <sub>2</sub> -A-015, $\Lambda = 10.0^\circ$ , $\alpha = -2.0^\circ$ , $Re = 2.5 \times 10^7$ . . . . .	92
21.	Grid convergence, stream wise velocity profiles at $x/c = 0.25$ , NACA 64 <sub>2</sub> -A-015, $\Lambda = 10.0^\circ$ , $\alpha = -2.0^\circ$ , $Re = 2.5 \times 10^7$ . . . . .	93
22.	Grid convergence, cross flow velocity profiles at $x/c = 0.25$ , NACA 64 <sub>2</sub> -A-015, $\Lambda = 10.0^\circ$ , $\alpha = -2.0^\circ$ , $Re = 2.5 \times 10^7$ . . . . .	93
23.	Comparison of grid parameters, flat plate. . . . .	94
24.	Grid convergence, skin friction, shape factor and $N$ -factor, NLF (1)–0416, $\alpha = 2.0^\circ$ , $Re = 4.0 \times 10^6$ , upper surface. . . . .	94
25.	Grid convergence, skin friction, shape factor and $N$ -factor, NLF (1)–0416, $\alpha = 2.0^\circ$ , $Re = 4.0 \times 10^6$ , lower surface. . . . .	95
26.	Grid convergence, shape factor and $N$ -factors, NACA 64 <sub>2</sub> -A-015, $\Lambda = 30.0^\circ$ , $\alpha = 0.5^\circ$ , $Re = 1.5 \times 10^7$ . . . . .	95
27.	Edge streamlines and transition locations, upper surfaces, generic transport aircraft, $\alpha = -4.0^\circ$ , $Re = 2.3 \times 10^6$ , $i_H = 4.0^\circ$ . . . . .	96
28.	Edge streamlines and transition locations, lower surfaces, generic transport aircraft, $\alpha = -4.0^\circ$ , $Re = 2.3 \times 10^6$ , $i_H = 4.0^\circ$ . . . . .	96
29.	NLF (1)–0416 airfoil. . . . .	97
30.	Test section turbulence levels, Langley Research Center Low-Turbulence Pressure Tunnel. . . . .	97
31.	Pressure distribution, NLF (1)–0416 airfoil, $Ma = 0.1$ , $Re = 4.0 \times 10^6$ . . . . .	98
32.	Predicted transition locations, NLF (1)–0416 airfoil, $Ma = 0.1$ , $Re = 1.0 \times 10^6$ . . . . .	99
33.	Predicted transition locations, NLF (1)–0416 airfoil, $Ma = 0.1$ , $Re = 2.0 \times 10^6$ . . . . .	99
34.	Predicted transition locations, NLF (1)–0416 airfoil, $Ma = 0.1$ , $Re = 3.0 \times 10^6$ . . . . .	100
35.	Predicted transition locations, NLF (1)–0416 airfoil, $Ma = 0.1$ , $Re = 4.0 \times 10^6$ . . . . .	100
36.	NLF (2)–0415 airfoil. . . . .	101
37.	Pressure distribution, NLF (2)–0415 airfoil, $Re = 1.93 \times 10^6$ . . . . .	101
38.	Predicted transition locations, NLF (2)–0415 airfoil. . . . .	102

39.	ONERA D airfoil. . . . .	102
40.	Wing with ONERA D profile, pressure distribution, pressure side, $\alpha_n = 6.0^\circ$ , $Re = 0.4 \times 10^6$ , $\Lambda = 40.0^\circ$ . . . . .	103
41.	Pressure distribution, ONERA D, $Re = 0.4 \times 10^6$ . . . . .	104
42.	Predicted transition locations, ONERA D. . . . .	105
43.	NACA 64 <sub>2</sub> -A-015 airfoil. . . . .	105
44.	Geometry, NACA 64 <sub>2</sub> -A-015 wing, NASA Ames 12-foot low-turbulence pressure tunnel. . . . .	106
45.	Sound pressure level and acoustic equivalent turbulence intensity, dependency on Mach number, NASA Ames 12-foot low-turbulence pressure tunnel. . . . .	107
46.	Pressure distribution, NACA 64 <sub>2</sub> -A-015 wing, $\Lambda = 0.0^\circ$ and $\Lambda = 50.0^\circ$ , $Re = 7.2 \times 10^6$ , $\alpha = 3.0^\circ$ . . . . .	107
47.	Pressure distribution, NACA 64 <sub>2</sub> -A-015, $Re = 7.2 \times 10^6$ , $\Lambda = 0.0^\circ$ . . . . .	108
48.	Pressure distribution, NACA 64 <sub>2</sub> -A-015, $Re = 7.2 \times 10^6$ , $\Lambda = 10.0^\circ$ . . . . .	108
49.	Pressure distribution, NACA 64 <sub>2</sub> -A-015, $Re = 7.2 \times 10^6$ , $\Lambda = 20.0^\circ$ . . . . .	109
50.	Pressure distribution, NACA 64 <sub>2</sub> -A-015, $Re = 7.2 \times 10^6$ , $\Lambda = 30.0^\circ$ . . . . .	109
51.	Pressure distribution, NACA 64 <sub>2</sub> -A-015, $Re = 7.2 \times 10^6$ , $\Lambda = 40.0^\circ$ . . . . .	110
52.	Pressure distribution, NACA 64 <sub>2</sub> -A-015, $Re = 7.2 \times 10^6$ , $\Lambda = 50.0^\circ$ . . . . .	110
53.	$N$ -factors at transition, NACA 64 <sub>2</sub> -A-015. . . . .	111
54.	Predicted transition locations, NACA 64 <sub>2</sub> -A-015, $\Lambda = 0.0^\circ$ . . . . .	112
55.	Predicted transition locations, NACA 64 <sub>2</sub> -A-015, $\Lambda = 10.0^\circ$ . . . . .	113
56.	Predicted transition locations, NACA 64 <sub>2</sub> -A-015, $\Lambda = 20.0^\circ$ . . . . .	114
57.	Predicted transition locations, NACA 64 <sub>2</sub> -A-015, $\Lambda = 30.0^\circ$ . . . . .	115
58.	Predicted transition locations, NACA 64 <sub>2</sub> -A-015, $\Lambda = 40.0^\circ$ . . . . .	116
59.	Predicted transition locations, NACA 64 <sub>2</sub> -A-015, $\Lambda = 50.0^\circ$ . . . . .	117
60.	Schematic of cross-flow $N$ -factor envelopes for different Reynolds numbers. . . . .	118
61.	DLR prolate spheroid. . . . .	118
62.	Stability diagram, $N_{TS}$ over $N_{CF}$ , DLR prolate spheroid. . . . .	118
63.	Predicted transition lines, DLR prolate spheroid, $Re = 1.5 \times 10^6$ , $\alpha = 5.0^\circ$ . . . . .	119
64.	Predicted transition lines, DLR prolate spheroid, $Re = 1.5 \times 10^6$ , $\alpha = 10.0^\circ$ . . . . .	119
65.	Predicted transition lines, DLR prolate spheroid, $Re = 1.5 \times 10^6$ , $\alpha = 30.0^\circ$ . . . . .	120
66.	Predicted transition lines, DLR prolate spheroid, $Re = 3.0 \times 10^6$ , $\alpha = 30.0^\circ$ . . . . .	120
67.	Predicted transition lines, DLR prolate spheroid, $Re = 6.5 \times 10^6$ , $\alpha = 5.0^\circ$ . . . . .	121
68.	Predicted transition lines, DLR prolate spheroid, $Re = 6.5 \times 10^6$ , $\alpha = 10.0^\circ$ . . . . .	121
69.	Predicted transition lines, DLR prolate spheroid, $Re = 6.5 \times 10^6$ , $\alpha = 15.0^\circ$ . . . . .	122
70.	Predicted transition lines, DLR prolate spheroid, $Re = 6.5 \times 10^6$ , $\alpha = 20.0^\circ$ . . . . .	122
71.	Predicted transition lines, DLR prolate spheroid, $Re = 6.5 \times 10^6$ , $\alpha = 24.0^\circ$ . . . . .	123
72.	Predicted transition lines, DLR prolate spheroid, $Re = 6.5 \times 10^6$ , $\alpha = 30.0^\circ$ . . . . .	123
73.	Predicted transition lines, DLR prolate spheroid, $Re = 4.5 \times 10^6$ , $\alpha = 30.0^\circ$ . . . . .	124
74.	Predicted transition lines, DLR prolate spheroid, $Re = 8.5 \times 10^6$ , $\alpha = 30.0^\circ$ . . . . .	124
75.	Predicted transition lines, DLR prolate spheroid, $Re = 4.5 \times 10^6$ , $\alpha = 30.0^\circ$ , alternative prediction approach. . . . .	125
76.	Predicted transition lines, DLR prolate spheroid, $Re = 6.5 \times 10^6$ , $\alpha = 30.0^\circ$ , alternative prediction approach. . . . .	125
77.	Validation of Reynolds number scaling, NACA 64 <sub>2</sub> -A-015. . . . .	135
78.	Attachment line transition and relaminarization criteria, NACA 64 <sub>2</sub> -A-015. . . . .	135

## List of Tables

1.	Initial values for stability computation . . . . .	33
2.	Relative sizes of elements of the transition module . . . . .	37
3.	Number of prism layers and target $y^+$ . . . . .	42
4.	Resolution of the laminar boundary layer . . . . .	43
5.	Number of surface grid points and surface cell sizes at transition . . . . .	45
6.	Computational grids characteristics . . . . .	47



## 1. Introduction

In the beginning there was laminar flow... and then OSBOURNE REYNOLDS started to mess around with dye [1]. This casual introductory sentence makes reference to the famous dye experiment of REYNOLDS, that marks the origin of systematic experimental investigations of laminar-turbulent transition in fluid flow and the beginning of intensified theoretical research on the topic.

REYNOLDS already distinguished two broadly different forms of motion of water, where either the fluid particles follow straight direct lines or they whirl around on winding paths [1]. For the first form of motion, these days referred to as laminar flow, particles flow with different velocities along different parallel layers and with no significant exchange of the fluid particles normal to the direction of the flow. The second form of motion, these days referred to as turbulent flow, shows a substantial difference in the flow behaviour. The flow is characterized by an unregularly strong lateral movement of the fluid particles that leads to an intense mixing normal to the direction of the flow.

In his classical experiment [1], REYNOLDS was able to visualize the two forms of motion of a fluid and the change, that is the transition, of one type of flow into the other in an apparent and pragmatic way. It was known by the time of the experiment, that the resistance of water flowing through a tube could be described by two distinct laws, where the resistance is either proportional to the square of the velocity or just proportional to the velocity, depending on the diameter of the tube and the velocity of the water. However, previous to REYNOLDS' work, the actual experimental conditions under which the change from one law to the other occurred have not been determined. REYNOLDS assumed that the change in the law of resistance is accompanied by the formation and the evolution of eddies in the pipe flow. In an approach to examine the relation between the mean velocity  $U$  along the pipe, the viscosity  $\mu/\rho$  of the fluid and the radius  $c$  of the pipe and its correlation with the appearance of eddies in the flow, REYNOLDS, in a practical way, gave answers to the following questions (REYNOLDS [1], p. 940):

*"Did steady motion hold up to a critical value and then eddies come in?"*

*"Did the eddies come in at a certain value of  $\frac{c\rho U}{\mu}$ ?"*

These and other postulates, all formulated as queries, were positively confirmed by measuring the resistance and the velocity for different diameters of the pipes and for different temperatures of the water. Additionally, and this leads back to the opening casual remark regarding the dye, REYNOLDS supported his theory by an experimental visualization of the appearance of eddies. For this, dye was injected into clear water moving along a glass pipe. For sufficiently low velocities, a coloured straight streak of dye, moving parallel to the longitudinal axis, developed. If the velocity was increased beyond a critical value, after a certain distance along the pipe, the initially straight streak of dye started to make strong lateral movements and eventually the dye completely mixed with the surrounding water. Visualizing this phenomenon just corresponds to the visualization of the transition from laminar to turbulent flow in the experiment.

For different pipe diameters and constant temperature of the water, the critical velocity, for which eddies first appeared in the flow, was found to be proportional to the inverse of the diameter, leading to the conclusion, *"that the general character of the motion of fluids in contact with solid surfaces depends on the relation between a physical constant of the fluid and the product of the linear dimensions of the space occupied by the fluid and the velocity"* (REYNOLDS [1], p. 935). This is summarized in a definition of a dimensionless number named after OSBOURNE REYNOLDS, the Reynolds number:

$$Re = \frac{c\rho U}{\mu}$$

For pipe flows, transition occurs if the Reynolds number exceeds a certain critical value, which is typically  $Re_{crit} \approx 2300$  [2]. The critical value depends also on the disturbance level at the inlet of the

tube. Transition of the flow in tubes is characterized by a strong increase in resistance, which in turn is related to the energy consumption of the turbulent mixing [2].

It took some time until it became apparent, that the flow phenomena of the pipe flow are also applicable to flows around general bodies. Following the introduction of the theory of the boundary layer [3], a thin region near the surface of a body where viscous effects are significant, it was found that the boundary layers of general bodies can also be laminar or turbulent [4]. The overall characteristics of the flow and the forces acting on the geometry through the flow are significantly depending on the state of the flow of the boundary layer.

The Reynolds number, which also represents the law of similarity of a flow and which can be considered as the ratio of inertial forces to viscous forces, is applicable to a general geometry if the geometry is specified by a characteristic length  $L$ :

$$Re = \frac{\rho UL}{\mu} = \frac{\text{inertial forces}}{\text{viscous forces}}$$

Generally, for low Reynolds numbers the flow is laminar and the viscous forces dominate. For higher Reynolds numbers the flow becomes turbulent and the flow is dominated by inertial forces.

A specific characteristic of a turbulent boundary layer, compared to a laminar boundary layer, can be seen for the flow over blunt bodies like spheres or cylinders. These bodies show a sudden decrease in drag coefficient with increasing Reynolds number. If the Reynolds number is low enough, the boundary layer over a sphere is laminar and separates relatively far upstream, creating a large backflow area that leads to a large pressure resistance of the flow [5]. If the Reynolds number is increased beyond its critical value, the boundary layer becomes turbulent and separates further downstream, leading to a smaller backflow area and a smaller pressure resistance. In this case the transition from laminar to turbulent flow has a positive effect, reducing the overall drag of the sphere.

Efforts to investigate the stability problem of laminar flows theoretically were commenced prior to the experimental research of REYNOLDS by LORD RAYLEIGH [6]. Some decades later, the theoretical work was revived by PRANDTL [7] who investigated the stability of laminar boundary layers along a flat plate. For two-dimensional flat plate boundary layers, the theoretical investigations came to a conclusion with the work of TOLLMEN and SCHLICHTING, who showed that above a critical Reynolds number amplification of small sinusoidal disturbances eventually lead to transition [8, 9]. This primary stability theory for laminar flows, which is based on the method of small oscillations and leads directly to the linear stability theory, was later experimentally confirmed by the work of DRYDEN [4] and SCHUBAUER and SKRAMSTAD [10].

The experiments confirmed, that the laminar boundary layer along a flat plate is superimposed by two-dimensional harmonic disturbances once the local indifference Reynolds number, which is based on the distance to the leading edge, is exceeded. These linear instabilities can be visualized in experiments and are the so called Tollmien-Schlichting waves, which can be described by the primary stability theory. Further downstream, the wave fronts of the Tollmien-Schlichting waves start to deform and three-dimensional disturbances in form of  $\Lambda$ -structures develop. These non-linear, secondary instabilities are replaced by turbulent spots that lead to a fully turbulent flow at the point where the local critical Reynolds number is reached [11].

As illustrated in figure 1 for the flat plate, laminar and turbulent boundary layer flows are characterized by different specific attributes. First of all, the different flow states are distinguished by a very different development of the boundary layer thickness  $\delta$  along the plate in streamwise direction  $x$ . The turbulent boundary layer grows much faster with  $x$ : Whereas the laminar boundary layer grows as  $\delta_{lam} \sim x^{1/2}$ , the turbulent boundary layer grows as  $\delta_{turb} \sim x^{4/5}$  [11]:

$$\delta_{lam} \approx 5.0 \sqrt{\frac{\nu x}{U}} \quad \delta_{turb} \approx 0.37 x \left( \frac{\nu}{Ux} \right)^{\frac{1}{5}}$$

Another major difference between laminar and turbulent flows appears for the shape of the boundary layer velocity profile. Because of the large fluctuations in lateral direction, turbulent boundary layer flows have a much larger momentum transfer normal to the wall, which leads to velocity profiles which are much fuller in their shape compared to laminar velocity profiles. This is represented by the shape factor  $H_{12}$  of the velocity profiles, which is defined as the ratio of displacement thickness and momentum loss thickness,  $H_{12} = \delta_1/\delta_2$  [11]. For laminar flat plate flow the value for the shape factor is  $H_{12} \approx 2.6$ . For decelerated laminar flow the value is increased and, vice versa, for accelerated flow the value is decreased but stays above  $H_{12} \approx 2.2$ . For turbulent flat plate flow the shape factor has a value of  $H_{12} \approx 1.4$ . For the shape factor applies, that the lower the value for  $H_{12}$ , the fuller the velocity profile.

The shape of the boundary layer profile has in turn a direct influence on the viscous drag, which is, according to Newton's friction law,  $\tau_w = \mu (du/dy)_w$ , determined by the velocity gradient at the wall. The very different velocity gradients of the two flow states results in an significant increase in viscous drag as soon as the laminar boundary layer changes to a turbulent boundary layer (Fig. 1).

The above summarizes some important aspects of laminar and turbulent flows from which it already becomes apparent, that the general state of the flow and especially the location of transition can have a major impact on the flow around general geometries. Laminar flows are characterized by thinner boundary layers and less friction drag compared to turbulent boundary layers. This can prove to be beneficial for the design of aerodynamic bodies regarding the overall drag. On the other hand, laminar boundary layers are less stable with respect to separation of the boundary layer. Here, a turbulent boundary layer can prove to be beneficial regarding the aerodynamic performance.

Since the numerical prediction of flows around aerodynamic geometries like airfoils, wings, general air vehicles et cetera, is now common in research and industry, the accurate knowledge and especially the accurate numerical prediction of the transition location is necessary for a precise prediction of the flow field around the geometry. The knowledge of the transition location is especially useful for the determination of the drag of aircrafts, respectively their general aerodynamic performance, under cruise conditions or for the design of low drag airfoils and wings. But a precise knowledge of the transition locations may become even more crucial for the accurate determination of flight states and flight conditions near the boundaries of the flight envelope of an aircraft. Here, the transition locations can for example have a major impact on the stall behaviour or the flutter characteristics of airplanes or on the dynamic stall phenomenon of helicopter rotor blades. A good part of the flow conditions appearing at the borders of the flight envelope can only be accurately predicted with numerical methods by considering the correct transition location. This becomes even more important regarding future projects with concepts like undertaking virtual flights along the flight envelope prior to the actual first flight of an aircraft or if it comes to visions like virtual certification of air vehicles.

### 1.1. Three-dimensional boundary layer

For three-dimensional flows the boundary layer velocity profile is decomposed into two components, a streamwise velocity profile  $u$  and a cross-flow velocity profile  $v$  (Fig. 2). The direction of  $u$  corresponds to the direction of the velocity at the boundary layer edge and the direction of  $v$  corresponds to the direction normal to it, in wall tangential direction. The three-dimensional boundary layer equations can be written in this streamline coordinate system, with  $x$  the coordinate in streamwise direction,  $y$  the coordinate in the cross-flow direction and  $z$  the wall normal coordinate. For incompressible flow the momentum equation in cross-flow direction is given by [12]:

$$\rho u \frac{\partial v}{\partial x} + \rho v \frac{\partial v}{\partial y} + \rho w \frac{\partial v}{\partial z} + \rho K_1 u^2 + \rho K_2 uv = -\frac{\partial p}{\partial y} + \mu \left( \frac{\partial^2 v}{\partial z^2} \right)$$

$K_1$  and  $K_2$  are the geodesic curvatures in streamwise and cross-flow direction, respectively. Considering the external flow as potential flow, at the boundary layer edge  $K_1$  is the curvature of the

streamlines and  $K_2$  is the curvature of the potential lines. The momentum equation in cross-flow direction, formulated at the boundary layer edge and the wall, respectively, yields:

$$\rho K_{1e} u_e^2 = -\frac{\partial p}{\partial y} \quad \frac{\partial p}{\partial y} = \mu \left( \frac{\partial^2 v}{\partial z^2} \right)_{z=0}$$

From this it can be seen, that there exists a balancing of pressure forces and centrifugal forces at the boundary layer edge. If the pressure gradient in cross-flow direction  $dp/dy$  vanishes the curvature of the streamline is zero (two-dimensional flow) and if the pressure gradient changes sign the curvature of the streamline changes its direction. Inside the boundary layer the centrifugal forces decrease ( $\sqrt{u^2 + v^2}$  becomes smaller) but according to boundary layer theory the pressure  $p$  and hence the pressure gradient in cross-flow direction  $dp/dy$  stays constant inside the boundary layer. The excess of the pressure forces creates a velocity component in cross-flow direction, which again vanishes towards the wall, where pressure forces and viscous forces are in balance. The local direction of the velocity vector inside the boundary layer changes from the direction of the external flow at the boundary layer edge to the direction of the wall shear stress vector at the wall (Fig. 2).

Following the description of reference [13] and the illustration of figure 3, the cross-flow velocity component is initially zero at the attachment line. From the attachment line to the pressure minimum, that is in accelerated flow, the cross-flow velocity component develops and is directed towards the concave part of the streamline. At the pressure minimum  $dp/dy$  changes sign and the curvature of the streamline changes direction. From this point on, the cross-flow velocity component starts to reverse, at first resulting in an s-shape velocity profile, until eventually the cross-flow velocity profile may become completely reversed.

## 1.2. Transition scenarios

The transition from laminar to turbulent flows of boundary layers is affected by several parameters, where the Reynolds number is probably the most important. Another crucial parameter is the pressure distribution. Often already a relatively small pressure increase in flow direction leads to a transition from laminar to turbulent flow. Whereas for two-dimensional flows a pressure decrease has a stabilizing effect this is not generally true for three-dimensional flows. Here an accelerated boundary layer flow can have a destabilizing effect on the laminar boundary layer, typically occurring for swept wing flows. The transition process is also influenced by external disturbances entering the laminar boundary layer. This process is referred to as boundary layer receptivity [14]. A typical receptivity source is the turbulence level of the free stream flow, other disturbance sources are sound fluctuations or pressure waves and the wall roughness. There are other paths from laminar to turbulent flow known, such as bypass transition or transient growth [15], but they are less important for external flows. For three-dimensional boundary layers there are more or less three important transition scenarios left which are relevant for the flow around aircrafts in free-flight and the flow around geometries in low turbulence wind tunnels.

*Streamwise instabilities* The streamwise velocity profile for a three-dimensional boundary layer flow corresponds in its shape to the classical two-dimensional velocity profile (Fig. 2). This means, that the same transition mechanisms that apply to two-dimensional flows also occur for three-dimensional flows. For subsonic and transonic flows, the governing instabilities are generally driven by the amplification of Tollmien-Schlichting waves (see above). When compressibility effects start to play an increasing role Tollmien-Schlichting waves are replaced by oblique waves as being the most unstable waves.

*Cross-flow instabilities* The cross-flow velocity profile has zero velocity at the wall and at the boundary layer edge and a maximum value inside the boundary layer (Fig. 2). This means, that the cross-flow velocity profile always contains an inflection point, thus leading to an inflectional instability for this type of flow. The cross-flow velocity profile is highly unstable whenever the cross-flow velocity increases

noticeable, typically in accelerated flows near the leading edge of swept wings [13].

*Attachment line instabilities* For a wing-like geometry, the attachment line divides the flow into one part following the upper surface of the geometry and one part following the lower surface of the geometry. The flow along the attachment line is two-dimensional with no cross-flow component and thus first of all streamwise instabilities play a role for this type of flow. These instabilities can be well described by Tollmien-Schlichting waves or, more rigorously, by Görtler-Hämmerlin disturbances, and the transition process is referred to as *natural* transition [13]. If a considered geometry is in contact with another wall that has a turbulent boundary layer, the attachment line can be contaminated by the turbulence originating from the turbulent wall. This is a non-linear phenomenon and closely related to bypass transition and referred to as attachment line *contamination*. Once the flow along an attachment line is turbulent, all the flow around a geometry that originates from the attachment line is also turbulent. For a wing-like geometry this results in fully turbulent flow on the upper and the lower surface of the geometry, from the attachment line to the trailing edge.

A special flow phenomenon appearing in the vicinity of the attachment line, and thus closely related to attachment line instabilities, is the ability of a turbulent boundary layer to return to a laminar state. This *relaminarization* is possible, if the flow undergoes a sufficiently strong acceleration for a sufficiently long distance. In this case a turbulent boundary layer originating at the attachment line can become laminar again and can then further downstream be subject to other instabilities like for example Tollmien-Schlichting or cross-flow instabilities.

### 1.3. Transition prediction methods

Various approaches exist to predict transition in an computational fluid dynamics environment. They differ in their modelling complexity and their physical accuracy or in the general maturity of the method. With a direct numerical simulation, for example, no modelling at all is involved and all of the flow scales are thus resolved. A large eddy simulation on the other hand includes modelling of the small scales of the flow but the large scales are resolved. However, both methods, direct numerical simulations of the Navier-Stokes equations and wall-resolved large eddy simulations, are currently not suitable as engineering approaches for high Reynolds number flows because of their computational demand regarding spatial and temporal resolution.

The most used and most practicable transition prediction methods in a RANS solver environment for engineering applications at present and in the foreseeable future can basically be classified as a combination of three approaches: 1) an approach for the determination of the necessary boundary layer data for transition prediction, 2) the actual transition prediction approach including the actual transition criterion and, 3) an approach for the analysis of the transition criterion:

- 1) Boundary layer data approach
  - a) Boundary layer code
  - b) RANS solver
  - c) Correlation
  
- 2) Transition modelling approach
  - a) Parabolized stability equations
  - b) Linear stability theory
  - c) Empirical transition criteria
  
- 3) Calculation/evaluation approach
  - a) Designated lines
  - b) Transport equations

## 1) Boundary layer data approach

*a) Boundary layer code* The classical approach to determine the boundary layer data needed for transition prediction is the use of a boundary layer method. Most commonly quasi two-dimensional boundary layer methods are used. They have the advantage, that, by considering the conical flow assumption [16], the three-dimensional boundary layer equations reduce to a form similar to the two-dimensional boundary layer equations. For quasi two-dimensional flows the boundary layer edge velocity can directly be derived from the pressure distribution of the RANS solution. Based on the underlying approximations, the conical boundary layer method can be applied in a very straight forward and efficient way to several line-in-flight cuts (wing sections in flight direction) distributed over a wing-like geometry and thus delivering three-dimensional laminar boundary solutions along these lines. The application of fully three-dimensional boundary layer methods is less straight forward. Generally, the boundary layer edge velocity can not be derived from the pressure distribution and needs to be determined from the RANS solution and possibly also needs to be interpolated to an individual structured surface grid needed for the solution of the boundary layer equations. Additionally, the three-dimensional methods need more complex initial solutions along the inflow boundaries of the computational domain that may not be as easily derivable as for the two-dimensional methods. Overall, this means that three-dimensional boundary layer methods are more demanding in their application and are practically more suitable to rather simple three-dimensional geometries. Generally, boundary layer methods deliver highly accurate boundary layer solutions that are independent on the resolution of the RANS grid but are limited in their general application, for example to less complex geometries and usually to attached flows only.

*b) RANS solver* Most of the geometrical constraints for the boundary layer methods no longer apply if the boundary layer data are directly extracted from the RANS solution. All three-dimensional effects are inherently included in the RANS boundary layer profiles and the accuracy is not compromised by modelling assumptions and approximations as for the boundary layer methods. Boundary layer data can also be determined with high confidence in the vicinity of geometrical obstacles like for example engine pylons of wings, near wing-body-junctions, near the wing tips or, generally, for very complex three-dimensional geometries. Additionally, the analysis and the prediction of transition for separated flows, including transition inside laminar separation bubbles, is feasible with boundary layer velocity profiles from the RANS solution. As will also be addressed within the scope of this work, a reasonable wall-normal resolution of the laminar boundary layer is required for the RANS solver to accurately compute fully three-dimensional boundary layers and to meet the requirements of the used transition prediction methods. This leads to an increased computational effort for the RANS computations compared to the lower demand on grid resolution if the boundary layer data is determined by a separate boundary layer method. Additional difficulties arise with regard to the implementation effort when fully three-dimensional parallel computations are considered or for the accurate determination of the boundary layer edge, essential for the accurate application of certain transition prediction methods. These two latter issues are also subject of the present work.

*c) Correlation* A different concept to determine boundary layer data is recently used more often, however in principle exclusively in conjunction with the application of transition prediction with transport equations approaches. For this, correlations, typically based on flat plate or Falkner-Skan [17] similarity solutions, have been established, that relate local flow quantities to integral boundary layer values. For example, for Falkner-Skan similarity flows, it can be shown, that the ratio between the maximum of the vorticity Reynolds number  $Re_v = (y^2/\nu)(du/dy)$ <sup>1</sup> [18] to the momentum loss Reynolds

---

<sup>1</sup>The vorticity Reynolds number is zero at the wall ( $y = 0$ ) and zero outside of the boundary layer ( $du/dy = 0$ ) and exhibits a local maximum inside the boundary layer.

number ( $Re_{\delta_2} = \delta_2 u_e / \nu$ ) is a function of the pressure gradient, respectively the shape factor  $H_{12}$ , only ( $Re_v / Re_{\delta_2} = f(H_{12})$ , for example  $f(2.59) \approx 2.2$  for zero pressure gradient flat plate flow). Approaches have also been derived to correlate local flow quantities to, for example, pressure gradient parameters and the shape factor [19, 20] or to integral values representative of the cross-flow strength [21]. Typically, these correlations exhibit similar requirements to the computational grid as the extraction of boundary layer profiles directly from the RANS solution. However, the correlated boundary layer values are generally less accurate compared to the computation of integral boundary layer data directly from the boundary layer velocity profile, especially for non-similar and fully three-dimensional flows. In conjunction with a transition prediction approach, the correlations also need further thorough calibration to be applicable for reliable transition prediction. The possibility to express non-local boundary layer data solely by local flow quantities makes the correlation approach very suitable for the application in conjunction with transport equations for transition prediction. The local character also highly simplifies the implementation and parallelization issues of the approach when integrated into a RANS solver environment.

## 2) Transition modelling approach

*a) Parabolized stability equations* The parabolized stability equations [22, 23] describe the amplification of disturbances in a laminar boundary layer, where the disturbances are represented by amplitude functions and wavenumber vectors that, for the general three-dimensional case, slowly vary in longitudinal (streamwise) and lateral direction. The parabolized stability equations account for curvature effects and include non-parallel effects, like, for example, the growth of the laminar boundary layer. In the non-linear formulation of the parabolized stability equations also non-linear effects like modal interactions or secondary instabilities are taken into account. Because of the parabolic nature of the equations the parabolized stability equations can be solved by marching procedures similar to those for the boundary layer equations [24]. The accuracy of the solution of the parabolized stability equation is highly dependent on the accurate determination of the boundary layer velocity profiles used for the stability analysis and an accurate computation of the derivatives of the velocity profiles in wall normal and streamwise direction. An additional challenge in the practical application of the parabolized stability equations is the designation of appropriate initial and boundary conditions. Generally, approaches based on the parabolized stability equations are difficult to operate in an autonomous and automatic way and still need some more correlation to experimental data for the method to be used as a reliable transition prediction approach in engineering applications [25]. However, solutions of the parabolized stability equations are comparable in accuracy to direct numerical simulations, but can be achieved at a much lower computational cost [22].

*b) Linear stability theory* The linear stability theory [13, 26] examines the stability of a laminar boundary layer by investigating the development of small perturbations and is derived from the linearised Navier-Stokes equations. The basic approach is to superimpose instationary harmonic waves as disturbances onto the stationary base flow. In contrast to the non-local parabolized stability equations streamwise changes are locally neglected and thus a locally parallel flow is assumed. The linear stability equations consist of a system of second-order differential equations that form an eigenvalue problem which can, for example, be solved with a matrix method. The accuracy of the solution of the linear stability equations is dependent on the accuracy of the analysed boundary layer profiles and their first and second derivatives in wall normal direction. Linear stability theory is usually applied together with the  $e^N$  method [27, 28] and is today a widely used transition prediction approach, used in computational fluid dynamics for aircraft wing design or simulations of flows around aircraft and general aerodynamic geometries.

*c) Empirical transition criteria* Empirical transition prediction criteria consist of empirical correlations of different parameters, typically based on integral boundary layer data, at the transition location.

Other characteristics like pressure gradient or turbulence intensity are often taken into account. Within the broad range of empirical transition criteria there exist correlations that are based on experimental data, other methods are derived from linear stability theory, for example from stability computations for Falkner-Skan [17] similarity flows. Since the empirical criteria are based on integral boundary layer data they are less sensitive to an accurate computation of the boundary velocity profile and thus are also very robust in their application. However, because of their limited physical modelling approach these methods often lack a certain kind of accuracy with respect to the predicted transition location.

### 3) Calculation/evaluation approach

*a) Designated lines* Generally, transition criteria can be evaluated along lines representative of the streamwise direction. For empirical transition criteria in three-dimensional flows the lines of application typically correspond to inviscid streamlines at the boundary layer edge or sections of a wing, normal to the leading edge or in flight direction. Linear stability theory together with the  $e^N$  method can also be applied along lines that can be determined by sections of a wing, inviscid streamlines or, additionally, trajectories representative of the amplification direction of the disturbances. The same holds for the parabolized stability equations, if the formulation of the stability equations allows the use of line marching procedures for the solution. For the general three-dimensional case the solution procedure advances in two designated directions, using a surface marching approach on a two-dimensional surface patch. Depending on the approach, the lines or surface patches for the application of the approaches need to be computed or defined a priori of the transition prediction and define in a way a separate computational grid for which boundary layer data or characteristics need to be extracted from the basic flow solution and possibly interpolated onto the auxiliary computational grid.

*b) Transport equations* To avoid non-local operations and the determination and calculation of designated lines, transport equations can be a suitable alternative in the application of transition prediction methods. If all essential data is locally available, transport equations can, for example, be used for information transport or the integration of scalar functions and thus can replace line-search or line-integration operations.

Not all of the approaches presented above can be combined with one another easily or in a sensible and direct way, however some combinations have emerged as useful and effective. Following ARNAL et. al. [29], four general approaches to incorporate transition prediction into RANS solvers can be identified: 1) coupling of a RANS solver with a boundary layer code and a stability code, 2) direct coupling of a RANS solver and a stability code, 3) direct implementation of empirical transition criteria into RANS solvers, and 4) transition prediction by transport equations.

Approaches 1) and 2), and, depending on the character of the application of the empirical transition criterion (local vs non-local), approach 3) need the definition of computational lines, respectively auxiliary grids, for which, in the general case, boundary layer velocity profiles need to be extracted from the RANS solution. Additionally, for these profiles the boundary layer edge needs to be detected with more or less high accuracy. However, for the application of boundary layer codes with conical flow assumption the extraction of the surface pressure distribution is sufficient. Approaches 1) and 2) make it also necessary to implement interfaces between the RANS solver and the, typically, external boundary layer and stability codes. These interfaces are needed for the data exchange between the different program parts and the control of the auxiliary codes.

Applied in a sensible and well thought out way approaches 1) to 3) can deliver highly accurate boundary layer solutions for transition prediction and, depending on the prediction method, can deliver physically very reliable transition locations. However, most of the above mentioned characteristics of the transition prediction methods make these approaches complex to implement into a RANS solver environment, especially with regard to a parallel execution of the solution procedure, and sometimes these methods also become very demanding in terms of application from a user perspective.

To avoid most of the implementation and application challenges incorporated in approaches 1) to 3) and consequently to establish a transition prediction methodology that is more compatible with modern CFD solver requirements, increasing attention is being paid to the further development of transport equation approaches for transition prediction. For these methods, to be compatible with a general transport equation approach, boundary layer data is generally approximated by local correlations and empirical transition criteria are applied. The transition criteria can partially be evaluated locally or a transport equation, representative of certain transition onset conditions, is used. For empirical transition criteria that are not formulated locally in their original derivation, transport equations are sometimes used for information transport or the integration of scalar functions. The transition prediction approach is then generally connected to the turbulence model of the RANS solver by the use of an additional transport equation for a value characteristic of the laminar-turbulent intermittency.

#### 1.4. Objective and structure of the work

The present work aims to provide a general and flexible transition prediction methodology for the use with a RANS solver. Based on the previously available transition prediction methods that use linear stability theory, the new approach is intended to extend the applicability of these methods and at the same time reduce the physical approximations incorporated in these methods. This is to be achieved by the application of the stability analysis along inviscid streamlines and by using the RANS data directly as input for the stability analysis. With this approach the application of the linear stability theory is expected to be applicable for complex three-dimensional geometries with fully three-dimensional boundary layer flows including all three-dimensional effects that are directly represented in the RANS boundary layer velocity profiles.

Chapter 2 gives first a short overview of the governing equations of the flow solver, including the turbulence model, used for the present work in section 2.1. The theory of the underlying transition prediction method based on the linear stability theory in form of the  $e^N$  method is presented in section 2.2. The basic methodology and the incorporation of the method in the RANS solver environment is described in section 2.3.

Chapter 3 deals with the specific implementation work of the transition prediction methodology into the RANS solver. The base for the application of the method to flows around complex three-dimensional geometries on appropriate computational grids is the parallelization of the specific elements of the prediction method. This is addressed in section 3.1 and will be taken up again in the following sections, especially for the procedures presented in each of them. First, the approaches for the extraction and determination of boundary layer velocity profiles and boundary layer data from the RANS solution are presented in sections 3.2 and 3.3. A crucial aspect for transition prediction using linear stability theory and velocity profiles from a RANS solution is the accurate detection of the boundary layer edge for each boundary layer velocity profile. This is dealt with separately in section 3.3.2.

One of the basic building blocks of the transition prediction methodology, the determination of the inviscid streamlines, is presented in section 3.4, divided into approaches for two-dimensional and three-dimensional flows. The core of the transition prediction method is the application of the stability analysis. All theoretical considerations for the implementation and the application of the stability analysis as well as the implementation itself are summarized in section 3.5. In the associated subsection special properties of the stability code and the coupling to the main transition prediction method are discussed and theories for automatic and robust application of the stability analysis are presented. The chapter regarding the implementation of the transition prediction methodology is concluded with the description of the actual application of the transition criterion and the interaction of the transition prediction method with the RANS solver in section 3.6, followed by some concluding remarks regarding the general implementation and the scope of the implementation work in section 3.7.

The application and evaluation of the implemented transition prediction method, presented in chapter 4, is divided into a general verification of the method, presented in section 4.1, and the actual validation of the method based on different test cases of varying complexity, presented in section 4.2.

The verification deals with the examination of the parallelization of the method in section 4.1.1, followed by a thorough grid convergence study in section 4.1.2 to determine resolution requirements for transition prediction based on boundary layer velocity profiles from a RANS solution. An exemplary application example for transition prediction around a general complex aircraft configuration is given in section 4.1.3.

The presented approach is validated for two less complex but widespread and often used test cases, namely the two-dimensional flow around an NLF (1)–0416 airfoil and the infinite swept wing flow around an NLF (2)–0415 wing. The description of these two test cases and the evaluation of the application of the transition prediction method is presented in sections 4.2.1 and 4.2.2. The validation is continued with a theoretically more complex test case, a three-dimensional wing with ONERA D profile, which revealed under closer inspection to also represent infinite swept wing flow conditions. This test case is presented in section 4.2.3.

Because of the large number of test conditions, the following validation test case is treated with a special method to derive the correct flow conditions from only a few basic computations. This approach is presented in appendix A.3 and is applied for the transition prediction evaluation for a three-dimensional swept NACA 64<sub>2</sub>-A-015 wing in section 4.2.4. The validation of the transition prediction method is concluded with the investigation of the fully three-dimensional flow around the DLR prolate spheroid in section 4.2.5.

Finally, in chapter 5 a summary of the work and a critical assessment of the transition prediction method is given.

## 2. Methods

A transition prediction methodology within a computational fluid dynamics environment always consists of different aspects. These include a set of equations that describe the flow around a considered geometry and which need to be solved basically. To distinguish between the computation of laminar and turbulent flow, the approach needs the incorporation of some kind of turbulence modelling. And finally, the transition prediction method itself, based on a certain theory and transition criterion, needs to be included.

### 2.1. RANS equations and turbulence model

The Navier-Stokes equations describe the motion of compressible linear-viscous Newtonian fluids. They consist of equations for conservation of mass, momentum and energy and are written in differential form using tensor notation and Einstein summation convention as [30]

$$\begin{aligned} \frac{\partial \rho}{\partial t} + \frac{\partial}{\partial x_i} (\rho u_i) &= 0 \\ \frac{\partial}{\partial t} (\rho u_i) + \frac{\partial}{\partial x_j} (\rho u_i u_j) &= -\frac{\partial p}{\partial x_i} + \frac{\partial \tau_{ij}}{\partial x_j} \\ \frac{\partial}{\partial t} (\rho E) + \frac{\partial}{\partial x_j} (\rho u_j H) &= \frac{\partial}{\partial x_j} (u_i \tau_{ij}) + \frac{\partial}{\partial x_j} \left( \lambda \frac{\partial T}{\partial x_j} \right) \end{aligned} \quad (1)$$

with  $u_i$  the velocity component in the respective coordinate direction  $x_i$ ,  $T$  the temperature,  $E$  the total energy and  $H$  the total enthalpy. The viscous stress tensor  $\tau_{ij}$ , utilizing Stoke's hypothesis, is given as:

$$\tau_{ij} = \mu \left[ \left( \frac{\partial u_i}{\partial x_j} + \frac{\partial u_j}{\partial x_i} \right) - \frac{2}{3} \frac{\partial u_k}{\partial x_k} \delta_{ij} \right] \quad (2)$$

If, for convenience, the corresponding notations for Reynolds- (and Favre-) averaging are omitted, equation 1 represents the Reynolds averaged Navier-Stokes (RANS) equations. Under the assumption of the Boussinesq hypothesis<sup>2</sup> the dynamic viscosity coefficient  $\mu$  in equation 1 is expressed as an effective value, given as the sum of a laminar and a turbulent component:

$$\mu = \mu_{lam} + \mu_{turb} \quad (3)$$

With the thermal counterpart of the Boussinesq hypothesis the same holds for the thermal conductivity coefficient  $\lambda$ , which is also expressed as an effective value of the sum of a laminar and a turbulent component:

$$\lambda = \lambda_{lam} + \lambda_{turb} = c_p \left( \frac{\mu_{lam}}{Pr_{lam}} + \frac{\mu_{turb}}{Pr_{turb}} \right) \quad (4)$$

$Pr_{lam}$  and  $Pr_{turb}$  are the laminar and turbulent Prandtl numbers and are assumed to be constant ( $Pr_{lam} = 0.72$  and  $Pr_{turb} = 0.9$ ) and  $c_p$  is the specific heat coefficient at constant pressure ( $c_p = \gamma(\gamma - 1)/R$ ). The heat capacity ratio  $\gamma$  (also referred to as isentropic coefficient) is given as  $\gamma = 1.4$  and the specific gas constant  $R$  is specified as  $R = 287 \text{ m}^2/(\text{K}\cdot\text{s}^2)$ .

The connection of pressure, density and temperature is defined by the ideal gas law ( $p = \rho RT$ ) and the laminar viscosity  $\mu_{lam}$  is computed from the Sutherland formula [31] (with Sutherland reference viscosity  $\mu_s$  and Sutherland reference temperature  $T_S$ ):

$$\mu_{lam} = \mu_s \left( \frac{T}{T_S} \right)^{\frac{3}{2}} \frac{T_S + 110K}{T + 110K} \quad (5)$$

<sup>2</sup>omitting the term  $(2/3)\rho k\delta_{ij}$  in the present representation, which is neglected for the Spalart-Allmaras turbulence model used in the present work

The only remaining quantity to be determined for the closure of the set of equations (Eqs. 1) is the turbulent (or eddy) viscosity  $\mu_{turb}$  in equation 3, which is obtained from a turbulence model.

The Spalart-Allmaras one-equation turbulence model is a linear eddy-viscosity models that utilizes a single transport equation for a modified kinematic eddy viscosity  $\tilde{\nu}$  (SA viscosity). The SA viscosity is related to the kinematic eddy viscosity by a relation  $\nu_{turb} = \tilde{\nu} f_{v1}$ .

In tensor notation the Spalart-Allmaras turbulence model can be written as [32]

$$\frac{\partial \tilde{\nu}}{\partial t} + u_j \frac{\partial \tilde{\nu}}{\partial x_j} = c_{b1} (1 - f_{t2}) \tilde{S} \tilde{\nu} - \left[ c_{w1} f_w - \frac{c_{b1}}{\kappa^2} f_{t2} \right] \left( \frac{\tilde{\nu}}{d} \right)^2 + \frac{1}{\sigma} \left[ \frac{\partial}{\partial x_j} \left( (\nu_{lam} + \tilde{\nu}) \frac{\partial \tilde{\nu}}{\partial x_j} \right) + c_{b2} \frac{\partial \tilde{\nu}}{\partial x_i} \frac{\partial \tilde{\nu}}{\partial x_i} \right] \quad (6)$$

The laminar kinematic viscosity is given by  $\nu_{lam} = \mu_{lam}/\rho$  and  $d$  is the distance to the nearest wall. The turbulent eddy viscosity in equation 3 is computed from

$$\mu_{turb} = \rho \tilde{\nu} f_{v1} \quad (7)$$

with

$$f_{v1} = \frac{\chi^3}{\chi^3 + c_{v1}^3} \quad \chi = \frac{\tilde{\nu}}{\nu_{lam}} \quad c_{v1} = 7.1$$

The terms on the right-hand side of equation 6 are the production, destruction and diffusion terms, with model coefficients

$$c_{w1} = \frac{c_{b1}}{\kappa^2} + \frac{1 + c_{b2}}{\sigma} \quad c_{b1} = 0.1355 \quad c_{b2} = 0.622 \quad \sigma = 2/3 \quad \kappa = 0.41$$

and can be broken down to

$$\begin{aligned} S_{prod} &= c_{b1} (1 - f_{t2}) \tilde{S} \tilde{\nu} \\ S_{dest} &= \left[ c_{w1} f_w - \frac{c_{b1}}{\kappa^2} f_{t2} \right] \left( \frac{\tilde{\nu}}{d} \right)^2 \\ S_{diff} &= \frac{1}{\sigma} \left[ \frac{\partial}{\partial x_j} \left( (\nu_{lam} + \tilde{\nu}) \frac{\partial \tilde{\nu}}{\partial x_j} \right) + c_{b2} \frac{\partial \tilde{\nu}}{\partial x_i} \frac{\partial \tilde{\nu}}{\partial x_i} \right] \end{aligned} \quad (8)$$

$\tilde{S}$ , appearing in the production term, is a scalar velocity gradient parameter and is defined as a modified vorticity based on the magnitude of the vorticity  $\Omega$ :

$$\tilde{S} = \Omega + \frac{\tilde{\nu}}{\kappa^2 d^2} f_{v2} \quad f_{v2} = 1 - \frac{\chi}{1 + \chi f_{v1}}$$

The destruction term is controlled by

$$f_w = g \left( \frac{1 + c_{w3}^6}{g^6 + c_{w3}^6} \right) \quad g = r + c_{w2} (r^6 - r) \quad r = \min \left( \frac{\tilde{\nu}}{\tilde{S} \kappa^2 d^2}, 10 \right) \quad c_{w2} = 0.3 \quad c_{w3} = 2$$

In the production and the dissipation term the function  $f_{t2}$  appears, which is used for modelling of the laminar-turbulent transition, and is given by

$$f_{t2} = c_{t3} \cdot \exp(-c_{t4} \chi^2) \quad c_{t3} = 1.2 \quad c_{t4} = 0.5$$

The  $f_{t2}$  function is deactivated in the formulation of the Spalart-Allmaras turbulence model that is used in the present work:  $f_{t2} = c_{t3} = 0$ . Transition is considered by limiting the production to be lower than the destruction in laminar regions

$$S_{prod} - S_{dest} = \min(S_{prod} - S_{dest}, 0) \quad (9)$$

with

$$\frac{\partial \tilde{v}}{\partial t} + u_j \frac{\partial \tilde{v}}{\partial x_j} = S_{prod} - S_{dest} + S_{diff} \quad (10)$$

## 2.2. Linear stability theory and $e^N$ method

The classical local linear stability theory evaluates the stability of a laminar boundary layer by examining the development of small disturbances. Several approaches exist to solve the stability equations and to use the linear stability theory for transition prediction. A thorough insight into the theory is for example given in references [13] and [33]. Here, the focus is on the approaches and theories eventually used within the scope of this work.

The principal approach of the linear stability theory is the superposition of a stationary mean flow  $q_0$  and an instationary disturbance  $\hat{q}$  [34]

$$q = q_0(x, y, z) + \hat{q}(x, y, z, t) \quad (11)$$

where  $x, y, z$  is a cartesian or curvilinear orthogonal coordinate system. The disturbance  $\hat{q}$  is assumed to be a harmonic wave

$$\hat{q}(x, y, z, t) = \hat{q}(z)e^{i(\alpha x + \beta y - \omega t)} \quad (12)$$

where  $\alpha, \beta$  and  $\omega$  are, in general, complex numbers. The complex amplitude function  $\hat{q}(z)$ , representing any fluctuating quantity (velocity, pressure, temperature), depends on the wall normal coordinate  $z$  only [13]. Inserting this approach into the Navier-Stokes equations leads to a system of non-linear disturbance differential equations, which, under the assumption of small disturbances, can be linearised.

The resulting linear stability equations form a system of second-order differential equations for the amplitude functions  $\hat{u}(z), \hat{v}(z), \hat{w}(z), \hat{p}(z)$  and  $\hat{T}(z)$  (velocity components, pressure and temperature). The equations can be written formally as [34]:

$$\frac{d^2}{dz^2} \begin{pmatrix} \hat{u}(z) \\ \hat{v}(z) \\ \hat{w}(z) \\ \hat{p}(z) \\ \hat{T}(z) \end{pmatrix} + A(\alpha, \beta, \alpha^2, \beta^2) \frac{d}{dz} \begin{pmatrix} \hat{u}(z) \\ \hat{v}(z) \\ \hat{w}(z) \\ \hat{p}(z) \\ \hat{T}(z) \end{pmatrix} + B(\alpha, \beta, \alpha^2, \beta^2) \begin{pmatrix} \hat{u}(z) \\ \hat{v}(z) \\ \hat{w}(z) \\ \hat{p}(z) \\ \hat{T}(z) \end{pmatrix} = \omega C \begin{pmatrix} \hat{u}(z) \\ \hat{v}(z) \\ \hat{w}(z) \\ \hat{p}(z) \\ \hat{T}(z) \end{pmatrix} \quad (13)$$

The (5,5)-matrices  $A, B$  and  $C$  depend on basic flow properties (Mach number, Reynolds number), on the local velocity and temperature profiles of the undisturbed laminar boundary layer and on the first and second derivatives in wall normal direction  $z$  of these profiles. Following the parallel flow assumption, the wall normal velocity component  $w_0$  and its first and second derivatives are set to zero and the  $x$ - and  $y$ -derivatives of  $u_0, v_0, p_0$  and  $T_0$  are neglected. In other words, the parallel flow approximation implies that the quantities of the stationary mean flow do not vary significantly in flow direction and hence are assumed to be functions of the wall normal coordinate  $z$  only [13]. This also means that stability at a particular station  $(x, y)$  in the boundary layer is determined locally, independent of all other stations.

Generally, a distinction between spatial and temporal theory can be made. In spatial theory  $\alpha$  and  $\beta$  are complex and  $\omega$  is real and in temporal theory  $\alpha$  and  $\beta$  are real and  $\omega$  is complex. Following temporal theory, the disturbances are

$$\hat{q}(x, y, z, t) = \hat{q}(z)e^{\omega_i t} e^{i(\alpha x + \beta y - \omega_r t)} \quad (14)$$

Here,  $\omega_i$  is the temporal amplification rate and, depending on the sign of  $\omega_i$ , the disturbances are amplified ( $\omega_i > 0$ ), damped ( $\omega_i < 0$ ) or neutral ( $\omega_i = 0$ ).  $\omega_r$  represents the frequency of the disturbance

wave and  $\alpha = \alpha_r$  and  $\beta = \beta_r$  form the wavenumber vector which gives the spatial propagation direction of the disturbance wave [13].

With homogenous boundary conditions and in temporal theory the stability equations (eq. 13) form an eigenvalue problem which is linear in the complex eigenvalue  $\omega$  if the wave numbers  $\alpha$  and  $\beta$  are prescribed. Non-trivial solutions exist only for certain combinations of  $\alpha$ ,  $\beta$  and  $\omega$ , leading to a dispersion relation in the form of  $\omega = f(\alpha, \beta)$  [34]. An advantage of using temporal theory and having stability equations which are linear in  $\omega$  is that a matrix method can be used to solve the eigenvalue problem [34].

In temporal theory the disturbances amplify or damp in time. If  $A$  represents the amplitude of any of the fluctuating flow variables  $\hat{q}(z)$  at any value of the wall normal coordinate  $z$  then the temporal amplification rate  $\omega_i$  follows from eq. 14 and is given by [26, 33]:

$$\omega_i = \frac{1}{A} \frac{dA}{dt} = \frac{d(\ln A)}{dt} \quad (15)$$

According to reference [26],  $A$  can be referred to as the amplitude of the wave, since  $A$  is independent of any specific flow variable and the wall distance  $z$ .

It is, however, possible to transform the temporal amplification rate  $\omega_i$  into a spatial amplification rate and to obtain a statement of the relative change of the amplitude of the disturbances in space. Using the Gaster transformation [35], the temporal growth can be converted into a spatial growth by using the group velocity vector<sup>3</sup>  $\vec{v}_g$  [13]. The group velocity vector is defined in temporal theory as:

$$\vec{v}_g = \left( \frac{\partial \omega_r}{\partial \alpha} \quad \frac{\partial \omega_r}{\partial \beta} \right) \quad (16)$$

The group velocity is the velocity at which energy is transported in conservative systems [13, 34]. With the norm of the group velocity vector  $\vec{v}_g$ , the relation between temporal amplification rate and spatial amplification rate is given by [13]:

$$\sigma_g = \omega_i / |v_g| \quad (17)$$

This transformation is technically only valid for small amplifications rates in the neighbourhood of the neutral curve, but gives sufficiently accurate results also for larger amplification rates [34]. After the conversion of temporal growth into spatial growth, the change of the amplitude  $A$  in space is defined along the group velocity trajectory  $s_g$  [13]:

$$\sigma_g = \frac{1}{A} \frac{dA}{ds_g} = \frac{d(\ln A)}{ds_g} \quad (18)$$

The spatial variation of the relative amplitude  $A/A_0$  can be computed by integrating the amplification rate along the group velocity trajectory  $s_g$ :

$$\ln(A/A_0) = \int_{s_{g,0}}^{s_g} \sigma_g ds_g = \int_{s_{g,0}}^{s_g} \frac{\omega_i}{|v_g|} ds_g \quad (19)$$

Along the group velocity trajectory the frequency stays constant for a single wave [34]. Generally, a specific wave is damped upstream of  $s_{g,0}$ . Downstream of  $s_{g,0}$  the wave is amplified until it may eventually be damped again further downstream (Fig. 4). For any point  $s_g > s_{g,0}$  the amplitude of the wave  $A(s_g)$  can be related to its initial amplitude  $A_0$  at  $s_{g,0}$  with equation 19. The point  $s_{g,0}$  is referred to as neutral or indifference point and the streamwise progress of the logarithm of the relative amplitude of a single wave is denoted as  $N$ -factor:

$$N_{wave} = \ln(A/A_0)_{wave} \quad (20)$$

<sup>3</sup>The group velocity vector is generally complex but the imaginary parts are usually neglected.

Thus,  $N_{wave}$  represents the amplification factor of the disturbance. If the variation of  $A/A_0$  is considered not only for a single wave but for various disturbance waves, the maximum amplification factor at each  $s_g$  is given by the envelope (Fig. 4) of the  $N_{wave}$ -distribution:

$$N_{env} = \max [\ln (A/A_0)] \quad (21)$$

The envelope at a certain streamwise station is the tangent to the  $N_{wave}$  curve of the wave that underwent the largest amplification since entering the unstable region [13]. Often, both  $N_{wave}$  and  $N_{env}$  are referred to just as  $N$ -factor. To compute the  $N$ -factor, different integration strategies exist. A general method is to separate the transition mechanisms described by linear local stability theory and to introduce different  $N$ -factors and hence different integration strategies for stream-wise and cross-flow instabilities [13, 34].

For streamwise instabilities, the frequency and the propagation direction for the waves can be prescribed [34]. Waves travelling in the direction of the inviscid flow are known as Tollmien-Schlichting waves [11] and the corresponding  $N$ -factor is denoted by  $N_{TS}$ . This  $N_{TS}$ -factor is mainly valid for low Mach numbers since for transonic and supersonic flows waves which travel in a direction differently to the inviscid flow direction eventually become more amplified than the Tollmien-Schlichting waves. The envelope of the  $N_{TS}$ -factor is computed by considering different amplified frequencies and, if the stability equations are formulated in a coordinate system aligned with the inviscid flow direction, by setting  $\beta = 0$ .

In the case of cross-flow instabilities the frequency and the wave length can be prescribed, leading to the cross-flow  $N$ -factor  $N_{CF}$  [34]. The initial idea behind this approach is based on the experimental observation, that a zebra pattern with stripes of approximately constant distance can be seen if transition is visualized with a sublimation technique [34]. This pattern is created by stationary cross-flow vortices with approximately constant wave length. For these stationary cross-flow instabilities, the envelope of the  $N_{CF}$ -factor is computed by considering different amplified wave lengths and setting the frequency to 0 Hz.

With the local linear stability theory  $N$ -factor curves and hence the variation of the relative amplitude  $A/A_0$  in stream-wise direction can be computed but the actual amplitudes  $A$  and  $A_0$  remain unknown. This means, if it is assumed that transition occurs when the amplitude  $A$  of the most amplified wave exceeds a critical value  $A_{crit}$  [13], an additional condition is needed to use the linear stability theory for transition prediction. This additional condition was independently suggested by SMITH and GAMBERONI [27] and VAN INGEN [28]. They observed for amplified Tollmien-Schlichting waves that the critical  $N$ -factor ( $N_{crit}$ ) at the measured transition point was nearly constant. This means that the initial amplitude  $A_0$  of the most unstable disturbance is amplified by a constant factor  $e^{N_{crit}}$  from the indifference point to the transition point and the prediction method is consequently termed  $e^N$  method:

$$A_{crit} = A_0 e^{N_{crit}} \quad (22)$$

The requirement to prescribe a critical  $N$ -factor adds a certain kind of empiricism to this method and the transition prediction with linear stability theory and  $e^N$  method is often referred to as a semi-empirical method. The crucial point is that the initial amplitude  $A_0$  and hence the critical  $N$ -factor is a measure of the disturbance environment [29] and that for a different environment a different critical  $N$ -factor needs to be used.

For Tollmien-Schlichting type transition Mack [26] showed that the initial amplitude  $A_0$  can be related to the turbulence level  $Tu$  and that  $A_0$  is approximately proportional to  $Tu^{2.4}$ . Based on experimental transition data for incompressible flat plate boundary layers the proposed correlation of turbulence level and critical  $N$ -factor is:

$$N_{TS,crit} = -8.43 - 2.4 \ln (Tu) \quad (23)$$

An expression, similar in form, exists for stationary cross-flow type transition. Crouch et. al. [36] relate the critical cross-flow  $N$ -factor for stationary cross-flow instabilities in a low turbulence envi-

ronment to the surface roughness of the considered geometry. Based on transition experiments for an infinite swept wing geometry [37] the following correlation was derived:

$$N_{CF,crit} = 2.3 - \ln(h_{rms}/\delta_1) \quad (24)$$

The critical cross-flow  $N$ -factor is based on the non-dimensionalized root-mean-square-value of the roughness height  $h_{rms}$ . For the non-dimensionalization the displacement thickness  $\delta_1$  at the indifference point of the critical wave is used.

Generally, the critical  $N$ -factors can also be determined using flight tests or wind tunnel tests. However, the so determined critical  $N$ -factors are only valid for the environment for which they are calibrated. This may for example lead to the restriction that a certain calibrated critical  $N$ -factor is strictly speaking only valid for a certain wind tunnel, namely exact that wind tunnel in which the calibration experiments were conducted.

An interaction of Tollmien-Schlichting and cross flow waves cannot be evaluated by linear local stability theory. Instead, if the approach of separating the transition mechanisms and considering streamwise  $N$ -factors and cross-flow  $N$ -factors is used ( $2N$ -factor method), a curve  $N_{CF,crit} = f(N_{TS,crit})$ , respectively  $N_{TS,crit} = f(N_{CF})$  is used. With this curve possible interactions of Tollmien-Schlichting and cross-flow waves can be modelled. Based on the convexity of the stability boundary given by the  $N_{TS,crit}$ - $N_{CF,crit}$ -curve, the intensity of the interaction is determined (see also Sec. 3.6).

### 2.3. Transition prediction methodology

For automatic transition prediction in Navier-Stokes computations for general three-dimensional configurations a transition prediction method has been developed and implemented into an unstructured compressible RANS solver. The commencement of the initial work is documented in references [38] and [39] and the fundamental elaboration of the methodology can be found in reference [40]. Further development paths, extensions and validations of the transition prediction method are presented in references [41], [42], [43] and [44]. Additional validation, a comprehensive overview and thorough evaluation of the method are given in references [45], [46], [25] and [47].

The transition prediction methodology consists of a coupled program system (Sec. 2.3.1) in form of a transition prediction module that is included in the DLR RANS code TAU [48]. The transition prediction method utilizes an external stability code (Sec. 2.3.2) for the application of the linear stability theory in form of the  $e^N$  method (Sec. 2.2). Details of the implementation of the transition module into the RANS solver are summarized in chapter 3.

#### 2.3.1. Coupled program system

The presented transition prediction methodology is included in a coupled program system, consisting of a RANS solver and a transition prediction module. Included in the transition module are two additional external stand-alone programs. The transition module supports the use of different empirical and semi-empirical transition criteria with focus in the present work on the application of the linear stability theory in form of the  $e^N$  method.

The application of the stability analysis and the transition criteria is based on boundary layer data that are directly extracted from the RANS solution. Alternatively, a boundary layer code [49], included as an external program accessible via file I/O in the transition module, can be used for the determination of the corresponding boundary layer data. The boundary layer code, utilizing the conical flow assumption [16], is generally limited to infinite swept wings and swept, tapered wings with high aspect ratio. The boundary layer data from the boundary layer code is only used for the computation of comparative and reference solutions in the scope of the presented work, implementation and validation aspects can be found in references [40] and [25]. In the presentation of the present work, emphasis has been placed on the accurate extraction of the necessary boundary layer data directly from the RANS solution.

For the presented method, the evaluation of the  $e^N$  method is performed along inviscid streamlines. For the application of the linear stability theory, the inviscid streamline is a sufficiently accurate representation of the group velocity trajectory. The group velocity trajectory in turn is a suitable integration path for the computation of the  $N$ -factor to be evaluated for the  $e^N$  method.

In the framework of the transition prediction methodology, the transition module is coupled to the RANS solver TAU of the German Aerospace Center (DLR) [48] (Fig. 5). The DLR TAU code is an unstructured compressible RANS solver for the simulation of viscous and inviscid external three-dimensional flows. The solver uses unstructured grids by utilizing a dual grid approach with a primary and a secondary grid. The primary grid describes the geometry and the spatial discretization around the geometry based on polyhedral elements with triangular and quadrilateral surfaces. The secondary grid is constructed from the primary grid and forms the control volumes for which the fluxes are computed. For the secondary grid a cell vertex grid metric or a cell centered grid metric can be used. For parallel computations a domain decomposition approach is used, where the grids are divided into a number of subdomains using a partitioning algorithm.

The flow solver is based on a finite volume approach and time integration can be carried out by using a multi-stage Runge-Kutta scheme or an implicit lower-upper symmetric Gauss-Seidel (LU-SGS) scheme. For steady state computations the convergence is accelerated by a local time-stepping approach, different residual smoothing methods and a multi-grid technique based on agglomerated coarse grids. The fluxes are computed using one of various upwind schemes with linear reconstruction for second-order accuracy or a second-order central scheme employing scalar or matrix artificial dissipation. For the improvement of the solution accuracy for incompressible flows low Mach number preconditioning can be applied.

Turbulent flows are modelled using different variants of one-equation Spalart-Allmaras type models, two-equation  $k-\omega$  type models or explicit algebraic Reynolds stress models. For scale-resolving simulations different hybrid RANS/LES models are available and a  $\gamma-Re_\theta$ -based transport equation approach can be used for transitional flows. Transitional flows can also be computed with predefined transition lines or with transition prediction using the method presented here. For these computations the turbulent production of the respective turbulence model is suppressed in the regions of the flow field designated as being laminar.

The transition module is divided into two program parts (Fig. 5). One part can be considered as a preprocessing step and is accessed from the RANS solver directly before the solver iterations start. The other part consists of the main transition module, comprising the actual transition prediction, and is called regularly from the solver. In the preprocessing step, parameters controlling the transition prediction are read and data not depending on the flow solution, mainly geometrical data, are processed (Sec. 3.2). In this step, viscous wall surface points are identified and special characteristics, for example sharp edges, of the geometry are determined. For each viscous wall surface point wall normal lines are identified. Along these lines the flow solution will eventually be interpolated to determine the boundary layer data.

The transition prediction is an iterative process itself within the actual RANS solver iterations (Fig. 5). The solution process of the RANS solver is regularly interrupted, ideally when the flow solution has reached a sufficiently high convergence level, and new transition locations are determined. For this, the general procedure shown in figures 6 and 7 is executed at each transition prediction step. For all viscous surface points of the geometry, boundary layer profiles are interpolated from the RANS solution along wall normal lines (Sec. 3.3.1). For each of the boundary layer profiles the boundary layer edge is detected (Sec. 3.3.2) and general boundary layer data are computed. The vectors of the velocity at the boundary layer edge are projected onto the surface of the geometry and are used for the calculation of inviscid streamlines (Sec. 3.4.1).

Starting at user defined starting points (Fig. 7(a)) the streamline integration is carried out (Fig. 7(b)) based on the projected edge velocity vectors. Using the same procedure as before for all of the

viscous wall surface points, boundary layer profiles are now interpolated from the RANS solution based on the coordinates defining the streamlines. For two-dimensional and quasi-two-dimensional flows the streamline computation can be omitted and data is directly extracted along the geometry (Sec. 3.4.2).

After all boundary layer profiles are determined along the streamlines, the stability analysis is started (Sec. 3.5) using an external stability code (Sec. 2.3.2), accessible via file I/O. The application of the stability code is fully automated and carried out in two consecutive executions of the external program, for the estimation of unstable frequencies/wave length and the actual computation of amplification rates (Sec. 3.5.1).

The stability analysis yields amplification rates for each amplified mode (Sec. 3.5.3), which are integrated along inviscid streamlines, or in the case of two- and quasi-two-dimensional flows along the group velocity trajectory, to give a series of  $N$ -factor curves (Sec. 3.5.2). The envelopes of the  $N$ -factor are compared to critical limiting  $N$ -factors, applying the  $2N$ -factor strategy, treating the  $N$ -factors for Tollmien-Schlichting and cross flow instabilities independently (Sec. 3.6). The application of the transition criterion gives single transition locations for every streamline (Fig. 7(c)), which are connected in the case of three-dimensional flows to give a polygonal line representing the transition line (Fig. 7(d)), and new laminar and turbulent regions in the flow solver are designated. In the laminar regions the turbulent production of the respective turbulence model is suppressed when the solver iterations in the RANS solver are resumed.

The transition prediction module supports parallel computing (Sec. 3.1), however parallelization regarding the transition prediction module is considered as the ability to process partitioned RANS solutions. A possible performance gain in terms of overall computational time does not have the highest priority and is not fully possible anyway. This is for example based on the unequal distribution of data needed for transition prediction over the computational domains or the execution of the external sequential stability code (Sec. 4.1.1).

### 2.3.2. Stability solver

The stability code LILO [50] is a sequential computer code written in standard Fortran 77. It can be used for an efficient stability analysis of three-dimensional laminar boundary layers and the calculation of amplification rates and  $N$ -factor curves. The code uses the temporal theory for the solution of the stability equations (Sec. 2.2) for compressible or incompressible flows. The temporal amplification rates are transformed into spatial amplification rates using an extended Gaster transformation [33]. LILO allows utilizing linear local and non-local stability theory. Stability computations can be performed with the consideration of curvature effects [51]. For the amplification rate and  $N$ -factor computation different integration strategies can be used, among them the prescribed-frequency/prescribed-propagation-direction integration strategy for the calculation of Tollmien-Schlichting amplifications and the prescribed-frequency/prescribed-wavelength integration strategy for the calculation of cross-flow amplifications (Sec. 2.2).

The stability equations in LILO are formulated in a streamline coordinate system, aligned to the inviscid flow direction at the boundary layer edge. This means, for example in equations 13 and 14,  $x$  represents the streamwise direction and  $y$  the cross-flow direction and, accordingly,  $\alpha$  and  $\beta$  are the wave numbers in streamwise and cross-flow direction.

In temporal theory, the stability equations (eq. 13) form a generalized eigenvalue problem for the complex eigenvalue  $\omega$ . In LILO, the generalized eigenvalue problem is analytically transformed into a standard eigenvalue problem. This is done by explicitly computing the inverse of the matrix  $C$  in equation 13 and multiplying equation 13 by  $C^{-1}$ .

For the amplitude functions of the velocities and the temperature, in case of a non-adiabatic wall, Dirichlet boundary conditions at the wall are used. For an adiabatic wall a Neumann boundary condition for the temperature amplitude function can also be used:

$$\hat{u}(0) = 0 \quad \hat{v}(0) = 0 \quad \hat{w}(0) = 0 \quad \hat{T}(0) = 0 \quad \text{or} \quad d\hat{T}(0)/dz = 0 \quad (25)$$

The amplitude functions follow an exponential decay with increasing distance to the wall. The theoretical infinite domain  $[0, \infty]$  is thus replaced by a finite domain  $[0, z_\infty]$ , where  $z_\infty$  is set to a sufficiently large value. The outer boundary conditions are then defined as Dirichlet boundary conditions, prescribing vanishing amplitudes for all disturbances:

$$\hat{u}(z_\infty) = 0 \quad \hat{v}(z_\infty) = 0 \quad \hat{w}(z_\infty) = 0 \quad \hat{p}(z_\infty) = 0 \quad \hat{T}(z_\infty) = 0 \quad (26)$$

The wall normal coordinate  $z$  is non-dimensionalized using the displacement thickness  $\delta_1$  of the stream-wise velocity profile. Following the theory for laminar flat plate boundary layers [11] the boundary layer approximately extends from  $z/\delta_1=0$  to  $z/\delta_1 \approx 3$ . The default value for  $z_\infty/\delta_1$  is then taken to be 200. An algebraic stretching function is used to transform the wall normal coordinate  $z/\delta_1$  to a new, non-equidistant grid, independent of the original resolution of the velocity and temperature profiles. The initial velocity and temperature profiles and their first and second derivatives are interpolated onto the new grid using local cubic splines. If the interpolated profiles are resolved with  $n$  grid points the eigenvalue problem is represented by a  $5n$  complex band matrix with a bandwidth of 19 elements [51]. A complete eigenvalue spectrum can be computed with a QR-decomposition, for the computation of a single eigenvalue a generalized inverse Rayleigh iteration for complex band matrices [52] is used. Typically, the computational effort for the QR-decomposition is proportional to  $125n^3$  whereas the effort of the inverse Rayleigh iteration scales with  $5n$ .

The computation of amplification rates is performed in two stages. First, an amplified eigenvalue is computed and a frequency range for Tollmien-Schlichting modes or a wave length range for cross-flow modes is determined. Second, based on the results of the first step, the amplification rates and the  $N$ -factor curves are computed.

The complete eigenvalue spectrum is computed in the first stage at a user defined initial station with prescribed values of the wave numbers  $\alpha$  and  $\beta$ . For the prescribed-frequency/prescribed-propagation-direction strategy for amplified Tollmien-Schlichting waves  $\beta$  is set to zero and  $\alpha$  is specified by the user and typically in the range of  $\alpha = 0.15$  to  $\alpha = 0.30$ . For cross-flow waves with the prescribed-frequency/prescribed-wavelength strategy the propagation direction  $\Psi = \tan^{-1}(\beta/\alpha)$  is approximated with the help of a database method for travelling cross-flow waves in three-dimensional, incompressible boundary layers [53]. It is assumed, that for relatively low frequencies, the direction of the most amplified cross-flow wave for travelling cross-flow is a sufficiently good approximation of the propagation direction for stationary cross-flow. With a suitable estimate of the wave length  $\lambda$  based on approximations from the boundary layer thickness [50] the wave numbers  $\alpha = \lambda \cos(\psi)$  and  $\beta = \lambda \sin(\psi)$  can be determined.

It has to be understood that, at this point,  $\alpha$  and  $\beta$  just need to be more or less good approximations, which ideally lead to the computation of an amplified eigenvalue. With specified values of  $\alpha$  and  $\beta$  the eigenvalue spectrum can be computed using the QR-decomposition. This is done starting at the initial station and marching downstream from there on until an amplified mode is found. If an amplified mode is found based on the initial values of  $\alpha$  and  $\beta$ , the frequency and the wave length are determined. Depending on the considered strategy, either the frequency or the wave length is kept constant, and the considered amplified mode is traced upstream and downstream until it is no longer amplified. Near the two bounding points of the unstable region, one upstream and one downstream of the initial point, the frequency/wave length is respectively increased or decreased, until the investigated mode is again not longer amplified. This procedure is done to estimate the maximum extension of the indifference curve of the stability diagram. This stability diagram shows the range of amplified waves as a function of frequency  $f$  or wave length  $\lambda$  over the streamwise distance  $x$  [13]. The upper and lower overall limits of the frequencies/wave lengths give an estimate of the range of amplified frequencies/wave lengths to be investigated for the amplification rate and  $N$ -factor calculation.

In the next stage, the actual computation of the amplification rates is performed. Starting with the amplified complex eigenvalue determined in the first part and investigating the previously determined spectrum of frequencies/wave length for each station and for each mode the amplification rate

is computed. The amplification rates can then be integrated considering the group velocity direction to determine  $N$ -factor curves for each mode.

Except for the computation of the whole eigenvalue spectrum, the inverse Rayleigh iteration is used for the computation of the complex eigenvalues. The Rayleigh iteration starts with an initial guess of the complex eigenvalue, which is initially the result of the QR-decomposition and in the following the value from the previous station for the same mode or the value from a different mode with different frequency/wave length at the same station.

### 3. Implementation

Based on previous work on transition prediction for three-dimensional flows with the DLR flow solver TAU [54, 38] the current implementation of the transition module has been newly rebuilt with special focus on the parallelization of the transition prediction approach and the incorporation of a stability code for the computation of amplification rates and  $N$ -factor curves. Initially, the transition prediction approach was directly and closely integrated in the programming structure of the actual solver part of TAU. During the rebuilt with all the extension and improvements now included, the approach became the character of a separate module, less closely coupled to the RANS solver. However, the transition prediction module works on the same data structure as the TAU code but is now placed in a separate library where it is part of several TAU program libraries.

#### 3.1. Overview of parallelization

The DLR TAU code uses a domain decomposition principle [55] for parallel computations: for a given number  $p$  of processors the computational grid is divided into  $p$  subgrids, respectively subdomains. Each of the processors computes on one of the subgrids. A continuous communication between the processes is performed on points lying in the overlap region between a certain domain and its neighbour domains using the message passing interface protocol MPI [56]. Only local data are communicated, that means data are only exchanged for grid points having a direct neighbour in another domain. In contrast to this, non-local data have to be communicated for the transition prediction process.

Parallelization by means of the transition prediction module is needed for the determination of wall-normal lines, the assembly of boundary layer profiles along the wall-normals, the determination of boundary layer data from the boundary layer profiles and the calculation of streamlines. The calculation of this data in form of lines is effectively an ordered assembly of a list of grid points (Figs. 8 and 9) along which data needs to be interpolated from the flow solution. The points on the lines are gathered, beginning at starting points (i.e. surface points, user-defined starting points) and ending at user-defined or geometrically provided endpoints. The assembly of the points follows more or less predefined lines (wall-normal vectors and streamlines). A limit of the determination of the lines for parallel computations is a domain boundary. In this case, the endpoints of the lines are communicated to the neighbour domain where they serve as new start points for another loop of the assembly of the lines. Thus, for parallel computations, a single line may be divided into several parts, where each part lies in a different domain. Data can then be interpolated along these line parts from the flow solution within the corresponding domain. The line parts with their interpolated data then need to be merged to be able to access the data as a whole along the complete line.

The data of the boundary layer profiles for each viscous wall point are saved in the domain where the base point of the boundary layer is located. Similar to this, the data of the boundary layer profiles along the streamlines are saved together with the remaining data (e.g. geometrical data) of the streamline on different processes. For this, a virtual distribution of the streamlines over all domains is done. An exactly evenly distribution is achieved if the number of streamlines  $n$  is an integer multiple  $i$  of the number of processes  $p$  ( $n = i \cdot p$ ). In this case data of  $i$  streamlines are stored on every process. Generally, the streamlines are distributed one after another to the different domains until all streamlines are distributed. If the number of streamlines is larger than the number of processes, the additional streamlines are further distributed to the domains, beginning again with the first domain and continuing with the remaining domains. After the streamlines are virtually distributed over the processes, all boundary layer data and velocity profiles along a certain streamline are collected from the different domains and the data is stored on the corresponding process.

Two different external programs can be used within the transition module: a boundary layer code for swept, tapered wings [49] for the computation of laminar boundary layers and a stability solver [50] for the solution of the stability equations of the linear stability theory. The external programs are separate, sequential stand-alone codes and are designed to process data of one streamline at a single sequential

run. For the quasi-parallelization of the external programs, for each process one external program is executed sequentially. If the RANS calculation is run on  $p$  processors, the external programs are started from each of the  $p$  processes independently. This means, that for example  $p$  stability analyses with the external stability code run at the same time on the  $p$  processes, so that  $p$  streamlines can be processed parallel and a parallel performance of the actually sequential external program is achieved. The advantage of this approach is that only few modifications of the source codes of the external programs need to be made, for example ensuring unique filenames are used for the communication between the external programs and the transition prediction module. A disadvantage is that no full parallelization is obtained, if the number of streamlines is not an integer multiple of the number of processes.

After all data relevant for transition prediction has been determined, the transition criteria can be applied for each streamline. This gives a single transition point for every streamline which, when connected, give a polygonal line that is used for determining the laminar and turbulent zones in the flow solver. If not all streamlines are available on all processes, the transition points have to be communicated over all domains so that the transition lines can be assembled.

Parallelization regarding the transition prediction module is considered as the ability to process partitioned Navier-Stokes solutions. For example for the calculation of wall-normal lines and streamlines only domains containing sections of these lines are involved in the computation. Domains not containing sections of these lines have to run idle during this calculation process. For this reason, a complete parallel execution is not possible in general but sequential execution of the transition module is kept as minimal as possible.

### 3.2. Geometrical data

In a preprocessing step before the start of the computation of the flow solution, data only depending on the computational grid and on geometrical data are calculated in the transition module. This is mainly the identification of viscous wall surface points and the assembly of grid point lists representing wall-normals.

Based on the general point-to-point connectivity available from the edge-based data structure of the RANS solver a point-to-point connectivity just for the viscous wall surface points is build. This is used for the streamline computation where it is necessary to follow the streamline on the surface of the geometry. The streamline is followed by continuously marching from a surface grid point to one of its neighbour grid points which lies in the direction of the inviscid flow (Sec. 3.4).

The point-to-point connectivity of the surface points is also used to determine sharp edges of the geometry. These sharp edges later define automatic ending points for the streamline integration. For the sharp edge detection, the wall-normal vector  $\vec{n}$  of a certain surface point is compared to the wall-normal vector  $\vec{n}_{nb}$  of its neighbouring surface points. The angle  $\phi_n$  between the normal vectors is then computed and compared to a user defined limiting value:

$$\phi_n = \cos^{-1} \left( \frac{\vec{n} \cdot \vec{n}_{nb}}{|\vec{n}| |\vec{n}_{nb}|} \right) \quad (27)$$

A value of  $\phi_{n,lim} = 20^\circ$  as limiting value has been proven to robustly detect sharp edges in regions where the surface grid is sufficiently fine resolved. Artefacts of wrongly detected sharp edges may occur in regions where curvatures are not properly resolved by the surface grid, however these are normally uncritical since they occur in regions where no transition prediction is performed. Typically, these artefacts occur for three-dimensional geometries at round wing tips. Sharp leading edges are explicitly excluded from being marked as ending points for the streamline computation. Thus, if the flow conditions permit, streamlines can be computed around sharp leading edges.

For certain occasions, lines extracted from cutting planes are determined. These are lines which are determined by the intersection of the geometry and a plane. They give the shape of the investigated geometry (generally the airfoil contour) for two-dimensional or infinite swept wing computations. For

three-dimensional geometries these lines represent so called line-in-flight cuts and are aligned to the direction of the oncoming flow (wing sections in flight direction). The collection of grid points along these lines is inspired by the computation of the streamlines (Sec. 3.4): The assembly of the grid lines is started at a given start coordinate, which is for two-dimensional cases and infinite swept wings the leading edge point of the airfoil, or in the case of multi-element airfoils each leading edge point of each element. These leading edge points are determined automatically and are found by searching for a wall point that has no neighbour upstream of itself. For three-dimensional geometries, start coordinates need to be, as in the case of the computation of inviscid streamlines, user defined. During the actual transition prediction, the lines extracted from cutting planes are divided into an upper side and an lower side at the stagnation point or the attachment-line point, respectively.

For the extraction of boundary layer profiles a sorted list of grid points along the wall-normal direction is needed. The determination of that list is following the general procedure shown in figure 8. Starting at every surface point the next point along the wall-normal direction is determined with a visibility cone method. All neighbouring grid points that are lying within a certain cone are considered to be the next point of the line. The relatively large opening angle of the cone that is used ( $\phi_{cone} \approx 188^\circ$ ) essentially just guarantees to walk away from the surface when collecting the wall-normal grid points. For the remaining neighbouring grid points lying inside the cone the vector  $\vec{r}$  from the wall point coordinate  $\vec{p}_w$  to the neighbouring grid point coordinate  $\vec{p}$  is calculated:

$$\vec{r} = \vec{p} - \vec{p}_w \quad (28)$$

The grid point located nearest to the wall-normal direction is then selected as next point on the wall-normal grid points list. As criterion, the angle between the wall-normal vector  $\vec{n}$  and the vector  $\vec{r}$  is determined

$$\phi = \cos^{-1} \left( \frac{\vec{n} \cdot \vec{r}}{|\vec{n}| |\vec{r}|} \right) \quad (29)$$

and checked for its minimum value over all neighbouring grid points.

If a domain boundary is reached, the wall-normal computation is suspended. For each grid point in the overlapping region between two domains the counterpart of a grid point in the neighbouring domain is known from the TAU data structure. The coordinates of the base point of the wall-normal (the coordinates of the surface point) and the wall-normal vector are then communicated and the computation continues in the neighbouring domain. Additionally, the domain identifier and the local point identifier of the base point of the wall-normal are communicated in order to set up a communication table to eventually communicate data back to the base point.

This procedure is repeated until the user defined maximum number of points to be assembled is reached. The concept of specifying a maximum number of points on a wall-normal is chosen to simplify the programming and reduce the communication effort. The disadvantage of this method is, if the limit is set too low, the boundary layer may exceed the maximum extent of the wall-normal. The best practice is to specify the maximum number of points on the wall-normals according to the number of prism layers which covers the investigated boundary layer.

### 3.3. Boundary layer data

The basis for the determination of boundary layer data from the Navier-Stokes solution is the knowledge of the wall-normal lines corresponding to the surface grid points and the list of grid points associated with these lines. The length of the wall-normals is limited by a maximum number of grid points defined by the user and usually in accordance with the extension of the structured part of the hybrid Navier-Stokes grid (Sec. 3.2). The boundary layer profiles are directly accessible, if the surface point and the point associated with the end of the wall-normal line are placed in the same domain. In this case only the knowledge of the point list for the wall-normal needs to be known and the flow values at each

wall-normal point are interpolated from the Navier-Stokes solution. If a boundary layer profile is cut by a domain boundary, the wall-normal lines are divided at the domain boundaries into separate wall-normal parts, where each part of the wall-normal lies in a different domain. The flow variables for each wall-normal part are interpolated from the Navier-Stokes solution of the corresponding domain and are communicated to the domain containing the surface point associated with the examined wall-normal.

After the boundary layer profiles are assembled, the boundary layer edge is detected and all relevant boundary layer data are calculated and stored together with the velocity vector of the boundary layer edge at the surface grid points.

The procedure to determine boundary layer data for each point along a streamline is essentially the same as before. For a streamline, boundary layer profiles are assembled for each streamline point and the whole profile is stored in an appropriate array connected to the streamline. The boundary layer profile corresponding to a certain streamline point can then be accessed as a whole and the boundary layer data can be determined.

### 3.3.1. Boundary layer profiles

The determination of the boundary layer profiles is based on the knowledge of the wall normal lines originating at the surface of the geometry and the grid points associated with these lines. Section 3.2 describes the determination of the grid point lists for the wall normals for partitioned computational grids. For parallel computations, the wall normals are generally divided into several sections with endpoints at the domain boundaries. A communication table is set up, relating every wall normal section unambiguously to its base point on the surface of the geometry and to the domain that contains the base point. With the communication table, data along the wall normal sections of a certain wall normal can be collected and communicated to an appropriate data structure, available for the base point. With this data structure the complete profile can be accessed on the corresponding process as a whole.

Before the communication, the relevant flow data are interpolated from the flow solution for every wall normal section, using an inverse distance weighting approach [57]. After the communication is done, all data for further operations on the profile are available at once. In the next steps the boundary layer edge is detected (Sec. 3.3.2) and the vector of the velocity at the boundary layer edge  $\vec{u}_e$  is saved at every surface point in an appropriate array. This vector field on the surface of the geometry is eventually used for the calculation of the inviscid streamlines (Sec. 3.4).

For the computation of boundary layer data and for the treatment in the stability code for the analysis with linear stability theory, the velocity profiles are transferred into a streamline-oriented coordinate system. For this the parallel part of the boundary layer edge velocity vector is used for the streamwise direction  $\vec{s}$ :

$$\vec{s} = \vec{u}_{e,p} \quad (30)$$

With the wall normal vector  $\vec{n}$  an orthogonal coordinate system is created by determining the cross-flow direction  $\vec{c}$  as the vector cross product of streamwise direction  $\vec{s}$  and wall normal direction  $\vec{n}$ :

$$\vec{c} = \vec{n} \times \vec{s} \quad (31)$$

With the three unit vectors of the streamline-oriented coordinate system the following transformation matrix is created:

$$T = (\vec{s}/|\vec{s}| \quad \vec{c}/|\vec{c}| \quad \vec{n}/|\vec{n}|) \quad (32)$$

The velocities can then be transformed from the standard cartesian  $x, y, z$ -coordinate system of TAU ( $xyz$ ) into the streamline-oriented coordinate system ( $scn$ ) simply by

$$\vec{u}_{scn} = T \vec{u}_{xyz} \quad (33)$$

Boundary layer values, for example integral boundary layer data, are then derived from values in the streamline-oriented coordinate system. For example, the incompressible displacement thickness of the streamwise velocity profile is defined as [58, 59, 60]:

$$\delta_{1,s} = \int_{z=0}^{\delta} \left( 1 - \frac{u_{scn}}{u_{scn,e}} \right) dz \quad (34)$$

The corresponding incompressible displacement thickness of the cross-flow velocity profile is determined from [58, 59]:

$$\delta_{1,c} = \int_{z=0}^{\delta} \left( -\frac{v_{scn}}{u_{scn,e}} \right) dz \quad (35)$$

### 3.3.2. Boundary layer edge

The accurate detection of the boundary layer edge for three-dimensional flows computed with a RANS solver is not an easy task but is crucial for the application of linear stability theory. One challenge with the boundary layer edge detection is, that the magnitude of the velocity inside the boundary layer asymptotically approaches its final value. If, as simple example, the flow with zero pressure gradient over a flat plate is considered, the boundary layer thickness (and hence the location of the boundary layer edge) can not be definitely determined [11]. The influence of viscosity decreases asymptotically with increasing distance to the wall and the wall parallel velocity  $u$  asymptotically approaches the value  $u_{\infty}$  of the potential flow. If the distance to the wall where  $u$  reaches 99% of the potential flow velocity  $u_{\infty}$  is arbitrarily defined as boundary layer edge, the boundary layer thickness along the flat plate becomes [11]

$$\delta \approx 5.0 \sqrt{\frac{\nu x}{u_{\infty}}} \quad (36)$$

and the boundary layer edge velocity is  $u_e = 0.99 \cdot u_{\infty}$ . However, the factor  $\eta = 5.0$  for the boundary layer thickness in equation 36 changes to  $\eta = 4.5$  for  $u_e = 0.98 \cdot u_{\infty}$  and to  $\eta = 6.2$  for  $u_e = 0.999 \cdot u_{\infty}$  [11]. These different definitions of the boundary layer edge show large differences for the boundary layer thickness with only small changes in the actual value of the velocity at the boundary layer edge. Generally, a less sensitive measure for the extent of the laminar boundary layer is the (incompressible) displacement thickness

$$\delta_1 = \int_{z=0}^{\infty} \left( 1 - \frac{u}{u_{\infty}} \right) dz \quad (37)$$

It is clear, that the contribution of the integrand  $1 - u/u_{\infty}$  to the integral becomes smaller and smaller (and thus more negligible) as  $u$  approaches  $u_{\infty}$ . This also shows, that empirical transition criteria are less sensitive to an accurate determination of the boundary layer edge, since they are generally only depending on integral boundary layer values.

For flows around arbitrary two- or three-dimensional geometries, the velocity at the boundary layer edge does not approach a single constant value  $u_{\infty}$ . Instead the velocity of the potential flow outside of the boundary layer varies, theoretically corresponding to the pressure distribution on the surface of the geometry. For small boundary layer thicknesses  $\delta$  (i.e. for large Reynolds numbers, theoretically  $Re \rightarrow \infty$ ) the boundary layer equations [11] state, that the pressure gradient in wall normal direction inside the boundary layer can be neglected:

$$\frac{dp}{dz} \approx 0 \quad (38)$$

This means that the static pressure at the boundary layer edge  $p_e$  can be approximated by the static pressure  $p_w$  at the wall ( $p_e \approx p_w$ ). From the formulation of the compressible Bernoulli-equation from infinity to the boundary layer edge

$$a_\infty^2 + \frac{\gamma - 1}{2} u_\infty^2 = a_e^2 + \frac{\gamma - 1}{2} u_e^2 \quad (39)$$

the theoretical boundary layer edge velocity can be derived:

$$\frac{u_e}{u_\infty} = \sqrt{\frac{1 - \frac{p_e}{p_\infty} \frac{\gamma - 1}{\gamma}}{0.5(\gamma - 1) Ma_\infty^2} + 1} \quad (40)$$

A straight forward way to define a general boundary layer edge criterion is to use equation 40 to compute the theoretical boundary layer edge velocity. The boundary layer edge is then determined at the wall distance  $z$  where the velocity inside the boundary layer  $u$  reaches a defined fraction  $f$  of the theoretical value:

$$u(z) = f \cdot u_e \quad (41)$$

This kind of criterion has been often used in the past with, for example, factors  $f$  of  $f = 0.98$  [39] or  $f = 0.99$  [54]. However, during the development of the transition module, it was found, that the accuracy of the detected boundary layer edge was often not high enough for transition prediction with linear stability theory.

The linear stability theory reacts very sensitively to the shape of the boundary layer velocity profiles. Thus, it is also important to have a smooth transition of the boundary layer flow into the external flow at the boundary layer edge. Very often it was seen that the theoretical value of equation 40 did not really fit the actual value found in the Navier-Stokes solution. In these cases, applying equations 41 and 40 lead to very badly shaped velocity profiles (in the form of steps in the vicinity of the boundary layer edge). It was found that, especially for three-dimensional flows, the consideration of the full Navier-Stokes equations for the computation of the flow solution seems to have a considerable impact on the actual value of the boundary layer edge velocity compared to the theoretical value of equation 40. Possibly, numerical characteristics of the considered RANS solver and of the used solution method also have a significant influence on the boundary layer edge velocity. Additionally, the boundary layer equations are not valid in the vicinity of the stagnation point. There, the local Reynolds number is low [11], thus making equation 40 less valid and accurate in these regions.

As a consequence, several different boundary layer edge criteria have been developed for the transition module. Those criteria focus more on the general shape of the boundary layer profile in the vicinity of the boundary layer edge, taking into account the wall-normal derivative of the velocity. The computation process of the current evolution of the boundary layer edge criterion used in the scope of this work can be divided into three steps. First, the maximum of the total pressure along the wall-normal lines is determined. Then, in the second step, the total pressure distribution normal to the wall is normalized with the maximum of the total pressure:

$$p_{t,n} = \frac{p_t(z) - p_{t,w}}{p_{t,max} - p_{t,w}} \quad (42)$$

Theoretically, the total pressure is constant outside of the boundary layer and decreases gradually inside the boundary layer. This means, that the normalized total pressure  $p_{t,n}$  should be approximately 1.0 outside of the boundary layer and  $p_{t,n} < 1.0$  inside the boundary layer.

Since the actual edge criterion is based on the magnitude of the derivative in wall-normal direction of the norm of the velocity vector ( $||[d|\vec{u}|/dz]||$ ), a smooth variation of  $||[d|\vec{u}|/dz]||$  is needed for a successful application. Therefore, in the third step, the edge criterion is applied where  $p_{t,n} > 0.6$ . This omits the near wall region and thus especially the reversed flow region of separated boundary layers.

The criterion determines the location of the first local minimum of the derivative of the velocity magnitude  $z(||[d|\vec{u}|/dz]||_{min})$ . With *first* occurrence the location which is nearest to the wall is described. A local minimum is determined by requiring the two values above and below the considered point of

the profile to be larger than the current value. The derivative of the velocity is computed using a 3rd degree polynomial, fitted through the current point of the profile and its two neighbouring points. The location of  $z(|[d|\vec{u}|/dz]|_{min})$  is then used as boundary layer thickness:

$$\delta = z(|[d|\vec{u}|/dz]|_{min}) \quad (43)$$

The development of this criterion is based on the typical characteristic shapes of velocity distributions (Fig. 10) seen in near-wall regions in a Navier-Stokes solution. Generally, the magnitude of the velocity  $|\vec{u}|$  evolves outside of the boundary layer from the value at the boundary layer edge to the value at infinity. A distinction can be made between profiles where  $|\vec{u}_e| < |\vec{u}_\infty|$  (Figs. 10(a) and 10(b)), characterized by a pressure coefficient larger than zero ( $c_p > 0$ ) and profiles where  $|\vec{u}_e| > |\vec{u}_\infty|$  (Fig. 10(c)), characterized by a pressure coefficient smaller than zero ( $c_p < 0$ ). Typically, from experience, there exists a section of nearly constant magnitude of  $|\vec{u}|$  in the vicinity of the boundary layer edge (Figs. 10(b) and 10(c)). In the vicinity of the stagnation point or the attachment-line the constant part often does not exist, however the velocity distribution exhibits an inflection point, characterized by a local minimum in  $d|\vec{u}|/dz$  (Fig. 10(a)). For velocity distributions with a section with nearly constant  $|\vec{u}|$  and  $|\vec{u}_e| < |\vec{u}_\infty|$  (Fig. 10(b)), the velocity derivative decreases inside the boundary layer towards  $d|\vec{u}|/dz \approx 0$  and increases afterwards with increasing wall distance, describing a minimum around the boundary layer edge. If  $|\vec{u}_e| > |\vec{u}_\infty|$  (Fig. 10(c)), the velocity derivative becomes eventually negative when the velocity magnitude starts to decrease towards its value at infinity. If the magnitude of the derivative  $|[d|\vec{u}|/dz]|$  is considered, a local minimum is again formed at the boundary layer edge. A special case has sometimes been observed in Navier-Stokes computations where the velocity magnitude overshoots at the boundary layer edge (Fig. 10(d))<sup>4</sup>. In this case the velocity overshoot is also characterized by a local minimum of  $d|\vec{u}|/dz$  and this location can be interpreted as the boundary layer edge.

From experiences of the application in the transition module together with the flow solver TAU, this criterion works satisfactory for the parts of the three-dimensional boundary layers which are of interest for transition prediction. That is, the boundary layer edge over attached and little to moderately separated laminar boundary layers is detected with sufficient accuracy. Also, no difficulties in the edge detection for turbulent boundary layers have been observed so far. The edge detection partly fails for strongly separated flows. An improvement may be achieved by adjusting the region normal to the wall where the criterion can be applied, by changing the lower limit for  $p_{t,n}$ . However, transition should have been taken place a short distance downstream of the laminar separation well before the separation exceeds a critical extent where the edge criterion does not work satisfactorily anymore.

The velocity at the boundary layer edge can directly be accessed at the position where  $z = \delta$

$$\frac{u_e}{u_\infty} = \frac{|\vec{u}(\delta)|}{u_\infty} \quad (44)$$

and can be used to compute other values at the boundary layer edge with the help of the compressible Bernoulli equation (Eq. 39) and isentropic relations. For the temperature at the boundary layer edge it follows that

$$\frac{T_e}{T_\infty} = 1 + \frac{\gamma - 1}{2} Ma_\infty^2 \left( 1 - \frac{u_e^2}{u_\infty^2} \right) \quad (45)$$

The dynamic viscosity at the boundary layer edge is given from Sutherland's law [31], with non-dimensional Sutherland reference Temperature  $\hat{T}_s$ :

$$\frac{\mu_e}{\mu_\infty} = \left( \frac{T_e}{T_\infty} \right)^{\frac{3}{2}} \frac{1 + \hat{T}_s}{\frac{T_e}{T_\infty} + \hat{T}_s} \quad (46)$$

<sup>4</sup>This overshoot seems to be accompanied by a small local excess of the total pressure compared to the value at infinity ( $p_{t,e} > p_{t,\infty}$ ) and may be a numerical artefact that has otherwise no impact on the solution accuracy.

The density at the boundary layer edge can be computed using the isentropic relation between density and temperature:

$$\frac{\rho_e}{\rho_\infty} = \left( \frac{T_e}{T_\infty} \right)^{\frac{1}{\gamma-1}} \quad (47)$$

### 3.4. Streamlines

#### 3.4.1. Three-dimensional streamlines

In the transition module, for three-dimensional flows, a distinction between two types of streamlines is made: i) inviscid streamlines, respectively boundary layer edge streamlines and ii) attachment lines. In this context it has to be noted that there exist no streamline that follows the boundary layer edge or is located parallel to it<sup>5</sup>. The flow generally crosses the imaginary and ambiguously (see Sec. 3.3.2 for the definition of boundary layer edge) defined surface (or line in two-dimensional flow) that would be defined by the boundary layer thickness. Referring to edge streamline means the *"local projections of the loci, where the streamlines cross the boundary layer edge"* (HIRSCHEL [61]). This also holds, if the term *inviscid streamline* is used, which refers to the inviscid, respectively potential flow, outside of the boundary layer. As stated before, there exists no potential flow streamline at or parallel to the boundary layer edge. The inviscid streamline can be thought of as a trajectory that follows locally the projected direction of the flow at the boundary layer edge, where the boundary layer flow transitions into the potential flow. The projection is conveniently made onto the surface of the considered geometry.

The attachment line is a particular streamline, which, for three-dimensional wing-like geometries, divides the flow into two parts, one part following the upper surface of the geometry and another part following the lower surface of the geometry [62]. In this case, the boundary layer edge streamlines originate in an attachment line and run over both sides of the wing-like geometry. In the general case the edge streamlines originate from a stagnation point.

For three-dimensional flow, the computation of the streamlines and attachment lines is done by solving the differential equation

$$\frac{d\vec{x}}{dt} = \vec{u} \quad (48)$$

for the position vector  $\vec{x}$  on the surface of the geometry. The velocity vector  $\vec{u}$  represents the local projected directions for the two different types of streamlines. Integrating equation 48 gives the trajectory, respectively the streamline approximation, on the surface of the geometry.

For the calculation of the edge streamlines the projected direction used in equation 48 is the part of the boundary layer edge velocity vector  $\vec{u}_e$  that is parallel to the surface:

$$\vec{u} = \vec{u}_{e,p} \quad (49)$$

The flow along the attachment line is two-dimensional and the local direction of the skin friction line coincides with the direction of the flow at the edge of the attachment line boundary layer. Because of that the attachment lines can be computed using the wall shear stress vector  $\vec{\tau}_w$  in equation 48:

$$\vec{u} = \vec{\tau}_w \quad (50)$$

With the usage of the wall shear stress distribution for the attachment line computation, possible inaccuracies in the detection of the boundary layer edge at or near the attachment line region are avoided.

<sup>5</sup>Consider the case of a flat plate: the boundary layer starts to evolve at the leading edge of the plate and thus the boundary layer thickness at the leading edge is 0. The boundary layer grows from there as  $\delta \approx 5.0\sqrt{\nu x/u_\infty}$  (eq. 36). If there would be a streamline following the boundary layer edge no flow could cross this streamline and the flow inside the boundary layer would have to develop from nowhere.

Equation 48 represents an initial value problem of the form

$$\frac{d\vec{x}(t)}{dt} = \vec{u}(t, \vec{x}(t)) \quad \vec{x}(t_0) = \vec{x}_0 \quad (51)$$

that can be solved with an explicit Runge-Kutta method. General explicit  $s$ -stage Runge-Kutta methods are defined by expressions of the following type:

$$\vec{x}_{n+1} = \vec{x}_n + h \sum_{i=1}^s b_i k_i \quad (52)$$

The Runge-Kutta approximation of the next value  $\vec{x}_{n+1}$  is based on the current value  $\vec{x}_n$  and the sum of  $s$  weighted intermediate steps  $k_i$ . The weighting coefficients  $b_i$  are defined by the respective Runge-Kutta method and the intermediate steps are given by:

$$k_i = \vec{u} \left( \vec{x}_n + h \sum_{j=1}^s a_{ij} k_j \right) \quad i = 1, \dots, s \quad (53)$$

The coefficients  $a_{ij}$  are another set of values characteristic of the respective Runge-Kutta method and  $h$  is the step size of the method.

The solution of equation 51 for the calculation of the streamlines is done using a 4-stage explicit Runge-Kutta method with coefficients ( $b_1 = b_4 = 1/6$ ), ( $b_2 = b_3 = 1/3$ ), ( $a_{21} = a_{32} = 1/2$ ) and ( $a_{43} = 1$ ). The step size  $h$  is based on a length  $l_{cell}$ , representative of the surface cell size of the computational grid, and the magnitude of the local velocity  $|\vec{u}|$ :

$$h = \frac{i_{dir} \cdot l_{cell}}{n_{rk} \cdot |\vec{u}|} \quad (54)$$

With this definition the direction and the resolution of the integration can be controlled. For an integration in upstream direction the parameter  $i_{dir}$  is set to  $i_{dir} = 1$  and for an integration in downstream direction  $i_{dir} = -1$ . The parameter  $n_{rk}$  controls the number of Runge-Kutta steps that are used to cover the distance  $l_{cell}$  based on the velocity  $\vec{u}$ . A value of  $n_{rk} = 10$  is used as default. With this relatively smooth resolution for the streamline computation the integration robustness and accuracy is benefiting. However, to keep the actual streamline resolution similar to the resolution of the surface of the computational grid and to keep the computational memory demand of the method low not all streamline points are saved.

The general procedure of the streamline computation is shown in figure 9 and is divided into the following steps:

- The integration of the streamlines is started at user defined start coordinates that are ideally defined in the vicinity of the surface of the considered geometry.
- Starting from the current coordinates and using the surface grid point located nearest to them as reference grid point, the Runge-Kutta integration (eq. 52) is executed. From the connectivity information of the surface grid points (Sec. 3.2) all neighbouring surface grid points of the reference point are known. The values of  $\vec{u}$  at the current streamline coordinate and at the support coordinates (eq. 53) of the Runge-Kutta method are linearly interpolated from the current reference point and the neighbouring points.
- If the distance of the current streamline coordinate to one of the neighbouring surface grid points is lower than the distance to the current reference point, the corresponding neighbouring point is taken as the new reference point. The previous reference point is stored in an appropriate streamline array together with the corresponding coordinate of the streamline.

- The previous three steps are repeated until a domain boundary is reached or one of several end criteria for the streamline computation is met. In case of a domain boundary the current streamline coordinate is communicated to the neighbouring domain together with a unique streamline identifier. The computation is then continued in the neighbouring domain with the first step. The streamline identifier ensures that data distributed over different streamline parts in different domains, can eventually be unambiguously gathered for a particular streamline.

The computation of a streamline is stopped when a user defined geometrical limit (limiting plane) is reached or the streamline approaches a stagnation point or a sharp edge of the geometry (Sec. 3.2). In the case of the computation of a boundary layer edge streamline the computation is also stopped if a previously computed attachment line is approached.

Another difference in the computation of edge streamline and attachment line, besides the different velocity vectors used in equation 48, is the integration direction. Whereas the edge streamlines are integrated upstream and downstream, starting from the initial coordinates, the attachment line integration is only executed against the streamwise direction. If the attachment line is followed in streamwise direction the computation is in an unstable equilibrium. Any small deviation from the actual attachment line during the computation process will force the computation to follow any of the wall friction lines diverging from the attachment line. If the attachment line is viewed from against the streamwise direction, the neighbouring wall friction lines converge towards the attachment line and the computation is in a stable equilibrium.

After the integration, every streamline is based on different streamline parts distributed over different domains. For all the streamline parts relevant surface data (e.g. surface pressure) are linearly interpolated from values of the nearest surface grid points. For each streamline point the boundary layer profiles are determined, following the same procedure as for a general surface grid point, described in section 3.3.1. After all data are computed for all streamline parts, a particular streamline is assembled by joining together all data and boundary layer profiles of the streamline parts on one particular computational process. The process of distributing the actual streamlines (virtually) over all computational processes is addressed in section 3.1.

### 3.4.2. Two-dimensional and quasi-two-dimensional flows

For two-dimensional flows and quasi-two-dimensional flows, that is flows over infinite swept wings and flows subject to the conical flow assumption, no explicit integration of streamlines (Sec. 3.4.1) is needed. For two-dimensional flows it is immediately evident that the projected edge streamlines are equivalent to the lines describing the surface of the two-dimensional geometry. Quasi-two-dimensional flows are of relevance for swept tapered wings of high aspect ratio in connection with the application of a boundary layer code. If the formulation of the boundary layer equations follows the conical flow assumption [16] the respective three-dimensional equations can be written in a form similar to the two-dimensional equations. The basic assumption for this is that the pressure isobars follow constant percent-chord lines of a wing with trapezoidal planform [16] and that other values of the flow are constant along these lines. The data for the boundary layer method can then be provided along lines of constant spanwise location, that is, line-in-flight cuts that are aligned to the direction of the oncoming flow (Sec. 3.2).

Flows over infinite swept wings can be computed in the DLR TAU code on a two-dimensional computational grid in a leading edge normal coordinate system  $(x', y', z')$ , using suitable angles of attack  $\alpha'$  and sideslip angles  $\beta'$ . In the standard TAU  $x, y, z$ -coordinate system the onflow direction is defined in the  $x$ - $z$ -plane if the sideslip angle  $\beta = 0^\circ$ . For the flow over a swept wing with sweep angle  $\Lambda$  and angle of attack  $\alpha = 0^\circ$  the angle between the direction normal to the leading edge  $x'$  and the onflow direction is  $\beta' = \Lambda$ . For angles of attacks  $\alpha \neq 0^\circ$  the angle  $\beta'$  can be derived from  $\sin \beta' = \cos \alpha \cdot \sin \Lambda$  and the angle of attack in the  $x'$ - $z'$ -plane is defined by  $\tan \alpha' = \tan \alpha / \cos \Lambda$ . For small values of  $\alpha$  the trigonometric functions can be approximated as  $\cos \alpha \approx 1$  and  $\tan \alpha \approx \alpha$  and the angle of attack  $\alpha'$  in the leading edge normal coordinate system  $x', y', z'$  is

$$\alpha' \approx \alpha / \cos \Lambda \quad (55)$$

and the sideslip angle  $\beta'$  reduces to

$$\beta' \approx \Lambda \quad (56)$$

For infinite swept wing flows and flows subject to the conical flow assumption, flow values are constant in spanwise direction. The three-dimensional edge streamlines, respectively the arc length along the edge streamlines, can be computed for these flows from geometrical relations if the boundary layer edge velocity vector is determined.

Summarizing, for two-dimensional flows and quasi-two-dimensional flows, the flow solution needs to be known along straight lines for transition prediction. The straight lines are defined by the intersection of appropriate cutting planes and the geometry. The cutting planes are either the plane where the geometry is defined (two-dimensional computational grid, trivial) or the plane in which the onflow vector is defined (line-in-flight cuts). The lines are computed in the preprocessing stage of the transition prediction process and are assembled by storing the intersection points of lines connecting two surface points with the cutting planes. During runtime, the pressure distribution along the lines is interpolated from the Navier-Stokes solution and the lines are divided into upper and lower surface parts at the location of maximum pressure (stagnation point for two-dimensional flows, attachment line location for three-dimensional flows).

### 3.5. Stability code

The stability solver LILO [50], described in section 2.3.2, is an external Fortran 77 program and is used in the transition module for the computation of amplification rates and  $N$ -factor curves based on linear stability theory. LILO is a sequential program which is accessed from the transition module via file I/O and system calls.

#### 3.5.1. General input and execution of the code

The stability solver needs the boundary layer profiles of the temperature and the streamwise and cross-flow velocity component and their first and second derivatives in wall normal direction along a streamline as input. The first and second derivatives of the boundary layer profiles are computed from analytical derivatives of a locally fitted 3rd degree polynomial. Additional input values along the streamline are boundary layer data (reference length  $l_{ref}$ , Reynolds number based on displacement thickness  $Re_{\delta_1} = \delta_1 u_e / \nu_e$ ) and boundary layer edge values (velocity  $u_e$ , temperature  $T_e$ , Mach number  $Ma_e$ , density  $\rho_e$ , viscosity  $\mu_e$ ). As reference length  $l_{ref}$  the dimensional displacement thickness  $\delta_1$  of the streamwise velocity profile is used. Boundary layer edge values are computed based on the boundary layer edge velocity  $u_e$  and equations 45 - 47, the displacement thickness  $\delta_1$  of the streamwise velocity profile is defined in equation 34.

All data along a single streamline are eventually written to an input file using the standard LILO format [50]. The stability code is run with the help of additional control scripts, executed externally from the transition module using a system call. A system call is a programmatic way in which an already executed computer program can create and execute a new process on the operating system. The control script contains additional input values for the stability computation and the command to execute the stability code LILO. The results of LILO are in turn written to an output file which can be accessed from the transition module after the system call is completed.

#### 3.5.2. $N$ -factor integration

For two-dimensional flows and quasi-two-dimensional flows (Sec. 3.4.2) the  $N$ -factors computed in the stability code are directly used for transition prediction. For these flows the integration path, which is

the group velocity trajectory (Sec. 2.2), is directly determined for each wave. This can be done since the streamline input is provided along straight lines parallel to the onflow direction (line-in-flight cuts, Sec. 3.4.2) and the conical flow assumption is applied. Expressed in a simple way, the local angle  $\theta$  between the direction of the inviscid flow and the line-in-flight cut is known. Together with the direction  $\Psi_g$ <sup>6</sup> of the group velocity with respect to the inviscid flow direction [13]

$$\Psi_g = \tan^{-1} \left( \frac{\partial \omega_r / \partial \beta}{\partial \omega_r / \partial \alpha} \right) \quad (57)$$

an increment  $ds_g$  in the arc-length of the group velocity trajectory can be computed from an increment  $ds$  of the line in flight cut by

$$ds_g = ds / \cos(\theta + \Psi_g) \quad (58)$$

In this case, the integration of the  $N$ -factors can be performed along the group velocity trajectory with the computed amplification rates  $\sigma_g$ , without further approximations, using equation 19.

Because each individual wave has its own direction of the group velocity each wave also has its own group velocity trajectory and thus its own integration path. It is possible to determine these different integration paths for two-dimensional and conical flows from information along a single streamline, as shown above. For general three-dimensional flows, to compute individual integration paths, the boundary layer profiles would need to be provided over a surface patch instead of being available along a line. Besides possible difficulties in determining initial conditions for the stability computation it is from a practical point of view often not reasonable to determine multiple integration paths, especially for large three-dimensional configurations. Generally, the group velocity direction is very close to the inviscid flow direction at the boundary layer edge, for both, streamwise and cross-flow instabilities [13]. This observation is also verified by numerical results [13] and leads to the conclusion that the angle  $\Psi_g$  between the group velocity direction and the potential flow direction is generally small.

Based on infinite swept wing computations for the flow over an swept wing with a NACA 64<sub>2</sub>-A-015 airfoil section normal to the leading edge (Sec. 4.2.4) the group velocity direction  $\Psi_g$  with respect to the inviscid flow direction has been analyzed for a number of flow conditions to prove the above statements. For a sweep angle of  $\Lambda = 50^\circ$ , an angle of attack of  $\alpha = -1.0^\circ$  and a Reynolds number of  $Re = 5.0 \times 10^6$  the absolute value of the angle  $\Psi_g$  is of the order of  $\Psi_g < 5.0^\circ$  for both, streamwise and cross-flow instabilities (Fig. 11). For other flow conditions, leading to a weaker three-dimensionality of the flow through a lower sweep angle,  $\Psi_g$  is substantially lower. For  $\Lambda = 30^\circ$ ,  $\alpha = 0.5^\circ$  and  $Re = 1.5 \times 10^7$ , the absolute value of  $\Psi_g$  is lower than  $0.5^\circ$  for streamwise instabilities and of the order of  $1.0^\circ$  for cross-flow instabilities. Even lower absolute values,  $\Psi_g < 0.1^\circ$  for streamwise instabilities and  $\Psi_g \approx 0.5^\circ$ , are determined for  $\Lambda = 10^\circ$ ,  $\alpha = -2.0^\circ$  and  $Re = 2.5 \times 10^7$ .

In summary, the above leads to the conclusion, that approximating the group velocity trajectory with an edge streamline is a practical and sufficiently accurate method for applying the linear stability theory for general three-dimensional flows. In this case, the integration of the  $N$ -factors along the inviscid streamline is carried out directly in the transition module with the amplifications rates  $\sigma_g$  determined by the stability code LILO<sup>7</sup>.

<sup>6</sup>The stability equations in LILO are formulated in the edge streamline coordinate system (Sec. 2.3.2),  $\alpha$  is the wavenumber in streamwise direction and  $\beta$  is the wavenumber in cross-flow direction. Thus,  $\Psi_g$  is also defined in the streamline coordinate system and is the angle between inviscid flow direction and group velocity direction.

<sup>7</sup>The internal  $N$ -factor integration in LILO always applies the angle  $\Psi_g$  to the arc length of the inviscid streamline. If for general three-dimensional flows the input data is already provided along inviscid streamlines instead of line-in-flight cuts, adding the angle  $\Psi_g$  to the integration is considered as not being consistent. The actual group velocity trajectories cannot be reproduced in this case, as mentioned in the text. Instead, some undefined integration path, arbitrarily located in the vicinity of the actual group velocity trajectory and the inviscid streamline, would be the result.

### 3.5.3. Computation of amplification rates

The general computation of amplification rates with the stability code is done in two steps (Sec. 2.3.2). The first step is used to define an amplified mode and an estimate of the unstable frequency or wave length range for streamwise and cross flow instabilities. The second step is the computation of amplification rates and  $N$ -factors based on values resulting from the first step.

The eventual computation of the amplification rates depends on the choice of the initial values for the first part of the computation process. The initial values are the non-dimensional wavenumbers  $\alpha$  and  $\beta$  and the initial station along the streamline where the analysis will be started. From experience, the computation should not be started in turbulent regions of the streamline, as the stability theory, strictly speaking, only evaluates the shape of the respective velocity profiles. Because turbulent velocity profiles are much fuller compared to laminar velocity profiles they are evaluated as stable from stability theory.

Table 1: Initial values for stability computation

	TS	CF
$s_0$	0.0	0.0
$f_{relax}$	0.5 - 0.9	0.0 - 0.9
$\alpha$	0.15 - 0.3	from database
$\beta$	0.0	from database

The initial stations are determined along the arc length  $s$  of the streamline, based on the following simple relaxation formula, with values of the different parameters from table 1:

$$s_{init} = s_0 + f_{relax} \cdot s_{tr} \quad (59)$$

Essentially, the stability analysis is simply started somewhere between the streamline origin  $s_0$  (the attachment line in three-dimensional flows) and the current transition location  $s_{tr}$ . A relaxation factor of  $f_{relax} = 0.5$  has been proven to be a good compromise to cover a large spectrum of flow situations with amplified streamwise instabilities (Tollmien-Schlichting, TS). For cross flow (CF) instabilities initial stations very close to the streamline origin are typically used ( $f_{relax} \approx 0.1$ ). This is to account for the accelerated flow in the vicinity of the attachment line where cross-flow instabilities are typically amplified<sup>8</sup>.

Typical initial values used for the non-dimensional wave numbers  $\alpha$  and  $\beta$  are also listed in table 1. For Tollmien-Schlichting (TS) instabilities the wavenumber  $\beta$  in cross-flow direction is  $\beta = 0$  (Sec. 2.3.2), the wavenumber  $\alpha$  is generally in the range of  $\alpha = 0.15 - 0.3$ . For cross-flow (CF) instabilities  $\alpha$  and  $\beta$  are defined based on results from a database method for travelling cross-flow instabilities [53] (Sec. 2.3.2). The database results in turn are based on a prescribed frequency, typically of the order of  $f_{db} = 500 - 100$  Hz.

After a suitable initialization, the stability analysis is performed in a relatively straightforward way (Sec. 2.3.2): in the first step of the stability analysis an amplified eigenvalue is computed and an estimate of the unstable frequency and wave length range is determined. Based on these values the second step of the stability analysis is started, in which the amplification rates are computed and the  $N$ -factor distribution is calculated (Sec. 3.5.2).

It is relatively crucial for the stability analysis to be suitably initialized. Ideally, the combination of initial values allows the stability analysis to start well within the unstable region of the stability diagram

<sup>8</sup>For cross-flow instabilities amplified modes can also be computed in decelerated flows after the cross flow velocity profile has completely changed its direction downstream of the pressure minimum (Fig. 3). From experience, they have no influence on transition.

defined in the  $f$ - $s$ -plane (Fig. 4) or the  $\lambda$ - $s$ -plane<sup>9</sup>. Since the shape of the indifference curve of the stability diagram is not known a priori for general arbitrary flow situations this can be a difficult task, especially if the extent of the unstable region in the  $f$ - $s$ - and  $\lambda$ - $s$ -planes is locally strongly narrowed or consists of multiple unconnected parts. These phenomena can occur for example for flows which are multiply accelerated and decelerated [42, 43] or for flows with suction applied at the wall.

For robustness reasons a looping algorithm for the initial values and initial stations has been implemented. This method omits a complex analysis of the flow situation (e.g. analysis of the form of the pressure distribution). Instead a much more robust brute-force method is used, where the stability analysis is performed multiple times for a single streamline with initial values covering their typical range as indicated in table 1. This is implemented as a nested loop system of three loops (Fig. 12).

The inner loop (Fig. 12) is a loop over the  $\alpha$  range for streamwise instabilities and a loop over the frequency  $f_{db}$  for the database for cross-flow instabilities. The latter is a strategy for a robust prediction of stationary cross-flow instabilities ( $f = 0$  Hz). The estimated propagation direction  $\Psi = \tan^{-1}(\beta/\alpha)$  from the database is based on travelling cross-flow instabilities ( $f_{db} \gg 0$  Hz) and this direction has to be adapted during the Rayleigh iterations (2.3.2) to eventually fit the propagation direction  $\Psi$  for  $f = 0$  Hz. The lower the frequency  $f_{db}$  the less accurate are the results from the database but the more robust is the Rayleigh iteration.

The station loop (Fig. 12) is simply a loop over the initial stations for the analysis of streamwise and cross-flow instabilities and is carried out by applying different values of  $f_{relax}$  in equation 59. The outer loop could be used for the analysis of oblique Tollmien-Schlichting waves by varying the propagation angle  $\Psi$  (not implemented). It has however been used to predict instationary cross-flow instabilities (Sec. 4.2.3) by performing a loop over the frequency  $f_{TCF}$  for travelling cross-flow.

### 3.6. Application of transition criteria

After the stability analysis and the integration of the amplification rates are completed (Sec. 3.5)  $N$ -factor envelopes for Tollmien-Schlichting and cross flow instabilities are available for each streamline. The envelopes are analysed to give a transition location, respectively for each instability. The provisional transition points are found where the value of  $N$  of the envelope exceeds a critical value  $N_{crit}$ , which can be individually specified for both instabilities. This resembles the  $N_{TS}/N_{CF}$ - or  $2N$ -factor method [13, 25].

The critical values  $N_{TS,crit}$  and  $N_{CF,crit}$  can be defined as independent and constant values or as a stability boundary in the  $N_{TS}$ - $N_{CF}$ -stability diagram, where the critical  $N$ -factor of one instability form depends on the local  $N$ -factor of the other instability form:  $N_{TS,crit} = f(N_{CF})$ , respectively  $N_{CF,crit} = f(N_{TS})$  [29]. The curve, defining the stability boundary, has to be calibrated from experimental data and can be used to model a possible interaction between Tollmien-Schlichting and cross-flow instabilities [63], which otherwise cannot be considered by linear stability theory. Based on the convexity of the stability boundary the intensity of the interaction is prescribed [13].

It can be observed, that for consecutive transition prediction steps, the critical  $N$ -factor value may be reached in the preceding prediction step but in the current transition step the maximum  $N$ -factor is everywhere lower than the same critical value. This can prevent the transition prediction to converge to a constant transition location. The reason for this phenomenon lies in a certain kind of upstream influence of the turbulence model starting from the current transition location. This upstream influence can be accompanied by a significant change in the shape of the boundary layer profile, visible for example in decrease of the shape factor  $H_{12}$  or an increase in the wall shear stress, represented by the skin friction coefficient  $c_f$  (Fig. 13). Simply said, the laminar velocity profile already transitions upstream of the actual transition location into a turbulent velocity profile. As discussed in section 3.5.3, as soon as the shape of the velocity profile becomes fuller, the instabilities will start to be damped, leading to  $N$ -factors which decrease with streamwise distance. The upstream influence has been found to mainly

<sup>9</sup>  $f$ : frequency,  $\lambda$ : wave length,  $s$ : streamwise distance

depend on the surface grid resolution in streamwise direction and has a more pronounced effect on the  $TS-N$ -factor. To overcome this problem, a simple linear extrapolation<sup>10</sup> of the  $N$ -factor envelope is used at the position of the local minimum of the skin friction distribution, upstream of the current transition location (Fig. 13).

Eventually, a single transition point  $s_{tr}$  is determined for every streamline. This is provisionally the point which is located at the most upstream position when comparing the transition points predicted by the different transition criteria that are applied to the respective streamline. To stabilize the whole computational process of solving the RANS equations together with an iterative transition prediction, the new transition location are applied with a certain underrelaxation (typically  $f_{relax}=0.8$ ):

$$s_{tr,n} = s_{tr,n-1} + f_{relax} \cdot (s_{tr} - s_{tr,n-1}) \quad (60)$$

Another stabilizing method is to limit the increment in transition movement by a maximum stepsize. This method is sometimes useful to slowly approach a transition location which is located downstream of a laminar separation point. With appropriately small values for  $ds_{max}$  the risk of creating a large laminar separation that strongly disturbs the convergence of the RANS equations is reduced. The limitation can also be used to avoid too large steps in the transient phase of the transition prediction:

$$s_{tr,n} = s_{tr,n-1} + \min(|ds_{max}|, |s_{tr} - s_{tr,n-1}|) \cdot \text{sgn}(s_{tr} - s_{tr,n-1}) \quad (61)$$

In the general case  $ds_{max}$  is set to large values to increase the convergence speed of the transition prediction.

Finally, if no transition location is found by applying the available transition criteria (typically in the transient phase of the computation) the transition is simply shifted downstream by a certain distance  $ds_{max}$ :

$$s_{tr,n} = s_{tr,n-1} + ds_{max} \quad (62)$$

Under the prerequisite that for three-dimensional cases the startcoordinates of the streamlines are ordered, the single transition points per streamline form a polygonal line on the surface of the geometry. Together with a limiting height this polygonal line is used to specify a laminar region over the corresponding surface. For this, the surface grid points lying upstream of the polygonal line are defined as laminar and those lying downstream as turbulent. The information of the prescribed flow state is prolonged in wall normal direction using a similar algorithm as for the wall-normal points determination (Sec. 3.2) and thus forming a laminar region above the surface. If a set of streamlines is defined respectively for different surface parts of the geometry, for each surface a transition line can be predicted and laminar regions are created above each surface. In this way transition can be predicted simultaneously on all surfaces of a three-dimensional geometry.

Within the designated laminar regions, the turbulent production term of the turbulence model is artificially suppressed (Equation 9, Sec. 2.1) during the RANS iterations. With this sharp division of the flow field into fully laminar and fully turbulent flow regimes the classical point transition approach is realised. In this approach the turbulence model is turned on at the predicted transition point, the predicted transition point then corresponds to the transition onset point. The modelling of the intermittent region and thus the transition process from laminar to turbulent flow is in this approach left to the turbulence model [64]. This approach provides acceptable modelling of the transition region for a variety of standard application cases when compared to experimental data [47]. Simple algebraic intermittency functions often do not model the physics of the transition region but may be needed for

<sup>10</sup>A potentially more robust method of a quasi-extrapolation of the  $N$ -factor envelope can be achieved by manipulating the input for the stability solver. The idea is to keep the input profiles constant downstream of the location  $s_0 = s(c_{f,min})$  in three possible ways: i) keeping the profiles and boundary layer data constant, ii) keeping the shape of the profile and the boundary layer edge velocity constant but considering a growth with  $\sqrt{s}$  of the boundary layer by a scaling of  $\delta_1(s) = \sqrt{s/s_0} \cdot \delta_1(s_0)$  iii) keeping the shape of the profile, considering  $\sqrt{s}$ -growth and take the boundary layer edge velocity from the transitional and turbulent boundary layer downstream of  $s_0$ . However, no detailed investigations on these approaches has been performed yet.

numerical robustness [65]. Since the general correct physical modelling with intermittency functions is considered a reasonably difficult problem [65] and because of the unclear applicability of these functions to fully three-dimensional flows, the high implementation effort needed to consider three-dimensional cases in an unstructured RANS solver is regarded to be not justified for now.

For the iterative transition prediction process (Fig. 5), a suitable calling sequence for the transition prediction module has to be applied. An appropriate choice of the start and end iteration and the iteration period between two consecutive calls of the transition prediction is highly dependent on the solution convergence of the RANS solver. If the boundary layer data for transition prediction is extracted directly from the RANS solution, a measure of the convergence of the laminar boundary layer would be needed. The consideration of the general velocity residual (or even density residual) of the RANS solver does not necessarily lead to an adequate information of the solution quality of the laminar boundary layer. The same is valid for the convergence of integral parameters of the solution, for example lift or drag coefficient. Disturbances in the flow field (for example at the trailing edge or small oscillations in the presence of a laminar separation bubble) may falsify the information on the local convergence of the velocity field or other integral parameters.

As best practice it is currently considered to choose calling sequence and start and end iteration based on experience. In a typical computation with transition prediction based on RANS boundary layer profiles, the transition module is called 5 to 8 times, every 1000 to 5000 iterations, during the RANS computation, with the first call of the transition module also after 1000 to 5000 iterations.

### 3.7. Concluding remarks and statistics

The main components of the coupled program system of RANS solver and transition module forming the transition prediction method are shown in figure 5. The transition module itself is coupled to the DLR RANS solver TAU, however outsourced as one of several TAU program libraries. The transition module library is based on the same data structure as the DLR TAU code and it can be accessed from different program parts of the DLR unstructured RANS code suite. Accordingly, a coupling of the transition module with the incompressible unstructured DLR RANS code THETA [66] was used for the prediction of transition on rotor blades [67] with simplified empirical transition criteria [68, 69].

The transition module was developed with focus on a compromise between computational performance and relative simplicity of code structure and code expandability. The latter results for example in a relatively high memory consumption during runtime, which may reach in peaks  $\sim 80\%$  of the memory consumption of the TAU solver. This is mainly due to the fact that the transition module is accessible from a library (see above). For this, the relevant flow data are copied to newly provided arrays to deal with different data formats of the attached RANS solvers. As a result, some data is kept essentially twice in memory at times during transition prediction.

Something similar can be seen for data particularly processed for the actual transition prediction. To ease the access to the data from a programmers point of view, data distributed over different domains is gathered within single domains. This is for example done for the inviscid streamlines for which the complete boundary layer profiles along the streamline are stored on one process. This data is basically also saved twice, however the data can eventually be accessed at once and no further effort in data communication within the code has to be undertaken. The problem, however, is inherently based on the different parallelization demands (in form of the shape of the partitioned sub-grids) of the RANS solver and the transition prediction method. Based on the ungrateful parallelization possibilities, the implementation of the transition prediction method is a question of either using more complex parallel communication structures within the code (which also may lead to increased runtime due to increased number of communications) or to deal with increased memory consumption during runtime.

In summary, the transition module consists of  $\sim 50.000$  lines of code with  $\sim 1.500$  functions. Looking at the absolute number of code lines<sup>11</sup> the transition module source code<sup>12</sup> has the size of  $\sim 20\%$  of the

<sup>11</sup>code lines also including comments and code formatting

<sup>12</sup>without the external programs

Table 2: Relative sizes of elements of the transition module

transition module element	size
streamlines	29%
general infrastructure	13%
stability code interface	12%
boundary layer edge and data	9%
boundary layer code interface	8%
criteria evaluation and application	8%
boundary layer profiles	5%
I/O	5%
utility functions	5%
wall data and wall normals	4%
curvature and gradients	4%
transition module	100%
communication	6%

source code of the RANS solver part of TAU. This also holds for the number of functions programmed in the two source codes, where the transition module has approximately a fifth of the number of functions of the RANS solver part of TAU.

Table 2 shows an estimation of the sizes of the different elements of the transition module. Distributed over the different elements, overall  $\sim 6\%$  of the code is related to the communication of data. One third of the transition module consists of routines for the calculation of streamlines and streamline relevant data (Sec. 3.4.1). This includes the integration of inviscid streamlines and the determination of line-in-flight cuts together with the detection of stagnation points and the automatic determination of leading edge and trailing edge sweep angles and the interpolation of surface data along the streamlines. The interface to the stability solver (Sec. 3.5), including preparation of input data, execution of the program, processing of the stability computation results and general infrastructure, occupies  $\sim 12\%$  of the extent of the transition module. Much smaller is the amount of code used for wall data and wall normals calculation (Sec. 3.2) and the determination of the boundary layer profiles (Sec. 3.3.1). The part for the determination of the boundary layer edge and the general boundary layer data (Secs. 3.3.2 and 3.3) includes several (partly provisional) edge criteria and also the infrastructure to provide boundary layer data (e.g. boundary layer edge vectors for the streamline integration) for the complete surface of the geometry and thus consists also of a relatively large portion of the transition module.



## 4. Results

In the following two sections the verification and validation of the implemented transition prediction method, described in chapter 3, is presented. Section 4.1 gives insight into the general computational performance of the method, highlights requirements for the computational grid for an accurate prediction of transition with boundary layer data from a RANS solver and introduces a first complex application example to demonstrate the applicability of the method. Section 4.2 presents the results, and their evaluation, of the application of the transition prediction method to different transitional wind tunnel experiments.

### 4.1. Verification

In this section substantial components for the application of the transition prediction method are verified. Subsection 4.1.1 gives an overview of the computational performance with regard to the parallel execution of the method and the computational demand in terms of execution time in relation to the execution time of the RANS solver and the overall computational time. In subsection 4.1.2 a decisive investigation on the requirements for the computational grids is given. Based on a suggested grid generation strategy (Sec. A.1), which has been applied throughout the present work, a thorough grid convergence study is presented. Finally, in subsection 4.1.3, the general application of the presented transition prediction method is shown for a generic three-dimensional transport aircraft configuration, which also gives an example of the intended application scenarios for the transition prediction method.

#### 4.1.1. Code parallelization

Different calculations, published in reference [40], have been performed to validate the parallelization of the transition module and to determine the impact of the parallelization on the computational effort. The conception of the validation study is to investigate the parallelization of the transition module based on one single transition prediction step applied to a fully converged transitional flow solution.

The basic test case for the study is the transition prediction for the flow around a 6:1 prolate spheroid [70] (Fig. 61, see also Sec. 4.2.5 for a general description of the case). For the flow parameters,  $\alpha = 5.0^\circ$ ,  $Re = 6.5 \times 10^6$ ,  $Ma = 0.13$ , both, Tollmien-Schlichting and cross flow instabilities are amplified, for nearly the complete laminar part of the flow over the prolate spheroid. An evaluation of both types of instabilities for the whole flow field leads to the maximum computational effort for the transition prediction if the transition prediction is based on the results of the stability analysis using the stability solver. From the evaluation of the computational time needed for one transition prediction step the maximum computational demand of the transition module can eventually be derived.

The computations were carried out on a hybrid computational grid with a prismatic grid part covering the boundary layer around the prolate spheroid. The overall number of points of the grid is 2.8 million, with a resolution of the prism layer with 128 grid points normal to the wall and a surface resolution of approximately 300 surface grid points in flow direction and an average of approximately 60 surface grid points in circumferential direction. The computations were carried out using an implicit LU-SGS time integration scheme, a  $3w$  multigrid cycle and low-Mach-number preconditioning. Turbulent flow was modelled using the Spalart-Allmaras turbulence model. The grid partitioning, and its effect on the domain shapes on the surface grid, is shown in figure 14 for a selection of different number of domains. The computations were executed using a cluster equipped with AMD opteron 2.2 GHz processors and 1-gigabit-ethernet.

As a reference, the computational demand of the TAU code itself was evaluated in terms of wall clock time and the wall clock time of one sequential TAU solver iteration step is used to normalize the computational demand of the transition prediction in the following. From the reference computation it can be seen that the TAU solver parallels well for the processor numbers used in the investigations of the code parallelization [40].

The overall computational demand of one transition prediction step depending on the number of edge streamlines and on the number of processors is displayed in figure 15. Based on the parallelization concept for the external stability solver (Sec. 3.1) a very good scaling is achieved, as long as the number of processors is an integer multiple of the number of streamlines processed by the transition module. Additionally, it can be seen that there exists a linear dependency of the computational effort on the number of processed streamlines and that most of the computational effort is caused by the execution of the linear stability equations solver.

The computational effort to process different streamlines with the stability solver may lead to very different computational times, since the different streamlines may exhibit varying indifference points and transition locations. By these two limits, in addition to the general length of the streamline, the number of boundary layer profiles to be analysed with the stability solver is determined and thus the computational demand of the stability analysis. However, the flow conditions chosen for this test are such that most streamlines are very similar in their properties, and thus in the computational effort needed for processing. On the other hand, the assignment of the streamlines to the different processes for the parallel execution is done regardless of their properties. Because of that, unfavourable combinations of streamlines are possible, where one domain processes several streamlines with higher computational demand. This may lead to an increased overall computational time, as the overall time for the transition prediction depends on the maximum time spent on one domain. An example can be found in figure 15, for the case of 12 streamlines on 6 processes. For this case the time needed for one transition prediction step is nearly the same as for the case of 12 streamlines on only 4 processes.

If the number of processes exceeds the number of streamlines, no further benefit is gained in terms of computational time from the parallel execution of the transition module. This is inherently based on the type of parallelization of the execution of the external stability solver (Sec. 3.1): if the number of processes is larger than the number of streamlines the additional processes run on idle while waiting on the stability analysis to finish on the other processes.

If the time needed for one transition prediction step is related to the computational time for one multigrid cycle of the TAU solver for the same number of processes, it can be seen that the relative ratio stays nearly constant with varying number of processes (Fig. 16), as long as the number of processes does not exceed the number of streamlines. For the case of the prolate spheroid the computational demand of processing 6 (12, 24) streamlines is constantly approximately 25 (45, 90) times as high as the computational demand of one TAU iteration for the number of processes varying from 1 to 14.

The main reason for the relatively high computational demand for one transition prediction step for the prolate spheroid is that the ratio of the average number of points on the streamlines to the overall number of grid points is rather high. The average number of points along the streamlines is approximately 300 (200 in the laminar part), giving a ratio of approximately 1/14,000 per streamline. An alternative computation was therefore performed with transition predicted only on the upper and lower surfaces of the horizontal tail plane of a generic transport aircraft with  $\alpha = -4.0^\circ$ ,  $i_H = 4.0^\circ$ ,  $Re = 2.3 \times 10^6$  and  $Ma = 0.2$ . (Sec. 4.1.3). For this case, as before, a hybrid grid was used, again with a prismatic grid part covering the boundary layers on the surfaces of the geometry, with a resolution of the prism layer normal to the wall of 48 grid points. With an overall number of grid points of 12 million and an average streamline length of 100 points (60 in the laminar part) on the horizontal tail plane, a ratio of the points of 1/120,000 per streamline is achieved.

For both test cases, the prolate spheroid as described before and the generic transport aircraft, now only Tollmien-Schlichting instabilities are considered. Different computations were carried out using 8 domains with 6, 12, and 24 edge streamlines respectively. If the computational time is again normalized with the corresponding time used for one TAU multigrid cycle (LU-SGS,  $3w$ ) a significant reduction in computational time is achieved for the transition prediction on the horizontal tailplane of the aircraft compared to the prolate spheroid.

The relatively high computational effort of one transition prediction step compared to one TAU multigrid cycle loses significance with regard to the overall computational effort of a complete, fully converged calculation of a flow with transition prediction. The majority of the computational time

is due to the iterative procedure of the transition prediction (Fig. 5). The main part of the overall computational cost comes from the numbers of multigrid cycles needed to get converged intermediate solutions after updating the transition location. For the flow around a prolate spheroid [40], an average overall number of time steps of 20.000 - 35.000 was needed, with 4-6 transition prediction steps to reach a well converged solution. The fraction of the overall consumed time used by the transition prediction process was then  $\sim 1\%$ .

#### 4.1.2. Grid convergence

A grid convergence study to analyse the influence of the grid resolution on the computations of amplification rates and  $N$ -factor curves with the stability solver has been published in reference [40]. For the study, the flow around an infinite swept wing with ONERA D profile (see Fig. 39 and Sec. 4.2.3) with flow conditions of  $\alpha_n = 4.0^\circ$ ,  $Ma = 0.23$ ,  $Re = 2.39 \times 10^6$  and a sweep angle of  $\Lambda = 60^\circ$  was investigated. Transition was prescribed for this study at  $x/c = 0.03$  on the upper surface (suction side) and at  $x/c = 0.85$  on the lower surface (pressure side) and the turbulent flow was modelled using the Spalart-Allmaras turbulence model. For comparison, computations with a boundary layer code [49] (Sec. 2.3.1) were performed, using the pressure distribution from the Navier-Stokes solution as input.

For the RANS computations different grids with different grid resolutions were used. The structured parts of the grids that cover the boundary layer are resolved with 128 to 512 grid points on the surface and 32 to 128 grid points normal to the wall. For the finest grid, approximately 60-120 grid points eventually resolve the laminar boundary layer. An assessment of the streamwise velocity profiles shows a good agreement of all RANS profiles with the profiles from the boundary layer code. The cross-flow velocity profiles differ significantly for the coarser grids from the reference profiles of the boundary layer code calculation but are accurately predicted in the RANS computation for the finer grids [40].

The accuracy of the velocity profiles has a direct influence on the  $N$ -factors computed with the stability code. From evaluation of the  $N$ -factor envelopes of all computations on the various grids and by comparison to the envelopes from the boundary layer code computations it is concluded, that for Tollmien-Schlichting instabilities a normal-to-wall grid resolution of 32 grid points gives already appropriate results for the computed  $N$ -factors [40]. For an accurate transition prediction for Tollmien-Schlichting instabilities at least 48 grid points are necessary and for cross flow instabilities a normal-to-wall resolution of up to 128 grid points is needed [40].

Another investigation on the grid resolution in wall normal direction for transition prediction in three-dimensional flows was carried out based on the flow around an infinite swept wing with a NACA 64<sub>2</sub>-A-015 profile normal to the leading edge (figure 43, Sec. 4.2.4). The computations were carried out using an implicit LU-SGS time integration scheme, a  $4w$  multigrid cycle, matrix artificial dissipation and low-Mach-number preconditioning. Turbulent flow was modelled using the Spalart-Allmaras turbulence model. This study additionally focused on the Reynolds number influence on the grid convergence. Accordingly, the flow around the infinite swept wing for three different Reynolds numbers was considered,  $Re = 3.0 \times 10^6$ ,  $Re = 15.0 \times 10^6$  and  $Re = 25.0 \times 10^6$ . The values for the other flow conditions (angle of attack  $\alpha$  and sweep angle  $\Lambda$ ) were chosen such that both Tollmien-Schlichting and cross-flow instabilities experience significant amplification. For the symmetric profile only stability results for the upper surface were considered.

For each Reynolds number, a grid series consisting of 7 grids was created, based on the grid generation strategy presented in section A.1. For all grids 512 grid points for the surface (upper and lower surface) of the geometry were used to resolve the streamwise direction. The height of the prismatic region was kept constant within each grid series, adapted to the respective Reynolds number. The resolution of the prismatic region in wall normal direction and the first wall distance were chosen according to the values given in table 3.

First of all, the results for the lowest Reynolds number confirm the results of the initial grid convergence study (see above). With relatively similar flow conditions ( $Re = 3.0 \times 10^6$ ,  $\Lambda = 50^\circ$  and  $\alpha = -2.5^\circ$ )

Table 3: Number of prism layers and target  $y^+$ 

$n_{prism}$	$y^+$
32	1.0
48	0.75
64	0.5
96	0.375
128	0.25
192	0.1875
256	0.125

as for the ONERA D infinite swept wing ( $Re = 2.39 \times 10^6$ ,  $\Lambda = 60^\circ$  and  $\alpha = 4^\circ$ ), grid convergence is also reached for 48 grid points in wall normal direction for the  $N_{TS}$ -envelope and for 128 grid points in wall normal direction for the  $N_{CF}$ -envelope (Fig. 18). However, for the coarsest grid with 32 points normal to the wall, the  $N_{TS}$ -factor is not predicted as accurate as before, with the  $N$ -factor being constantly too low by a  $\Delta N$  of 1 compared to the grid converged result. The cross-flow  $N$ -factor on the coarsest grid is too small by a factor of 2 compared to the  $N_{CF}$ -factor of the finest grid. This is in turn again in accordance with the previous findings.

For higher Reynolds numbers the grid convergence seems to be more demanding. Looking at the remaining two cases with  $Re = 15.0 \times 10^6$  and  $Re = 25.0 \times 10^6$ , grid convergence begins at an increased number of wall normal points compared to the case with relatively low Reynolds number (Figs. 19 and 20). First of all it can be seen, that for the Tollmien-Schlichting  $N$ -factor now 64 grid points normal to the wall are at least needed for grid convergence. Whereas on the coarsest grid for the low Reynolds number the accuracy for the  $N_{TS}$ -factor is still reasonable this is not true for the higher Reynolds numbers. For the highest Reynolds number the  $N_{TS}$ -factor is even barely existing anymore on the coarsest grid.

A similar trend can be seen for the  $N_{CF}$ -envelope: no amplifications are computed by the stability code for the coarsest grid, for the highest Reynolds number this is even extended to the second coarsest grid with a resolution of 48 grid points normal to the wall. For grid converged cross-flow  $N$ -factor curves, for the higher Reynolds numbers a resolution of 192 to 256 grid points normal to the wall is needed, compared to 128 for the lowest Reynolds number.

An indication of the origin of the poorer grid dependency with increasing Reynolds number can be seen when looking at the boundary layer profiles and their first and second derivatives for the highest considered Reynolds number (Figs. 21 and 22). First of all, it can be seen, that the second derivatives of the streamwise and cross-flow profiles for the coarsest grids differ significantly from the respective shape of the converged profiles. Moreover, on the coarser grids the shape of the actual velocity profiles in the vicinity of the boundary layer edge does not match the shape of the corresponding profiles on the finer grids. If already the shape of the velocity profile differs, it is clear that this difference is immediately transferred to the first and second derivatives.

A crucial point for the accurate computation of the laminar velocity profiles is the actual resolution of the laminar boundary layer. The grids are designed to cover a fully turbulent or transitional boundary layer inside the prismatic region (Sec. A.1). As a measure for a good size of the prism layer, ideally the complete boundary layer extent near the trailing edge of the considered geometry is just included within the prismatic region. Looking at some of the actual values for the considered grids (table 4) this has been successfully achieved, since at the trailing edge  $n_{turb} \approx n_{prism}$  for all cases.

A relatively large difference can be seen for the number of grid points actually resolving the laminar boundary layer ( $n_{lam}$  in table 4). This may partly be related to the different transition locations, since a more upstream positioned transition location implies a shorter and hence thinner laminar part of the boundary layer.

Table 4: Resolution of the laminar boundary layer

$Re$	$n_{prism}$	$n_{lam}$	$n_{turb}$ at TE	$x_{tr}/c$
$25.0 \times 10^6$	128	48 – 80	$\approx 128$	0.35
$25.0 \times 10^6$	256	96 – 160	$\approx 256$	0.35
$15.0 \times 10^6$	128	48 – 85	$\approx 128$	0.5
$15.0 \times 10^6$	256	96 – 170	$\approx 256$	0.5
$3.0 \times 10^6$	128	56 – 96	$\approx 128$	0.6
$3.0 \times 10^6$	256	112 – 192	$\approx 256$	0.6

The main reason for the worse resolution of the laminar boundary layer and the whole grid convergence problem seems to stem from the large difference in growth of a laminar boundary layer compared to a turbulent boundary layer with increasing Reynolds number together with following certain requirements needed for an accurate resolution of the turbulent near wall flow ( $y^+ \leq 1$ , Sec. A.1).

The results for the different grid convergence studies indicate, that for a Reynolds number of the order of  $\sim 1.0 \times 10^6$  a grid suitable for turbulent boundary layer flow is also relatively suitable for a laminar boundary layer. If the flow over a flat plate of length  $L$  is considered, a suitable grid for both types of flow for a Reynolds number of  $Re = 1.0 \times 10^6$  could have a wall distance  $y_0/L$  of the first wall normal grid point satisfying  $y^+ = 1$ . If it is assumed, that the distribution of grid points along the wall normal direction is suitable to accurately predict the laminar boundary layer for  $Re = 1.0 \times 10^6$  the same relative distribution of grid points along the wall normal direction would be desirable for laminar boundary layers at higher Reynolds numbers<sup>13</sup>. To achieve this, starting from the grid for  $Re = 1.0 \times 10^6$ , the prismatic region covering the boundary layer would need to be scaled according to the respective height of the laminar boundary layer  $\delta_{lam}/L$ . That means, the stretching factor  $q$  would stay constant with increasing Reynolds number and the first wall distance would be proportional to the laminar boundary layer thickness,  $(y_0/L) \sim (\delta_{lam}/L)$  (Fig. 23)<sup>14</sup>. This, however, means that this grid has an  $y^+ \approx 4$  for a Reynolds number of  $Re = 25.0 \times 10^6$ , as can be seen from figure 23.

From the correlations for the flat plate boundary layer thicknesses for laminar flow [11]

$$\delta_{lam}/L = 5.0 \cdot Re_L^{-1/2} \quad (63)$$

and for turbulent flow [11]

$$\delta_{turb}/L = 0.37 \cdot Re_L^{-1/5} \quad (64)$$

it can be seen, that with increasing Reynolds number the height of the laminar boundary layer decreases faster compared to the turbulent boundary layer. The ratio is changing with  $Re_L^{3/10}$ : for  $Re = 1.0 \times 10^6$  the turbulent boundary layer is 4.7 times as large as the laminar boundary layer, for  $Re = 10.0 \times 10^6$  the factor is 9.3. Considering the first wall distance another relation holds. Ideally, the first wall distance for a grid suitable for laminar flow scales, according to equation 63, as:

$$(y_0/L) \sim Re_L^{-1/2} \quad (65)$$

However, for a certain constant value of  $y^+$ , e.g.  $y^+ = 1$ , the wall distance of the first wall point scales approximately as

$$(y_0/L) \sim Re_L^{-9/10} \text{ for } y^+ = \text{const} \quad (66)$$

<sup>13</sup>An adequate resolution of the laminar boundary layer would be an equidistant distribution of the grid points normal to the wall [25].

<sup>14</sup>The stretching factor  $q$  in figure 23 is based on 32 points normal to the wall.

This approximation is based on equations 77 to 80. Applying those equations leads to a (almost) straight line for  $y_0/L$  in the logarithmic plot of figure 23 (denoted by " $y_0/L$  for  $y^+ = 1$ ") with a slope of approximately  $-9/10$ .

Equations 63 to 66 show two negative effects for the grid generation for transitional flows for large Reynolds numbers: Firstly, relative to the laminar boundary layer extent, the higher the Reynolds number the more grid points are concentrated in close proximity to the wall for  $y^+ = \text{const}$  ( $y^+ \neq f(Re)$ ). Secondly, for increasing Reynolds numbers the wall normal grid points need to be spread over an increasingly larger distance, relative to the laminar boundary layer, to cover the turbulent boundary layer. That is, from the perspective of the laminar boundary layer, more and more points of the prism layer are placed outside of the laminar boundary layer the larger the Reynolds number.

The first effect is characterized by the ratio of the expressions in equations 65 and 66 and the second effect by the ratio of the expressions in equations 63 and 64. Both effects lead to the fact that the laminar velocity profile is resolved increasingly worse near the boundary layer edge<sup>15</sup>.

Based on the grid convergence investigations, a fine resolution in wall normal direction is much more crucial for an accurate prediction of the cross-flow velocity profile and, accordingly, an accurate computation of the cross-flow  $N$ -factor, than it is for the streamwise velocity profile. For the cross-flow velocity profile an overall resolution of the prismatic region with 128 grid points normal to the wall is often sufficient enough, especially if the Reynolds number is low enough (unit Reynolds number  $Re/L \sim 1 \times 10^6$  1/m). For higher Reynolds numbers, depending on the actual accuracy requirements, definitely up to 256 grid points may be needed for transition prediction with linear stability theory and boundary layer profiles from the RANS solution.

It has to be noted, that all grids used for the grid convergence studies presented here have a constant extent of the prismatic region and a constant value for the distance of the first wall point around the complete geometry. A variation of these distances can possibly improve the grid convergence for higher Reynolds numbers. A more simple approach would be to adapt the extent of the prismatic region and the first wall distance of the grid according to a general boundary layer growth. This means, that the prismatic region and the first wall distance are increasingly smaller towards the leading edge compared to their values near the trailing edge.

This, however, does generally not solve the problem with the two very differently developing boundary layers for laminar and turbulent flow. Here, a grid adaptation according to the respective boundary layer properties would be beneficial [71]. For this, the current transition location, or better, the boundary layer development over the laminar and the turbulent part of the flow, needs to be known a priori to the adaptation of the grid.

Another, less attractive alternative for an improved grid convergence for transition prediction for higher Reynolds numbers would be to lower the grid requirements for the turbulent part of the boundary layer (e.g.  $y^+ > 1.0$  or turbulent boundary layer not entirely covered by the prismatic region).

Accompanying the grid convergence studies for the wall normal resolution a grid convergence study with special focus on streamwise resolution of the boundary layer was carried out. This study was used to investigate the influence of the current transition point on the laminar flow upstream of the transition point. A certain upstream influence, possibly affecting the transition prediction, has been seen for some computations (see also Sec. 3.6, Fig. 13).

The investigations presented here were executed for two cases, the two-dimensional flow over an NLF (1)–0416 airfoil (Fig. 29, Sec. 4.2.1) and the flow over an infinite swept wing with a NACA 642-A-015 profile normal to the leading edge (see above). The computations were carried out using an implicit LU-SGS time integration scheme, a  $4w$  multigrid cycle, matrix artificial dissipation and low-Mach-number preconditioning. Turbulent flow was modelled using the Spalart-Allmaras turbulence model.

<sup>15</sup>This also holds for turbulent boundary layers. Without the constraint  $y^+ = \text{const}$  the first wall distance would be scaled by  $(y_0/L) \sim Re_L^{-1/5}$ . However,  $y^+ = \text{const}$  requires, as shown, a scaling of  $(y_0/L) \sim Re_L^{-9/10}$

Different grids have been created, with a constant number of grid points normal to the wall in the prismatic region and varying number of points on the surface of the geometry in circumferential direction. For the sake of simplicity no special local refinement of the transition region was used, instead the overall number of surface grid points was increased, leading to the surface cell sizes at the transition location as indicated in table 5.

Table 5: Number of surface grid points and surface cell sizes at transition

$n_{surf}$	$\Delta s/c$ at $s_{tr}$
256	0.01200
512	0.00600
1024	0.00300
2048	0.00150
4096	0.00075

For the NLF (1)-0416 case for  $\alpha = 2.0^\circ$  and  $Re = 4.0 \times 10^6$  a definite influence of the grid resolution in streamwise direction can be seen for the shape factor  $H_{12}$  and the skin friction coefficient  $c_f$  (upper surface in figure 24, lower surface in figure 25). Both parameters are sensible parameters for the description of the shape of the boundary layer velocity profiles, however a clearly visible influence on the predicted  $N$ -factor envelopes is only seen for the coarsest grid. The reduced influence on the  $N$ -factor may be explained by the fact that both transition locations, on upper and lower surface, are located in a flow with relatively strong adverse pressure gradient (Fig. 31(b)). The pressure gradient is strong enough in that sense that the laminar boundary layer is about to separate, especially seen for the lower surface, as indicated by the low magnitude of the skin friction coefficient a short distance upstream of the transition point (Fig. 25). Velocity profiles with an inflection point, or in this case velocity profiles that are about to develop an inflection point, are highly unstable, leading to large amplification rates and a steeper slope of the  $N$ -factor envelope. The steep slope shortly before transition may in this case mask the differences in  $N$  which would have been expected from the differences in  $H_{12}$ .

The trend, that the  $N$ -factor computation is less sensitive to the streamwise resolution is supported by the result of the NACA 64<sub>2</sub>-A-015 infinite swept wing computations. For  $\Lambda = 30.0^\circ$ ,  $\alpha = 0.5^\circ$  and  $Re = 1.5 \times 10^7$  an influence of the transition location on  $H_{12}$  is visible (Fig. 26) which in turn does not translate to a significant variation of the  $N$ -factors for Tollmien-Schlichting and cross-flow instabilities. This is also true for  $\Lambda = 50.0^\circ$ ,  $\alpha = -1.0^\circ$  and  $Re = 5.0 \times 10^6$  (not shown here). However, for both infinite swept wing cases transition is, as for the 2D case, located in adverse pressure gradient flow (deduced from the pressure distribution for  $\Lambda = 30.0^\circ$  and  $\alpha = 1.5^\circ$ , figure 50).

Based on the observations presented here, it appears that the  $N$ -factor computations is relatively uncritical with respect to the streamwise resolution. However, if the flow around a two-dimensional NACA 65<sub>(215)</sub>-114 airfoil [72] at high Reynolds numbers is considered (not presented here), the previous statement is no longer valid. Due to the large Reynolds numbers ( $Re = 15 \times 10^6$  to  $50 \times 10^6$ ) transition is now located in the favourable pressure gradient region and a strong influence of the transition location on pressure distribution and shape factor ( $H_{12}$ ) can be seen. The large Reynolds numbers also mean that the influences on the pressure distribution and on  $H_{12}$  leads to large deviations in the calculated  $N$ -factor. For the lower Reynolds numbers the  $N$ -factor deviations are relatively small over the different grids used in the study, however they are becoming significant for Reynolds numbers from  $Re = 25 \times 10^6$  on. For the higher Reynolds numbers, a resolution of the surface grid of  $\Delta s/c \approx 0.0017$  gave sufficiently accurate results in terms of grid convergence of the  $N$ -factor curves. For the next coarser grid ( $\Delta s/c \approx 0.0043$ ) this was not valid anymore. For the worst cases ( $Re = 50 \times 10^6$ ,  $\Delta s/c \approx 0.0043$ ,  $\Delta s/c \approx 0.0063$ ) the  $N$ -factor at transition was approximately 30% larger on the coarse grids compared to the  $N$ -factor on the finest grid ( $N \approx 14$  and  $N \approx 11$ ).

### 4.1.3. Feasibility

A feasibility study of the transition prediction method has been published in references [39] and [40] for the flow around a generic, complex three-dimensional aircraft configuration. The objective was to predict transition simultaneously on all relevant surfaces of the configuration, namely fuselage, vertical tail plane and upper and lower surfaces of main wing and horizontal tail plane respectively. A hybrid grid was used, with an overall number of grid points of 12 million and a very moderate resolution of the prism layer, with generally 32 grid points normal to the wall, except for the horizontal tail plane with 48 points normal to the wall. This grid resolution of the boundary layer results in a fairly accurate prediction of boundary layer profiles while keeping the overall computational demand relatively low. The test case was run completely in parallel mode, using a partitioning of 8 domains for the grid. For faster convergence, low-Mach-number preconditioning was applied, together with an implicit LU-SGS time integration scheme. Turbulent flow was modelled using the Spalart-Allmaras turbulence model.

The flow conditions were chosen to ensure attached flow over nearly all surfaces ( $\alpha = -4.0^\circ$ ,  $i_H = 4.0^\circ$ ,  $Re = 2.3 \times 10^6$  and  $Ma = 0.2$ ). With regard to the moderate resolution of the boundary layers, only streamwise instabilities were considered. Typically, a much higher grid resolution is needed for accurate prediction of cross flow instabilities. Because of the very coarse resolution of the laminar boundary layer on the fuselage, both in wall-normal and streamwise direction, a simplified transition criterion was applied, predicting transition a short distance downstream of the pressure minimum. The main wing is equipped with a deflected flap, leading to large separated areas well before transition would have been predicted by linear stability theory. Here the laminar separation point was used as transition point instead, in order to avoid unsteadiness effects and convergence problems of the Navier-Stokes iterations. Transition on all other surfaces was predicted using linear stability theory in form of the  $e^N$ -method. A critical  $N$ -factor of 7.5 was arbitrarily assumed, corresponding to a turbulence intensity of  $\sim 0.13\%$ .

Figures 27 and 28 show the calculated edge streamlines together with the converged transition lines. For all wing like surfaces 6 streamlines have been used, respectively, and the fuselage is covered with 11 streamlines. The predicted transition lines are located in the adverse pressure gradient region, as expected for the investigated transition scenario. This test case gives an understanding of the ability of the transition module to predict transition on all relevant transitional surfaces of a generic transport aircraft configuration. It is especially demonstrated that the approach using edge streamlines from the Navier-Stokes is suitable for transition prediction for geometrically very different components (fuselage, wing) in one and the same computation.

## 4.2. Validation

The presented transition prediction method has been validated based on transition data of different wind tunnel experiments with varying complexity of model geometry and flow topology. With increasing complexity, the following test cases are considered in the subsequent subsections. First, the two-dimensional flow over the natural laminar flow profile NLF (1)–0416 is computed (Sec. 4.2.1). Next, the infinite swept wing flow over a natural laminar flow wing with NLF (2)–0415 airfoil section (Sec. 4.2.2) and the infinite swept wing flow over an variable sweep wing with ONERA D profile (Sec. 4.2.3) is considered. The investigations are concluded with two fully three-dimensional test cases, one for the flow over a variable sweep wing with a NACA 64<sub>2</sub>-A-015 profile (Sec. 4.2.4), the other for the flow over the DLR prolate spheroid (Sec. 4.2.5).

For all test cases, computational grids have been created according to the grid generation strategy presented in section A.1 and the most significant grid characteristics are summarized in table 6. All grids are unstructured grids with a prismatic region resolving the boundary layers. Grids that have been used for transition prediction have a wall normal resolution of 128 grid points for the prismatic region. The first wall distance for the grids has been chosen to yield  $y^+$  values below 0.5, respectively 0.25, in the RANS computations. Grids for wing geometries consist of o-type grids at the trailing edge

of the geometry, grids that have a farfield boundary (type *FF* in table 6) have a distance of 100 lengths of the geometry from the surface of the geometry to the farfield and grids that include wind tunnel walls (type *WT* in table 6) have an extent of the wind tunnel walls of 100 lengths of the geometry in upstream and downstream direction. For the computations the inflow and outflow of the wind tunnel is simply modelled by farfield boundary conditions, the tunnel walls are simulated as inviscid walls, neglecting the growth of the tunnel wall boundary layers.

Table 6: Computational grids characteristics

Geometry	$n_{prism}$	$n_{surf}$	$n_{all}$	$y^+$	type
NLF (1)–0416	128	512	70.000	0.5	2D FF
NLF (2)–0415	128	512	202.000	0.25	2D WT
ONERA D	128	512	140.000	0.5	2D FF
NACA 64 <sub>2</sub> -A-015	128	512	73.000	0.25	2D FF
ONERA D	32	260.000	9.000.000	0.5	3D FF
NACA 64 <sub>2</sub> -A-015	128	130.000	22.000.000	0.25	3D WT
DLR spheroid	128	20.000	2.800.000	0.25	3D FF

All computations, except where indicated, have been carried out using an implicit LU-SGS time integration scheme, a  $4w$  multigrid cycle, matrix artificial dissipation and low-Mach-number preconditioning. Turbulent flow was modelled using the Spalart-Allmaras turbulence model. The amplification rates for the different test cases have been computed using incompressible stability theory. For almost all test cases, a separate  $N$ -factor calibration has been carried out (not presented in detail here) and the calibrated  $N$ -factors, with previous critical evaluation, have generally been used for transition prediction.

For the calculation and calibration of critical  $N$ -factors and for the comparison of numerically predicted transition lines with experimental data, an uncertainty range has been sought to be applied for the different experiments. For the ONERA D test case (Sec. 4.2.3) not enough information could be found for the experimental determination of the transition locations and no uncertainty has been considered. For the NLF (2)–0415 experiment (Sec. 4.2.2) uncertainty ranges of the applied transition detection methods are given in the corresponding reports and have been applied accordingly together with transition locations based on different measuring techniques. In the experiments of the NLF (1)–0416 (Sec. 4.2.1) and the NACA 64<sub>2</sub>-A-015 (Sec. 4.2.4) test cases a similar transition detection approach has been used, that gives no exact transition location but rather a streamwise distance within which transition occurred. The minimum and maximum streamwise extent of this region has been used as uncertainty range for these test cases for visualization and calibration of the  $N$ -factors. For the DLR prolate spheroid (Sec. 4.2.5) a more sophisticated determination of the uncertainty of the transition location has been applied by computing the combined standard uncertainty of different separate uncertainties [73] (Eq. 73).

Another source of uncertainty, besides the certain possible resolution uncertainty in the experimental transition determination, is the definition of the transition point in the experiments. From the applied transition measurement techniques of the considered experiments and the reported amount of data, it is for most of the considered test cases not possible to conclude whether the experimental transition location corresponds to the beginning or the end of the transition region or to a location in-between. However, it is clear from an implementation point of view, that in the used numerical transition prediction method the transition point is associated with the onset of the transitional region (see Eq. 9, Sec. 3.6 and Sec. 2.1). With the current implementation, the transitional region has to be modelled by the turbulence model since explicit modelling with intermittency approaches is dispensed. However, the reported (and supposedly and apparently exact) transition locations of the considered experiments, irrespective of their exact definition, give no exact positions, but transition is generally located within

a certain streamwise extent. It is assumed, that the length of the transition region is relatively short for the considered test cases and that the unconsidered uncertainty of the transition point definition is covered by the considered uncertainty of the applied measurement technique with respect to the spatial resolution. For the DLR prolate spheroid (Sec. 4.2.5) no transition locations are explicitly given and the transition locations are derived from the wall shear stress magnitude. In certain regions the resolution of the experimental data in streamwise direction is high enough to draw conclusions on the length of the transition region. By comparing the development of the wall shear stress magnitude from the experiment and numerical investigations with the present transition prediction approach, it can be seen, that the transition region between the minimum and the maximum of the wall shear stress magnitude is short and very similar in shape and length for experiment and computation [47].

#### 4.2.1. NLF (1)–0416

The NLF (1)–0416 airfoil [74] (Fig. 29) is a natural laminar flow airfoil with a design lift coefficient of  $c_l = 0.4$  and a maximum relative thickness of  $t/c = 0.16$ . The airfoil was designed based on a multipoint inverse airfoil design method with the objective of combining high maximum lift with low cruise drag [74]. Low drag for moderate angles of attack is achieved because the profile design enables significant portions of accelerated or mildly decelerated flow leading to relatively long portions of laminar flow.

Experiments for this airfoil were conducted in the Langley Low-Turbulence Pressure Tunnel (LTPT) [74]. The tunnel is a single-return, closed-throat tunnel with a 3ft  $\times$  7.5ft rectangular test section of 7.5ft length [75, 76]. The wind tunnel model of the NLF (1)–0416 airfoil has a chord length of  $c = 0.609\text{m}$  ( $\hat{=}$  2ft) and spans the complete test section of 0.914m ( $\hat{=}$  3ft). Transition in the experiments was basically detected with microphones connected to certain orifices on the model. The beginning of the turbulent flow is characterized by an increase in noise level compared to the laminar flow. No turbulence intensity of the wind tunnel or for the experimental flow conditions is specified in the report of the measurements (Ref. [74]).

The missing turbulence level for the experiments leads to an inherent problem of the linear stability theory and the  $e^N$ -method<sup>16</sup>: a critical  $N$ -factor needs to be specified, taking into account the disturbance environment of the experiment (Sec. 2.2). A critical  $N$ -factor can usually be approximated as a function of the turbulence intensity, for incompressible flows with the help of equation 23. Alternatively, the critical  $N$ -factor can be taken from a previous calibration, if available.

Research on the general turbulence intensity of the corresponding wind tunnel does not necessarily give a much clearer picture. Initial measurements of the turbulence intensity of the Langley Low-Turbulence Pressure Tunnel [75] were conducted at constant tunnel pressure (4 atmospheres) for different unit Reynolds numbers ( $Re/L \hat{=}$   $Re$  per ft) but not at constant Mach number. Other available data have been collected after the NLF (1)–0416 experiments and, more crucial, after a modification of the wind tunnel [76, 77]. However, fortunately the earlier results for a tunnel pressure of 4 atmospheres were confirmed (up to  $Re/L \approx 5 \times 10^6$  per ft), thus leading to the conclusion that the turbulence intensities of the later investigations are also representative of the tunnel condition at the time of the NLF (1)–0416 experiments. The later experiments include also the evaluation of the turbulence intensity for varying Reynolds number at constant Mach numbers. For  $Ma = 0.1$ , the measured turbulence intensity [77] corresponds to a critical  $N$ -factor of  $N = 9.5$  to  $10.5$  (rather  $10.5$  but definitely not lower than  $9$  for the unit Reynolds number range of the NLF (1)–0416 experiments, see figure 30).

The result of an  $N$ -factor calibration based on the experimental transition locations for this test case revealed a varying critical  $N$ -factor with varying Reynolds number (not shown here). The averaged value of the critical  $N$ -factor decreased from  $N_{crit} = 10.5$  for  $Re = 1.0 \times 10^6$  to  $N_{crit} = 7.9$  for  $Re = 4.0 \times 10^6$ . The value of  $N_{crit}$  differed between upper and lower surface of the airfoil with the critical  $N$ -factor for the upper surface being larger by a value of  $\Delta N = 3$ , respectively. The final averaged critical  $N$ -factor value, eventually used for the computations with transition prediction, is  $N_{crit} = 9.0$ .

<sup>16</sup>Actually a problem of all transition prediction methods that need to take into account the disturbance environment.

The relatively small model size compared to the tunnel (relative tunnel height  $h/c = 3.75$ ) made it unnecessary to include the modelling of the wind tunnel walls in the two-dimensional RANS computations. This is underlined by the predicted pressure distributions compared to the experimental values for  $Ma = 0.1$  and  $Re = 4.0 \times 10^6$  for a range of angles of attack (Fig. 31). Otherwise relevant characteristics of the computational grid are given in table 6.

Based on the measuring technique for the detection of the transition locations, the exact experimental transition locations are not available. Instead the streamwise range is given within which transition occurs. This range is bounded by two of the orifices used for the detection of the state of the boundary layer flow. The upstream bound is the last orifice for which still laminar flow was encountered, the downstream bound is, accordingly, the first orifice for which turbulent flow was encountered during the experiment.

For the four experimentally investigated Reynolds numbers, at a Mach number of  $Ma = 0.1$ , the predicted transition locations for angles of attack ranging from  $\alpha = -12^\circ$  to  $\alpha = 12^\circ$  are presented in figures 32 to 35. Transition prediction is based for all cases on a critical  $N$ -factor of  $N_{crit} = 9.0$ . For all Reynolds numbers transition on the lower surface is characterized to occur over a laminar separation bubble for angle of attacks larger than approximately  $\alpha = 0^\circ$ . The location of the laminar separation corresponds to the beginning of the pressure recovery region of the lower surface at  $x/c \approx 0.65$  (see Fig. 31). Depending on the Reynolds number, the extent of the predicted laminar separation bubble in this region varies, with the largest extent for  $Re = 1.0 \times 10^6$  ( $\Delta x/c \approx 0.15$ , Fig. 32) and decreasing in size with increasing Reynolds number ( $\Delta x/c < 0.15$  for  $Re = 4.0 \times 10^6$ , Fig. 35).

The relatively large laminar separation bubble for  $Re = 1.0 \times 10^6$  exhibits small oscillations during the steady RANS computation, preventing the solution to fully converge in terms of the density residual. Relevant flow coefficients ( $c_l$ ,  $c_d$ ) however reach a steady state. For moderate angles of attack, the flow for the two lowest Reynolds numbers is also accompanied by a small separation bubble on the upper surface of the airfoil. The existence of a separation bubble is confirmed by an oil flow visualization from the experiments [74] for  $\alpha = 0^\circ$ ,  $Re = 2.0 \times 10^6$  and  $Ma = 0.14$ .

Overall, a very good accordance with the experimental transition locations is achieved for all considered flow conditions. Large deviations are only visible for large negative angles of attack ( $\alpha < -8^\circ$ ) for the predicted transition locations on the upper surface (Figs. 33 and 35). A thorough investigation on the critical  $N$ -factor reveals however, that the predicted transition locations are rather insensitive to the critical  $N$ -factor actually applied in the calculations for this case (not shown here). It can be seen, that a variation of the critical  $N$ -factor from  $N_{crit} = 8.0$  to  $N_{crit} = 10.5$  leads to equally accurate predicted transition locations within the error bounds prescribed by the orifices used for the transition detection in the experiment.

#### 4.2.2. NLF (2)–0415

The NLF (2)–0415 airfoil (Fig. 36) was designed as an unswept low-drag wing [78, 79]. It is characterized by a relatively small leading edge radius and for the upper surface the airfoil shape is merely convex. For the design angle of attack  $\alpha = 0^\circ$  the minimum pressure on the upper surface is at  $x/c \approx 0.71$ . The long negative pressure gradient region is intended to keep streamwise instabilities subcritical for the unswept wing [78].

The airfoil is considered to be ideal for the investigation of isolated cross-flow instabilities in three-dimensional flows using a relatively small negative angle of attack and an appropriate sweep angle [79]. The small leading edge radius prevents attachment line instabilities to become significant and the long extent of accelerated flow amplifies cross-flow instabilities while at the same time damping Tollmien-Schlichting instabilities.

Experiments for the NLF (2)–0415 airfoil with sweep angle of  $\Lambda = 45^\circ$  and angle of attack of  $\alpha = -4^\circ$  have been carried out in the Arizona State University transition research facility [79]. The facility is a low turbulence, closed return tunnel with a  $1.4\text{m} \times 1.4\text{m}$  rectangular test section of 5m length [80].

The turbulence intensity is lower than  $Tu=0.04\%$ <sup>17</sup>.

The wind tunnel model of the NLF (2)–0415 wing has a streamwise chord length of  $c=1.83\text{m}$ . To eliminate wing tunnel wall interference effects and to simulate infinite swept wing flow in the experiment contoured end liners have been attached to the wind tunnel walls at each end of the wing. The end liners in conjunction with the relatively large wing model size (tunnel height relative to stream wise chord length of the model:  $h/c=0.765$ ) add disturbances to the flow leading to an increased turbulence level of  $Tu=0.09\%$  [79]. Transition in the experiments was detected from naphthalene sublimation flow visualization techniques, surface mounted hot film gauges and boundary layer hot wire probes for Reynolds numbers from  $Re=1.93\times 10^6$  to  $Re=3.73\times 10^6$ .

For the infinite swept wing computations a two-dimensional grid has been used with relevant parameters as given in table 6. The computational grid has the upper and lower tunnel walls included as inviscid walls. With the consideration of the tunnel walls, the predicted pressure distribution for  $Re=1.93\times 10^6$  is in relatively good agreement with the experimental pressure distribution (Fig. 37).

The experiments were accompanied by a thorough theoretical analysis of the cross flow instabilities, based on linear stability theory. From this analysis,  $N$ -factors at transition for stationary cross flow instabilities were determined. These critical  $N$ -factors are in the range of  $N_{crit}=6.4$  to  $6.8$  [79]. While stationary cross-flow instabilities are considered as the dominant instabilities, the simultaneous presence of travelling cross-flow waves was observed in the experiments. The respective  $N$ -factors at transition for travelling cross-flow are determined by linear stability theory in the range of  $N_{crit}=8.5$  to  $9.1$  [79]. The theoretically calibrated critical  $N$ -factors for stationary and travelling cross-flow waves are confirmed by stability analysis with linear stability theory in reference [81], where  $N_{SCF,crit}=6.4$  and  $N_{TCF,crit}=8.5$  were determined.

In a subsequent experiment the influence of the surface roughness of the model on the transition location was investigated [37]. For this, the paint of the initial wing model with a measured peak-to-peak roughness of  $h\approx 9\mu\text{m}$  (equivalent to  $h_{rms}\approx 3.3\mu\text{m}$ ) was removed and the surface of the model was polished in two steps to achieve rms roughness values of  $h_{rms}\approx 0.5\mu\text{m}$  and  $h_{rms}\approx 0.25\mu\text{m}$  respectively. Based on the experimental transition locations for the three surface roughnesses, CROUCH et. al. derived an expression for the critical cross-flow  $N$ -factor for stationary cross-flow instabilities in dependence of surface roughness [36]. This expression, given by equation 24, is valid for a low turbulence environment.

An independent calibration of the critical  $N$ -factor for stationary cross-flow instabilities gives critical  $N$ -factors in the range of  $N_{crit}=6.5$  to  $7.0$  (not shown here), in close agreement to the findings presented above. It can be shown, that the lower value gives transition locations which are in close agreement with the experiments for the larger Reynolds numbers but more or less fails to do so for the smaller Reynolds number. The opposite holds for the upper limit of the critical  $N$ -factor.

Transition has eventually been predicted using the correlation of the critical  $N$ -factor with the roughness height (Eq. 24). With this a very good agreement of the predicted transition locations within the given uncertainty range of the experimental data [79] is achieved (Fig. 38). This is, however, not very surprising, since some of the experimental data of this test case were, in turn, used before to determine the equation for the critical  $N$ -factor (see above).

<sup>17</sup>Two different turbulence intensities,  $Tu=0.02\%$  and  $Tu=0.04\%$ , are given for the wind tunnel in the report of the experiments (Ref. [79]). In reference [80] it is stated, that the measured streamwise velocity fluctuations are, unusually, larger than the vertical velocity fluctuations. It is concluded, that most of the measured streamwise velocity fluctuations are introduced downstream of the actual test section to the flow and that the vertical velocity fluctuations are more representative of the actual flow quality. If the fluctuations of all velocity components are considered for the turbulence intensity, then  $Tu\approx 0.04\%$ . If only the vertical components are considered, then  $Tu\approx 0.02\%$ .

### 4.2.3. ONERA D

The AFV-D wing (AFV: aile à flèche variable) is a rectangular wing model with variable sweep and a symmetric ONERA D profile (Fig. 39) normal to the leading edge. The sweep angle of the wing can be adjusted between  $\Lambda = 0^\circ$  and  $\Lambda = 60^\circ$ . In its unswept configuration the wing has an aspect ratio of 8, which is however significantly lower for the largest possible sweep angles [82].

Experiments with the AFV-D wing have been conducted in two different wind tunnels, the ONERA S1Ca wind tunnel and the ONERA S2Ch wind tunnel [82, 83, 84]. Both wind tunnels are unpressurised Eiffel type wind tunnels with circular test section of diameter  $d = 3\text{m}$ . The turbulence intensity of the flow is specified as  $Tu \approx 0.3\%$  and transition has been detected in the experiment based on sublimation techniques. Transition measurements were conducted for five different Reynolds numbers, based on the chord length normal to the leading edge, from  $Re = 0.4 \times 10^6$  to  $Re = 1.4 \times 10^6$ . For an angle of attack of  $\alpha_n = 6^\circ$  transition locations were measured on the pressure side of the wing.

The wing model is attached on one side to the wind tunnel wall, the other end is positioned freely in the air stream. The chord length normal to the leading edge of the wing is  $c = 0.3\text{m}$ , the half span of the model is  $b = 1.2\text{m}$  for the unswept case and  $b \approx 1.0\text{m}$  for a sweep angle of  $\Lambda = 40^\circ$  (Fig. 40).

The experimental pressure distributions have been measured for other sweep angles (but for the same angle of attack) and not in the same wind tunnel<sup>18</sup> as has been done for the transition location presented in references [82, 83, 84]. For this reason, a cross-correlation has been carried out based on the pressure experiments to retrieve the correct flow conditions for the transition experiments in the RANS computations. The transferability of the result is guaranteed since both wind tunnels are basically identical.

First, to also consider possible three-dimensional finite-span effects, fully three-dimensional computations were performed. The computational grids were based on the parameters given in table 6. Because the wing model size is relatively small compared to the wind tunnel test section extent, the wind tunnel walls were not included in the computations. For the four sweep angles  $\Lambda = 0^\circ$ ,  $\Lambda = 35^\circ$ ,  $\Lambda = 45^\circ$  and  $\Lambda = 55^\circ$  the computed pressure distribution are presented in figure 41. The numerical pressure distribution is extracted from the three-dimensional flow field at the position of the pressure row from the experiment,  $y_1/b_0 = 0.6$ , as indicated in figure 40. From the experiments complete pressure distributions are only available for  $\Lambda = 0^\circ$  and  $\Lambda = 55^\circ$  (Figs. 41(a) and 41(d)). For  $\Lambda = 35^\circ$  and  $\Lambda = 45^\circ$  experimentally determined values of the pressure are only available at a few measuring stations, marked by filled symbols in figure 41(b) and figure 41(c). The remaining space is covered by the pressure distribution from the unswept case and applying simple sweep theory ( $c_p = c_{p,(\Lambda=0^\circ)} \cos^2 \Lambda$ ), indicated by open symbols in the respective figures. Summarizing, the comparison of experimental and numerical pressure distributions for  $\alpha_n = 6^\circ$  and  $Re = 0.4 \times 10^6$  shows a good agreement for all four sweep angles for the three-dimensional computations.

From the above investigation it can be concluded, that the experimental pressure distribution can be accurately predicted from three-dimensional RANS computations. Based on this, it can furthermore be assumed with certain confidence, that the flow solutions for the unreported sweep angles represent the actual flow states in the experiment. Additionally, from the numerical pressure distribution on the wing surface (Fig. 40, for  $\Lambda = 40^\circ$ ) it can be seen, that the isobars are nearly perfectly aligned parallel to the leading edge, indicating that the flow state corresponds to infinite swept wing conditions.

In a next step infinite swept wing computations have been performed, with the relevant parameters for the computational grid again summarized in 6. As for the three-dimensional case, the wind tunnel walls have been excluded from the RANS computations. If for all sweep angles the angle of attack is reduced to  $\alpha_n = 5^\circ$ , to account for three-dimensional effects that can not be modelled directly in infinite swept wing computations, a good agreement with the experimental pressure distributions and the numerical pressure distributions is achieved.

<sup>18</sup>Pressure measured in the S1Ca wind tunnel, transition measured in the S2Ch wind tunnel.

This is shown in figure 41 for the sweep angles where an experimental pressure distribution is available. A good agreement between the two numerical results is also achieved for other sweep angles, always under the premise, that the angle of attack for the infinite swept wing computations is  $\alpha_n = 5^\circ$  instead of  $\alpha_n = 6^\circ$  for the three-dimensional computations and in the experiment. Additionally, without further proof, it is assumed, that the flow conditions in the two, in principle identical, wind tunnels are the same for the investigated flow conditions. Summarized, it is concluded, that the transition experiments can be analysed with certain confidence by conducting infinite swept wing computations.

The calibration of the critical  $N$ -factors (not shown here) for this test case revealed, that for sweep angles larger than  $30^\circ$ , based on linear stability theory, only cross-flow instabilities are responsible for transition for the considered flow conditions. Furthermore it was found, that the computed  $N$ -factors for the experimental transition locations had a lesser spread for travelling cross flow instabilities compared to  $N$ -factors for stationary cross flow instabilities. The assumption of travelling cross-flow instabilities being the critical instabilities is justified by the general understanding that travelling waves may become dominant for turbulence intensities larger than  $Tu \approx 0.2\%$  [36].

The respective critical values from the  $N$ -factor calibration are  $N_{SCF,crit} = 4.0$  and  $N_{TCF,crit} = 6.25$ . The value of  $N_{SCF,crit} = 4.0$  for stationary cross flow instabilities is supported by findings from reference [85]. There it is shown, that independent of the surface roughness, the values of  $N_{SCF,crit}$  is nearly constant for turbulence levels larger than approximately 0.3%. It is suggested, that this is an indication of travelling cross flow modes being the dominant transition mechanism. The nearly constant value in this correlation is  $N_{SCF} \approx 4.0$ . In the same reference a dependence of the critical  $N$ -factor for travelling cross flow waves from the turbulence intensity is depicted, from which a simple correlation can be approximated:

$$N_{TCF,crit} \approx 0.11 - \ln(Tu) \quad (67)$$

With this approximation and the turbulence intensity for the wind tunnel used for the experiments ( $Tu \approx 0.3\%$ ) an critical  $N$ -factor of  $N_{TCF,crit} = 5.9$  can be determined, which is in relatively close agreement to the previously calibrated critical  $N$ -factor ( $N_{TCF,crit} = 6.25$ ).

If transition is predicted for stationary and travelling cross flow for the AFV-D wing based on the previously defined critical  $N$ -factors ( $N_{SCF,crit} = 4.0$  and  $N_{TCF,crit} = 6.25$ ) a fairly good agreement with the experimental transition locations is achieved (Fig. 42). Because of the sparse distribution of the experimental data points, the predictions for both instability types appear to be relatively accurate, with a slightly better fit for travelling cross flow. For a better assessment additional experimental data points are needed, as the variation in predicted transition locations differs significantly for flow conditions not covered by the experiment.

#### 4.2.4. NACA 64<sub>2</sub>-A-015

A swept wing model with a symmetric NACA 64<sub>2</sub>-A-015 airfoil section (Fig. 43) normal to the leading edge has been used for comprehensive experiments to analyse the effect of sweep angle on boundary layer transition [86]. The semi-span model consists of an untapered wing that is mounted at the wing root to the wind tunnel wall while the wing tip is positioned freely in the air stream (Fig. 44). The wing has a variable sweep that is adjustable between  $\Lambda = 0^\circ$  and  $\Lambda = 50^\circ$  in steps of  $\Delta\Lambda = 10^\circ$ . For sweep angles larger than  $\Lambda = 20^\circ$ , the otherwise straight wing tip has an extension of approximately triangular shape [86] (Fig. 44).

The investigations were conducted in the NASA Ames 12-foot pressure tunnel. This facility is a single-return, closed-throat pressurized tunnel with low turbulence intensity in the free stream [87]. The wind tunnel has a circular test section of diameter  $d = 12\text{ft}$  (Fig. 44). The wing model used in the experiments has a chord length normal to the leading edge of  $c = 4\text{ft}$ , in the unswept configuration the half span of the model is  $b = 10\text{ft}$  (Fig. 44), giving an aspect ratio of 5 for  $\Lambda = 0^\circ$ . Pressure and transition was measured at two rows of measuring orifices, the inboard row being located at  $y/b \approx 0.45$  and the outboard row at  $y/b \approx 0.8$ , with  $y/b$  based on the unswept geometry (Fig. 44). Transition locations

were determined for 6 different sweep angles and 13 different angles of attack ( $\Lambda=0^\circ$  to  $\Lambda=50^\circ$  in steps of  $\Delta\Lambda=10^\circ$  and  $\alpha=-3^\circ$  to  $\alpha=3^\circ$  in steps of  $\Delta\alpha=0.5^\circ$ ).

Transition in the experiments was detected with subsurface microphones connected to the pressure orifices of the model. The onset of transition is characterized by an increased noise level when the flow state of the boundary layer turns from laminar to turbulent. Hot-wire anemometer measurements indicate that the turbulence intensity based on velocity fluctuations is less than  $Tu \approx 0.02\%$  in the wind tunnel test section [88]. Determination of the sound pressure level indicates however an increase in noise level in the test section with increasing Mach number. Following certain assumptions, the sound pressure level measured in the test section can be transferred to an acoustic equivalent turbulence intensity  $Tu=(u'/u_\infty)$  [88]<sup>19</sup>:

$$Tu = \frac{10^{0.05 L_p - 3.7}}{\gamma Ma p} \quad (68)$$

Measurements of the sound pressure level were conducted over a range of Mach numbers from  $Ma \approx 0.05$  to  $Ma \approx 1.0$  for different values of the stagnation pressure of the tunnel [88] (Fig. 45(a)). Using equation 68, the values of the sound pressure level  $L_p$  for the different stagnation pressures, expressed as acoustic equivalent turbulence intensity, all collapse on a single line for  $Ma < 0.9$  (Fig. 45(b)):

$$Tu = e^{(4.58 Ma - 9.14)} \quad (69)$$

The authors of the report of the experiments state, that *"all of the wing data presented have been corrected for blockage effects by the method of reference 6"*<sup>20</sup> (BOLTZ et. al. [86], page 7). However, this is believed (and will be tried to be demonstrated later) to not hold for the experimental pressure distributions over the wing. A first indication is that the given reference for the wind tunnel corrections seems to only specify corrections for apparent velocity of the free stream and hence for density, dynamic pressure, Reynolds number, Mach number and drag coefficient [89]. No explicit formula is given for a correction of the pressure coefficient around the wing, as for example in reference [90].

A large part of the preparation of the numerical investigations presented here is based on this preliminary remark. To cover wall-interference effects and three-dimensional finite-span effects, initial computations have been set up by modelling the full three-dimensional experimental arrangement. The computational grid has been constructed using an overset grids method [91]. For this, a fully unstructured grid consisting of  $\sim 4$  million grid points has been created to represent the wind tunnel. The wind tunnel walls are considered in the RANS computations as inviscid walls (thus neglecting the tunnel wall boundary layers). The grid resolves the nearly circular shape of the test section and is extended in upstream and downstream direction by 100 chord lengths of the wing. A farfield boundary conditions is simply used for the in- and outflow boundaries of the grid. For the computations a second grid around the actual wing is embedded within the wind tunnel grid. This second grid consists of  $\sim 18$  million grid points, the wall normal and surface resolutions are given in table 6. Six different wing grids have been created, one for each sweep angle. The angle of attack of the problem is considered during the computations by rotating the wing grid with respect to the wind tunnel grid around the longitudinal axis by the respective angle.

Pressure distributions have been measured in the experiment at atmospheric pressure at a Mach number of  $Ma = 0.27$ . Assuming a temperature of  $T = 303^\circ\text{K}$ ,<sup>21</sup> the corresponding Reynolds number based on chord normal to the leading edge is  $Re = 7.2 \times 10^6$ . For these flow conditions<sup>22</sup> three-dimensional RANS computations for the angle of attack and sweep angle range from the experiment have been performed. A general inspection of the surface pressure distribution (Fig. 46) revealed the following:

<sup>19</sup>pressure  $p$  in dynes/cm<sup>2</sup>, reference pressure amplitude for sound pressure level  $L_p$ :  $p_0 = 0.002$  dynes/cm<sup>2</sup>

<sup>20</sup>"reference 6" corresponds to reference [89] of this work

<sup>21</sup>temperature range of the wind tunnel:  $T = 278^\circ\text{K}$  to  $T = 339^\circ\text{K}$  [87]

<sup>22</sup>A Mach number of  $Ma \approx 0.1$  was used for the three-dimensional computations which are based on the computational strategy for the stability computations (Sec. A.3). Subsequent infinite swept wing computations have been carried out for  $Ma \approx 0.1$  and  $Ma = 0.27$ . They did not show any significant difference in the pressure distribution for the two Mach numbers.

on the pressure side of the wing, for all angles of attack, isobars are seen that are parallel to the leading edge, indicating infinite span conditions. This is in particular true for the wing region at the outboard pressure row but does not hold for the larger sweep angles for the inboard pressure row. The latter is explained by the fact, that for larger sweep angles the downstream part of the inboard pressure row is located very close to the wind tunnel wall (Fig. 44). For the pressure side of the wing the situation is different: especially for the higher angles of attack and also more pronounced for the smaller sweep angles, the consequence of the wing having a finite span lets the flow conditions differ from infinite swept wing flows. This is, of course, more pronounced at the outboard pressure row (Fig. 46). The three-dimensional effect of a finite span wing is also seen in the experimental data, where differences exist in the pressure distributions at the inboard section compared to the outboard section (Figs. 47 to 52).

If nonetheless the spanwise pressure variations are assumed to be small and the flow is approximated as infinite swept wing flow in the RANS computations, a correction of the angle of attack was found to be necessary. Additionally, it was possible to extend the correction to infinite swept wing computations without tunnel walls. The angle of attack normal to the wing leading edge for infinite swept wing computations with farfield boundary conditions is approximated as:

$$\alpha_{n(ISW,FF)} \approx (0.0091 \cdot \Lambda + 0.69) \alpha_{(3D,WT)} \quad (70)$$

With the corrected angle of attack it is possible to predict the experimental pressure distributions fairly accurate. Of course, the pressure difference in spanwise direction seen in the experiment cannot be reproduced with infinite swept wing computations, however the numerical pressure distribution lies for all considered cases usually between the experimental values or very close to one of the two pressure distributions from the two orifice rows (Figs. 47 to 52). The difference in pressure distribution between inboard and outboard pressure row, most evident for the smaller sweep angles ( $\Lambda \leq 20^\circ$ ), is, however, well predicted with the fully three-dimensional computations (Figs. 47 to 49). For the higher sweep angles ( $\Lambda \geq 30^\circ$ ), the difference in spanwise direction is less visible in the experimental data and as a consequence the data is equally well predicted by both computational methods (Figs. 50 to 52).

Summarizing, to correctly predict the (seemingly) uncorrected pressure distributions of the experiments, fully three-dimensional computations including wind tunnel walls are necessary. By appropriately modifying the onflow conditions reasonably accurate results can also be achieved for infinite swept wing computations without tunnel walls. For this it is obviously possible to balance out infinite-span effects and tunnel wall interference effects. Computations have also been carried out on a three-dimensional grid with farfield boundary condition and on infinite swept-wing grids with tunnel walls included. In both cases it was not achieved to adjust the computations (by an angle of attack correction) in a way to predict the pressure distribution from the experiment as accurate as before.

Transition locations have been determined in the experiment for 6 different sweep angles  $\Lambda$  and 13 different angles of attack  $\alpha$ , giving a test matrix of 78  $\Lambda$ - $\alpha$ -pairs. For the experimental flow conditions transition is reported to lie generally between  $x/c \approx 0.2$  and  $x/c \approx 0.6$ , detected at 9 orifices approximately equally distributed within this range. On average, approximately 6 transition locations are documented for each  $\Lambda$ - $\alpha$ -pair, resulting in an overall test matrix consisting of  $\sim 500$  data points. The relation of transition location with onflow condition in terms of the free stream Reynolds number has been determined in the experiment as follows: regarding a certain orifice, the Reynolds number in the experiment was increased until the state of the boundary layer flow at this particular orifice was found to turn from laminar to turbulent. This means, that each of the  $\sim 500$   $\Lambda$ - $\alpha$ - $x_{tr}$ -data-points is related to a unique Reynolds number, synonymous with a unique  $\Lambda$ - $\alpha$ - $Re$ -relation for the flow condition of each data point.

The numerical analysis of the experimental transition locations and the subsequent computations with transition prediction have been carried out following the strategy presented in section A.3. Input for the stability analysis is taken from the solution of 42 basic computations, computed at a Reynolds

number of  $Re = 7.2 \times 10^6$  and a Mach number of  $Ma \approx 0.1$ . Since the NACA 64<sub>2</sub>-A-015 wing is symmetrical, the initial 78  $\Lambda$ - $\alpha$ -pairs are reduced to 42  $\Lambda$ - $|\alpha|$ -pairs used for the basic computations. The boundary layer data extracted from the solutions of the basic computations are scaled according to the theory presented in section A.2 to match the actually considered Reynolds number.

All transition data points from the experiment have been used to determine critical Tollmien-Schlichting and cross-flow  $N$ -factors (not shown here). The calibration is based on the fully three-dimensional numerical results and the stability analysis is respectively carried out along a streamline that goes through the experimental transition location at the outboard row of orifices.

For the unswept wing, the resulting Tollmien-Schlichting  $N$ -factors at transition are evaluated depending on the Mach number<sup>23</sup> (Fig. 53(a)). It can be seen that the  $N$ -factors at transition vary on average linearly with the Mach number, approximated by the following straight line equation:

$$N_{TS,crit} = -11 \cdot Ma + 12.0 \quad (71)$$

This is in accordance with the evaluation of the acoustic equivalent turbulence intensity (Eq. 69), which, when applied to Mack's  $N$ - $Tu$ -correlation (Eq. 23), also gives a linear variation of the  $N$ -factor with the Mach number, however shifted to a higher level by  $\Delta N = 1.5$ :

$$N_{TS,crit} = -11 \cdot Ma + 13.5 \quad (72)$$

For  $Ma = 0$ , respectively  $Ma \approx 0.14$ , equations 71 and 72 give a critical  $N$ -factor of 12. A value of  $N = 12$  corresponds to a turbulence intensity of 0.02%, which is also reported for the wind tunnel for the turbulent velocity fluctuations at low Mach numbers [88].

For the swept wing cases, the  $N$ -factor pairs at transition are plotted in the  $N_{TS}$ - $N_{CF}$ -plane (Fig. 53(b)). They form a relatively narrow rectangular shaped band, bounded by limiting values for  $N_{TS}$  and  $N_{CF}$ . The upper bound is approximated by the values  $N_{TS} = 12$  (corresponding to  $Tu \approx 0.02\%$ ) and  $N_{CF} = 7.5$  while the lower bound is given by  $N_{TS} = 10$  (corresponding to  $Tu \approx 0.045\%$ ) and  $N_{CF} = 6.0$ . The rectangular shape of the stability limit indicates that there have been no or only very little interactions of Tollmien-Schlichting and cross-flow instabilities present in the experiment.

For transition prediction for the NACA 64<sub>2</sub>-A-015 wing the computational approach as before, described in section A.3, has been used. For the lower sweep angles ( $\Lambda = 0^\circ$  to  $\Lambda = 20^\circ$ ), the investigated Reynolds number range is divided, on average, into intervals of  $\Delta Re = 2.0 \times 10^6$ . For the larger sweep angles ( $\Lambda = 30^\circ$  to  $\Lambda = 50^\circ$ ) the intervals are reduced to  $\Delta Re = 1.0 \times 10^6$ . In overall this results in  $\sim 1100$  flow conditions ( $\Lambda$ - $\alpha$ - $Re$ -relations) for the transition prediction.

Transition has been predicted based on the solution of the fully three-dimensional computations as well as the infinite swept wing computations. For the unswept case, the critical  $N$ -factor is based on the Mach number (Eq. 71), for the cases with sweep  $\Lambda > 0^\circ$  constant critical  $N$ -factors for Tollmien-Schlichting and cross-flow instabilities have been used,  $N_{TS} = 10$  and  $N_{CF} = 6.0$ .

For low magnitudes of angle of attack the flow is accelerated up to  $x/c = 0.4$ , in accordance with the numbering system for 6-series NACA airfoils<sup>24</sup>. For higher angles of attack this is also true for the pressure side of the wing, independent of sweep angle (Figs. 47 to 52). For these kind of pressure distributions, for small sweep angles, transition is located even for high Reynolds numbers (in this case up to  $Re = 40 \times 10^6$ ) downstream of  $x_{tr}/c = 0.2$ . For larger sweep angles, the long extent of accelerated flow leads to significant cross-flow amplifications.

For certain flow conditions particular phenomena like transition caused by attachment line contamination or relaminarization of the turbulent boundary layer can be seen from the analysis of the flow

<sup>23</sup>There is some uncertainty in the numerical Mach number, since the temperature in the experiment is not known from reference [86]. The Mach numbers shown here are based on a temperature of  $T = 303^\circ\text{K}$ .

<sup>24</sup>The 4 in NACA 64<sub>2</sub>-A-015 "denotes the chordwise position of minimum pressure in tenths of the chord behind the leading edge for the basic symmetrical section at zero lift." (ABBOTT et. al. [92], page 5)

near the attachment line of the wing (A.3.3). These phenomena become relevant for the considered configuration for sweep angles larger than  $\Lambda = 20^\circ$  (Fig. 78).

The results of the transition prediction study are presented in figures 54 to 59. In these figure the predicted transition location for the infinite swept wing computations and the three-dimensional computations are compared to the experimental transition locations. For the three-dimensional computations, the transition locations at the inboard and the outboard stations are shown, to also evaluate the variation of transition location in spanwise direction. The transition locations from the experiment are those that were determined at the outboard row of orifices and are the only ones specified in reference [86]. There it is stated, that the transition locations determined at the inboard row and the outboard row of orifices were found to be in close agreement.

Based on the transition detection approach used in the experiment, that is to detect transition at single orifices, the exact experimental transition locations are not known. Instead, the position of the last orifice for which still laminar flow was determined, and the first orifice for which already turbulent flow was determined, are given. These two locations mark the streamwise distance within which transition occurred in the experiment.

**Sweep angle  $\Lambda = 0^\circ$**  For the unswept case, the comparison of predicted and experimental transition locations is shown in figure 54. For the higher angles of attack ( $\alpha > 1.5^\circ$ ) a variation of predicted transition locations between inboard and outboard section can be seen for the three-dimensional computation, which is an indication of the finite-span effect, also seen in the pressure distribution. At these angles of attack, the infinite swept wing transition locations are located further downstream than the transition locations from the three-dimensional computation, however still close to the range for the experimental transition locations. For low angles of attack and high Reynolds numbers, the predicted transition locations from both methods start to differ more visibly, but due to the lack of experimental data no assessment of the accuracy can be made. The slight scatter in the experimental transition locations at  $Re \approx 30 \times 10^6$  to  $35 \times 10^6$  for  $\alpha < -0.5^\circ$  may be caused by a change in tunnel-drive fan blade angle that was necessary to cover the whole Mach number and Reynolds number range of the experiment [88]. In general the experimental transition location are predicted with high accuracy by both computational methods, based on the variable critical  $N$ -factor,  $N = f(Ma)$ . For constant values of either  $N = 10$  or  $N = 12$  the accuracy of the predicted transition locations was not given as before (not shown here). Differences occurred for  $N = 10$  for lower Reynolds numbers and for  $N = 12$  for higher Reynolds numbers.

**Sweep angle  $\Lambda = 10^\circ$**  The predicted transition locations for this case are shown in figure 55. Generally a very good accordance of the predicted transition location for both computations, and for inboard and outboard stations, with the experiment is achieved, up to a Reynolds number of  $Re \approx 25 \times 10^6$ . At  $Re \approx 25 \times 10^6$  the experimental transition location show a sudden upstream movement which is not covered by the transition prediction. The reason for the upstream movement remains unknown for the time being. Computations with a boundary layer code with consistent Mach number throughout the computation process<sup>25</sup> however show, that cross-flow instabilities start to become significant at this Reynolds number. For  $\alpha = -2^\circ$  the critical cross-flow  $N$ -factor of 6.0 is reached at  $Re \approx 30 \times 10^6$  and transition starts to move (slowly) upstream with increasing Reynolds number. The same holds for example for  $\alpha = -3^\circ$  and a Reynolds number of  $Re \approx 25 \times 10^6$ . This indicates, that significant cross-flow amplifications may already be present in the flow at  $Re \approx 25 \times 10^6$  and below, possibly leading to interactions with Tollmien-Schlichting instabilities.

<sup>25</sup>If the boundary layer code solution is computed for incompressible flow ( $Ma = 0$ ), the predicted transition locations are essentially the same as in figure 55. If, however, the Mach number is set according to the Reynolds number, the cross-flow amplifications become remarkably larger. This indicates, that even for small Mach numbers, compressibility effects can have a significant influence on the determination of the cross-flow velocity profile.

**Sweep angle  $\Lambda = 20^\circ$**  The trend of the transition prediction and the behaviour of the experimental transition locations for  $\Lambda = 10^\circ$  is continued for  $\Lambda = 20^\circ$ , as shown in figure 56. The transition locations are accurately predicted, until the experimental values start to move upstream for angles of attack  $\alpha \geq 0^\circ$ . Now, in contrast to  $\Lambda = 10^\circ$ , the upstream movement is also predicted by the computations, however it starts at lower Reynolds numbers and is much smoother compared to the movement in the experiment. The beginning of the upstream movement of the predicted transition locations is associated with the switch of the dominant instability type from Tollmien-Schlichting to cross-flow.

The sudden movement in the experimental transition locations may possibly be explained by a saturation of the cross-flow modes [93, 94]. This effect, based on non-linear effects that can not be modelled by linear theory, cause the cross-flow instabilities to saturate at a particular amplitude, leading to a plateau at constant  $N$  in the  $N_{CF}$ -envelope (schematic in Fig. 60). For a certain Reynolds number, the plateau in the  $N$ -factor envelope may lie just under the critical  $N$ -factor and thus does not lead to transition. If the Reynolds number is increased, the plateau may eventually exceed the critical  $N$ -factor and transition jumps suddenly to the location where the plateau starts to develop in the  $N$ -factor envelope (location  $s_2$  versus  $s_3$  in figure 60(b)). This plateau may not be present, if the  $N$ -factors are computed by linear stability theory. Instead, for a certain Reynolds number, the  $N$ -factor envelope steadily increases in streamwise direction until the critical  $N$ -factor is reached and transition is predicted. With increasing Reynolds number, due to the slope in the  $N$ -factor envelope, the predicted transition location smoothly moves upstream (location  $s_1$  to  $s_3$  in figure 60(a)), as seen in figure 56.

**Sweep angle  $\Lambda = 30^\circ$**  The predicted transition locations for  $\Lambda = 30^\circ$  are shown in figures 57. This case more or less resembles the findings for  $\Lambda = 20^\circ$ : The same phenomena occur, however the sudden movement in transition location in the experiment is now starting at even lower angles of attack. Again, the computations show a much smoother upstream movement of the predicted transition locations compared to the sudden upstream jump in the experimental transition locations. The explanation of the immediate upstream movement may possibly be again, as for  $\Lambda = 20^\circ$ , given by saturation processes of the cross-flow modes. One significant observation can be made for  $\alpha = -3^\circ$ : after the experimental transition locations have jumped from  $x/c \approx 0.6$  to  $x/c \approx 0.3$ , the experimental transition locations follow the predicted ones for the next two data points. As a result, the transition prediction is quite accurate before and after the jump in the transition location.

As can also be seen in figure 57, the rapid transition movement in upstream direction is generally decreased for certain angles of attack, more or less approaching the predicted transition locations. As reference, the Reynolds number at which attachment line contamination can occur is depicted in figure 57, indicating that the jump in transition locations is not caused by attachment line transition for this sweep angle.

**Sweep angle  $\Lambda = 40^\circ$**  A definitely new situation arises for  $\Lambda = 40^\circ$ : Although still similar to the previous sweep angle, the transition locations from the experiment now move much more smoothly in upstream direction when cross-flow instabilities start to become the dominating instability form (Fig. 58). For this case, the upstream movement is accurately predicted by both computational methods, infinite swept wing and fully three-dimensional computations, and a good agreement with the experiment is achieved for the investigated Reynolds number and angle of attack range.

For this sweep angle and the flow conditions investigated in the experiment, instability phenomena at the leading edge of the wing start to play a significant role in the transition process over the wing. Although not directly included in the transition prediction, regions where attachment line transition due to turbulent contamination and relaminarization may occur are marked in figure 58. According to section A.3.3 the free stream Reynolds number limits are given. For attachment line transition ( $Re_{\theta_{AL}} > 105$ ) the Reynolds number limit indicates a lower bound, for Reynolds numbers larger than this value attachment line transition is expected to occur. For relaminarization ( $K > 2.8 \times 10^{-6}$ ) the opposite concerning the Reynolds number limit is true: This is now an upper bound, for Reynolds

numbers smaller than this value relaminarization of a turbulent boundary layer is possible. For  $\Lambda = 40^\circ$  and for angles of attack  $\alpha \geq 1^\circ$  the two limits for attachment line transition and relaminarization enclose a region in which, theoretically, the attachment line boundary layer in the experiment was turbulent from contamination from the turbulent tunnel wall boundary layer and underwent relaminarization in the accelerated part of the flow shortly downstream of the attachment line. Both criteria have more or less a relative large uncertainty range for their critical values (Sec. A.3.3) and the input values for both criteria may also exhibit certain inaccuracies in their determination from the flow solution. Because of this, the limiting Reynolds numbers highlighted in figure 58 are also subject to some uncertainty. With this in mind, the scatter and upstream movement of the experimental transition locations for  $\alpha = 1^\circ$  could point to the existence of an attachment line contamination in the experiment. However, from the numerical results it can be seen, that at the corresponding Reynolds number also cross-flow instabilities may cause the transition location to move upstream.

**Sweep angle  $\Lambda = 50^\circ$**  For the largest sweep angle considered in the experiment and the computations the transitional flow phenomena at the leading edge become even more evident compared to the smaller sweep angle of  $\Lambda = 40^\circ$ . As can be seen in figure 59, the sudden upstream movement of the transition locations in the experiment can now be much more definitely associated with attachment line transition. Whereas the situation between attachment line transition and relaminarization is not entirely clear for  $\alpha = 2^\circ$ , at  $\alpha = 1.5^\circ$ , based on the empirical criteria, the flow over the wing is entirely turbulent as soon as the acceleration in the boundary layer is not sufficiently large enough anymore to relaminarize the turbulent flow originating at the contaminated attachment line. For angles of attack larger than  $\alpha = 1.5^\circ$  relaminarization does not play any role in the transition process anymore for the flow conditions of the experiment. For  $\alpha = 1^\circ$  to  $-0.5^\circ$ , the sudden upstream movement is clearly related to attachment line transition according to the empirical criterion. The limiting Reynolds number, that marks the beginning of the Reynolds number range for which  $Re_{\theta_{AL}} > 105$ , corresponds relative accurately to the Reynolds number at which the transition locations exhibit the sudden upstream movement.

For  $\alpha = 0^\circ$  and  $\alpha = -0.5^\circ$  cross-flow instabilities start to be responsible for a slow upstream movement of the transition location until the free stream Reynolds number becomes eventually large enough for attachment line contamination to take over the transition process. For  $\alpha < -1^\circ$ , the experimental free stream Reynolds numbers are too low to trigger attachment line transition and the reported experimental transition locations are caused by cross-flow instabilities and are accurately predicted by the computations.

**Summary** Generally, it can be seen from the numerical computations, that, as soon as the transition locations start to move more significantly in upstream direction with increasing Reynolds number, the corresponding transition scenario changes, from Tollmien-Schlichting instabilities to stationary cross-flow instabilities being the most unstable instabilities. For the majority of the considered flow conditions, when transition is caused by Tollmien-Schlichting or cross-flow instabilities, the transition locations have been predicted with high accuracy compared to the experimental data. It can also be concluded, that for this test case the interaction of Tollmien-Schlichting and cross-flow waves plays generally a subordinate role, respectively no role. For some of the transition locations with a more rapid upstream movement with increasing Reynolds number, the cause of the upstream movement can not directly be explained by the available information from the linear stability computations and the predicted transition locations differ significantly from the experimental ones.

The rapid upstream movement in the experimental transition locations may possibly be explained by interaction of Tollmien-Schlichting and cross-flow modes ( $\Lambda = 10^\circ$ ) or saturation of the cross-flow instabilities due to non-linear effects ( $\Lambda = 20^\circ$  and  $\Lambda = 30^\circ$ ). Both effects cannot be modelled by linear stability theory and thus cannot be verified with the present method to be relevant or not for these flow conditions.

For the higher sweep angles ( $\Lambda = 40^\circ$  and  $\Lambda = 50^\circ$ ), the sudden upstream movement in transition

location is well explained by the presence of attachment line contamination in the experiment. Although not included in the current prediction method as automatically applicable transition criteria, a manual assessment of the empirical criteria for attachment line transition and relaminarization reveals a very good agreement in predicted critical Reynolds number compared to the experiment.

The computational results reveal, that for this test case the flow condition, in the regions where transition was measured in the experiment, corresponds to infinite swept wing conditions. To accurately predict transition for this case, infinite swept wing computations (with suitably adjusted angle of attack) are sufficient. The statement, that the transition locations do not differ significantly at the two measuring rows from the experiment [86], is confirmed by the results of the fully three-dimensional computations. Significant differences in the predicted transition locations between the methods are only seen in regions, where the transition locations moves more rapidly upstream from one investigated Reynolds number to the next. The differences seen here can most certainly be reduced if a higher resolution of the Reynolds number range for the computations is used.

The stated superiority of the fully three-dimensional transition prediction approach comes probably into play at regions of the wing where no measured transition locations are available, that is at regions near the wing root or near the wing tip where three-dimensional and finite-span effects become more significant.

#### 4.2.5. DLR prolate spheroid

The DLR prolate spheroid [95] is a slender body of revolution of fineness ratio 6 (Fig. 61). The model has been used in wind tunnel experiments for the investigation of three-dimensional laminar and turbulent flows. One basic idea was to use experimentally obtained results for the improvement of turbulence models and separation and transition criteria [70]. The 6:1 prolate spheroid model is mounted on a rear sting in connection with a sting support system. With the support system the pitch center of rotation is in the center of the model and angles of attack of  $\alpha = 0^\circ$  to  $30^\circ$  can be realised. The model can be rotated around the longitudinal axis from  $\phi = 0^\circ$  to  $360^\circ$ . The 6:1 prolate spheroid has a length of 2.4m, with major half axes of 1.2m and 0.167m.

Experiments have been carried out in the DLR 3m Low Speed Wind Tunnel Göttingen (NWG). This facility is a low speed Göttingen-type wind tunnel with a closed return and an open test section of 3m height, 3m width and 6m length. The tunnel operates at atmospheric conditions and the turbulence intensity in the test section varies between  $Tu = 0.1\%$  and  $Tu = 0.2\%$ , depending on the Reynolds number in the experiment [96]. Surface hot film probes to measure the local wall shear stress were applied to the model at 12 different cross sections. By rotating the spheroid model around the longitudinal axis, 30 to 120 measuring positions in circumferential direction have been realized in the experiment. From the evaluation of the local wall shear stress magnitude detailed information of the laminar-turbulent transition of the boundary layer are achieved. The experimental results include data for Reynolds numbers from  $Re = 1.5 \times 10^6$  to  $Re = 8.5 \times 10^6$  and angles of attack from  $\alpha = 5^\circ$  to  $\alpha = 30^\circ$  [97].

**Previous work** Results of the transition prediction for the DLR prolate spheroid with the transition prediction approach presented here have been previously published in references [40] and [47].

In the first publication (Ref. [40]), transition was predicted for two Reynolds numbers,  $Re = 1.5 \times 10^6$  and  $Re = 6.5 \times 10^6$ , and for angles of attack of  $\alpha = 5^\circ$  and  $\alpha = 10^\circ$  for both Reynolds numbers and  $\alpha = 15^\circ$  only for the higher Reynolds number. The transition prediction method used for these computations differed in some minor approaches compared to the current one, as a more significant example, the boundary layer edge determination was based on a less sophisticated approach. Differences also exists in the computational grids, in that the grid used in the previous computations has a farfield distance of only  $d = 20/L$ , compared to  $d = 100/L$  for the grids used in the present work. The surface resolution and the resolution of the boundary layer is basically identical for both investigations. In the previous work, transition was predicted on 31 inviscid streamlines using linear stability theory together with the  $e^N$  method. The predicted transition lines are compared to the skin friction coefficient distribution of the

experiment. The beginning of the turbulent regions, indicated by an increase in skin friction magnitude, is predicted with reasonable accuracy [40]. Some of these results are also shown in references [25], [98], [41], [42] and [47].

In the second publication (Ref. [47]), transition was predicted for a Reynolds number of  $Re = 6.5 \times 10^6$  and angles of attack from  $\alpha = 5^\circ$  to  $\alpha = 30^\circ$ . The transition prediction method used corresponds to the same stage of development as the method used in this work. For the computations the same unstructured grid as in the present work was used. Transition prediction was carried out using the Menter SST  $k-\omega$  turbulence model and the SSG/LRR- $\omega$  differential RSM turbulence model for the RANS computations [47]. Results of comparative computations for the DLR prolate spheroid are also shown, with transition prediction based on a transition transport equation approach, using a  $\gamma-Re_{\theta t}-CF$  model coupled to the SST turbulence model and the RSM turbulence model [21, 99] (Sec. 4.3). The transition prediction results are assessed by directly comparing the skin friction coefficient distribution of the computations and the experiment. For better quality evaluations, iso- $c_f$ -lines extracted at the same iso-values from the experimental and the numerical  $c_f$ -distributions are also compared. For the transition prediction using linear stability theory and  $e^N$  method, the predicted transition lines are nearly independent of the turbulence model used in the RANS computations and are generally in very good agreement with the experiment for  $\alpha = 5^\circ$  to  $\alpha = 20^\circ$ . For the higher angles of attack, already visible at  $\alpha = 20^\circ$ , the predicted transition locations start to deviate from the experiment and are predicted too far upstream.

**Uncertainty of experimental transition locations** Experimental transition locations have been approximated based on the experimental skin friction coefficient distribution. For this, transition is assumed to occur in the middle of the streamwise increase in skin friction magnitude. That is, transition is supposed to take place at the location where  $c_{f,tr} = 0.5(c_{f,min} + c_{f,max})$ . This corresponds approximately to the position of maximum slope of the skin friction distribution  $(dc_f/ds)_{max}$ . Evaluating  $c_{f,tr}$  was found to be less sensible to the variation of the experimental data and results in smoother transition lines.

The criterion for the transition locations is evaluated along potential flow streamlines calculated from the potential flow solutions for ellipsoids [100, 101]. The combined standard uncertainty  $u_c(s_{tr})$  [73], with no correlated errors, of the experimental transition locations  $s_{tr}$  in streamline direction is estimated as:

$$u_c^2(s_{tr}) = u^2(\tau_w) + u^2(r_m) + u^2(c_{f,tr}) \quad (73)$$

The standard uncertainty based on the error for the wall shear stress magnitude ( $\Delta\tau_w \pm 20\%$  [97]) is computed from  $u(\tau_w) = \Delta s_{\tau_w}/\sqrt{3}$ , assuming a rectangular probability distribution. The standard uncertainty for the resolution of the measuring locations  $r_m$  is determined from the distance between two cross sections ( $\Delta x/L \approx 0.08$ ) where surface hot film probes are placed and the circumferential positions of these locations ( $\Delta\phi \approx 1^\circ$  to  $\Delta\phi \approx 6^\circ$ ) during the experiment. Again a rectangular probability distribution is assumed:  $u(r_m) = \Delta s_{r_m}/\sqrt{3}$ . For the standard uncertainty of the criterion for the transition location a triangular probability distribution is used and the uncertainty is determined from  $u(c_{f,tr}) = \Delta s_{c_{f,tr}}/\sqrt{6}$ .

The combination of an explicit transition line together with an uncertainty band allows for better quality evaluations of the experimental transition locations and to assess the accuracy of stability computations for  $N$ -factor calibration or transition prediction. For the lower angles of attack, when the potential flow streamlines are more aligned to the longitudinal axis of the spheroid, the uncertainty band is broadened compared to the higher angle of attack cases. This is caused by the rather coarse resolution of the measuring points in longitudinal direction. For the higher angles of attack the streamlines follow the circumferential direction more strongly, where the resolution of the measuring points is rather high, and the uncertainty band is relatively narrow. The resolution of the measuring points has the largest contribution to the uncertainty of the transition locations, with the two other two uncertainties typically being less important.

**Transition prediction** Transition has been predicted for the DLR prolate spheroid using a computational grid of 2.8 million grid points with a resolution of 60 - 100 grid points of the laminar boundary layer (Tab. 6). The computations were performed using 192 processes and, appropriately, transition has been predicted on 192 streamlines using linear stability theory in form of the  $e^N$  method. The critical  $N$ -factors were taken from the same stability diagram that has also been used in [40] and [47] (Fig. 62). With the stability boundary given in this stability diagram a strong interaction of Tollmien-Schlichting and cross-flow modes is modelled. For pure Tollmien-Schlichting transition, the critical  $N_{TS}$ -factor is  $N = 8$ , corresponding to a turbulence intensity of  $Tu \approx 0.11\%$  according to equation 23. For pure cross-flow transition, the critical  $N_{CF}$ -factor is  $N = 5.5$ .

Transition has been predicted for the prolate spheroid for Reynolds numbers from  $Re = 1.5 \times 10^6$  to  $Re = 8.5 \times 10^6$  and angles of attack from  $\alpha = 5^\circ$  to  $\alpha = 30^\circ$ . The investigated cases can be divided into cases where transition is caused by Tollmien-Schlichting instabilities, cases with mixed Tollmien-Schlichting and cross-flow transition and cases where transition is mainly caused by cross-flow instabilities.

The predicted transition lines are shown in figures 63 to 74 and are compared to the experimental data. The figures are each divided into two parts. The upper part shows the three-dimensional spheroid from three different views, the view from the top, the view from the bottom and the view from the side. In the three-dimensional plots the predicted transition line (solid line) is shown in comparison to the uncertainty band for the transition location of the experiment (shaded area). The lower part of the figures contains a two-dimensional plot of the semi-spheroid unrolled along the azimuth angle  $\phi$ , with  $0^\circ < \phi < 180^\circ$ , where  $\phi = 0^\circ$  corresponds to the lower symmetry line and  $\phi = 180^\circ$  to the upper symmetry line of the model. In the two-dimensional plot the predicted transition line (solid line) is shown in comparison to the experimental transition line (dashed line) and the uncertainty band of the experimental transition line (shaded area). As a reference, the location of the pressure minimum of the RANS computation is shown (thin solid line).

**Pure TS transition** The low Reynolds number cases presented in this section ( $Re = 1.5 \times 10^6$  and  $Re = 3.0 \times 10^6$ ) are all characterized by the fact that transition is predicted to be caused solely by Tollmien-Schlichting instabilities. For  $Re = 1.5 \times 10^6$  and  $\alpha = 5^\circ$ , respectively  $\alpha = 10^\circ$ , no transition locations are predicted near the upper symmetry line ( $\phi > 150^\circ$ ). While this is confirmed for  $\alpha = 5^\circ$  by the experimental data (Fig. 63), the situation for  $\alpha = 10^\circ$  is less clear (Fig. 64). Although already indicated by the broad uncertainty band, the increase in wall shear stress is not as strong as for the transition front between  $\phi = 80^\circ$  and  $\phi = 150^\circ$ . Additionally, the maximum magnitude of the wall shear stress is definitely lower for  $\phi > 150^\circ$  than it is between  $\phi = 80^\circ$  and  $\phi = 150^\circ$ . This points to the possibility, that the experimental transition line is reproduced incorrectly. This is also supported by the fact, that the numerically predicted wall shear stress distribution is very similar to the experimental one in this area (not shown here), despite the apparently different transition lines.

For all cases discussed in this section, no transition is found for the lower part of the spheroid. The apparently predicted transition lines from the computations simply mark the end of the inviscid streamline computation. For the two cases with  $\alpha = 30^\circ$  ( $Re = 1.5 \times 10^6$ , figure 65, and  $Re = 3.0 \times 10^6$ , figure 66) transition near the upper symmetry line ( $\phi > 150^\circ$ ) is predicted downstream of a laminar separation. Here, no clear information can be obtained from the experimental wall shear stress distribution. This is due to the formation of a vortex in this region that prevents the wall shear stress to increase. This is principally confirmed in the computations, when comparing the numerical and experimental skin friction distributions (not shown here).

Although classified here as cases with pure Tollmien-Schlichting transition, both high angle of attack cases ( $\alpha = 30^\circ$ ) exhibit relatively large cross-flow  $N$ -factors. They are, however, assumed to be not relevant for transition. It is believed that the interaction of Tollmien-Schlichting and cross-flow instabilities is limited to accelerated flows and, according to further investigations for the spheroid test cases, the interaction stops relatively immediately downstream of the pressure minimum (not shown here).

Summarizing, for all four cases discussed here, transition is predicted in very good agreement with the

experiment, with the exception of the unclear situation near the upper symmetry line for  $Re = 1.5 \times 10^6$  and  $\alpha = 10^\circ$ .

**Mixed TS/CF transition** The cases discussed here are for a Reynolds number of  $Re = 6.5 \times 10^6$  and have moderate to high angles of attack,  $\alpha = 5^\circ$ ,  $\alpha = 10^\circ$  and  $\alpha = 15^\circ$ . The cases grouped together in this section have in common, that transition near the upper and lower symmetry line is caused by Tollmien-Schlichting instabilities, whereas for the remaining part cross-flow instabilities and the interaction of both instabilities become more significant with increasing angle of attack. For all of these cases, transition is predicted too far upstream in the region where cross-flow  $N$ -factors become significant ( $\phi = 60^\circ$  to  $140^\circ$ ).

For  $\alpha = 5^\circ$  (Fig. 67), the cross-flow  $N$ -factors are everywhere lower than  $N_{CF} \approx 3.5$ , however they need to be considered in some kind of interaction approach for transition prediction to reproduce the curvature of the transition line in upstream direction, which is also seen, to a lower extent, in the experimental transition line. Neglecting these relatively small  $N$ -factors results in a curvature of the transition line in downstream direction, which is clearly not representative of the experimental transition line.

For  $\alpha = 10^\circ$  (Fig. 68), the predicted transition line shows a kink at  $\phi \approx 30^\circ$ , whereas the experimental transition line runs relatively smoothly towards the lower symmetry line. This area is characterized by an interaction of Tollmien-Schlichting and cross-flow instabilities, which is obviously not modelled appropriately enough in the computation. The kink in the numerical transition line corresponds to the location of vanishing cross-flow  $N$ -factor.

For angles of attack  $\alpha > 10^\circ$  a kink develops in the experimental transition lines, approximately at  $\phi = 130^\circ$ . Accordingly, this kink is seen for  $\alpha = 15^\circ$  but is not represented by the numerical transition line (Fig. 69). The numerically predicted transition line is smooth in this region, because it is defined by a smooth change from pure streamwise transition to transition defined by the interaction of Tollmien-Schlichting and cross-flow instabilities. According to further investigations for the prolate spheroid, the interaction of Tollmien-Schlichting and cross-flow instabilities is limited to accelerated flows and stops already a short distance downstream of the pressure minimum. If the interaction of the instabilities is suppressed downstream of the pressure minimum, a kink also develops in the numerical transition line (not shown here).

Despite some inaccuracies, the general accordance between predicted and experimental transition lines is relatively good. Especially the transition in the upper and lower symmetry lines is predicted with satisfying accuracy. The flow near the upper symmetry line is characterized by transition occurring relatively far downstream of the pressure minimum in decelerated flow. It is assumed, since the streamlines are converging in this region, that additional material is pushed into the boundary layer along a streamline, leading to a fuller laminar boundary layer velocity profile which is more stable with respect to transition. The opposite can be seen near the lower symmetry line. Transition is now occurring in accelerated flow and the laminar length is relatively short for an accelerated flow. Since the streamlines in this region are now diverging, it is assumed that material is removed from the boundary layer along a streamline. This leads to a less fuller laminar boundary layer velocity profile compared to a velocity profile in a two-dimensional flow with the same pressure gradient. This is in accordance with observations reported in reference [59], where for the flow at the lower symmetry line of the prolate spheroid parallels are drawn to the attachment line flow of a cylinder with sweep angle  $\Lambda = \alpha$ . For this type of flow it was not possible to predict transition accurately with empirical transition criteria. Only the application of linear stability theory lead to the prediction of transition locations in good agreement with the experiment.

**Pure CF transition** The trend from the previous cases with lower angles of attack is continued for the cases with high angles of attack ( $\alpha = 20^\circ$  to  $30^\circ$  for  $Re = 6.5 \times 10^6$  and  $\alpha = 30^\circ$  for  $Re = 4.5 \times 10^6$  and  $Re = 8.5 \times 10^6$ ). Near the upper symmetry line ( $\phi \approx 130^\circ$  to  $180^\circ$ ) transition is caused by streamwise

instabilities, partly accompanied by the beginning of laminar separation. At  $\phi \approx 130^\circ$  a kink in the experimental transition line is seen, where pure Tollmien-Schlichting transition changes to pure cross-flow transition. The transition line never drops to lower values of  $\phi \approx 30^\circ$ , so that the lower part of the spheroid and the lower symmetry line are fully laminar (Figs. 70 to 74).

In the numerically determined transition lines, a smooth change between the pure Tollmien-Schlichting part and the pure cross-flow part of the transition line (from  $\phi \approx 130^\circ$  to  $\phi \approx 100^\circ$ ) is seen. This is caused by a continuously increasing cross-flow  $N$ -factor, and, at the same time, continuously decreasing Tollmien-Schlichting  $N$ -factor in this region, in combination with the modelling of a strong interaction of the instabilities (according to figure 62).

Common for all cases is, that the transition is predicted accurately for Tollmien-Schlichting instabilities ( $\phi \approx 130^\circ$  to  $180^\circ$ ), but is predicted too far upstream for the rest of the spheroid compared to the experimental transition location. The upstream distance in the predicted cross-flow transition locations compared to the experimental data is increased with increasing angle of attack (Figs. 70 to 72), but is again decreased for  $\alpha = 30^\circ$  for increasing Reynolds number (Figs. 72 to 74).

For  $Re = 6.5 \times 10^6$  and  $\alpha = 20^\circ$  (Fig. 70) the predicted transition line is for  $\phi > 140^\circ$  and for  $x/L > 0.5$  in good agreement with the experimental transition line. For the rest of the spheroid, the transition is predicted too far upstream. The same can be seen for  $Re = 6.5 \times 10^6$  and  $\alpha = 24^\circ$  (Fig. 71), however the proportion of accurately predicted transition is reduced for the lower part of the spheroid. Now, for  $x/L > 0.75$  the predicted transition line approaches again the experimental data.

For  $Re = 4.5 \times 10^6$  and  $\alpha = 30^\circ$  (Fig. 73) the discrepancy between numerically predicted transition line and experimental transition line is by far the most significant. For increasing Reynolds number,  $Re = 6.5 \times 10^6$ , figure 72 and  $Re = 8.5 \times 10^6$ , figure 74, the discrepancy to the experiment in the region of pure cross flow is reduced. For the higher Reynolds number, the predicted transition line for the rear part of the spheroid ( $x/L > 0.5$ ) is in acceptable agreement with the experiment.

**Summary** For all considered cases, transition locations based on Tollmien-Schlichting instabilities are predicted in good agreement with the experiment. This is especially true for the transition at the upper and lower symmetry line of the spheroid for the low angle of attack cases at  $Re = 6.5 \times 10^6$ . For these cases, the predicted transition lines based on cross-flow transition are in acceptable agreement compared to the transition locations of the experiment. For larger angles of attack transition predicted based on cross-flow instabilities is predicted with less accuracy and is located too far upstream compared to the experiment.

A consistent and good agreement is achieved between different computations with the same method (present work, reference [47] and reference [40]) for corresponding cases, independent of stage of development of the method or turbulence model used for the RANS computations.

In contrast to the presented results, especially for the high angle of attack cases, a very good agreement with experimental data for the DLR prolate spheroid is presented in reference [102]. The principle approach for transition prediction is very similar, by using linear stability theory in form of the  $e^N$  method and applying the same critical  $N$ -factors correlation (Fig. 62). However, velocity profiles for the stability analysis are computed by a three-dimensional boundary layer method with input derived from the potential flow solution for a spheroid.

Different investigations have been carried out to find a cause for the discrepancies in predicted cross-flow transition lines compared to the experiment and to the data of reference [102]. A grid refinement study, with a resolution of the prism region with 192 and 256 grid points normal to the wall, revealed that the current solutions are already grid converged. Anyway, under-resolved boundary layer profiles lead normally to an under-prediction, instead of an over-prediction, of the cross-flow  $N$ -factor. Computations considering curvature effects in the stability analysis and the prediction of travelling cross-flow instabilities have been performed but did not yield a better correlation for the critical cross-flow  $N$ -factor and thus did not improve the outcome of the transition prediction. First comparisons with the solution of a three-dimensional boundary layer code showed, that the streamwise and cross-

flow velocity profiles of the RANS solution were nearly identical to the ones from the boundary layer code. A rough comparison of integral boundary layer data from the present method with the same data from the boundary layer computations and results presented in reference [102] showed in principle equal values for the Reynolds number based on the displacement thickness of the streamwise velocity profile for all approaches. The Reynolds number based on the displacement thickness of the cross-flow velocity profile showed significant differences for data from the present method and from the boundary layer code computations compared to the data presented in reference [102].

Summarizing, the cause for the over-prediction of the cross-flow  $N$ -factor remains unknown for the time being. A possible explanation would be a saturation of the cross-flow instabilities in the experiment, that cannot be modelled by linear stability theory. This would lead to the computation of larger amplification rates compared to the ones actually present in the flow.

In subsequent investigations, basically for the calibration of critical  $N$ -factors for this case, it was found, that the critical cross-flow  $N$ -factor in regions of pure cross-flow relates to the normal curvature in cross-flow direction. A relation was also seen for the curvature in streamwise direction but was less definite. By considering the observation that interaction of Tollmien-Schlichting and cross-flow instabilities is limited to accelerated flows (not shown here) and by relating the maximum  $N_{CF}$ -value in the stability limit (Fig. 62) to the normal curvature in cross-flow direction a significant improvement for the prediction of the transition for the DLR prolate spheroid for high angles of attack was achieved. By using

$$N_{CF} = 25.6 - 7.4 \ln(\kappa_{nc}/L) \quad (74)$$

for the correlation between cross-flow  $N$ -factor and normalized normal curvature in cross-flow direction ( $\kappa_{nc}/L$ ) the predicted transition locations for  $\alpha = 30^\circ$  and  $Re = 4.5 \times 10^6$  (Fig. 75) and  $Re = 6.5 \times 10^6$  (Fig. 75) are in much better agreement with the experiment compared to the original approach (Figs. 73 and 72). Similar trends with this approach are seen for  $Re = 6.5 \times 10^6$  and  $\alpha = 24^\circ$ , respectively  $\alpha = 20^\circ$  and for  $Re = 8.5 \times 10^6$  and  $\alpha = 30^\circ$ . For the lower angles of attack some improvement can be seen in some regions, but is accompanied by some worsening in other regions.

### 4.3. Comparison to transport equation approaches

The classical transition prediction methods are apparently increasingly competing with novel transition prediction approaches that are based on transport equations. The classical transition prediction methods typically rely on the coupling of external, separate, non-parallel codes in form of stability solvers or boundary layer methods with the actual RANS solver. The coupled approaches often incorporate line-search or line-integration operations for the determination of boundary layer data and lines for transition prediction and contain more or less complex interfaces between the RANS solver and the external programs. This makes these classical approaches difficult to implement into modern CFD solvers, especially with regard to parallelisation. Depending on the complexity of the scope of application, these transition prediction approaches can also be very demanding in terms of general applicability, for the preparation of the computations or the general robustness of the prediction capability with respect to the overall result of the transition prediction.

The transport equation approaches avoid the complex implementation and parallelisation issues as well as the non-local line-search and line-integration operations of the classical approaches by using more or less fully local formulations for all aspects of the transition prediction. Because of this, they generally rely on local correlations for integral boundary layer data and apply simple empirical transition criteria. Harshly speaking, from a physical point of view because of the rather crude approximation for the boundary layer data, the theoretically rather not well founded transition criteria and the huge amount of calibration often involved, these approaches mean a step backwards by decades with respect to the actual transition prediction. However, in terms of the potential simplicity in implementation and application this drawback is in a certain way compensated and justified, especially in view of industrial and engineering access to transition prediction in RANS solvers. Additionally, based on their formulation and by typically using an additional transport equation for a value representative of the

intermittency, the transport equation approaches are thought to be better suited to incorporate the modelling of the transition region and to account for bypass transition effects, especially caused by turbulent wake flows.

Based on the principle novelty of the transport equation approaches and in an attempt to overcome the physical shortcomings several different formulations for these approaches exist today. These many new ideas, which also are currently constantly being expanded, still need to be channelled in some way to concentrate on fewer development paths. However, meanwhile some approaches can be identified to seemingly enjoy significant popularity. One approach, which also apparently triggered the increased interest in the transport equation methods, is the  $\gamma$ - $Re_{\theta t}$  local correlation based transition model [103]. This model consists of two transport equations, one for the intermittency  $\gamma$  and one for a transition momentum thickness Reynolds number  $Re_{\theta t}$  and incorporates a modified ABU-GHANNAM and SHAW empirical transition criterion for streamwise instabilities [104]. For this transport equation model different cross-flow extension are available, typically not dependent on another additional transport equation [105, 21, 99]).

Another approach is the amplification factor transport transition model (AFT) [20] that takes a step towards improved physical modelling by applying a empirical transition criterion derived from linear stability theory. Originally omitting an intermittency transport equation, in its latest formulation the amplification factor transport transition model consists of two transport equations. The approach now includes a transport equation for a modified intermittency ( $\tilde{\gamma} = \ln \gamma$ ) and additionally incorporates a transport equation for the amplification factor. The amplification factor transport equation is derived from a reformulation of the empirical approximate envelope method of DRELA and GILES [106, 107] and is representative of the  $N$ -factor envelope for streamwise Tollmien-Schlichting disturbances [107, 20]. The amplification factor transport transition model is currently lacking a consistent extension for cross-flow instabilities.

The concept of applying advection or transport equations for the integration of scalar quantities without the need for the computation of the integration path (for example the boundary layer edge streamline) and an analytical integration along this path has advanced to be a meaningful addition in the application of transition criteria with higher physical content [108]. To further restrict insufficiencies in the physical modelling, hybrid approaches are possible for this concept, that compute integral boundary layer data in the classical non-local way and apply for example empirical envelope methods (URANGA [107]) or database methods (BÉGOU et. al. [109]) for the computation of amplification rates and then use the transport equation for the integration of amplification factors. However, in contrast to these approaches, other transport equation model development paths are concentrated on the reduction of complexity by only considering one transport equation for an intermittency variable and employing fully local correlations [19].

The continuous application of different transition transport equation approaches has in many cases revealed a good agreement between predicted transition locations and experimental data. Although often still in the development phase and sometimes for example not including approaches to cover cross-flow instabilities, the transport equation methods increasingly become a valuable addition to the portfolio of transition prediction methods in RANS solvers.

For a few selected transition transport equation approaches that so far show the general ability to predict reliable transition locations, a comparison in prediction accuracy with the presented method has been conducted and which is presented below. It can be found, that for the validation test cases considered in the present work often a reasonably good agreement between transport equation approaches, linear stability theory and experiment can be achieved. However, since only results for properly working transport equation approaches are considered and since for these approaches especially the quantitative intersection with the presented method of investigated flow conditions for the considered test cases is often very limited, no absolutely clear picture can yet be derived. Additionally, there exist disagreement about the exact flow conditions in the experiments for certain cases, for example about the turbulence intensity for the NLF (1)–0416 and the NACA 64<sub>2</sub>-A-015 cases or about the effective angle of attack for

the infinite swept wing computations for the ONERA D and NACA 64<sub>2</sub>-A-015 cases. Based on these observations, at best, for now the potential of the transport equation approaches is confirmed with the comparative results discussed below.

Regarding the overall computing time, from experience, the transition transport equation approaches generally show no real advantage compared to the presented method. The time needed for additional iterations for the iterative coupling of RANS solver and stability analysis in the presented approach is compensated by the additional computational effort to solve the additional transport equations.

**NLF (1)–0416** The flow around the NLF (1)–0416 airfoil (Sec. 4.2.1) can be considered as one of the standard validation test cases for two-dimensional transitional flows. Unfortunately this test case is, for a broad range of experimental flow conditions, relatively insensitive to the turbulence intensity, respectively the critical  $N$ -factor, applied in the computations, see section 4.2.1. Accordingly, transition prediction methods, irrespective of their modelling approach, typically deliver transition locations in good agreement with the experiment for this case. Thus, for example for a Reynolds number of  $Re = 4.0 \times 10^6$ , for different transport equation approaches [110, 111, 108] as well as for the presented method (Sec. 4.2.1, Fig. 35) transition locations are predicted in very close agreement among each other and with respect to the experiment.

**NLF (2)–0415** For the prediction of cross-flow induced transition in three-dimensional flows the flow over the NLF (2)–0415 infinite swept wing (Sec. 4.2.2) is another standard validation test case. In this case another questionability for the validation of some transition prediction methods arises. Based on the limited amount of suitable validation test cases for cross-flow transition, the experimental data of the NLF (2)–0415 wing is regularly used for the calibration of cross-flow transition criteria in transport equation approaches [105, 112, 99] or for the calibration of critical cross-flow  $N$ -factors [36]. Expectedly, predicted transition locations using these calibrations are in very good agreement with the experiment, as well as for the transport equation approaches as for the application of the presented method (Fig. 38, Sec. 4.2.2).

**ONERA D** For the variable sweep wing model with ONERA D profile (Sec. 4.2.3) transition has been predicted using a  $\gamma$ - $Re_{\theta t}$ - $CF$  model for different sweep angles and Reynolds numbers of  $Re = 1.0 \times 10^6$  and  $Re = 1.5 \times 10^6$  [21]. The presented transition locations are in good agreement with the experiment for two different cross-flow transition correlations and are comparable to those predicted with linear stability and the presented transition prediction method (Fig. 42, Sec. 4.2.3). However, for the results presented in figure 42 and section 4.2.3 an angle of attack of  $\alpha_n = 5^\circ$  was used for the infinite swept wing computations as opposed to  $\alpha_n = 6^\circ$  in reference [21].

**NACA 64<sub>2</sub>-A-015** The swept wing model with symmetric NACA 64<sub>2</sub>-A-015 airfoil section (Sec. 4.2.4) has been used for validation purposes in reference [108] for the unswept case and in reference [21] for sweep angles of  $\Lambda = 40^\circ$  and  $\Lambda = 50^\circ$ . In reference [108] a dependency of the turbulence intensity on the Mach number according to equation 69 and an angle of attack correction according to equation 70 is used and transition is predicted for  $\alpha = 0^\circ$ ,  $\alpha = 0.5^\circ$  and  $\alpha = 1.0^\circ$  for the complete Reynolds number range in very good agreement with the experiment and with similar accuracy as the presented transition prediction method (Fig. 54, Sec. 4.2.4). In reference [112] a  $\gamma$ - $Re_{\theta t}$ - $CF$  model is used to predict the transition for a few Reynolds numbers at  $\alpha = -3^\circ$ . Only the predicted transition locations with one of two different cross-flow transition correlations are in very good agreement with the experiment for all investigated cases, the other correlation shows a certain reasonably small downstream offset for  $\Lambda = 40^\circ$ . The better of the predicted transition locations also compare well with the transition locations predicted with the presented method (Figs. 58 and 59, Sec. 4.2.4). However, no angle of attack correction as it is used in the present work is reported in reference [112] for the infinite swept wing computations.

**DLR prolate spheroid** The DLR prolate spheroid (Sec. 4.2.5) has been investigated in reference [47] by the present author using a  $\gamma$ - $Re_{\theta t}$ - $CF$  transport equation approach [21, 99] for a Reynolds number of  $Re = 6.5 \times 10^6$  and angles of attack from  $\alpha = 5^\circ$  to  $\alpha = 30^\circ$ . For the presented transition prediction approach using linear stability theory and  $e^N$  method, the predicted transition lines are generally in very good agreement with the experiment for  $\alpha = 5^\circ$  to  $\alpha = 20^\circ$  (Figs. 67 to 70, Sec. 4.2.5). However, for the higher angles of attack the predicted transition locations start to deviate from the experiment and are predicted too far upstream (Figs. 71 and 72, Sec. 4.2.5). For these angles of attack, the  $\gamma$ - $Re_{\theta t}$ - $CF$  model gives much more accurate results compared to the experiment. However, for the lower angles of attack,  $\alpha < 20^\circ$ , the transport model approach fails to predict transition accurately at the lower half of the spheroid and especially at the lower symmetry line. For the lower symmetry line the experiment shows transition clearly upstream of the trailing edge of the spheroid, caused by streamwise instabilities, which is not captured by the transport equation approach. The transition for the lower part of the spheroid is only for transition prediction with linear stability theory and  $e^N$  method in accordance with the experiment. A related observation is reported in reference [59], where, for the lower part of the spheroid, transition predicted with empirical transition criteria was not in good agreement with the experiment. Only after applying linear stability theory, transition was predicted with a very good accuracy compared to the experiment.



## 5. Conclusion

In the present work the development of a transition prediction methodology for the application to general three-dimensional flows is presented. The transition prediction method utilizes the linear stability theory in form of the  $e^N$  method. The methodology follows the approach of a coupled program system consisting of a transition prediction module, including an external stability code, incorporated into the DLR RANS solver TAU. According to assumptions regarding the amplification direction of small sinusoidal disturbances, the stability analysis is applied along three-dimensional inviscid streamlines and boundary layer data needed for the stability analysis are directly extracted from the RANS solution. The stability analysis yields  $N$ -factor envelopes for each streamline from which the transition locations are determined by critical  $N$ -factors, applied in form of the  $2N$ -factor strategy. The transition locations of all streamlines are connected to polygonal lines that are used to create laminar and turbulent zones for the RANS computation. In the laminar areas the turbulence production of the turbulence model is then limited. The general implementation strategy and particularly the parallelization aspects of the transition prediction method are presented and specific elements of the method for the determination of data relevant for transition prediction are introduced in detail. This includes aspects for the computation of the inviscid streamlines, the determination of the boundary layer edge or the computation of boundary layer velocity profiles. The focus is also on the presentation of aspects of an automatic and autonomous application of the stability solver.

The presented transition prediction method represents a novel approach in that it utilizes the combination of using a stability code in conjunction with inviscid streamlines and boundary layer data extracted from the RANS solution. This combination of different procedural elements and the consequent way of implementing and applying this combination of elements represents a unique approach compared to other existing transition prediction approaches. The usage of boundary velocity profiles from the RANS solution enables the method to predict transition downstream of laminar separation, for example for transition over laminar separation bubbles. This is typically not possible with general boundary layer codes that are based on formulations of the boundary layer equations that become singular at laminar separation. By using the boundary layer profiles from the RANS solution an increase of physical accuracy is expected to be achieved, since all three-dimensional effects are inherently included in the RANS velocity field for three-dimensional computations. Boundary layer codes normally rely on certain approximations, for instance the conical flow assumption, or need initial and boundary condition that often are difficult to determine, especially when coupled to a RANS solver. With the inviscid streamlines approach a very flexible application of the transition prediction method is achieved, facilitating the transition prediction based on linear stability theory for general three-dimensional geometries. Using this approach together with boundary layer data from the RANS solution refrains the transition prediction method from being limited to wing-like geometries.

The application of the linear stability theory is considered a good compromise of physical accuracy in the modelling as well as robustness and maturity of the method. The accuracy of the transition prediction method has been validated against several wind tunnel test cases for flows of varying complexity, also verifying that streamwise and cross-flow velocity profiles can be determined with sufficient accuracy from the RANS solution. For the two-dimensional flow around the NLF (1)–0416 airfoil a very good agreement is achieved compared to the experiment for the complete range of experimental flow conditions. The results for this test case also show that it is possible to predict transition over laminar separation bubbles when the boundary layer velocity profiles are extracted from the RANS solution. For infinite swept wing flows, the predicted transition locations are again in very close agreement with the experimental data for the NLF (2)–0415 infinite swept wing and a three-dimensional wing with ONERA D section. For the three-dimensional NACA 64<sub>2</sub>-A-015 wing it was possible to accurately predict transition over a wide range of experimental flow conditions. However, for certain flow conditions a rapid movement of the transition location with increasing Reynolds number is seen in the experiment that can not be resolved with the applied transition prediction method. The physical reason for this upstream movement remains unknown for now but may be identified by applying higher order or non-linear stabil-

ity computations to this test case. For the fully three-dimensional flow around the DLR prolate spheroid transition based on streamwise instabilities was predicted in very good accordance with the experiment using the presented transition prediction approach. For cross-flow transition the predicted results for the low to moderate angles of attack are also in good agreement with the experiment. However, for high angles of attack the transition was predicted too far upstream. The definite reason for this remains unknown but may also be explained by non-linear effects that cannot be resolved by linear stability theory.

For some time now, the field of transition prediction methods for RANS solvers has been extended by local correlation based transport equation approaches. They avoid some of the implementation and application challenges of the more classical transition prediction approaches that often rely on non-local line-search and line-integration operations. The different, more or less novel, transport equation approaches meanwhile include several modelling ideas and development paths that still need to be channelled and the most promising approaches have to be identified and become established. A certain trend in this direction can already be seen, in that certain approaches are now being applied more often than others and are being further developed by different research groups. Some of the approaches show some good results compared to experimental data and stability theory based computations and overall transport equation approach have seemingly a lot of potential, especially with regard to robust and engineering-based prediction methods in RANS solvers.

However, with regard to the accuracy of the predicted transition locations, it is striking that many good results are shown in the literature, but sometimes very different flow conditions, for example with respect to the turbulence intensity, are used. This is not an inherent problem for the transport equation approaches alone but can also be transferred to the classical transition prediction approaches. However, it makes it difficult to assess the transport equation methods, especially since they are still in the transient development phase and their general transition prediction ability is not yet fully established. This problem leads to the necessary definition of well-documented standard test cases for the validation of transition prediction methods and thus to another problem: from the author's point of view, it turns out that actually many, if not all, of the available standard validation test cases are not documented well enough, at least not in a way to eliminate most or all uncertainties for the flow conditions. This concerns above all the actual flow conditions in wind tunnel tests for which a clear and consistent specification of the turbulence intensity is needed. Additionally, for example all three-dimensional flow phenomena and wind tunnel wall effects need to be documented and accurately incorporated in the RANS computations.

If in the medium term some of the weaknesses in physical modelling can be rectified, the transport equation approaches will become even more accepted. However, from the author's point of view, in the foreseeable future, the transport equation approaches will in terms of physical modelling not be able to keep up with transition prediction methods based on local linear stability theory or parabolized stability equations, unless better and, above all, more physical correlations between transition onset and local flow quantities can be found. Meanwhile, both methods, transport equation approaches and stability theory based prediction methods, will coexist and serve different target groups. For the foreseeable future, especially due to the principal ease of use, the transport equation approaches will primarily be of use to non-experts in everyday use, for example, for engineering applications. The transition prediction methods based on stability theory, which can be much more demanding with respect to application, for example in terms of preparation of the computation and assessment of the transition prediction quality, will be reserved for more experienced users and experts in the field of transition prediction. This will be particularly true when it comes to transition prediction for three-dimensional flows over more complex geometries or for in principal unknown or new flow conditions, for example for computations near the boundary of the flight envelope of aircrafts. Other areas of application of stability theory based methods will include the provision of reference solutions and reference data for the calibration and validation of correlation based transport equation approaches, the evaluation of free flight and wind tunnel experiments or the support for the continuing understanding of transition phenomena and the physics of the transition process.

The presented transition prediction method is thought to enhance the more classical approach of linear stability analyses with boundary layer data from boundary layer codes towards improved physical accuracy and with this also to somewhat close the gap a little more that exists towards approaches based on parabolized stability equation. This is mainly achieved by reducing the level of approximations incorporated in the transition prediction chain with regard to fully three-dimensional boundary layers. With the extraction of the boundary layer velocity profiles directly from the RANS solution, inaccuracies for the boundary layer flow are avoided that may be introduced in regions where the underlying assumptions of the boundary layer methods, for example the conical flow assumption, are no longer justified. Unfortunately, this potential of the presented transition prediction approach could not be fully exploited in the present work, mainly due to the lack of missing experimental data, for example for transition near the wing tip.

In terms of full applicability to three-dimensional flows, the presented transition prediction method is similarly demanding with regard to implementation and application as approaches that utilize boundary layer codes. However, a reasonable challenge for the presented approach is a possible influence of the laminar boundary layer by portions of the turbulent flow. Within the scope of the present work this is most prominently the case for the upstream influence of the turbulence model in the vicinity of the transition point, which was overcome with an extrapolation of the  $N$ -factor envelope. However, not only an upstream influence is conceivable but also an influence in lateral direction is possible, if, for example for a wing with strongly varying flow conditions in spanwise direction, the transition front exhibits rapid changes in streamwise direction over a short spanwise distance. Here, an extrapolation of the  $N$ -factor envelope proves also useful, however from experience, the actual implementation requires increased care. Related to this problem is the influence of the laminar boundary layer by turbulent wake flows. Here, a suitable bypass transition criterion may be beneficial if the turbulence intensity acting on the boundary layer is strong enough. However, that does not entirely resolve the problem that, strictly speaking, for a successful stability analysis fully laminar boundary layer velocity profiles are mandatory. Accordingly, of course, the application of a boundary layer method could in turn be advantageous in these cases.

The calculation of the flow over the DLR prolate spheroid with the presented method is one of the few examples for successful and reasonably accurate transition prediction for a fuselage configuration within a RANS solver environment in conjunction with the application of stability theory and for a broad range of flow conditions. Other calculations consider the application of boundary layer codes with input from potential flow theory for transition prediction without the coupling to a RANS solver [113, 114, 102], or the application of correlation based transition transport models [99, 21, 47]. The application to the DLR prolate spheroid test case also partially proves the desired versatility of the presented transition prediction method and this is supported by the application to, for example, a flow-through nacelle [64], a helicopter fuselage [25] or a wing with spanwise varying cross-flow [115]. Further application challenges can, for example, include the application to cases with suction or to cases including surface roughness and waviness or surface irregularities like steps and gaps. Based on the strategy to extract boundary layer velocity profiles from the RANS solution, the first application scenarios should already be covered inherently and would need only further validation, especially regarding a suitable adaptation of the critical  $N$ -factor. Since steps and gaps represent discontinuities of the surface, depending on the size of the obstacles the general functionality of the method and the validity of the underlying theory need first to be verified and validated.

Potentially one of the weakest parts in the application of linear stability theory in form of the  $e^N$  method is the definition of the critical  $N$ -factor. For a simple scalar value the  $N$ -factor may need to include quite a few informations, as the  $N$ -factor for example remains the main parameter to include receptivity effects or to account for the general disturbance environment. Approaches are available to incorporate turbulence intensity effects [26, 116, 85] or surface roughness effects [36, 85] into the critical  $N$ -factor. With further research, based for example on experimental data or data from higher

quality methods, it could be worth to try to include the effects of non-parallelism, receptivity and non-linear mechanism into an advanced critical  $N$ -factor formulation. If successful, with such an ambitious approach the gap to the parabolized stability equation based methods could be further closed.

The linear stability theory itself is mature and has little potential for improvement and remains, despite some advances with high-fidelity transition prediction methods, one of the standard approaches for transition analyses. These high-fidelity methods, like non-local, linear or non-linear stability theory based methods, should however be used in the present case to still gain a better understanding of the application weaknesses of linear stability theory, for example in areas where the underlying assumptions restrict the validity of the approach. Based on the observations for the DLR prolate spheroid and the NACA 64<sub>2</sub>-A-015 wing regarding possible non-linear effects, higher quality methods can help to hopefully verify and further understand why and under which circumstances the linear stability fails to accurately predict experimental transition locations. A step towards the verification of the aforementioned issues and at the same time, if the result is a automatic, autonomous and robust prediction method, an improvement of the current transition prediction method is the extension of the method to incorporate a parabolized stability equations based approach. If such an approach is formulated in a streamline based coordinate system and a streamline-marching procedure [24] for the solution is used, the existing infrastructure could be used to develop a potentially versatile and more accurate transition prediction method. Based on the current implementation, the then already included linear stability theory approach may be used to formulate appropriate initial and boundary conditions for the stability problem.

## 6. Published data

The present work builds on the work presented in reference [40]. Some of the data presented here have been presented in a similar way in other publications, that is in references [39], [40] and [47], all publications published by the author of this work as first author.

Figures 1, 2 and 3 occur in the same form or in a slightly modified form in a not freely available presentation held by the author of the present work as part of training courses for transition prediction with the DLR TAU code. Figure 5 and 6 have been used in the same form or in a slightly modified form in reference [40]. Section 4.1.1 is based on a paragraph published in reference [40]. In the same reference figures 14, 15, 16 and 17 have been published in the same form or in a slightly modified form. The results for the grid convergence study for the ONERA D wing of section 4.1.2 have also been published in reference [40]. The feasibility study in section 4.1.3 has already been published in references [40] and [39]. In the same references figures 27 and 28 appear in the same form or in a slightly modified form. Some results for the prolate spheroid (Sec. 4.2.5) have also been published in references [40] and [47]. These published results are different from the results presented in this work. The results in reference [40] are based on an older variant of the transition prediction methodology and computations have been performed on different computational grids. The results in reference [47] are based on computations using different turbulence models compared to the turbulence model used in this work. A comparison and a more detailed description of the results is given in section 4.2.5.

Some figures in the present work have been derived according to figures appearing in publications of other authors. Figures 3 and 4 have been adapted from figures in reference [13] and have been newly created with additional and adjusted information fitting the respective approaches in this work. Figure 44 has been adapted from a figure in reference [86] but is based on the actual geometry used for the grid generation for the investigations presented in section 4.2.4.



## 7. References

- [1] Reynolds, O., “XXIX. An experimental investigation of the circumstances which determine whether the motion of water shall be direct or sinuous, and of the law of resistance in parallel channels,” *Philosophical Transactions of the Royal Society of London*, , No. 174, 1883, pp. 935–982.
- [2] Schlichting, H., “Über die Theorie der Turbulenzentstehung,” *Forschung auf dem Gebiete des Ingenieurwesens*, Vol. 16, No. 3, 1949, pp. 66–78.
- [3] Prandtl, L., “Über Flüssigkeitsbewegung bei sehr kleiner Reibung,” *Gesammelte Abhandlungen zur angewandten Mechanik, Hydro- und Aerodynamik*, edited by W. Tollmien, H. Schlichting, and H. Görtler, Springer, Berlin/Göttingen/Heidelberg, 1961, pp. 575–584.
- [4] Dryden, H. L., “Some Recent Contributions to the Study of Transition and Turbulent Boundary Layers,” 1947, NACA TN 1168.
- [5] Prandtl, L., “Der Luftwiderstand von Kugeln,” *Gesammelte Abhandlungen zur angewandten Mechanik, Hydro- und Aerodynamik*, edited by W. Tollmien, H. Schlichting, and H. Görtler, Springer, Berlin/Göttingen/Heidelberg, 1961, pp. 597–608.
- [6] Strutt, J. W. (Baron Rayleigh), “On the Stability, or Instability, of Certain Fluid Motions,” *Scientific Papers*, Cambridge University Press, 1899, pp. 474–487, also: Lord Rayleigh, London Math. Soc. Proc. XI., pp. 57–70, 1880.
- [7] Prandtl, L., “Bemerkungen über die Entstehung der Turbulenz,” *Gesammelte Abhandlungen zur angewandten Mechanik, Hydro- und Aerodynamik*, edited by W. Tollmien, H. Schlichting, and H. Görtler, Springer, Berlin/Göttingen/Heidelberg, 1961, pp. 687–696.
- [8] Tollmien, W., “Über die Entstehung der Turbulenz. 1. Mitteilung,” *Nachrichten von der Gesellschaft der Wissenschaften zu Göttingen, Mathematisch-Physikalische Klasse 1929*, 1929, pp. 21–44.
- [9] Schlichting, H., “Zur Entstehung der Turbulenz bei der Plattenströmung,” *Nachrichten von der Gesellschaft der Wissenschaften zu Göttingen, Mathematisch-Physikalische Klasse 1933*, 1933, pp. 182–208.
- [10] Schubauer, G. B. and Skramstad, H. K., “Laminar boundary-layer oscillations and transition on a flat plate,” *J. Res. Nat. Bur. Stand.*, Vol. 38, No. 251, 1947, pp. 92.
- [11] Schlichting, H., *Grenzschicht-Theorie*, G. Braun, Karlsruhe, 8th ed., 1982.
- [12] Stewartson, K., *The Theory of Laminar Boundary Layers in Compressible Fluids*, Oxford University Press, Amen House, London, 1964.
- [13] Arnal, D., “Boundary layer transition: predictions based on linear theory,” *Special Course on Progress in Transition Modelling*, 1994, AGARD-R-793.
- [14] Henkes, R. A. W. M. and van Ingen, J. L., “Overview of stability and transition in external aerodynamics,” *Series 01: Aerodynamics, 12*, 1998, Delft University Press.
- [15] Arnal, D., Houdeville, R., Séraudie, A., and Vermeersch, O., “Overview of laminar-turbulent transition investigations at ONERA Toulouse,” *41st AIAA Fluid Dynamics Conference and Exhibit, AIAA Paper 2011-3074*, Honolulu, 2011.
- [16] Kaups, K. and Cebeci, T., “Compressible Laminar Boundary Layers with Suction on Swept and Tapered Wings,” *Journal of Aircraft*, Vol. 14, No. 7, 1977.

- 
- [17] Falkner, V. and Skan, S. W., “Solutions of the boundary-layer equations,” *The London, Edinburgh, and Dublin Philosophical Magazine and Journal of Science*, Vol. 12, No. 80, 1931, pp. 865–896.
- [18] Van Driest, E. and Blumer, C., “Boundary layer transition: freestream turbulence and pressure gradient effects,” *AIAA journal*, Vol. 1, No. 6, 1963, pp. 1303–1306.
- [19] Menter, F. R., Smirnov, P. E., Liu, T., and Avancha, R., “A one-equation local correlation-based transition model,” *Flow, Turbulence and Combustion*, Vol. 95, No. 4, 2015, pp. 583–619.
- [20] Coder, J. G., “Further development of the amplification factor transport transition model for aerodynamic flows,” *AIAA SciTech 2019 Forum, AIAA Paper 2019-0039*, 2019.
- [21] Grabe, C., Nie, S., and Krumbein, A., “Transport Modeling for the Prediction of Crossflow Transition,” *AIAA Journal*, Vol. 56, No. 8, 2018, pp. 3167–3178.
- [22] Bertolotti, F. P., *Linear and nonlinear stability of boundary layers with streamwise varying properties*, Ph.D. thesis, The Ohio State University, 1991.
- [23] Herbert, T., “Parabolized stability equations,” *Annual Review of Fluid Mechanics*, Vol. 29, No. 1, 1997, pp. 245–283.
- [24] Chang, C.-L., “LASTRAC.3d: Transition Prediction in 3D Boundary Layers,” *34th AIAA Fluid Dynamics Conference, AIAA Paper 2004-2542*, Portland, 2004.
- [25] Krumbein, A., Krimmelbein, N., and Grabe, C., “Streamline-Based Transition Prediction Techniques in an Unstructured Computational Fluid Dynamics Code,” *AIAA Journal*, Vol. 55, No. 5, 2017, pp. 1548–1564.
- [26] Mack, L. M., “Transition prediction and linear stability theory,” *Laminar-Turbulent Transition*, 1977, AGARD-CP-224.
- [27] Smith, A. M. O. and Gamberoni, N., “Transition, Pressure Gradient and Stability Theory,” 1956, Douglas Aircraft Company Inc., El Segundo, California, U.S.A, Report ES 26388.
- [28] van Ingen, J. L., “Een semi-empirische methode voor de bepaling van de ligging van het omslaggebied van de grenslaag bij onsamendrukbare tweedimensionale stromingen,” 1956, Technische Hogeschool Vliegtuigbouwkunde Delft, Nederland, Rapport V.T.H.-71.
- [29] Arnal, D., Casalis, G., and Houdeville, R., “Practical Transition Prediction Methods: Subsonic and Transonic Flows,” *Advances in Laminar-Turbulent Transition Modeling, RTO-EN-AVT-151-07*, 2008.
- [30] Blazek, J., *Computational fluid dynamics: principles and applications*, Butterworth-Heinemann, 2015.
- [31] Sutherland, W., “LII. The viscosity of gases and molecular force,” *Philosophical Magazine Series 5*, Vol. 36, No. 223, 1893, pp. 507–531.
- [32] Spalart, P. R. and Allmaras, S. R., “A One-Equation Turbulence Model for Aerodynamic Flows,” *La Recherche Aérospatiale*, Vol. 1, 1994, pp. 5–21.
- [33] Mack, L. M., “Boundary-Layer Linear Stability Theory,” *Special Course on Stability and Transition of Laminar Flow*, 1984, AGARD-R-709.
- [34] Schrauf, G., “Transition prediction using different linear stability analysis strategies,” *12th AIAA Applied Aerodynamics Conference, AIAA Paper 1994-1848*, Colorado Springs, 1994.

- [35] Gaster, M., "A note on the relation between temporally increasing and spatially increasing disturbances in hydrodynamic stability," *J. Fluid. Mech.*, Vol. 14, 1962.
- [36] Crouch, J. D. and Ng, L. L., "Variable N-factor method for transition prediction in three-dimensional boundary layers," *AIAA Journal*, Vol. 38, No. 2, 2000, pp. 211–216.
- [37] Radeztsky, R. H., Reibert, M. S., and Saric, W. S., "Effect of micron-sized roughness on transition in sweptwing flows," *31st Aerospace Sciences Meeting & Exhibit, AIAA Paper 93-0076*, Reno, 1993.
- [38] Krimmelbein, N., "Erweiterung und Verifikation eines numerischen Verfahrens zur Berechnung der Transitionslage für Grenzschichten an 3D Rumpfkörpern," 2003, Technische Universität Braunschweig, Institut für Strömungsmechanik, Diplomarbeit Nr. 292.
- [39] Krimmelbein, N., Radespiel, R., and Nebel, C., "Numerical Aspects of Transition Prediction for Three-Dimensional Configurations," *35th AIAA Fluid Dynamics Conference and Exhibit, AIAA Paper 2005-4764*, Toronto, 2005.
- [40] Krimmelbein, N. and Radespiel, R., "Transition prediction for three-dimensional flows using parallel computation," *Computers & Fluids*, Vol. 38, 2009, pp. 121–136.
- [41] Krimmelbein, N. and Krumbein, A., "Automatic Transition Prediction for Three-Dimensional Configurations with Focus on Industrial Application," *Journal of Aircraft*, Vol. 48, 2011, pp. 1878–1887.
- [42] Krimmelbein, N., "Automatic Transition Prediction with the  $e^N$ -Method for Three-Dimensional, Industrially Relevant Configurations," *11th ONERA-DLR Aerospace Symposium - ODAS. CD-ROM Proceedings*, Toulouse, 2011.
- [43] Krimmelbein, N., Krumbein, A., and Togiti, V., "Industrialization of Automatic Transition Prediction for Three-Dimensional Configurations with the  $e^N$ -Method," *New Results in Numerical and Experimental Fluid Mechanics VIII. Contributions to the 17th STAB/DGLR Symposium Berlin, Germany 2010*, edited by A. Dillmann, G. Heller, H.-P. Kreplin, W. Nitsche, and I. Peltzer, Springer, Berlin Heidelberg, 2013, pp. 533–540, ISBN 978-3-642-35679-7.
- [44] Krimmelbein, N., "Industrialization of the Automatic Transition Prediction in the DLR TAU Code," *Computational Flight Testing. Results of the Closing Symposium of the German Research Initiative ComFliTe, Braunschweig, Germany, June 11th-12th, 2012*, edited by N. Kroll, R. Radespiel, J. van der Burg, and K. Sørensen, Springer, Berlin Heidelberg, 2013, pp. 89–98, ISBN 978-3-642-38876-7.
- [45] Krumbein, A., Krimmelbein, N., and Schrauf, G., "Automatic Transition Prediction in a Hybrid Flow Solver - Part 1: Methodology and Sensitivities," *Journal of Aircraft*, Vol. 46, No. 4, 2009, pp. 1176–1190.
- [46] Krumbein, A., Krimmelbein, N., and Schrauf, G., "Automatic Transition Prediction in a Hybrid Flow Solver - Part 2: Practical Application," *Journal of Aircraft*, Vol. 46, No. 4, 2009, pp. 1191–1199.
- [47] Krimmelbein, N., Krumbein, A., and Grabe, C., "Validation of Transition Modeling Techniques for a Simplified Fuselage Configuration," *55th AIAA Aerospace Sciences Meeting. AIAA Science and Technology Forum and Exposition (SciTech 2018), AIAA Paper 2018-0030*, Kissimmee, 2018.
- [48] Schwamborn, D., Gerhold, T., and Heinrich, R., "The DLR TAU-Code: Recent Applications in Research and Industry," *European Conference on Computational Fluid Dynamics. ECCOMAS CFD 2006*, edited by P. Wesseling, E. Onate, and J. Periaux, 2006.

- 
- [49] Schrauf, G., “COCO - A program to compute velocity and temperature profiles for local and nonlocal stability analysis of compressible, conical boundary layers with suction,” 1998, ZARM Technik Report.
- [50] Schrauf, G., “LILO 2.1. User’s Guide and Tutorial,” 2006, GSSC Technical Report 6, originally issued Sep. 2004, modified for Version 2.1.
- [51] Schrauf, G., “Curvature effects for three-dimensional compressible boundary-layer stability,” *Zeitschrift für Flugwissenschaften und Weltraumforschung*, Vol. 16, 1992, pp. 119–127.
- [52] Schrauf, G., “Algorithm 696. An inverse Rayleigh iteration for complex band matrices,” *ACM Transactions on Mathematical Software*, Vol. 17, No. 3, 1991, pp. 335–340.
- [53] Casalis, G. and Arnal, D., “Development and validation of the simplified method for pure crossflow instability at low speed,” 1996, ELFIN II Technical Report 145.
- [54] Nebel, C., Radespiel, R., and Wolf, T., “Transition Prediction for 3D Flows Using a Reynolds-Averaged Navier-Stokes Code and N-Factor Methods,” *33rd AIAA Fluid Dynamics Conference and Exhibit, AIAA Paper 2003-3593*, Orlando, 2003.
- [55] “Technical Documentation of the DLR TAU-Code Release 2019.1.0,” Technical Report, Institute of Aerodynamics and Flow Technology Braunschweig/Göttingen, Deutsches Zentrum für Luft- und Raumfahrt, 2019.
- [56] “MPI: A message-passing interface standard 1.0. Technical report,” <http://www.mpi-forum.org>, 1994.
- [57] Sadarjoen, I. A., van Walsum, T., Hin, A. J. S., and Post, F. H., “Particle tracing algorithm for 3D curvilinear grids,” *Scientific Visualisation - Overviews, Methodologies and Techniques*, edited by G. Nielsen, H. Müller, and H. Hagen, 1997, IEEE, pp. 299–332.
- [58] Arnal, D., Habiballah, M., and Coustols, E., “Laminar instability theory and transition criteria in two and three-dimensional flow,” *La Recherche Aéronautique*, Vol. 2, 1984, pp. 45–63.
- [59] Arnal, D., “Three-dimensional boundary layers: Laminar-turbulent transition,” *Computation of Three-Dimensional Boundary Layers including Separation*, 1987, AGARD-R-741.
- [60] Stock, H. W., Wild, J., and Krumbein, A., “Computation of an Infinite Swept High Lift System at Four Angles of Attack – RANS Computations Coupled to the 2 N-Factor  $e^N$  Transition Prediction,” 2004, HiAer Report D.1.4-2, DLR Braunschweig.
- [61] Hirschel, E. H., *Basics of Aerothermodynamics*, Springer, Berlin Heidelberg, 2005, ISBN 978-3-540-26519-1.
- [62] Arnal, D. and Juillen, J. C., “Leading edge contamination and relaminarisation on a swept wing at incidence,” *Fourth Symposium on Numerical and Physical Aspects of Aerodynamic Flows. 16-19 January 1989, California State University, Long Beach, California, U.S.A.*, edited by T. Cebeci, Springer, 1989.
- [63] Redeker, G., Horstmann, K. H., Köster, H., Thiede, P., and Szodruch, J., “Design of a natural laminar flow glove for a transport aircraft,” *AIAA Paper 90-3043*, 1990.
- [64] Probst, A., Radespiel, R., and Rist, U., “Linear-stability-based transition modeling for aerodynamic flow simulations with a near-wall Reynolds-stress model,” *AIAA journal*, Vol. 50, No. 2, 2012, pp. 416–428.

- 
- [65] Cliquet, J., Houdeville, R., and Arnal, D., “Application of laminar-turbulent transition criteria in Navier-Stokes computations,” *AIAA Journal*, Vol. 46, No. 5, 2008, pp. 1182–1190, also AIAA Paper 2007–515.
- [66] Lambert, M. and Kessler, R., “Radiation heat transfer in mixed convection flows,” *New Results in Numerical and Experimental Fluid Mechanics VII*, Springer, 2010, pp. 563–570.
- [67] Kühn, T., Altmikus, A., Daboul, H., Radi, A., Raasch, S., Knigge, C., Böske, L., Schwarz, T., Heister, C., Länger-Möller, A., et al., “Results of the research project AssiSt,” *Journal of Physics: Conference Series*, Vol. 1037, No. 2, 2018.
- [68] Heister, C., “Methodik zur näherungsweisen Vorhersage des laminar-turbulenten Umschlags an Hubschrauberrotoren,” Forschungsbericht 2016-37, Deutsches Zentrum für Luft- und Raumfahrt, Institut für Aerodynamik und Strömungsmechanik, Braunschweig, 2016.
- [69] Kaufmann, K., Ströer, P., Richez, F., Lienard, C., Gardarein, P., Krimmelbein, N., and Gardner, A. D., “Validation of boundary-layer-transition computations for a rotor with axial inflow,” *Vertical Flight Society 75th Forum, Philadelphia, Pennsylvania, May 13-16*, 2019.
- [70] Kreplin, H.-P., Meier, H. U., and Maier, A., “Wind Tunnel Model and Measuring Techniques for the Investigation of Three-Dimensional Turbulent Boundary Layers,” *10th AIAA Aerodynamic Testing Conference, AIAA Paper 78-781*, San Diego, 1978.
- [71] Stock, H. W. and Haase, W., “Feasibility Study of  $e^N$  Transition Prediction in Navier-Stokes Methods for Airfoils,” *AIAA Journal*, Vol. 37, No. 10, 1999, pp. 1187–1196.
- [72] Braslow, A. L. and Visconti, F., “Investigation of boundary-layer Reynolds number for transition on a NACA 65<sub>(215)</sub>-114 airfoil in the Langley two-dimensional low-pressure tunnel,” 1948, NACA TN 1704.
- [73] Taylor, B. N. and Kuyatt, C. E., “Guidelines for evaluating and expressing the uncertainty of NIST measurement results,” *NIST technical note 1297*, 1994, National Institute of Standards and Technology Gaithersburg, MD.
- [74] Somers, D., “Design and experimental results for a natural-laminar-flow airfoil for general aviation applications,” 1981, NASA TP 1861.
- [75] Von Doenhoff, A. E. and Abbott, F. T., “The Langley two-dimensional low-turbulence pressure tunnel,” 1947, NACA TN 1283.
- [76] McGhee, R. J., Beasley, W. D., and Foster, J. M., “Recent modifications and calibration of the Langley low-turbulence pressure tunnel,” 1984, NASA TP 2328.
- [77] Stainback, P., McGhee, R., Beasley, W., and Morgan, H., “The Langley Research Center’s Low-Turbulence Pressure Tunnel,” *14th Aerodynamic Testing Conference, AIAA Paper 86-762*, 1986.
- [78] Dagenhart, J. R., “Crossflow stability and transition experiments in a swept-wing flow,” 1992, NASA-TM-108650.
- [79] Dagenhart, J. R. and Saric, W. S., “Crossflow stability and transition experiments in swept-wing flow,” 1999, NASA TP-1999-209344.
- [80] Saric, W. S., “The ASU Transition Research Facility,” *17th Aerospace Ground Testing Conference, AIAA Paper 92-3910*, Nashville, 1992.

- 
- [81] Sousa, J. M. M. and Silva, L. M. G., “Transition prediction in infinite swept wings using Navier–Stokes computations and linear stability theory,” *Computers & Structures*, Vol. 82, No. 17-19, 2004, pp. 1551–1560.
- [82] Manie, F., Rehbach, C., and Schmitt, V., “Etude d’une aile à flèche variable en écoulement sub ou transsonique,” *International Council of the Aeronautical Sciences, Congress, 11th, Lisbon, Portugal*, Vol. 2, 1978.
- [83] Schmitt, V. and Manie, F., “Écoulements subsoniques et transsoniques sur une aile a flèche variable,” *La Recherche Aérospatiale*, Vol. 4, 1979, pp. 219–237.
- [84] Manie, F., Rehbach, C., and Schmitt, V., “Study of a variable sweep wing in sub or transonic flow,” 1987, NASA TT–20117.
- [85] Crouch, J. D., Ng, L. L., Kachanov, Y. S., Borodulin, V. I., and Ivanov, A. V., “Influence of surface roughness and free-stream turbulence on crossflow-instability transition,” *Procedia IUTAM*, Vol. 14, 2015, pp. 295–302.
- [86] Boltz, F. W., Kenyon, G. C., and Allen, C. Q., “Effects of sweep angle on the boundary-layer stability characteristics of an untapered wing at low speeds,” 1960, NACA TN D–338.
- [87] Peñaranda, F. E. and Freda, M. S., “Aeronautical Facilities Catalogue. Volume 1: Wind Tunnels,” 1985, NASA RP–1132.
- [88] Boltz, F. W., Kenyon, G. C., and Allen, C. Q., “The boundary-layer transition characteristics of two bodies of revolution, a flat plate, and an unswept wing in a low-turbulence wind tunnel,” 1960, NACA TN D–309.
- [89] Herriot, J. G., “Blockage Corrections for Three-Dimensional-Flow Closed-Throat Wind Tunnels, With Consideration of the Effect of Compressibility,” 1953, NACA Rep. 995.
- [90] Garner, H. C., Rogers, E. W. E., Acum, W. E. A., and Maskell, E. C., “Subsonic wind tunnel wall corrections,” AGARDograph 109, 1966.
- [91] Benek, J., Buning, P., and Steger, J., “A 3-D Chimera Grid Embedding Technique,” *AIAA Paper 85–1523*, 1985.
- [92] Abbott, I. H., von Doenhoff, A. E., and Stivers, L. S., “Summary of airfoil data,” 1945, NACA Rep. 824.
- [93] Herbert, T. and Schrauf, G., “Crossflow-dominated transition in flight tests,” *34th Aerospace Sciences Meeting and Exhibit, AIAA Paper 1996–0185*, Reno, 1996.
- [94] Atkin, C. J. and Schrauf, G., “Progress in linear stability methods for design applications,” *European Congress on Computational Methods in Applied Sciences and Engineering. ECCOMAS 2000*, Barcelona, 2000.
- [95] Kreplin, H.-P., “Three-dimensional boundary layer and flow field data of an inclined prolate spheroid,” *A Selection of Experimental Test Cases for the Validation of CFD Codes*, Vol. II, 1994, AGARD-AR-303.
- [96] Meier, H. U. and Kreplin, H.-P., “Experimental investigation of the boundary layer transition and separation on a body of revolution,” *Zeitschrift für Flugwissenschaften und Weltraumforschung*, Vol. 4, No. 2, 1980, pp. 65–71.

- 
- [97] Kreplin, H.-P., Vollmers, H., and Meier, H. U., “Wall Shear Stress Measurements on an Inclined Prolate Spheroid in the DFVLR 3m x 3m Low Speed Wind Tunnel, Göttingen,” 1985, DFVLR-AVA, Report IB 22-84 A 33.
- [98] Krimmelbein, N. and Krumbein, A., “Automatic Transition Prediction for Three-Dimensional Configurations with Focus on Industrial Application,” *40th AIAA Fluid Dynamics Conference and Exhibit, AIAA Paper 2010-4292*, Chicago, 2010.
- [99] Nie, S., Krimmelbein, N., Krumbein, A., and Grabe, C., “Extension of a Reynolds-Stress-Based Transition Transport Model for Crossflow Transition,” *Journal of Aircraft*, Vol. 55, No. 4, 2018.
- [100] Maruhn, K., “Druckverteilungsrechnungen an elliptischen Rümpfen und in ihrem Außenraum,” *Jahrbuch der deutschen Luftfahrtforschung, S. I*, 1941, pp. 135–147.
- [101] Tuckerman, L. B., “Inertia factors of ellipsoids for use in airship design,” 1926, NACA-TR-210.
- [102] Stock, H. W., “ $e^N$  Transition Prediction in Three-Dimensional Boundary Layers on Inclined Prolate Spheroids,” *AIAA Journal*, Vol. 44, No. 1, 2006, pp. 108–118.
- [103] Menter, F., Langtry, R., and Völker, S., “Transition modelling for general purpose CFD codes,” *Flow, turbulence and combustion*, Vol. 77, No. 1-4, 2006, pp. 277–303.
- [104] Abu-Ghannam, B. and Shaw, R., “Natural transition of boundary layers: the effects of turbulence, pressure gradient, and flow history,” *Journal of Mechanical Engineering Science*, Vol. 22, No. 5, 1980, pp. 213–228.
- [105] Langtry, R. B., Sengupta, K., Yeh, D. T., and Dorgan, A. J., “Extending the  $\gamma-Re_{\theta t}$  Correlation Based Transition Model for Crossflow Effects,” *45th AIAA fluid dynamics conference, AIAA Paper 2015-2474*, 2015.
- [106] Drela, M. and Giles, M. B., “Viscous-inviscid analysis of transonic and low Reynolds number airfoils,” *AIAA journal*, Vol. 25, No. 10, 1987, pp. 1347–1355.
- [107] Uranga, A., *Investigation of transition to turbulence at low Reynolds numbers using Implicit Large Eddy Simulations with a Discontinuous Galerkin method*, Ph.D. thesis, Department of Aeronautics and Astronautics, Massachusetts Institute of Technology, 2011.
- [108] Ströer, P., Krimmelbein, N., Krumbein, A., and Grabe, C., “Stability-Based Transition Transport Modeling for Unstructured Computational Fluid Dynamics Including Convection Effects,” *AIAA Journal*, Vol. 58, No. 4, 2020, pp. 1506–1517.
- [109] Bégou, G., Deniau, H., Vermeersch, O., and Casalis, G., “Database approach for laminar-turbulent transition prediction: Navier–Stokes compatible reformulation,” *AIAA Journal*, 2017, pp. 3648–3660.
- [110] Coder, J. G., “Enhancement of the amplification factor transport transition modeling framework,” *55th AIAA Aerospace Sciences Meeting, AIAA Paper 2017-1709*, 2017.
- [111] Nie, S., Krimmelbein, N., Krumbein, A., and Grabe, C., “Coupling of a Reynolds Stress Model with the  $\gamma-Re_{\theta t}$  Transition Model,” *AIAA Journal*, Vol. 56, No. 1, 2018, pp. 146–157.
- [112] Grabe, C., Nie, S., and Krumbein, A., “Transition transport modeling for the prediction of crossflow transition,” *34th AIAA applied aerodynamics conference, AIAA Paper 2016-3572*, 2016.
- [113] Vijgen, P. M. H. W., Dodbele, S. S., Pfenninger, W., and Holmes, B. J., “Analysis of Wind-Tunnel Boundary-Layer Transition Experiments on Axisymmetric Bodies at Transonic Speeds Using Compressible Boundary-Layer Stability Theory,” *26th AIAA Aerospace Sciences Meeting, AIAA Paper 88-0008*, Reno, 1988.

- [114] Mazin, C., *Calcul de couches limites tridimensionnelles par une technique de caractéristiques*, Ph.D. thesis, École nationale supérieure de l'aéronautique et de l'espace, 1991.
- [115] Kruse, M., Munoz, F., and Radespiel, R., "Transition prediction results for sickle wing and NLF (1)-0416 test cases," *2018 AIAA Aerospace Sciences Meeting, AIAA Paper 2018-0537*, Kissimmee, 2018.
- [116] van Ingen, J. L., "The  $e^N$  method for transition prediction. Historical review of work at TU Delft," *38th AIAA Fluid Dynamics Conference and Exhibit, AIAA Paper 2008-3830*, Seattle, 2008.
- [117] Pope, S. B., *Turbulent flows*, Cambridge University Press, 2000.
- [118] Tetervin, N., "A review of boundary-layer literature," 1947, NACA TN 1384.
- [119] Cumpsty, N. A. and Head, M. R., "The Calculation of Three-Dimensional Turbulent Boundary Layers: Part II: Attachment-Line Flow on an Infinite Swept Wing," *The Aeronautical Quarterly*, Vol. 18, No. 2, 1967, pp. 150–164.
- [120] Treadgold, D. and Beasley, J., "Some examples of the application of methods for the prediction of boundary-layer transition on sheared wings," 1973, Her Majesty's Stationery Office, C.P. No. 1246.
- [121] Pfenninger, W., "Flow phenomena at the leading edge of swept wings," *Recent developments in boundary layer research, AGARDograph 97, Part IV*, 1965.
- [122] Launder, B. E. and Jones, W. P., "On the prediction of laminarisation," 1969, Her Majesty's Stationery Office, C.P. No. 1036.

## 8. Figures

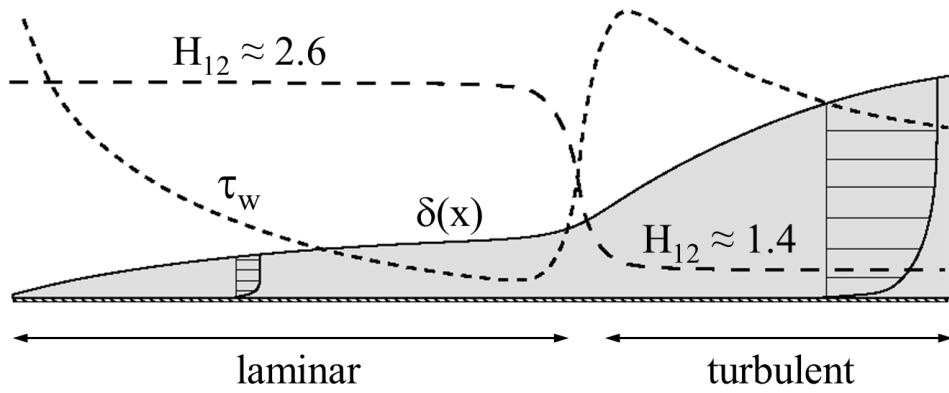


Figure 1: Evolution of a transitional boundary layer along a flat plate.

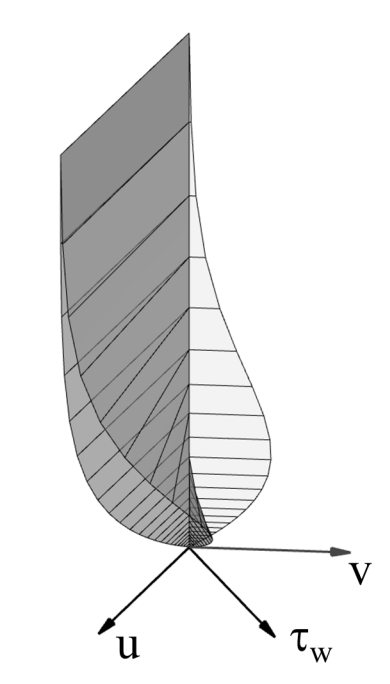


Figure 2: Three-dimensional boundary layer profile.

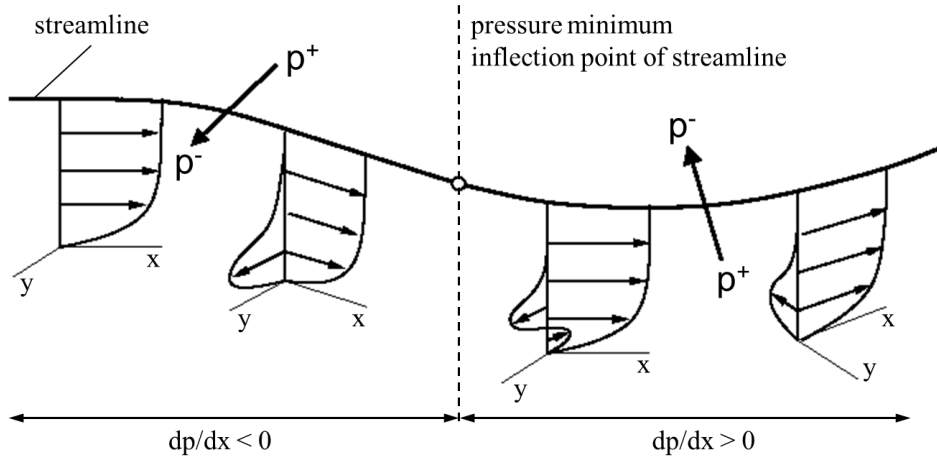


Figure 3: Development of cross-flow velocity profiles in three-dimensional flow (figure adapted from reference [13]).

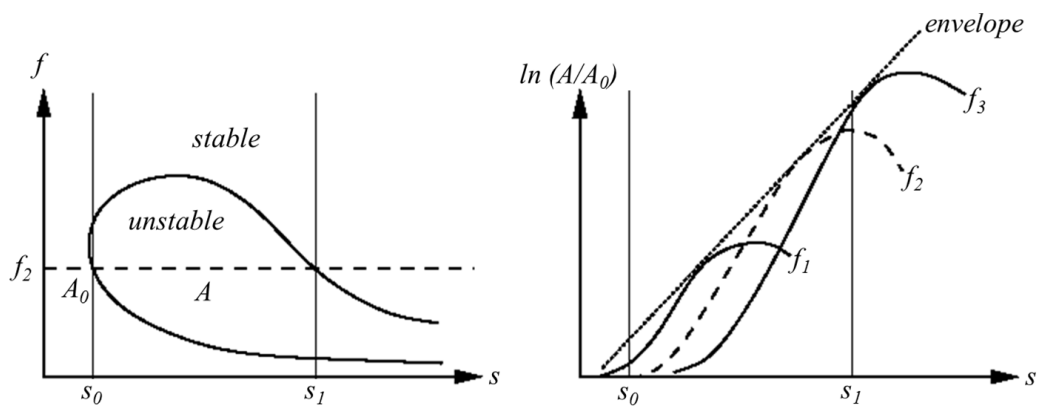


Figure 4: Principle of the  $e^N$  method (figure adapted from reference [13]).

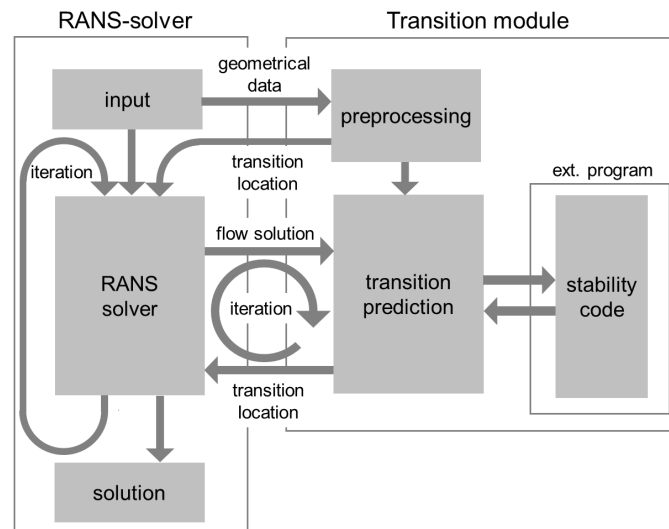


Figure 5: Coupled program system of RANS solver and transition module.

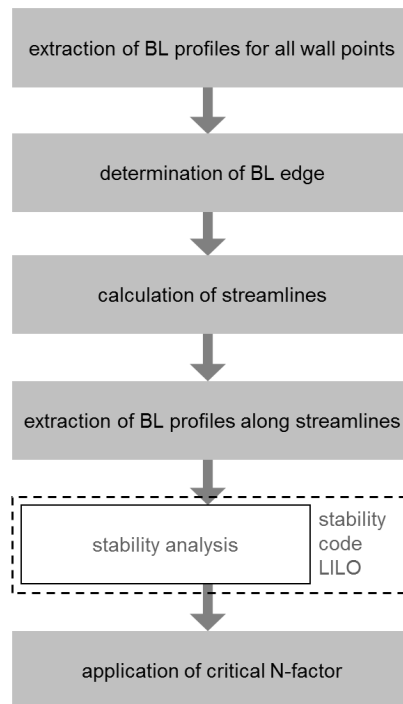


Figure 6: General structure of the transition module.

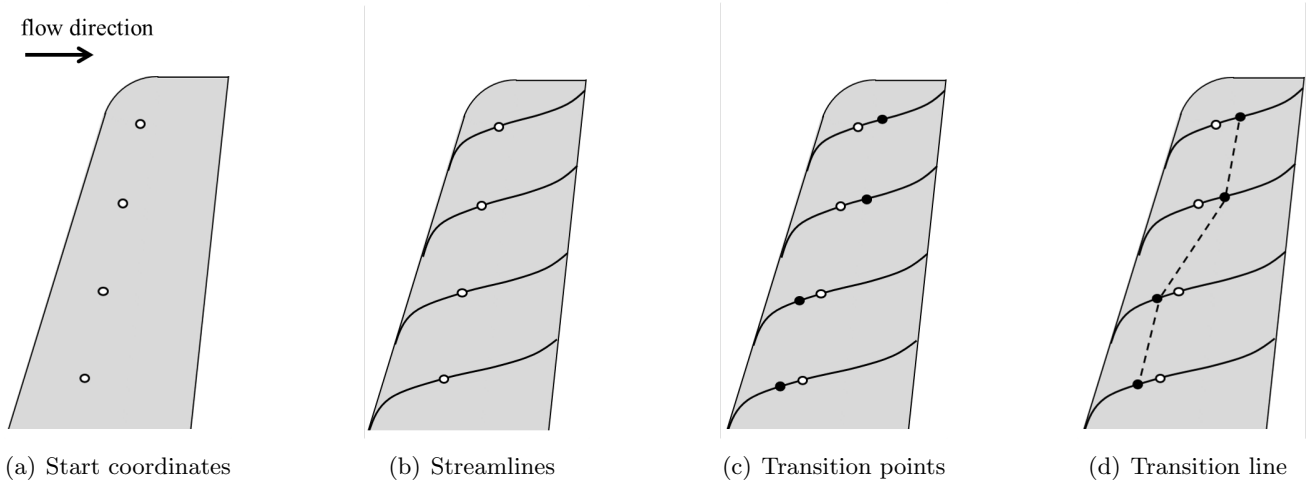


Figure 7: Basic steps for transition prediction for three-dimensional flows.

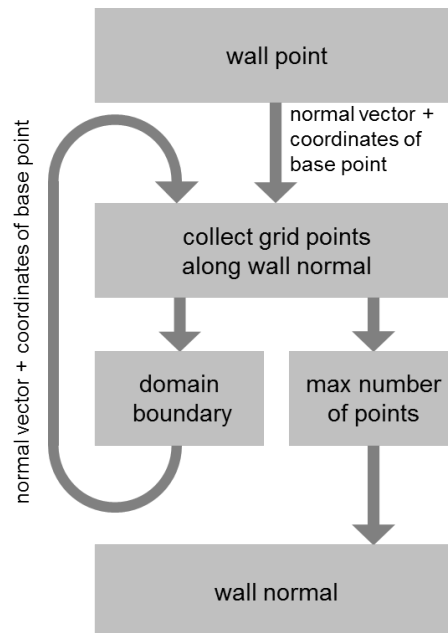


Figure 8: Structure for the determination of wall-normal lines.

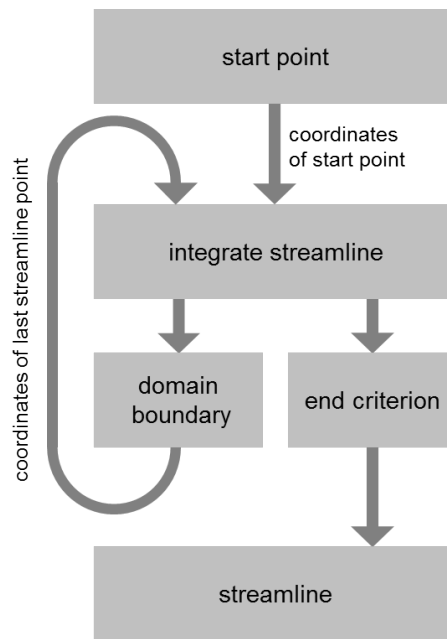


Figure 9: Structure for the determination of inviscid streamlines.

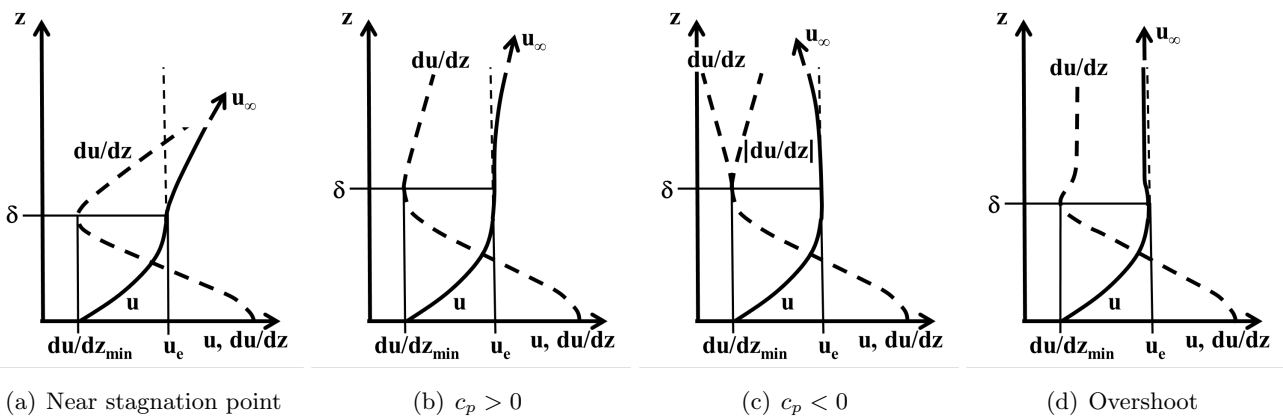


Figure 10: Schematic of typical boundary layer velocity profiles in a RANS solution.

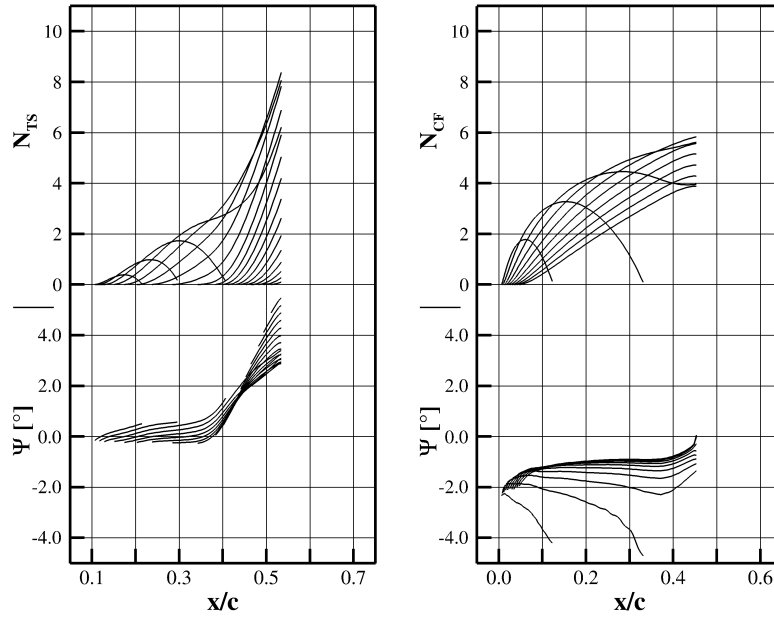


Figure 11:  $N$ -factors and group velocity direction, NACA 64<sub>2</sub>-A-015,  $\Lambda = 50.0^\circ$ ,  $\alpha = -1.0^\circ$ ,  $Re = 5.0 \times 10^6$ .



Figure 12: Nested loops for stability computation.

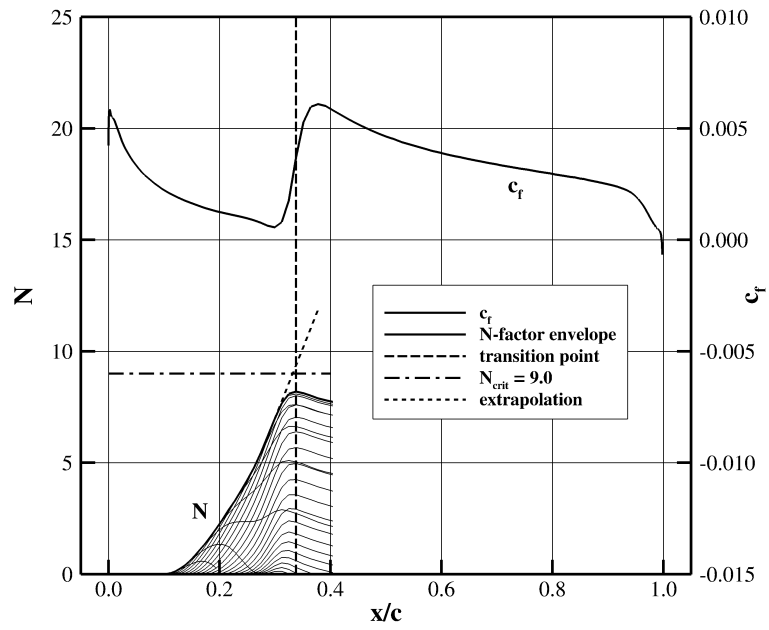
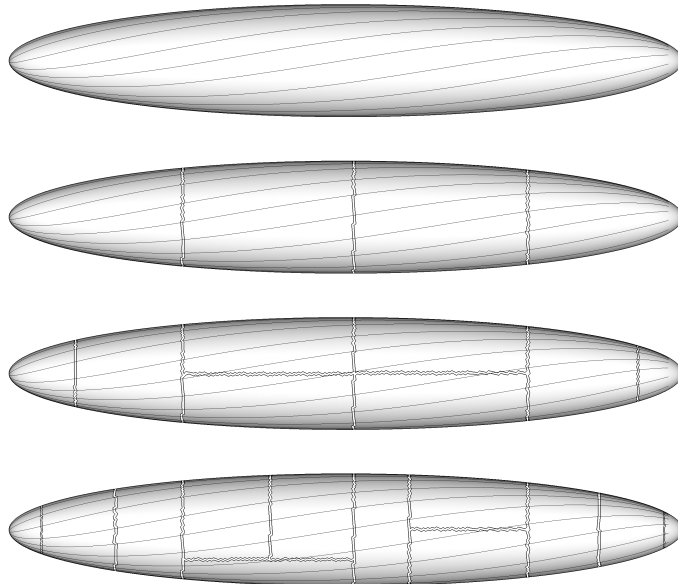
Figure 13: Extrapolation of  $N$ -factors.

Figure 14: Edge streamlines and domain boundaries, 1, 4, 8 and 12 domains, 6:1 prolate spheroid.

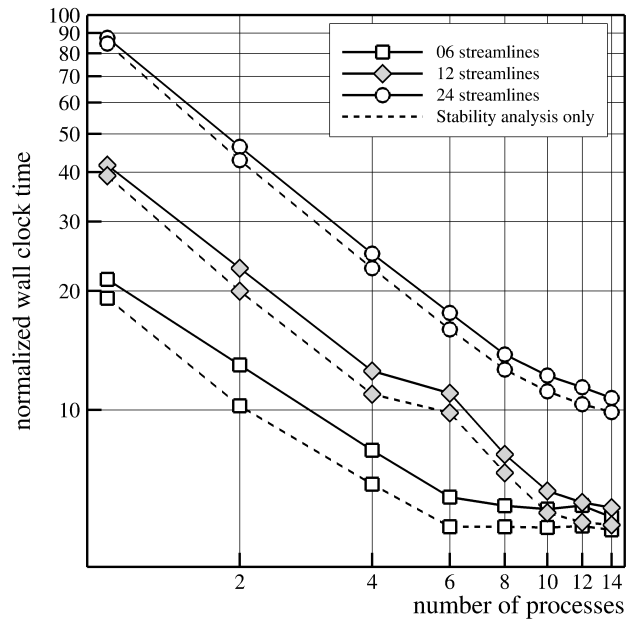


Figure 15: Computational time vs number of processes, transition prediction step and execution of stability code, 6, 12 and 24 streamlines.

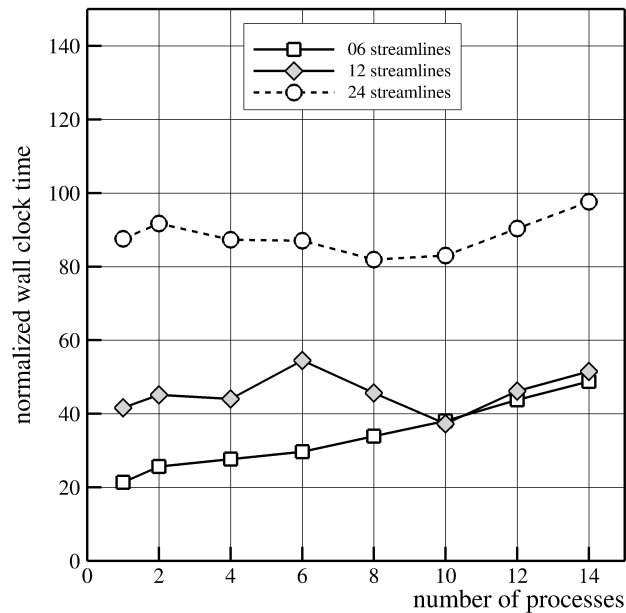


Figure 16: Computational time vs number of processes, transition prediction step, normalized with time for one multigrid cycle of the TAU solver, 6, 12 and 24 streamlines.

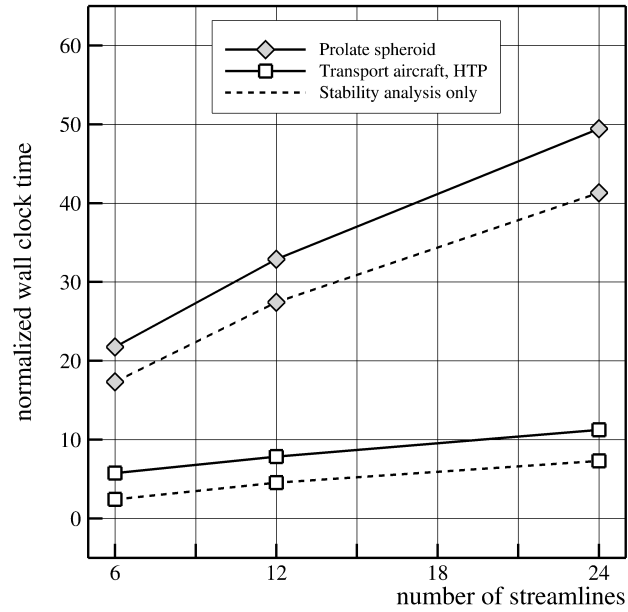


Figure 17: Computational time vs number of streamlines, 6:1 prolate spheroid and generic transport aircraft, 8 domains.

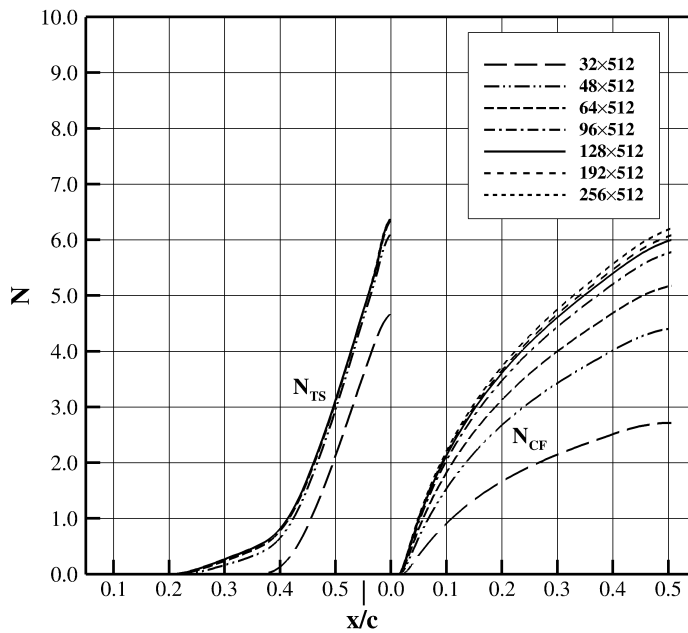


Figure 18: Grid convergence,  $N$ -factors, NACA 64<sub>2</sub>-A-015,  $\Lambda = 50.0^\circ$ ,  $\alpha = -2.5^\circ$ ,  $Re = 3.0 \times 10^6$ .

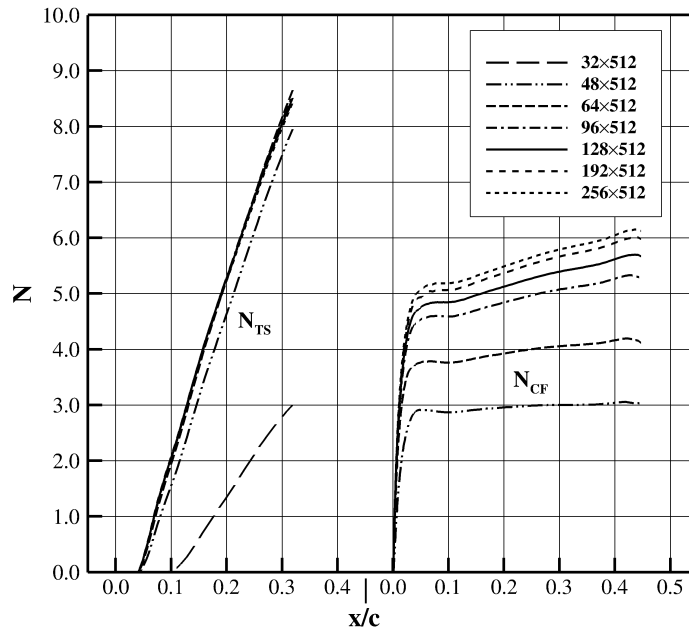


Figure 19: Grid convergence,  $N$ -factors, NACA 64<sub>2</sub>-A-015,  $\Lambda = 30.0^\circ$ ,  $\alpha = 0.5^\circ$ ,  $Re = 1.5 \times 10^7$ .

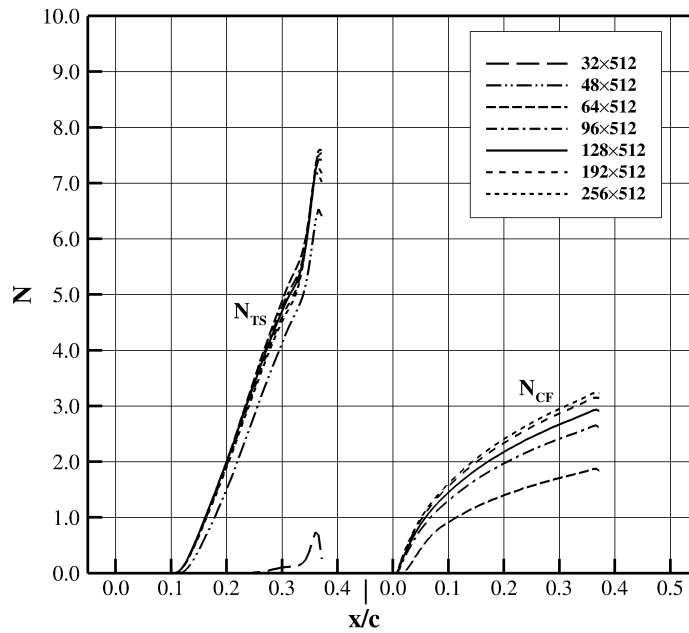


Figure 20: Grid convergence,  $N$ -factors, NACA 64<sub>2</sub>-A-015,  $\Lambda = 10.0^\circ$ ,  $\alpha = -2.0^\circ$ ,  $Re = 2.5 \times 10^7$ .

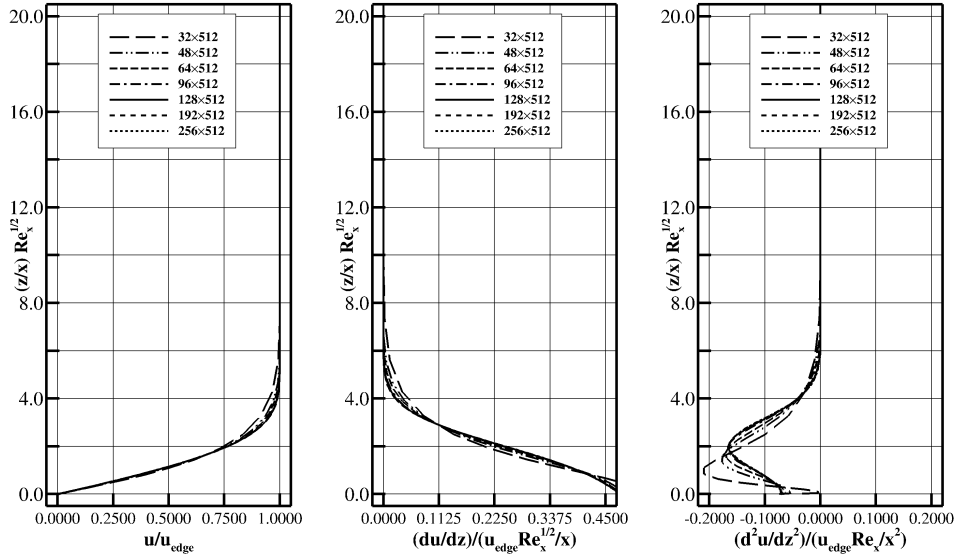


Figure 21: Grid convergence, stream wise velocity profiles at  $x/c = 0.25$ , NACA 64<sub>2</sub>-A-015,  $\Lambda = 10.0^\circ$ ,  $\alpha = -2.0^\circ$ ,  $Re = 2.5 \times 10^7$ .

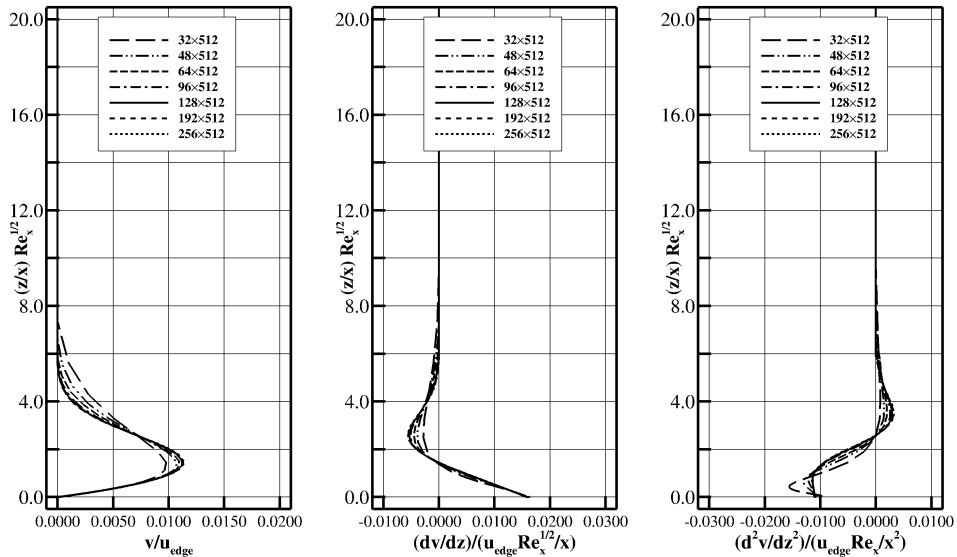


Figure 22: Grid convergence, cross flow velocity profiles at  $x/c = 0.25$ , NACA 64<sub>2</sub>-A-015,  $\Lambda = 10.0^\circ$ ,  $\alpha = -2.0^\circ$ ,  $Re = 2.5 \times 10^7$ .

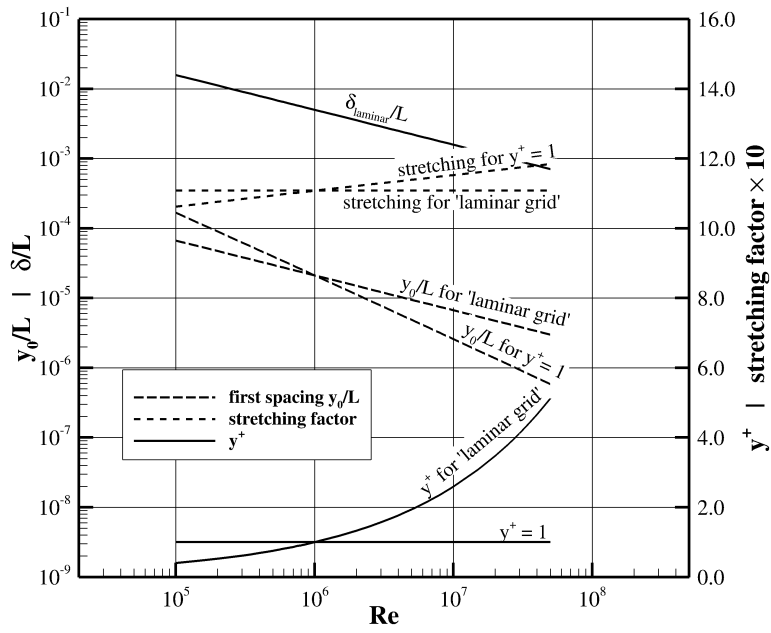


Figure 23: Comparison of grid parameters, flat plate.

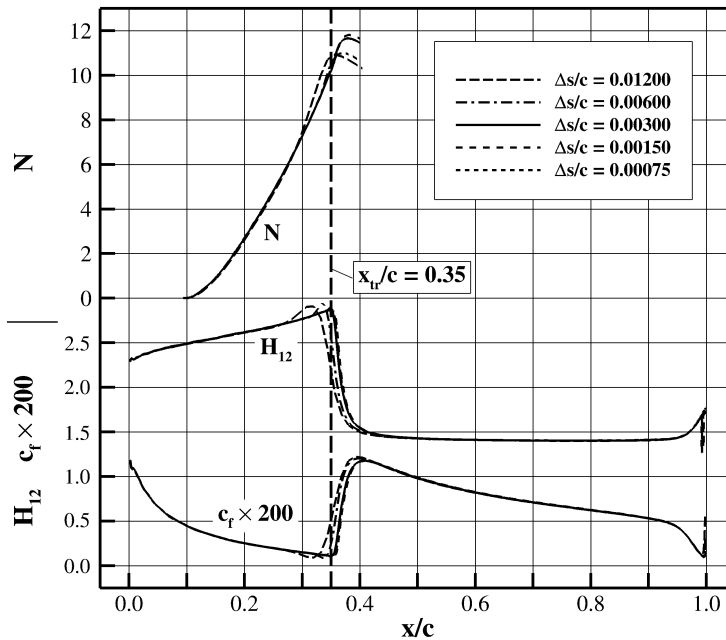


Figure 24: Grid convergence, skin friction, shape factor and  $N$ -factor, NLF (1)-0416,  $\alpha = 2.0^\circ$ ,  $Re = 4.0 \times 10^6$ , upper surface.

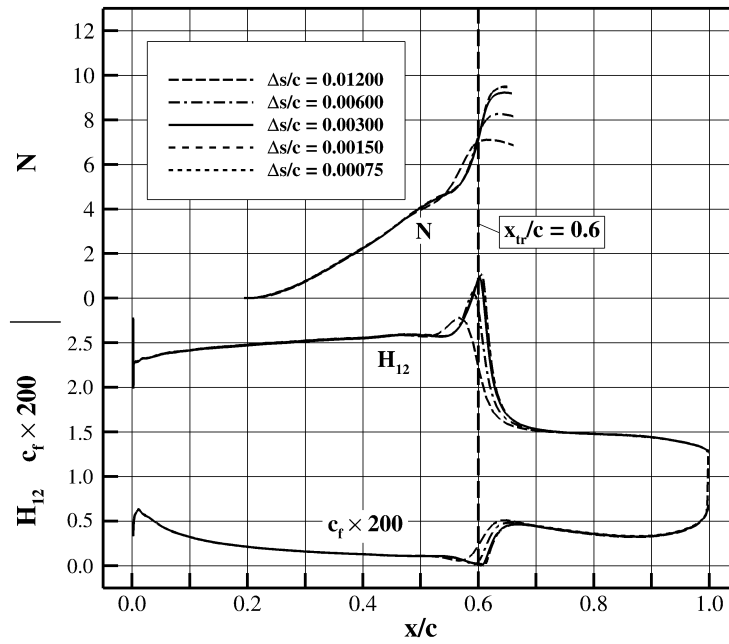


Figure 25: Grid convergence, skin friction, shape factor and  $N$ -factor, NLF (1)-0416,  $\alpha = 2.0^\circ$ ,  $Re = 4.0 \times 10^6$ , lower surface.

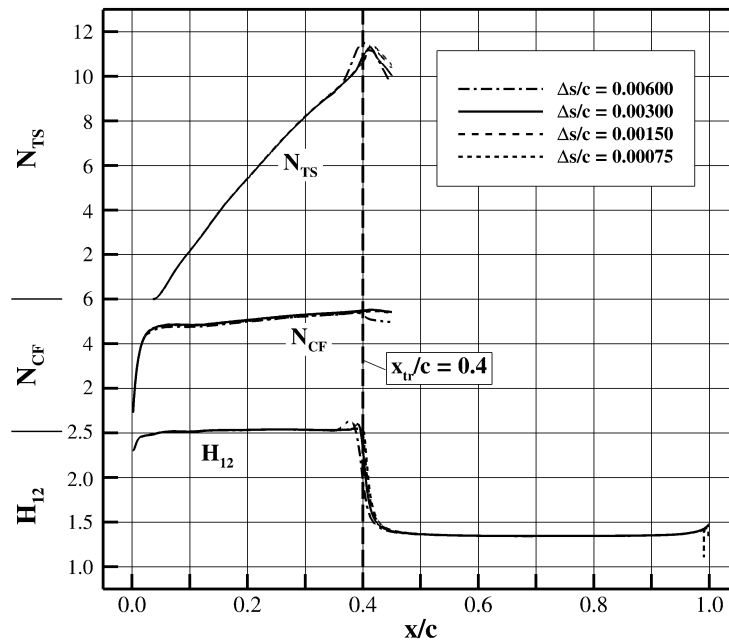


Figure 26: Grid convergence, shape factor and  $N$ -factors, NACA 642-A-015,  $\Lambda = 30.0^\circ$ ,  $\alpha = 0.5^\circ$ ,  $Re = 1.5 \times 10^7$ .

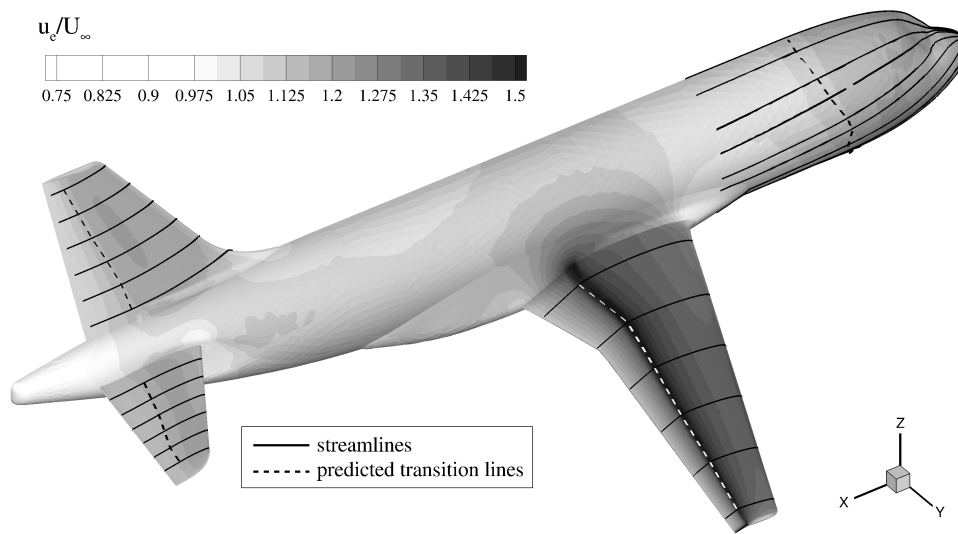


Figure 27: Edge streamlines and transition locations, upper surfaces, generic transport aircraft,  $\alpha = -4.0^\circ$ ,  $Re = 2.3 \times 10^6$ ,  $i_H = 4.0^\circ$ .

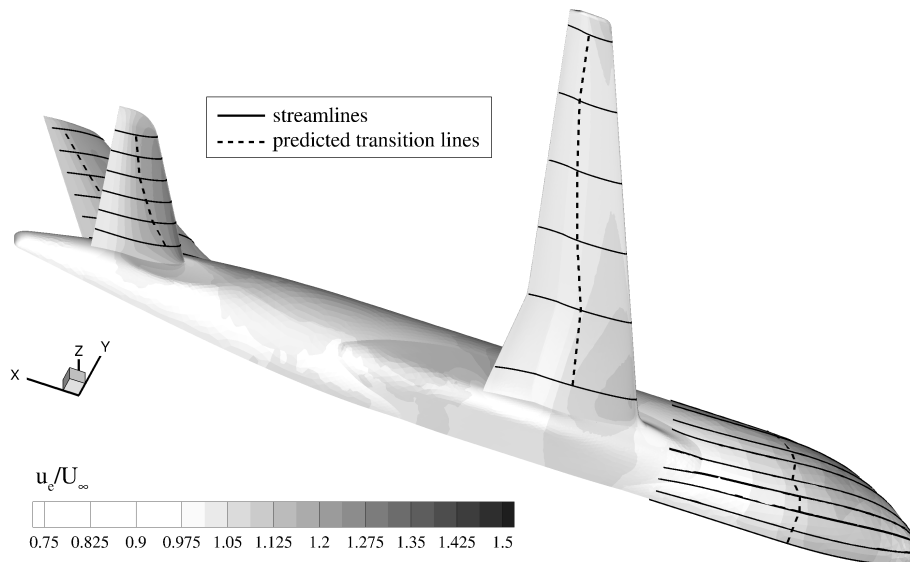


Figure 28: Edge streamlines and transition locations, lower surfaces, generic transport aircraft,  $\alpha = -4.0^\circ$ ,  $Re = 2.3 \times 10^6$ ,  $i_H = 4.0^\circ$ .

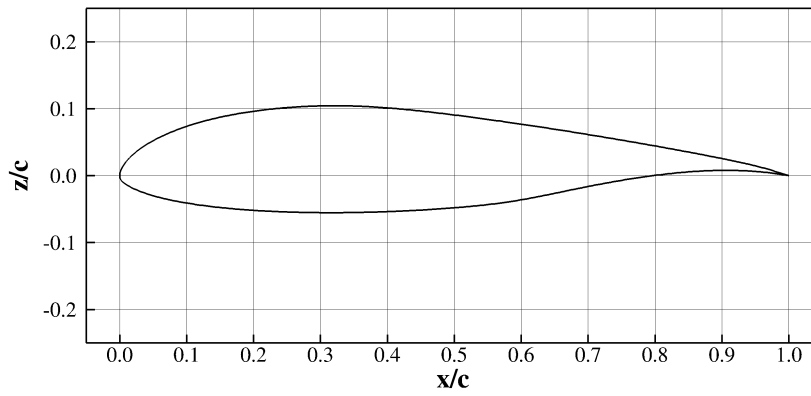


Figure 29: NLF (1)-0416 airfoil.

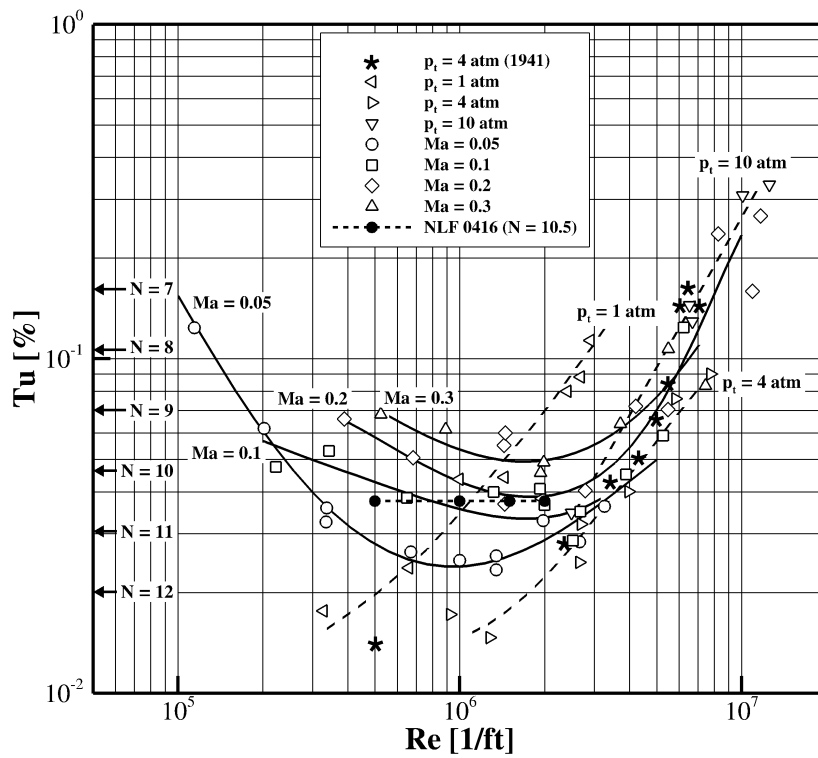
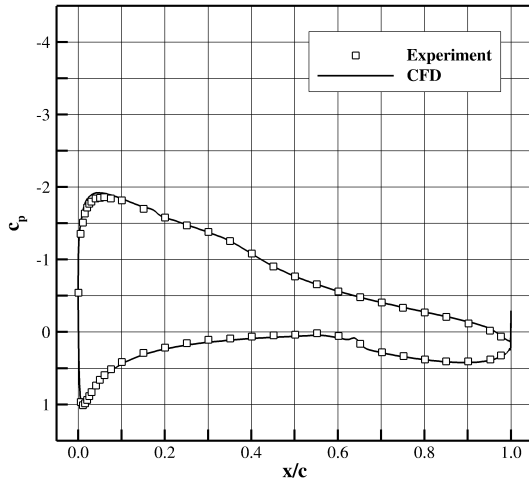
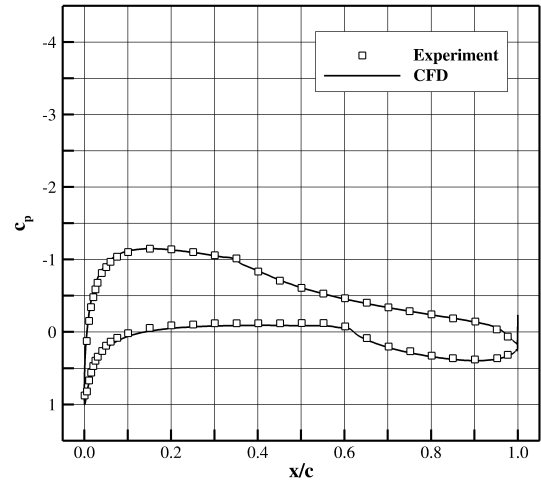
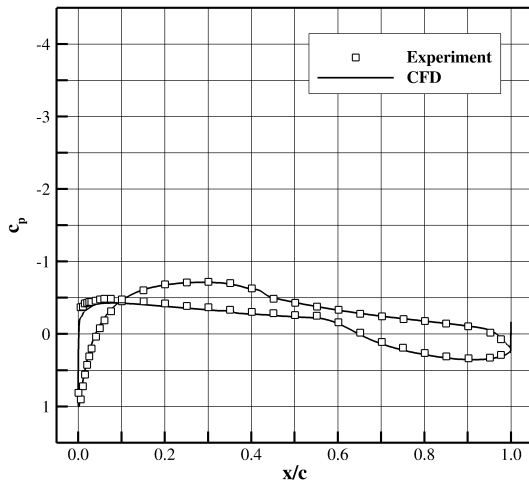
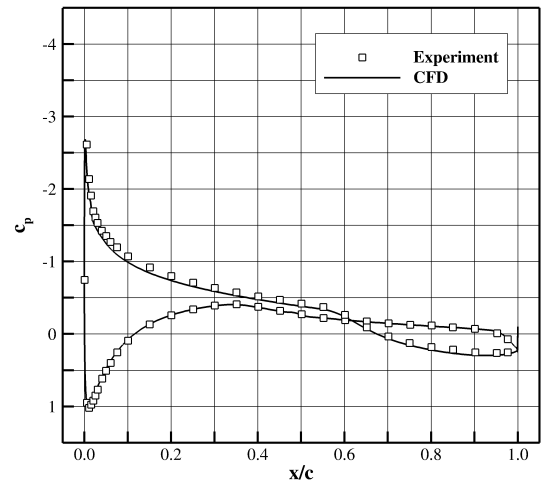


Figure 30: Test section turbulence levels, Langley Research Center Low-Turbulence Pressure Tunnel.

(a)  $\alpha = 6.0^\circ$ (b)  $\alpha = 2.0^\circ$ (c)  $\alpha = -2.0^\circ$ (d)  $\alpha = -6.0^\circ$ Figure 31: Pressure distribution, NLF (1)-0416 airfoil,  $Ma=0.1$ ,  $Re=4.0 \times 10^6$ .

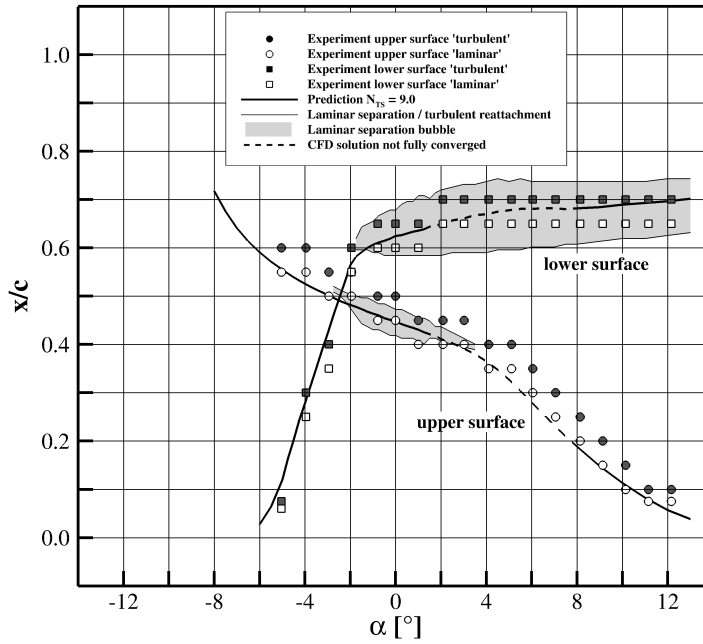


Figure 32: Predicted transition locations, NLF (1)-0416 airfoil,  $Ma=0.1$ ,  $Re=1.0 \times 10^6$ .

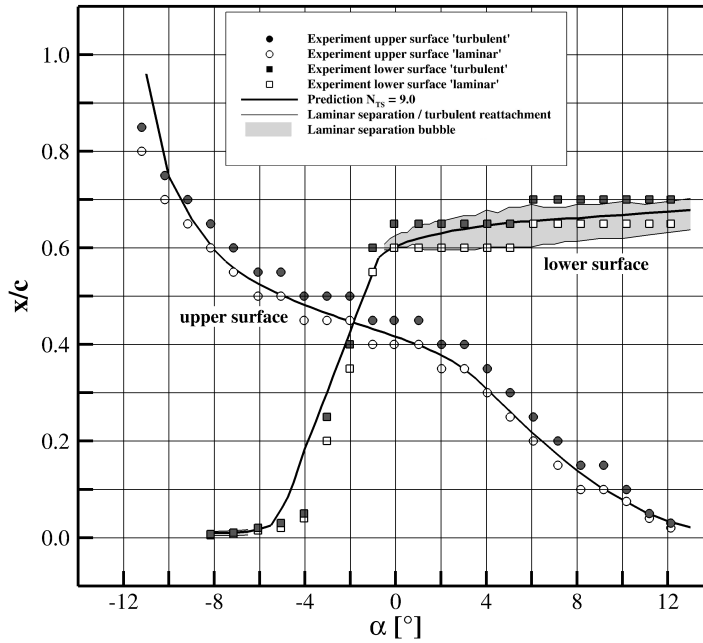


Figure 33: Predicted transition locations, NLF (1)-0416 airfoil,  $Ma=0.1$ ,  $Re=2.0 \times 10^6$ .

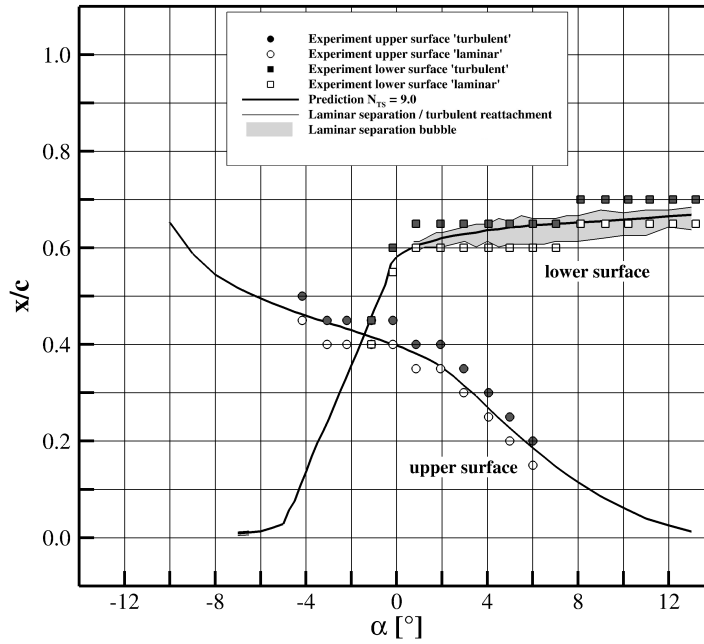


Figure 34: Predicted transition locations, NLF (1)-0416 airfoil,  $Ma=0.1$ ,  $Re=3.0 \times 10^6$ .

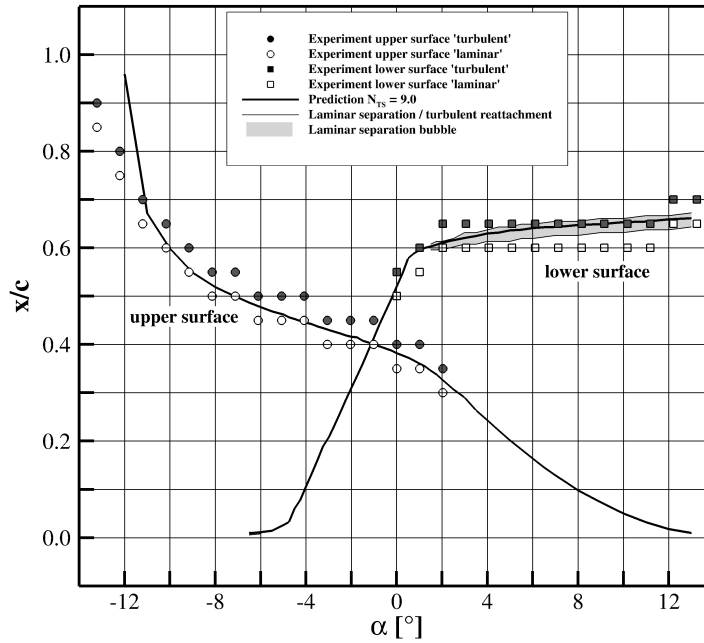


Figure 35: Predicted transition locations, NLF (1)-0416 airfoil,  $Ma=0.1$ ,  $Re=4.0 \times 10^6$ .

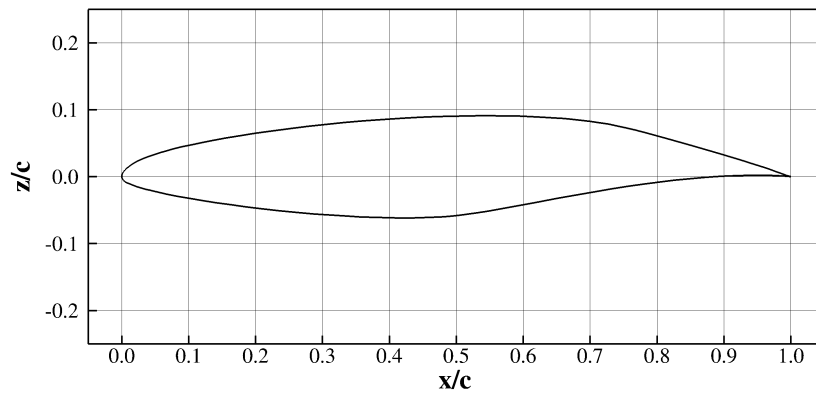
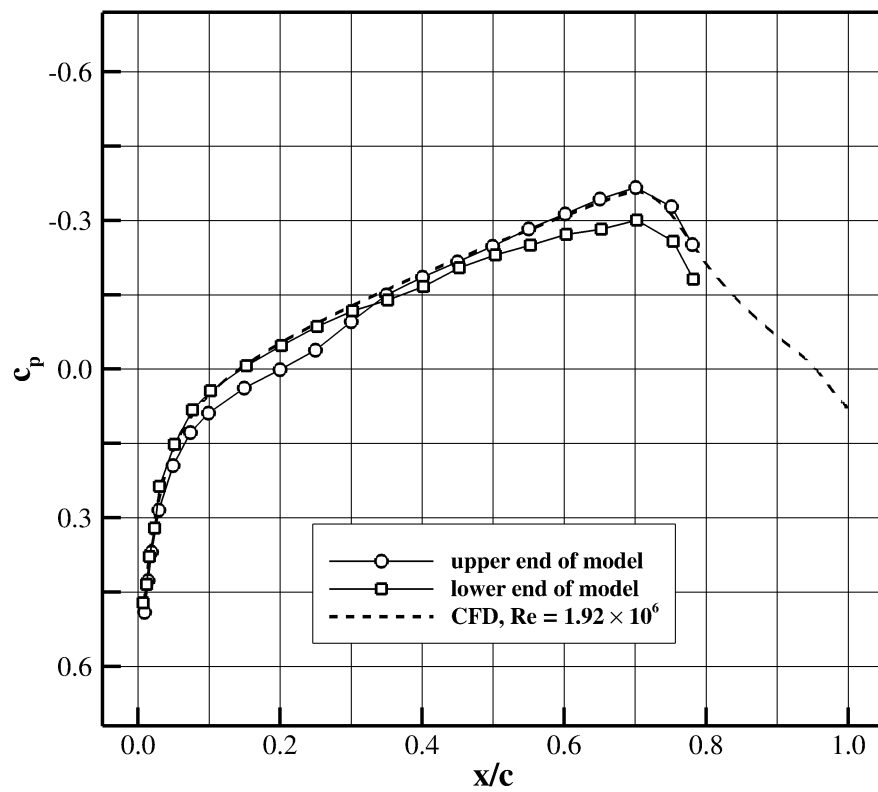


Figure 36: NLF (2)-0415 airfoil.

Figure 37: Pressure distribution, NLF (2)-0415 airfoil,  $Re = 1.93 \times 10^6$ .

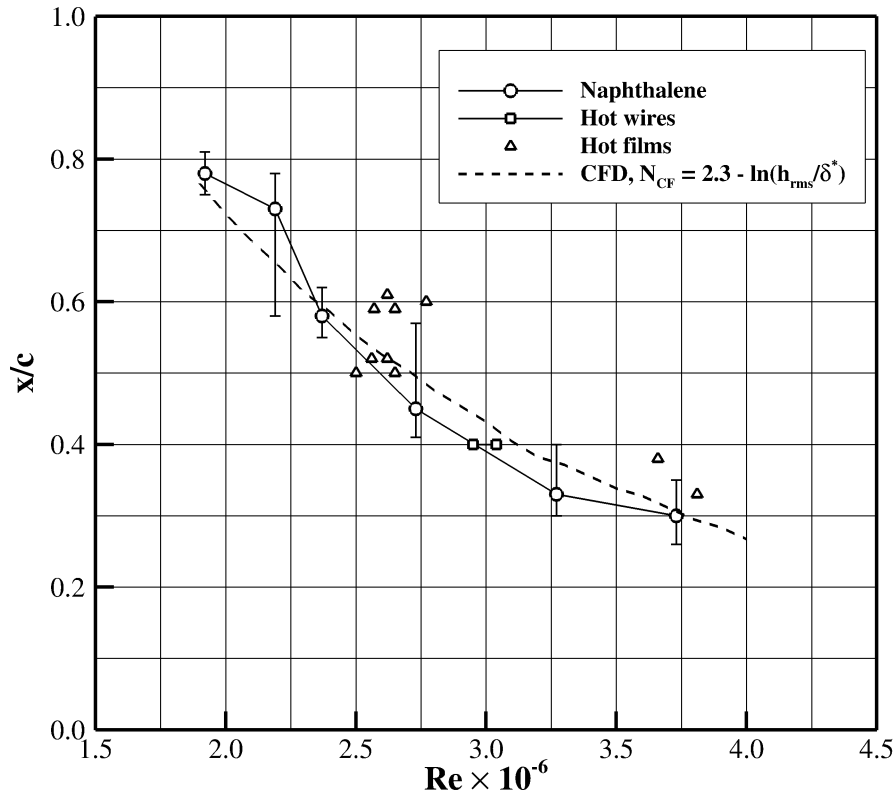


Figure 38: Predicted transition locations, NLF (2)-0415 airfoil.

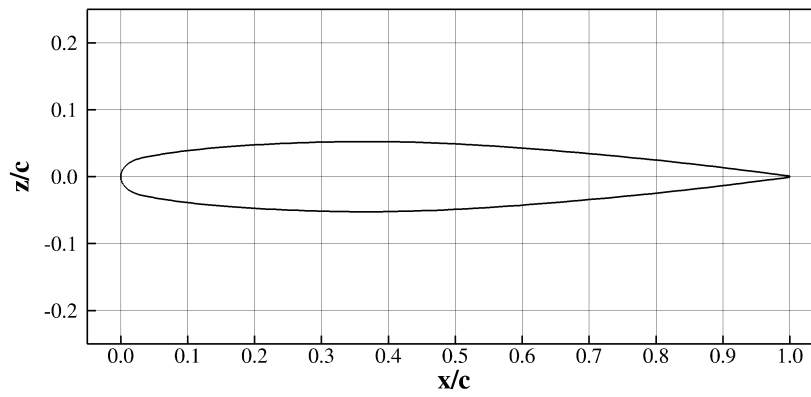


Figure 39: ONERA D airfoil.

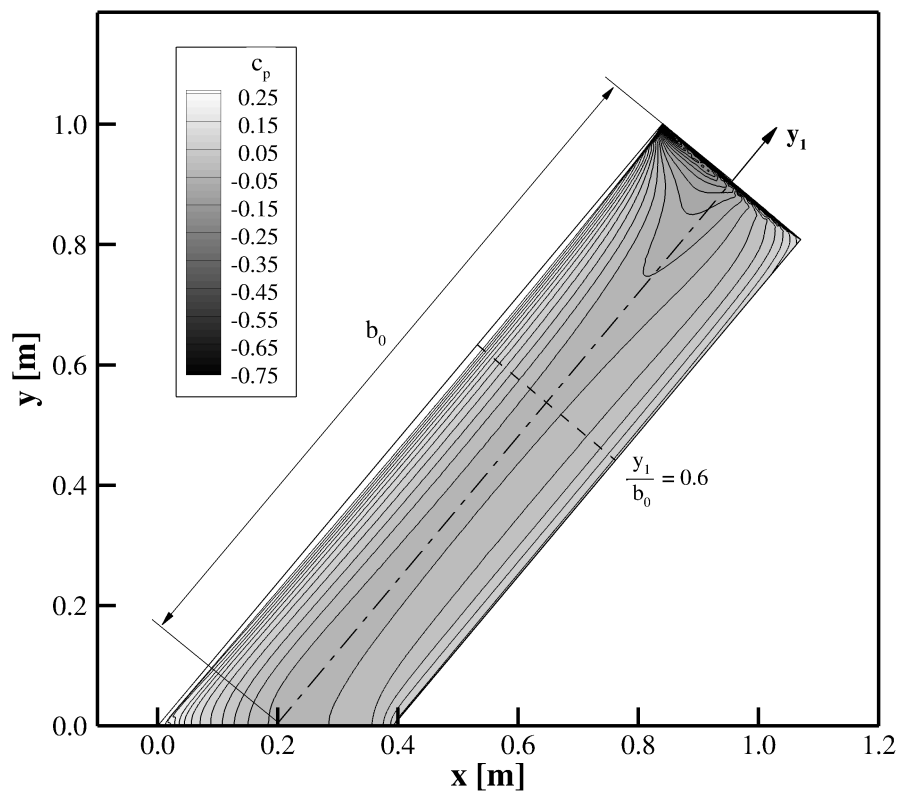
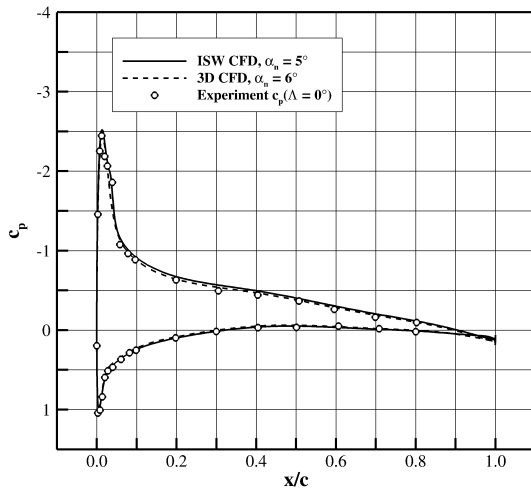
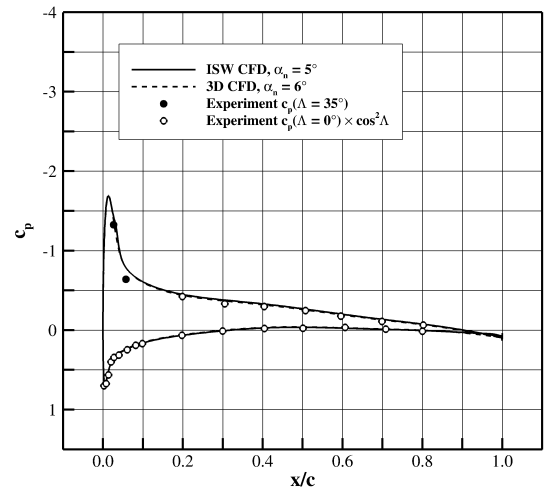
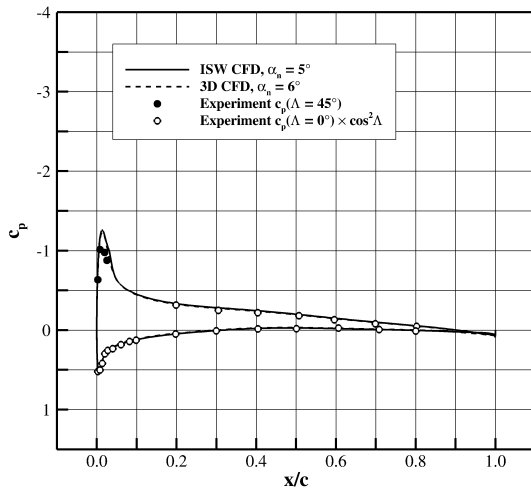
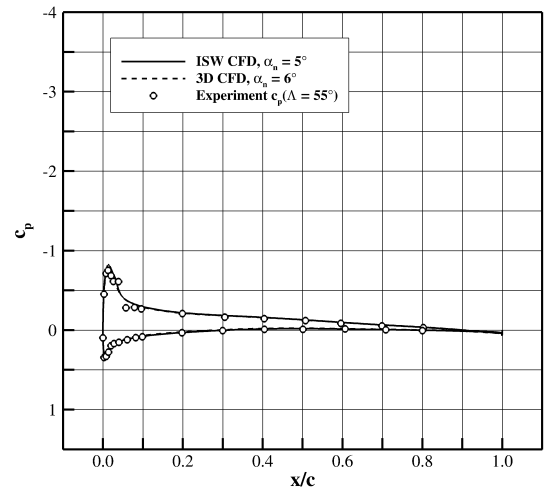


Figure 40: Wing with ONERA D profile, pressure distribution, pressure side,  $\alpha_n = 6.0^\circ$ ,  $Re = 0.4 \times 10^6$ ,  $\Lambda = 40.0^\circ$ .

(a)  $\Lambda = 0.0^\circ$ (b)  $\Lambda = 35.0^\circ$ (c)  $\Lambda = 45.0^\circ$ (d)  $\Lambda = 55.0^\circ$ Figure 41: Pressure distribution, ONERA D,  $Re = 0.4 \times 10^6$ .

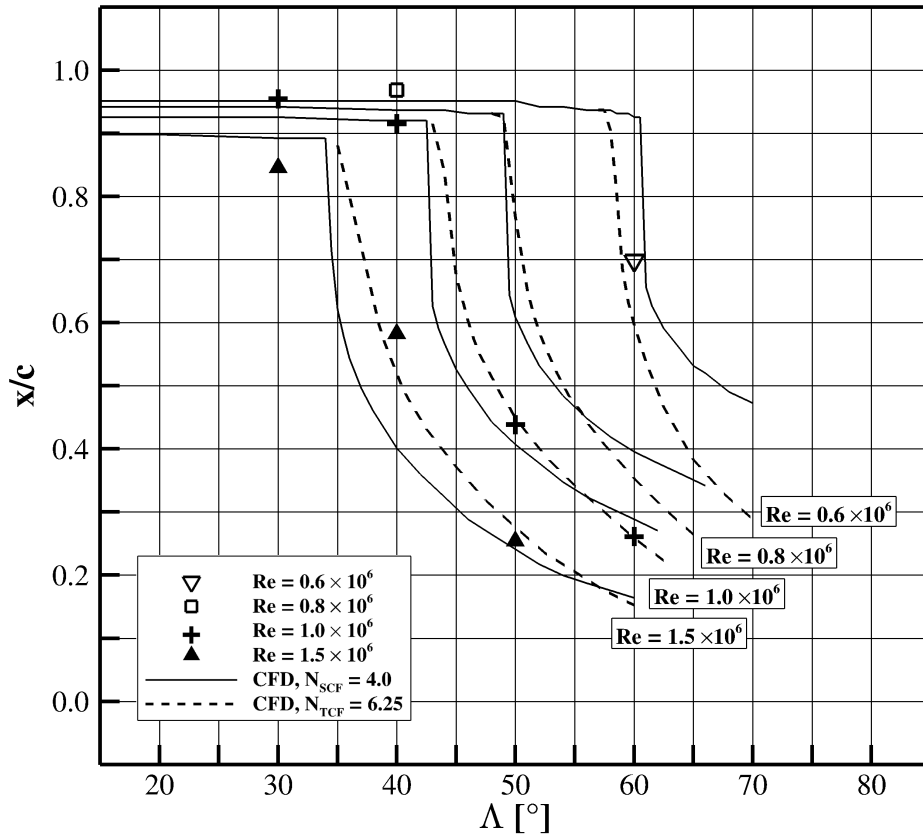
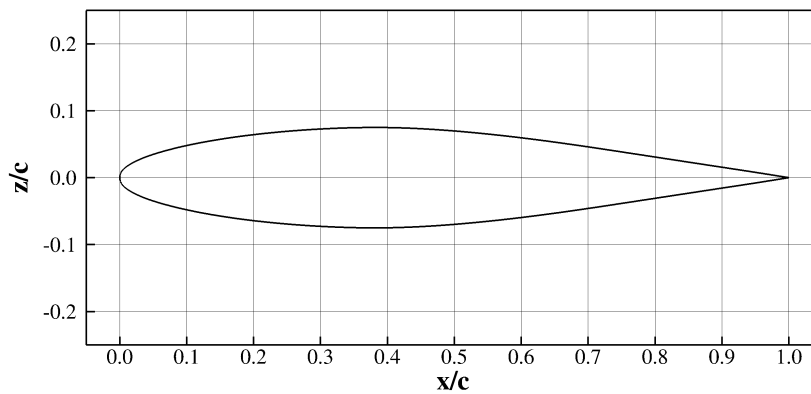


Figure 42: Predicted transition locations, ONERA D.

Figure 43: NACA 64<sub>2</sub>-A-015 airfoil.

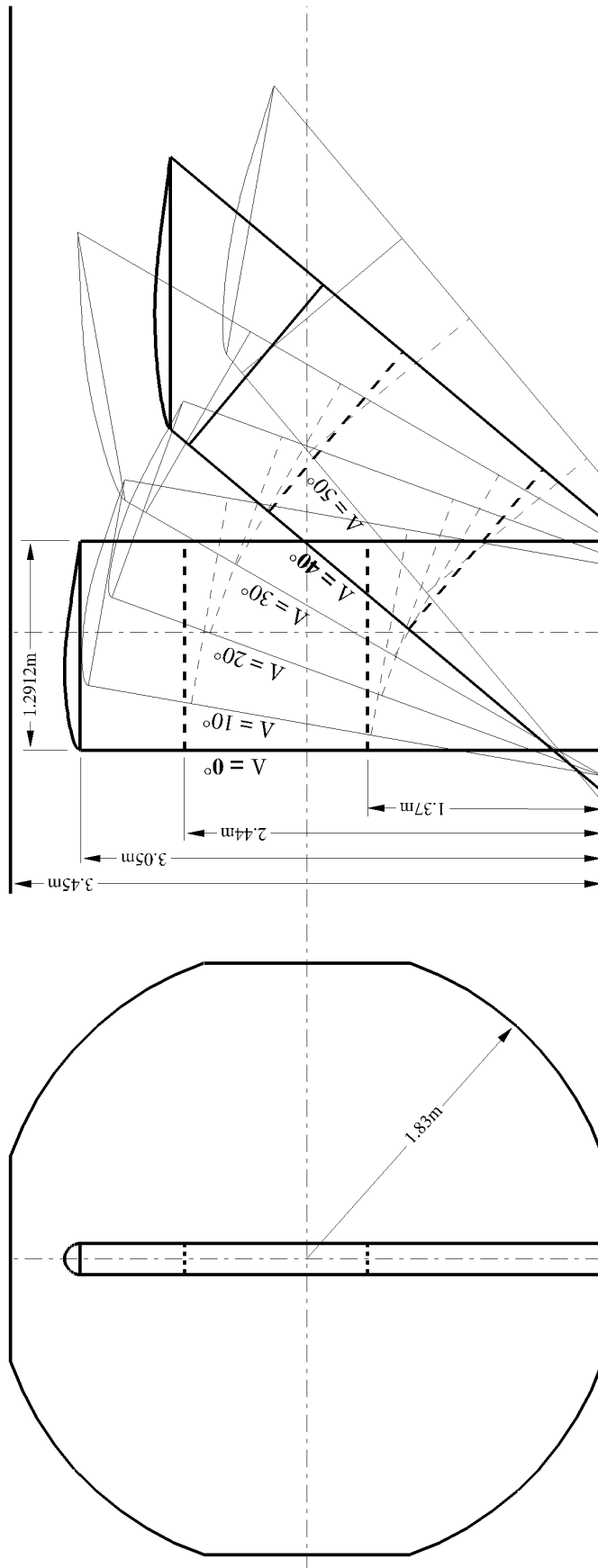


Figure 44: Geometry, NACA 642-A-015 wing, NASA Ames 12-foot low-turbulence pressure tunnel (figure adapted from reference [86]).

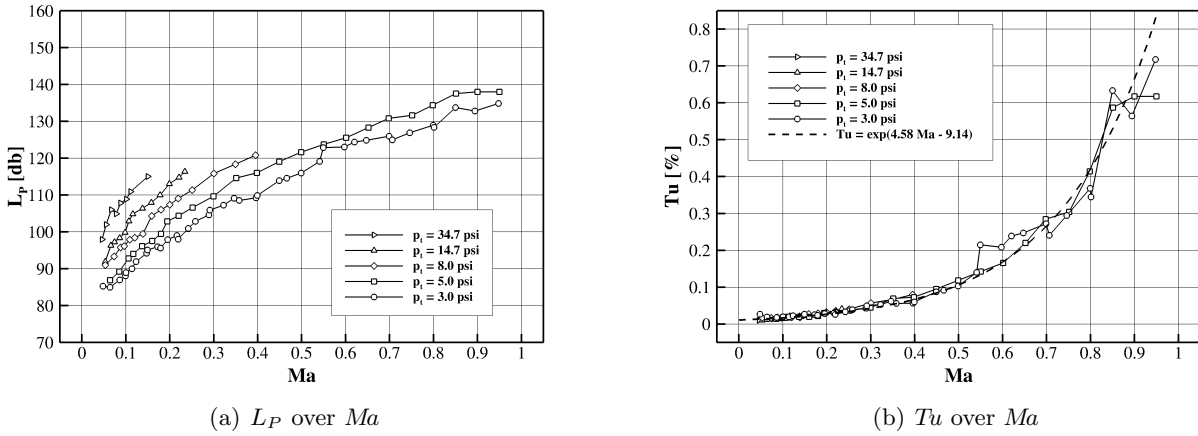


Figure 45: Sound pressure level and acoustic equivalent turbulence intensity, dependency on Mach number, NASA Ames 12-foot low-turbulence pressure tunnel.

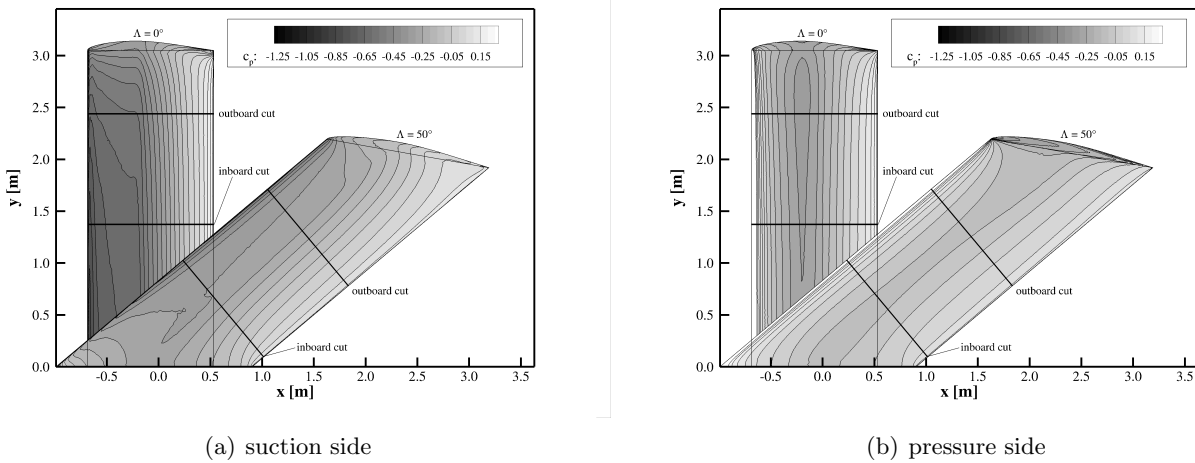
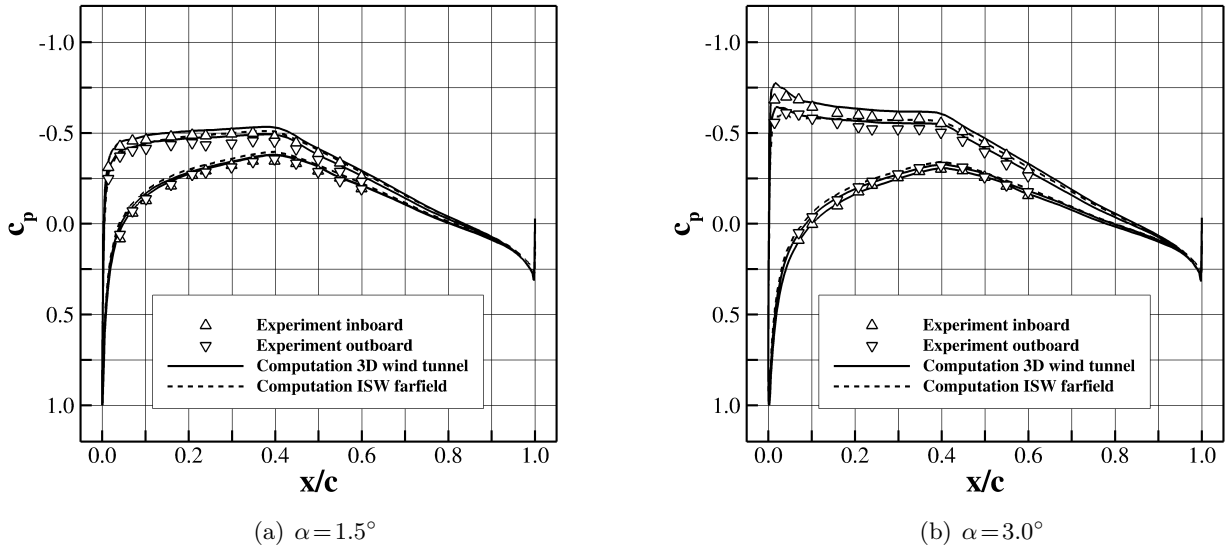
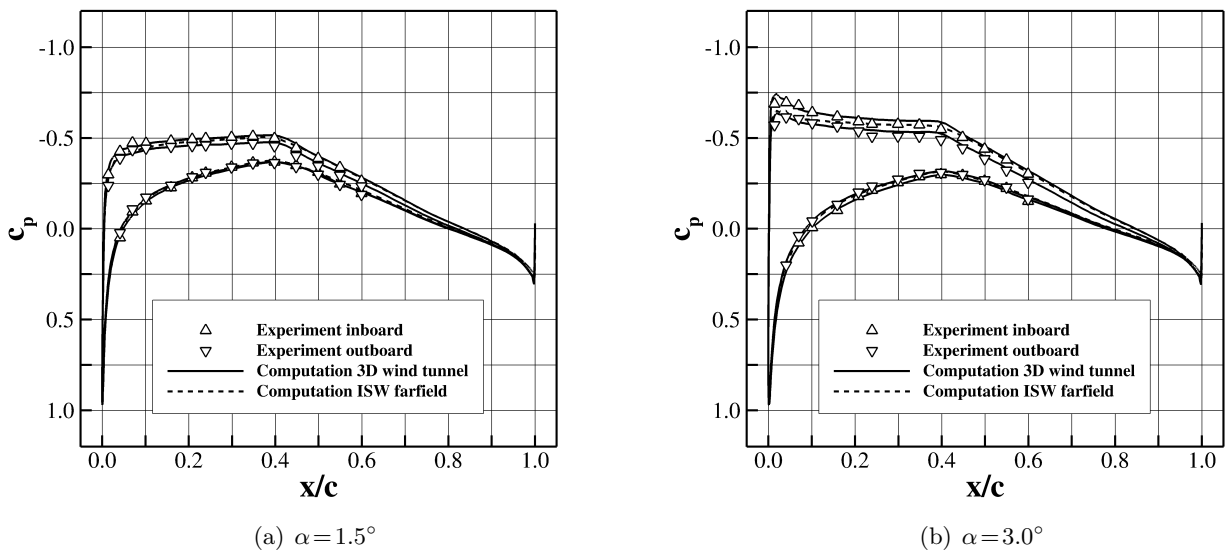
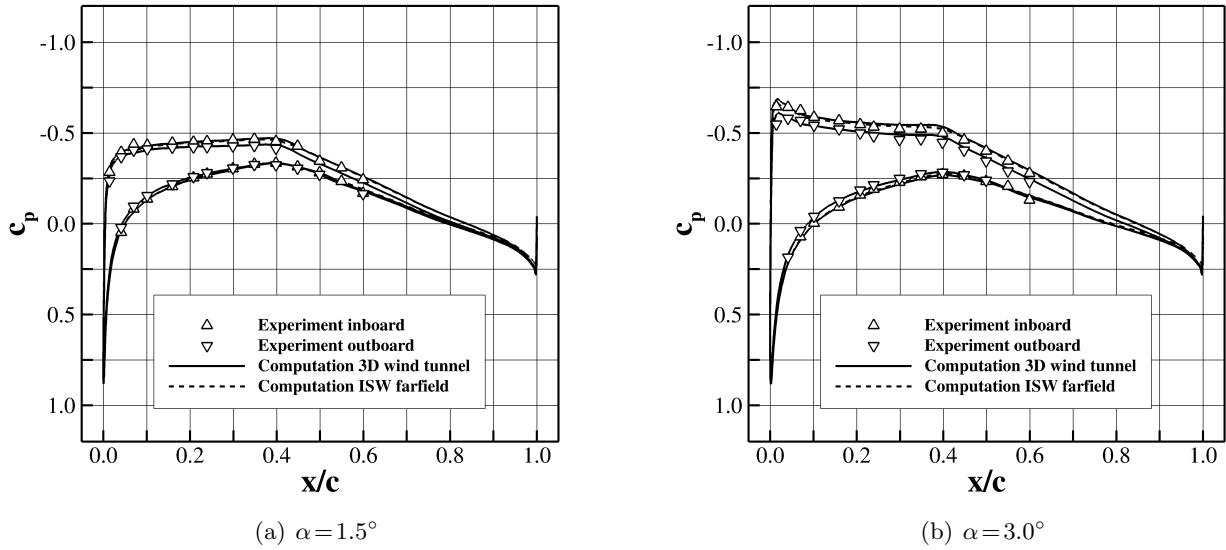
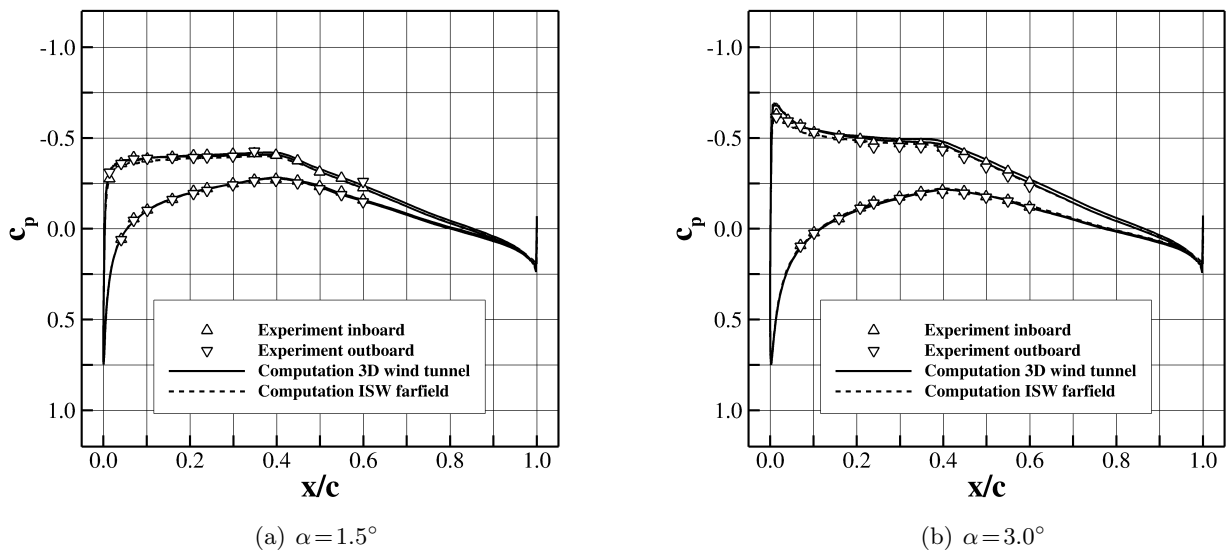
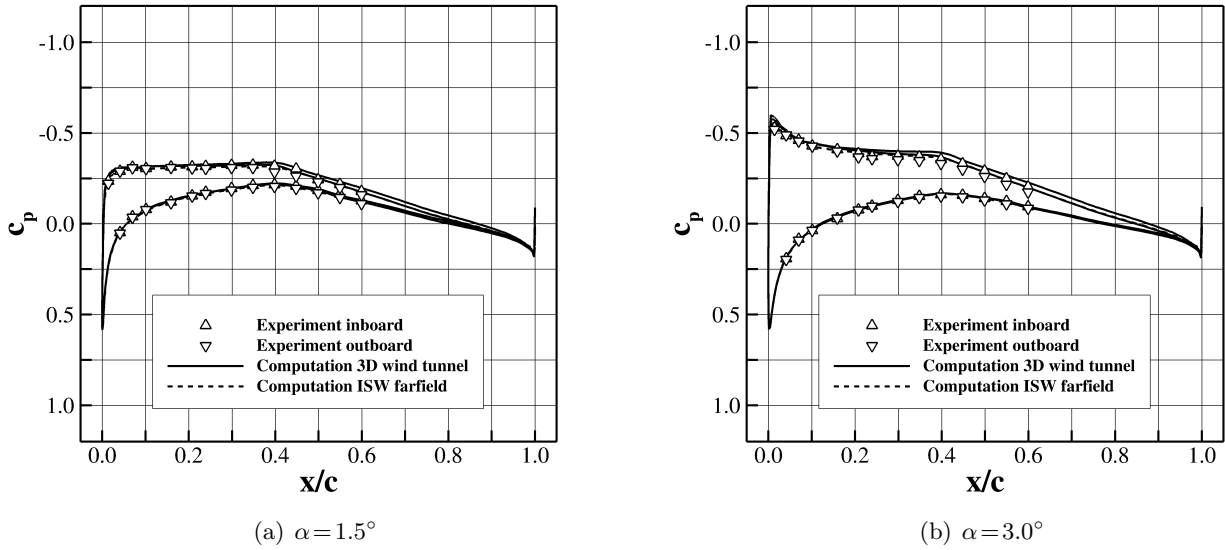
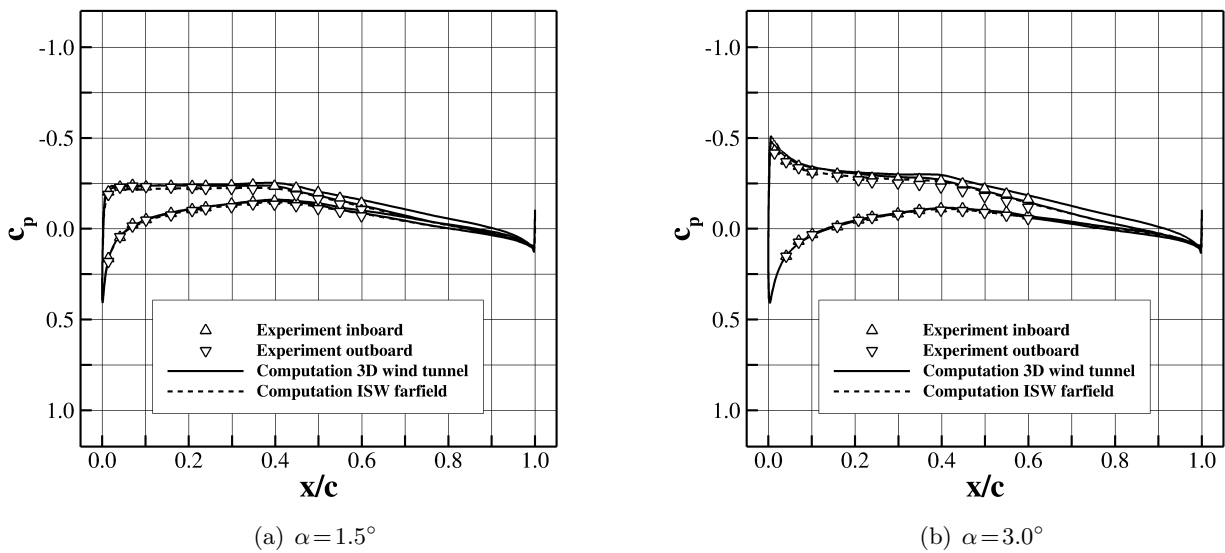
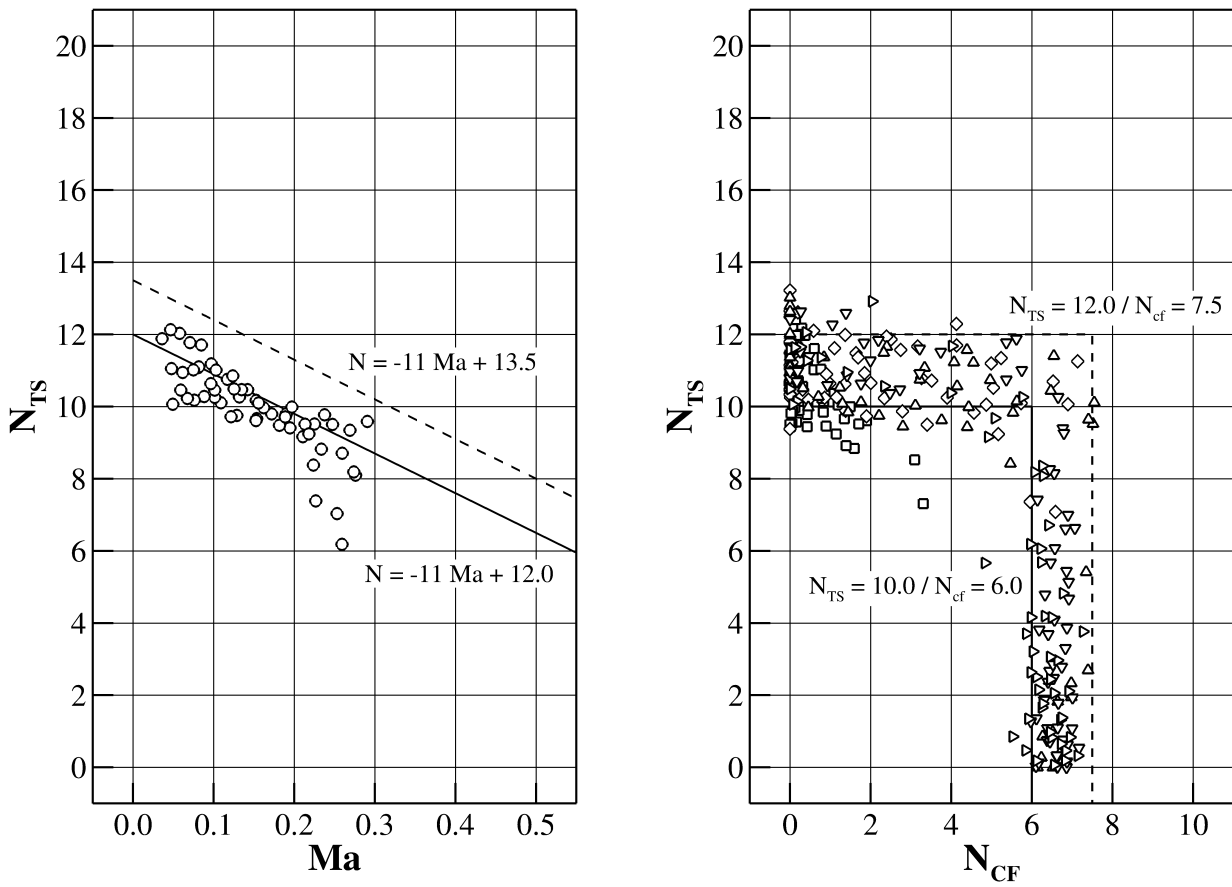


Figure 46: Pressure distribution, NACA 64<sub>2</sub>-A-015 wing,  $\Lambda = 0.0^\circ$  and  $\Lambda = 50.0^\circ$ ,  $Re = 7.2 \times 10^6$ ,  $\alpha = 3.0^\circ$ .

Figure 47: Pressure distribution, NACA 64<sub>2</sub>-A-015,  $Re = 7.2 \times 10^6$ ,  $\Lambda = 0.0^\circ$ .Figure 48: Pressure distribution, NACA 64<sub>2</sub>-A-015,  $Re = 7.2 \times 10^6$ ,  $\Lambda = 10.0^\circ$ .

Figure 49: Pressure distribution, NACA 64<sub>2</sub>-A-015,  $Re = 7.2 \times 10^6$ ,  $\Lambda = 20.0^\circ$ .Figure 50: Pressure distribution, NACA 64<sub>2</sub>-A-015,  $Re = 7.2 \times 10^6$ ,  $\Lambda = 30.0^\circ$ .

Figure 51: Pressure distribution, NACA 64<sub>2</sub>-A-015,  $Re = 7.2 \times 10^6$ ,  $\Lambda = 40.0^\circ$ .Figure 52: Pressure distribution, NACA 64<sub>2</sub>-A-015,  $Re = 7.2 \times 10^6$ ,  $\Lambda = 50.0^\circ$ .

(a)  $N_{TS}$  over  $Ma$ ,  $\Lambda = 0^\circ$ (b)  $N_{TS}$  over  $N_{CF}$ ,  $\Lambda = 10^\circ - 50^\circ$ Figure 53:  $N$ -factors at transition, NACA 64<sub>2</sub>-A-015.

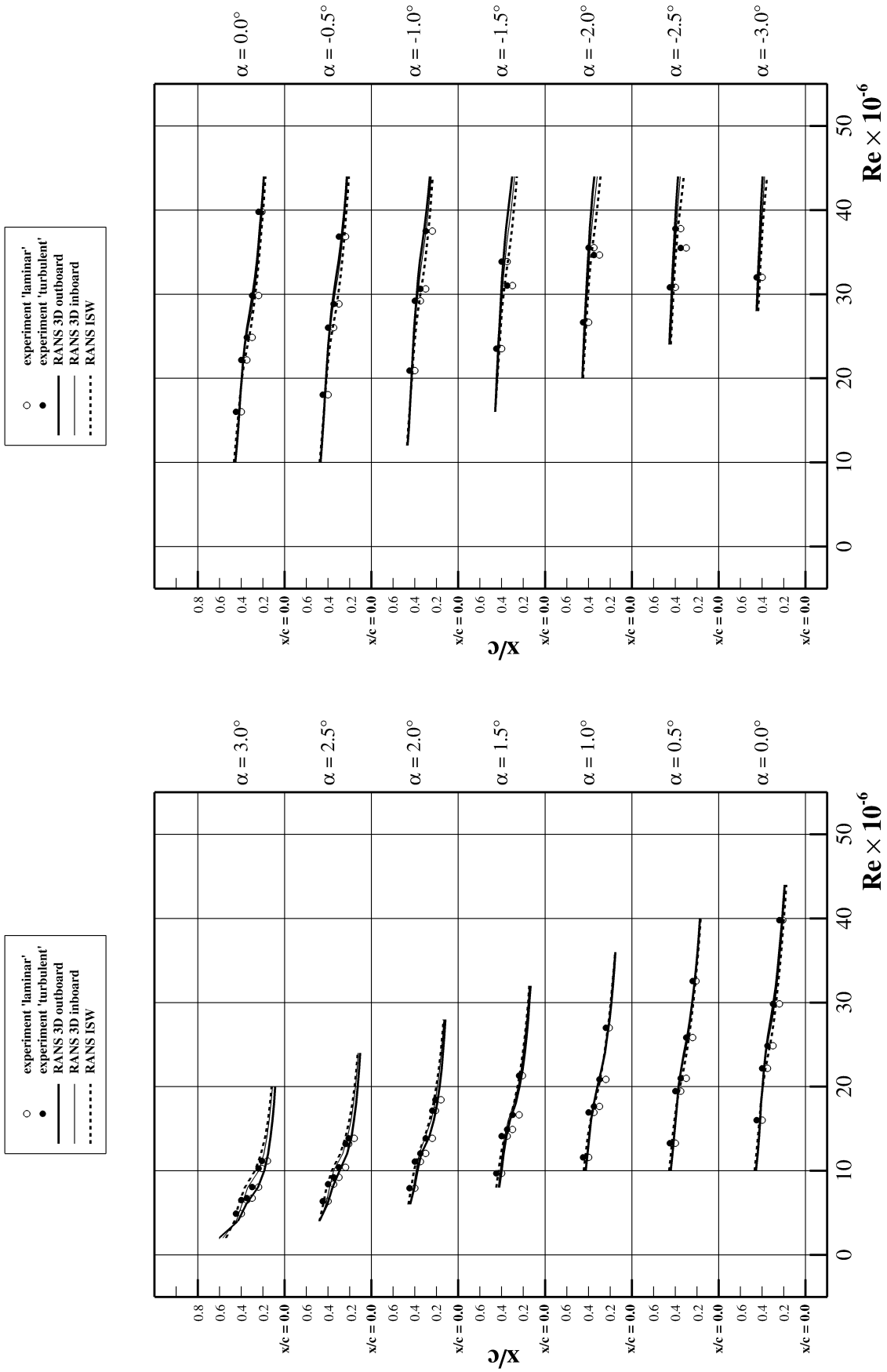


Figure 54: Predicted transition locations, NACA 642-A-015,  $\Lambda = 0.0^\circ$ .

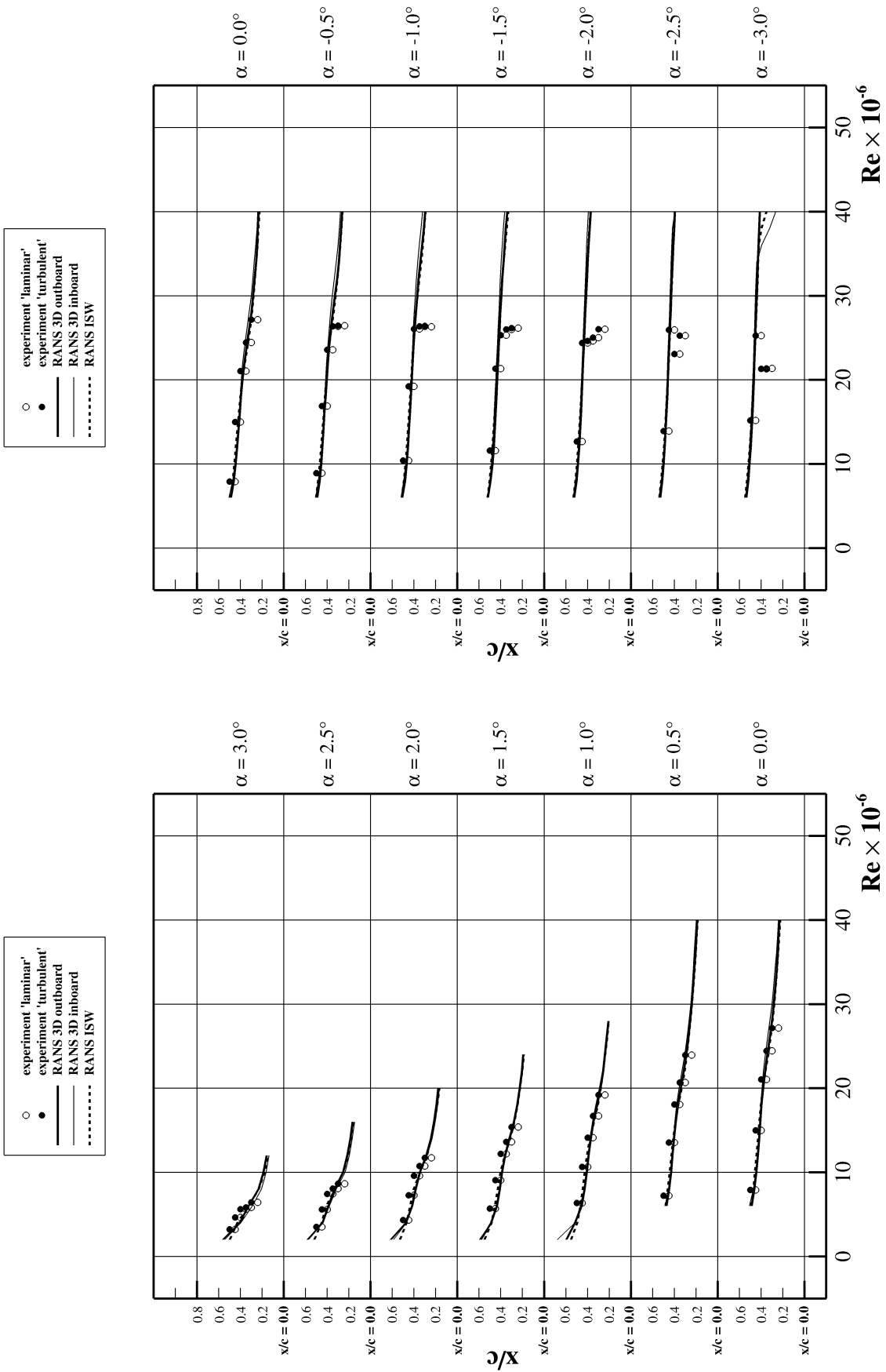


Figure 55: Predicted transition locations, NACA 64<sub>2</sub>-A-015,  $\Lambda = 10.0^\circ$ .

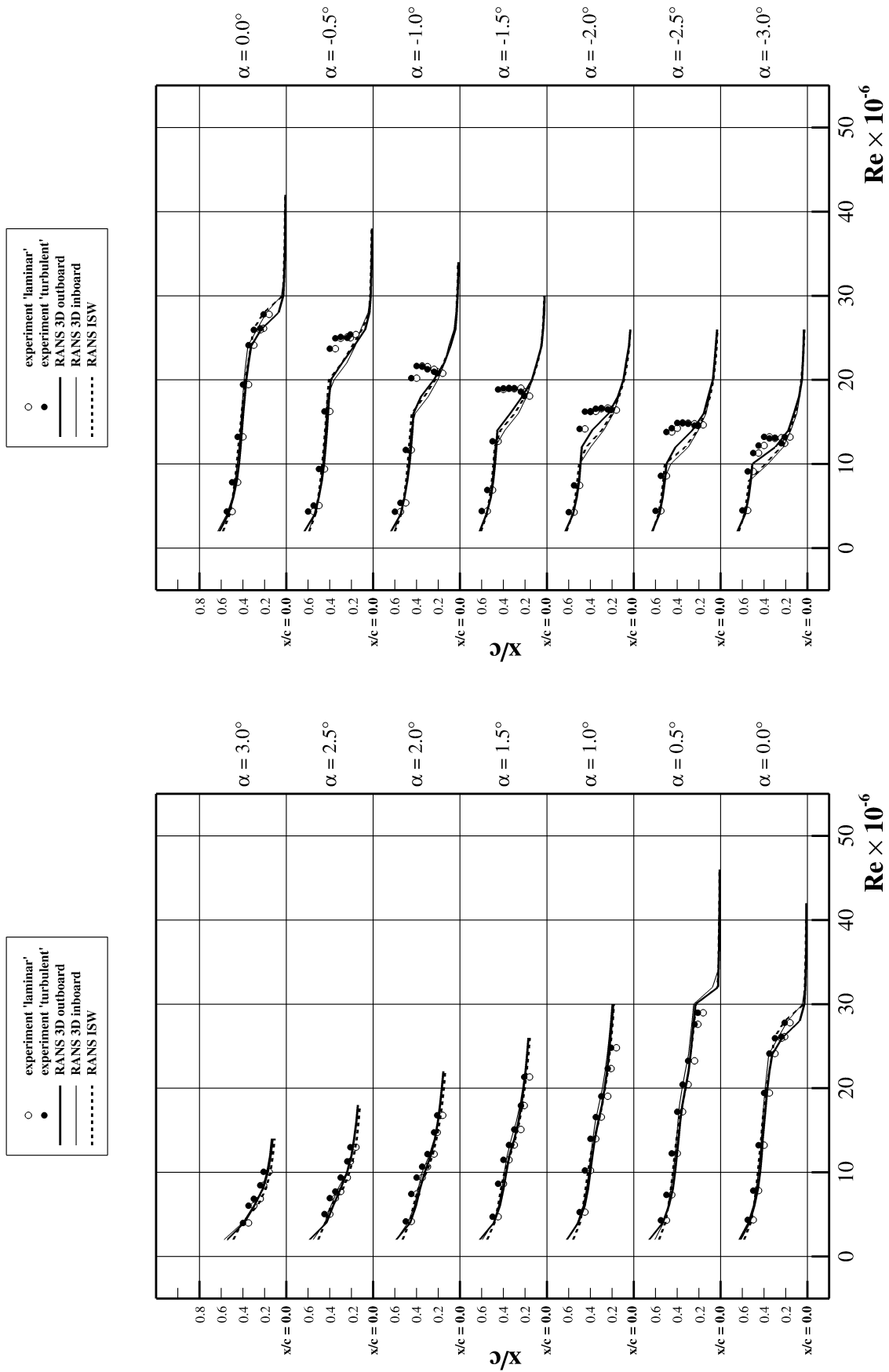


Figure 56: Predicted transition locations, NACA 64<sub>2</sub>-A-015,  $\Lambda = 20.0^\circ$ .

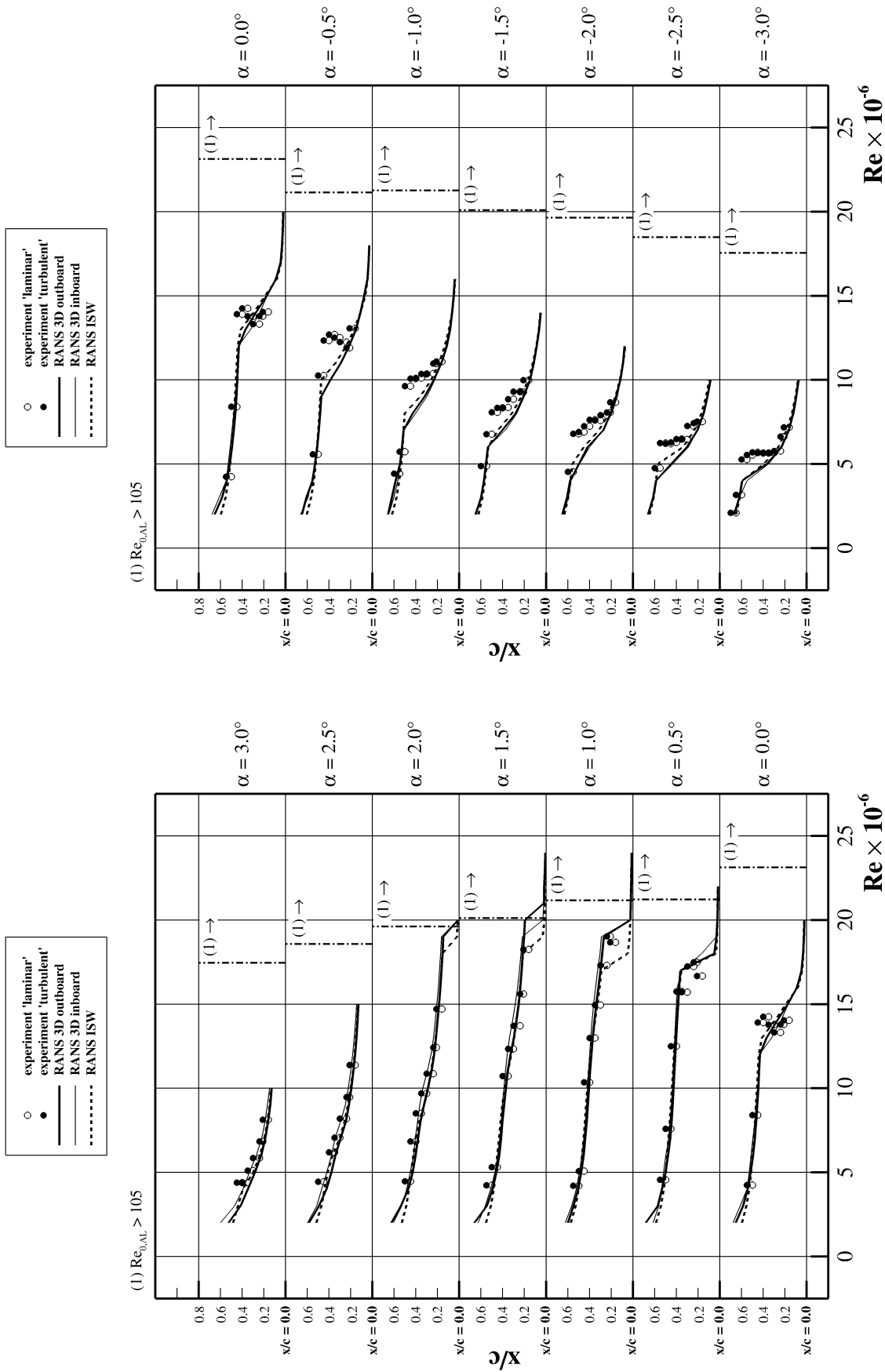


Figure 57: Predicted transition locations, NACA 642-A-015,  $\Lambda = 30.0^\circ$ .

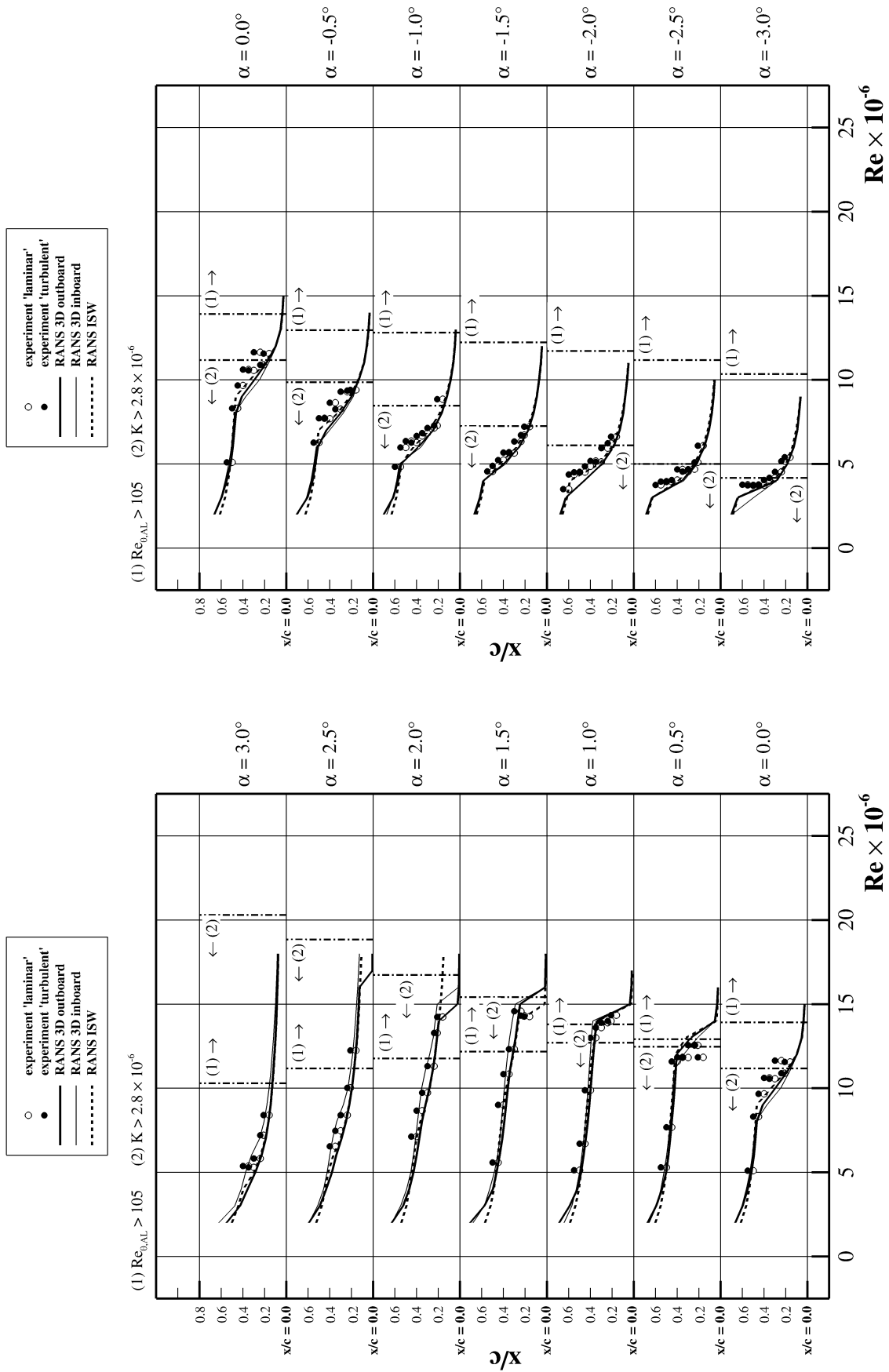


Figure 58: Predicted transition locations, NACA 642-A-015,  $\Lambda = 40.0^\circ$ .

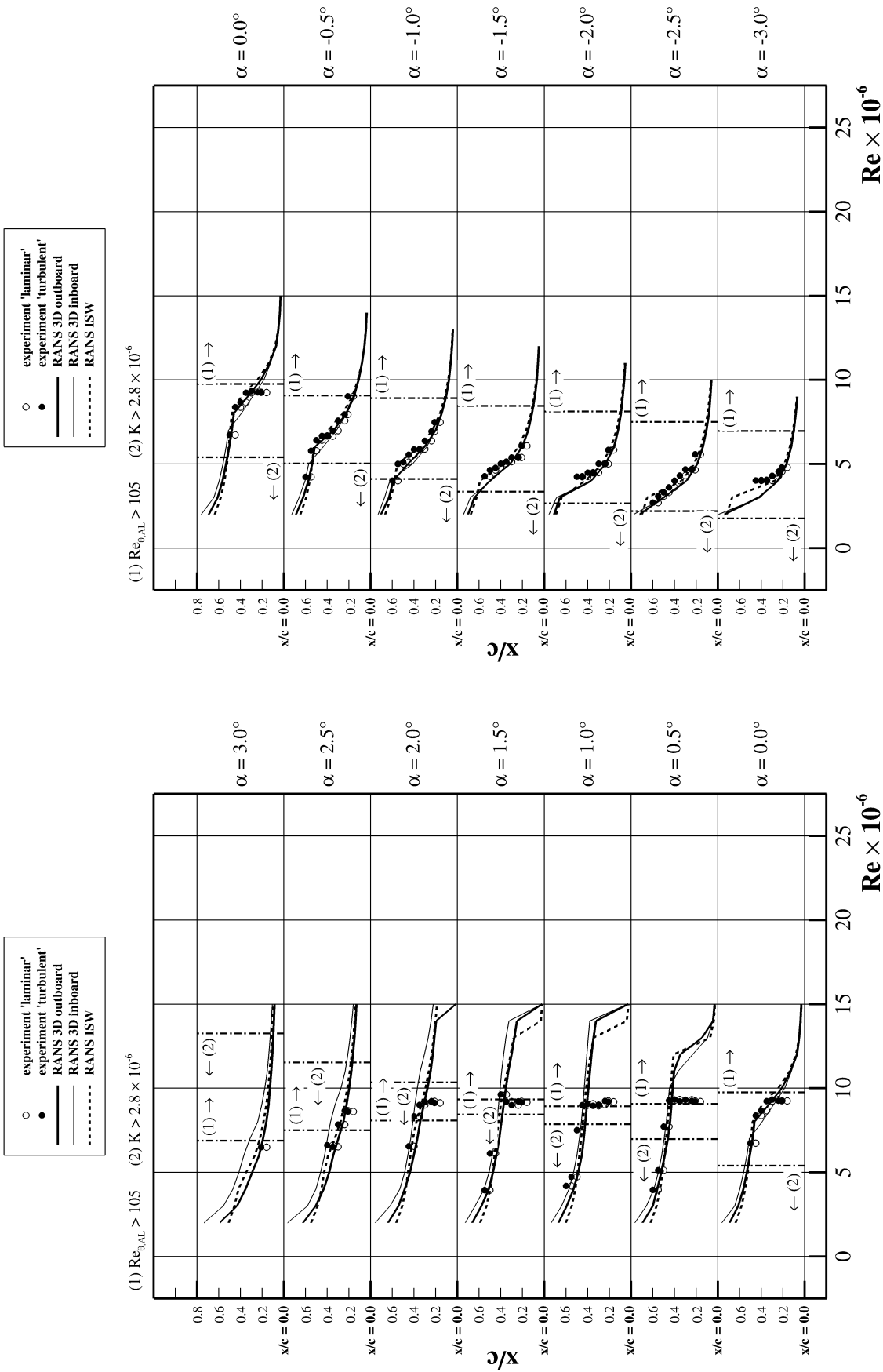


Figure 59: Predicted transition locations, NACA 642-A-015,  $\Lambda = 50.0^\circ$ .

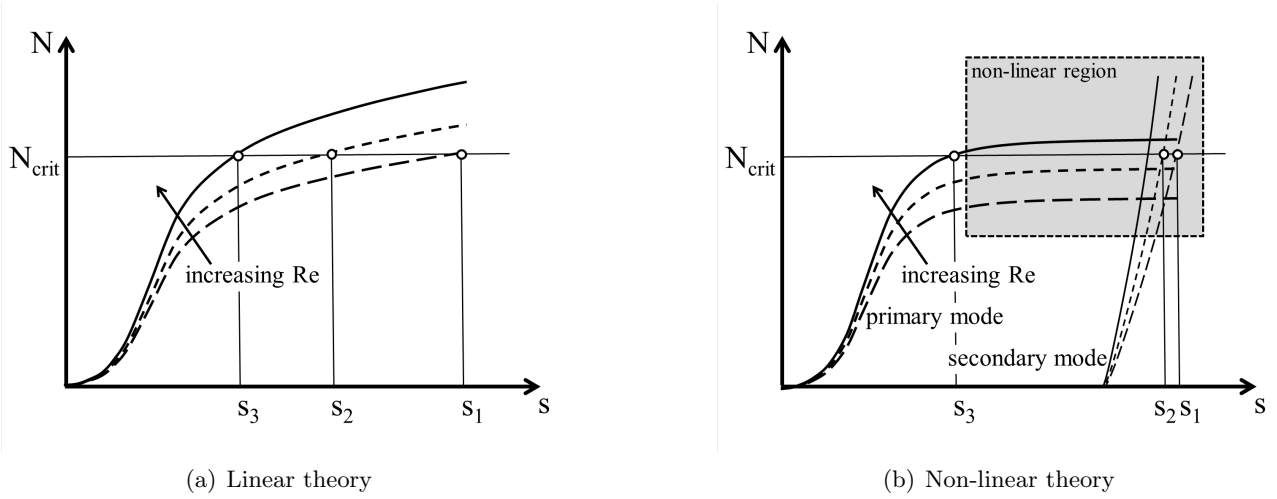


Figure 60: Schematic of cross-flow  $N$ -factor envelopes for different Reynolds numbers.

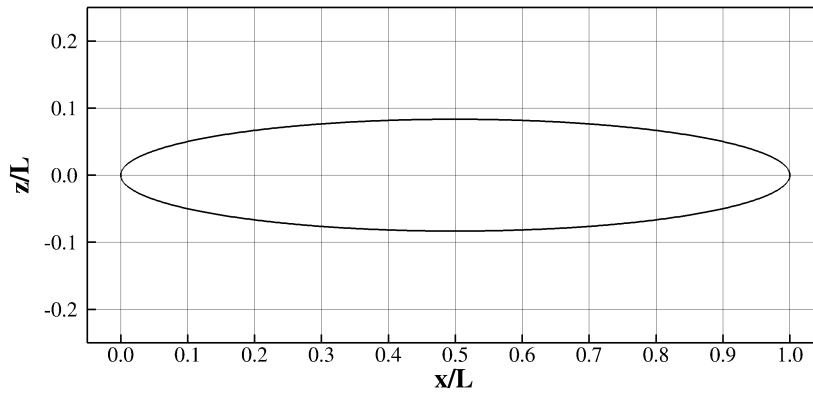


Figure 61: DLR prolate spheroid.

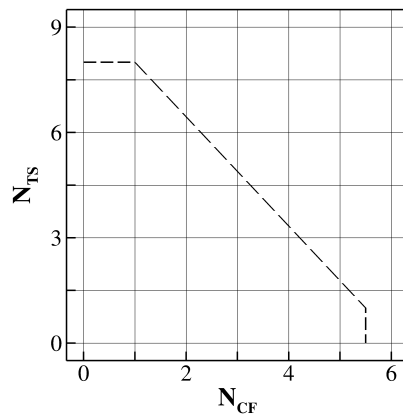


Figure 62: Stability diagram,  $N_{TS}$  over  $N_{CF}$ , DLR prolate spheroid.

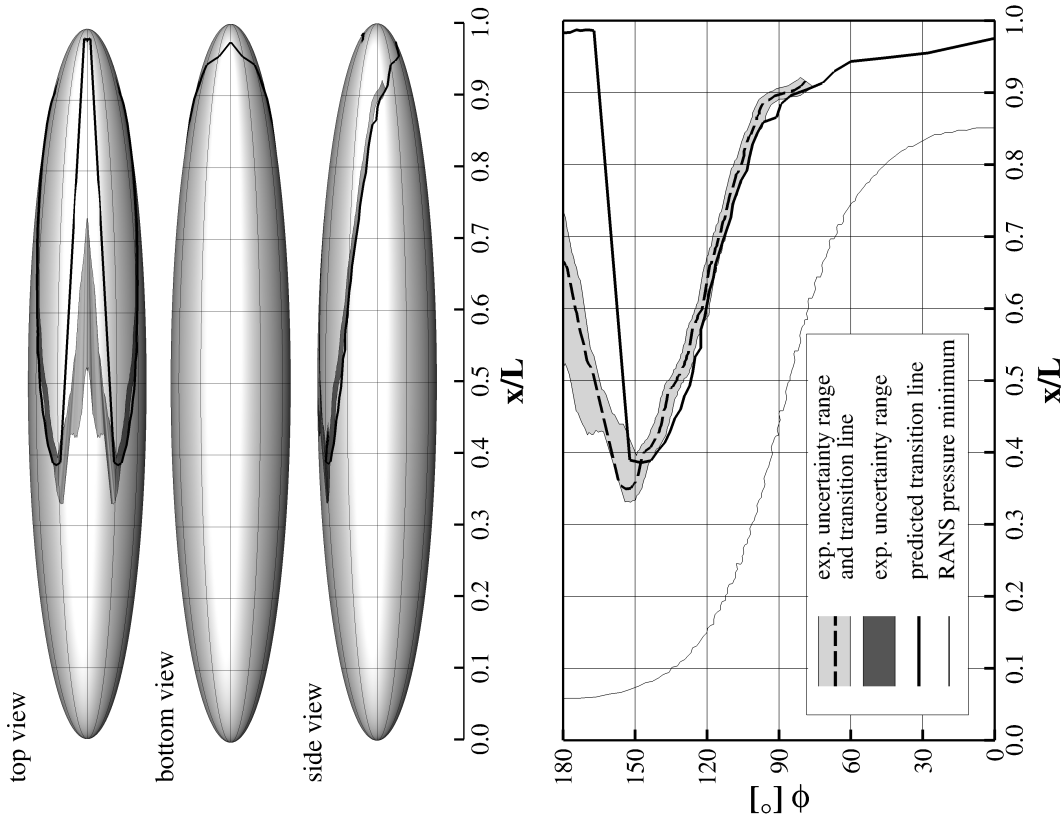


Figure 63: Predicted transition lines, DLR prolate spheroid,  $Re = 1.5 \times 10^6$ ,  $\alpha = 5.0^\circ$ .

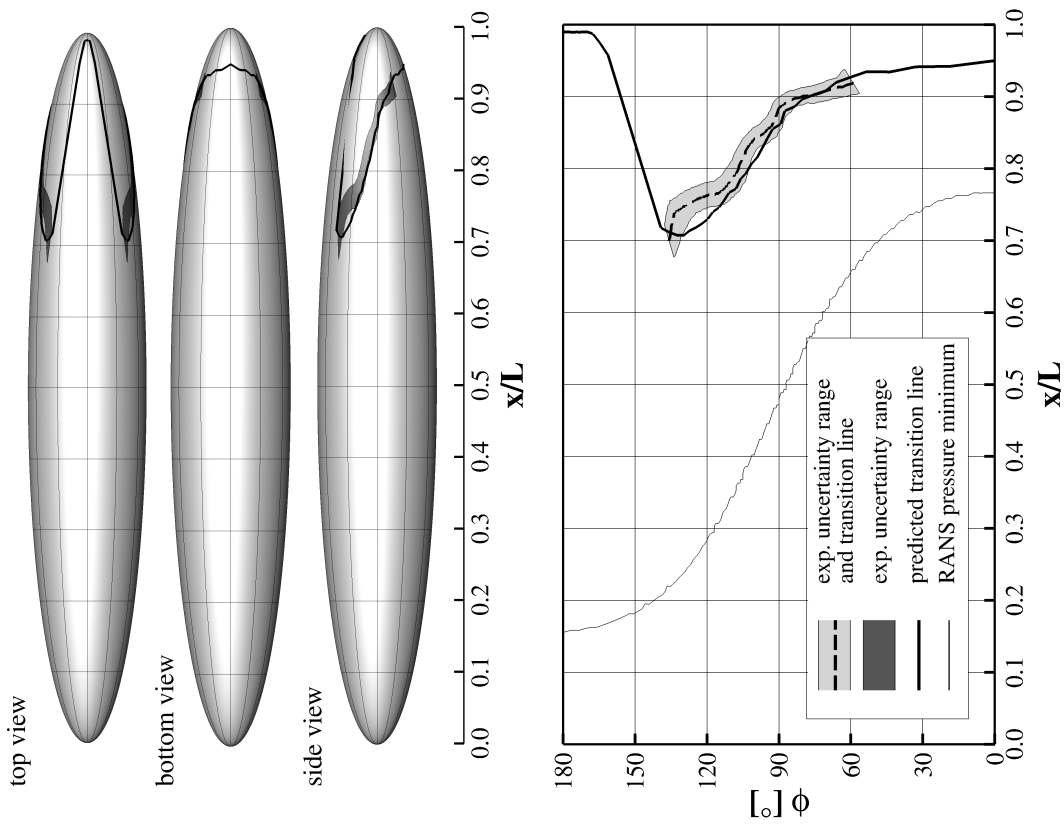


Figure 64: Predicted transition lines, DLR prolate spheroid,  $Re = 1.5 \times 10^6$ ,  $\alpha = 10.0^\circ$ .

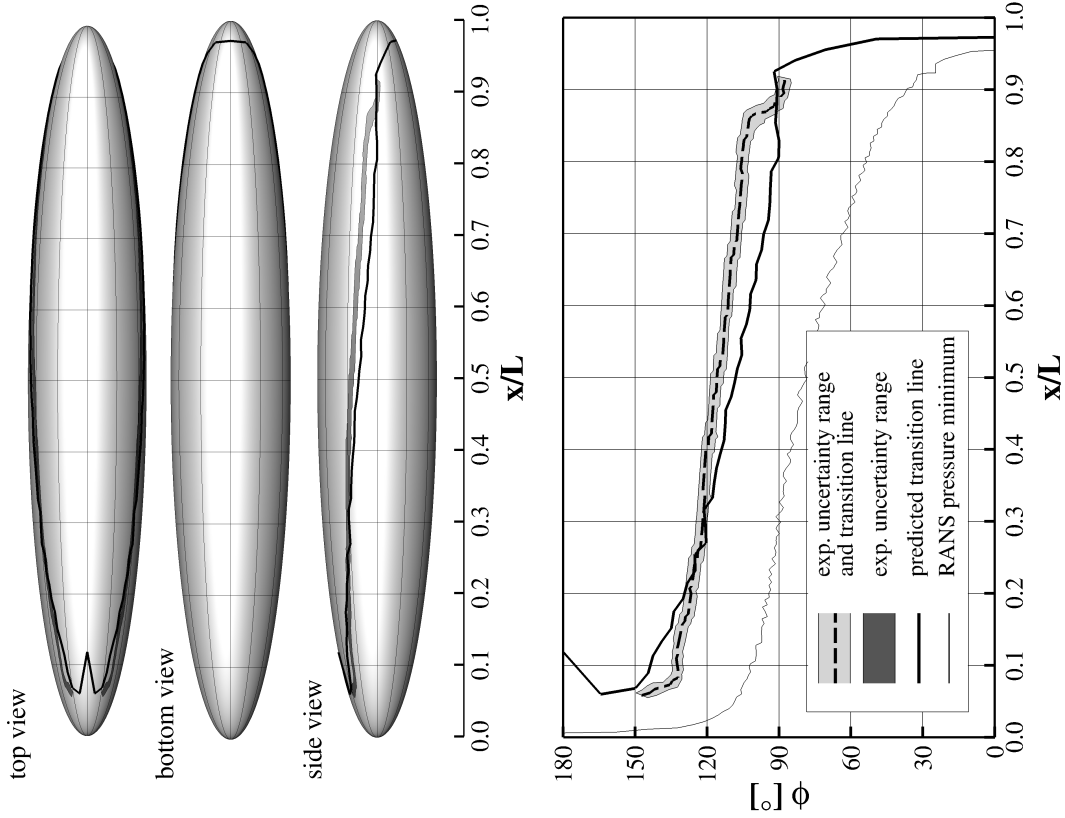


Figure 66: Predicted transition lines, DLR prolate spheroid,  $Re = 3.0 \times 10^6$ ,  $\alpha = 30.0^\circ$ .

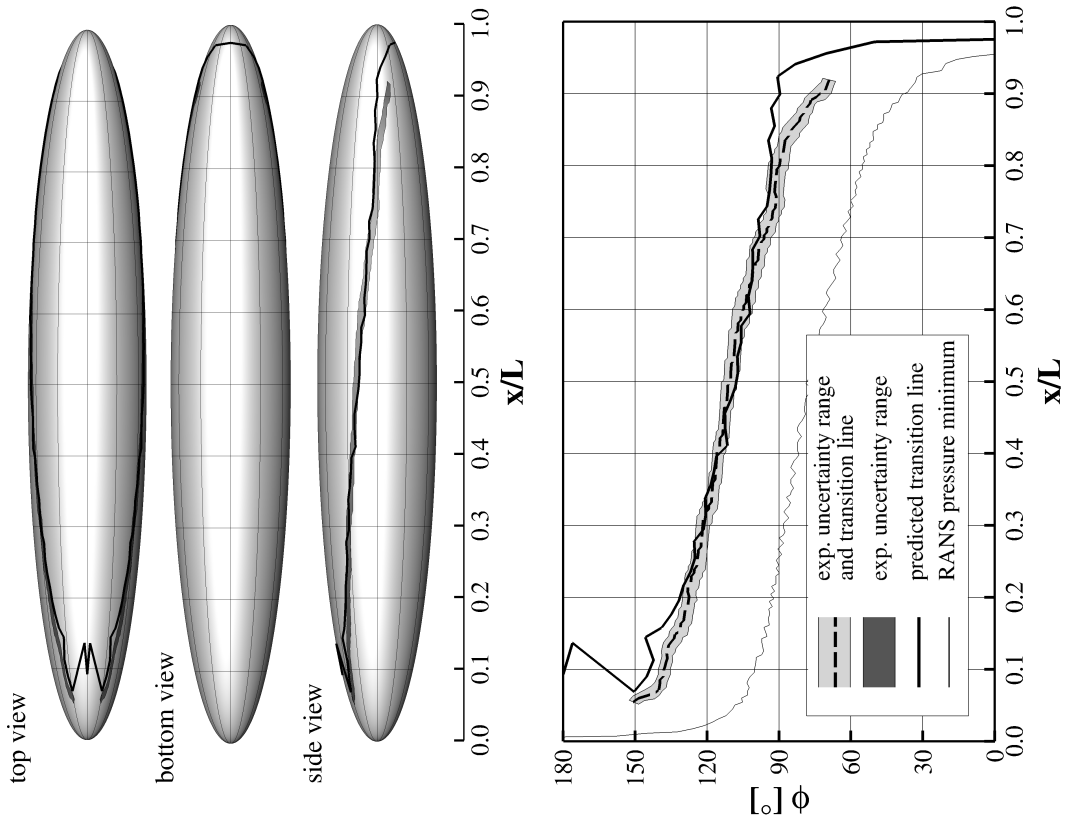


Figure 65: Predicted transition lines, DLR prolate spheroid,  $Re = 1.5 \times 10^6$ ,  $\alpha = 30.0^\circ$ .

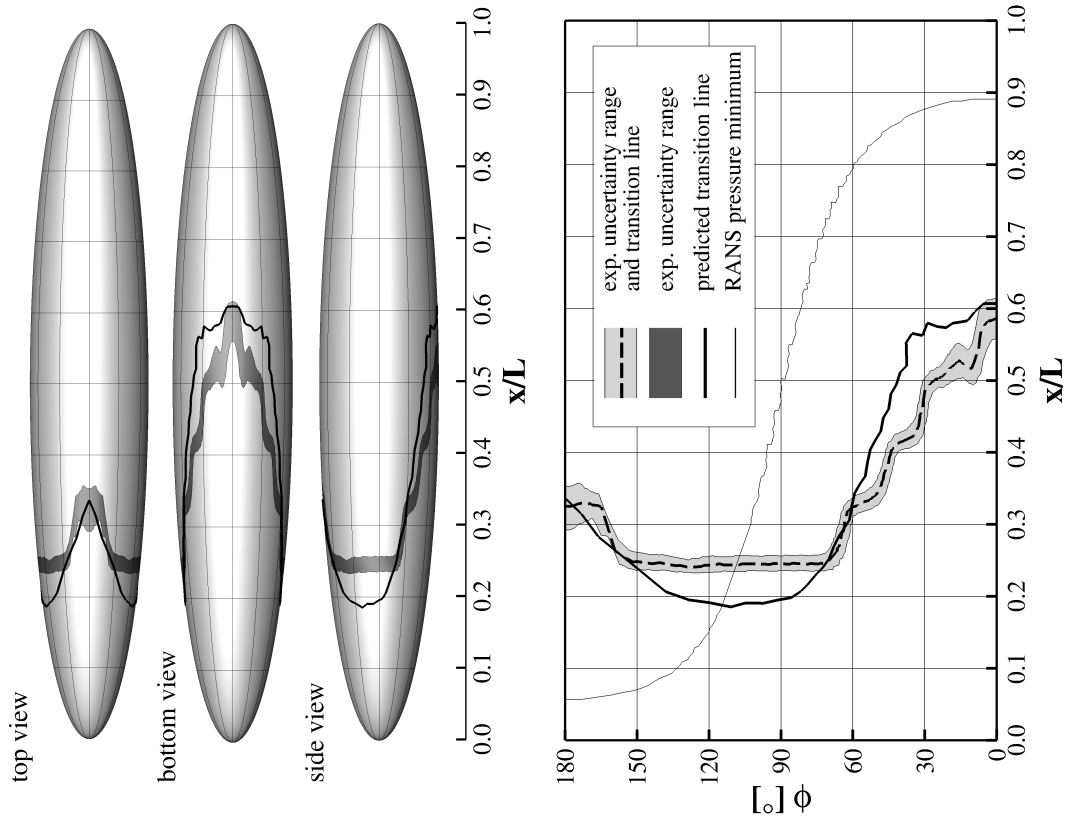


Figure 67: Predicted transition lines, DLR prolate spheroid,  $Re = 6.5 \times 10^6$ ,  $\alpha = 5.0^\circ$ .

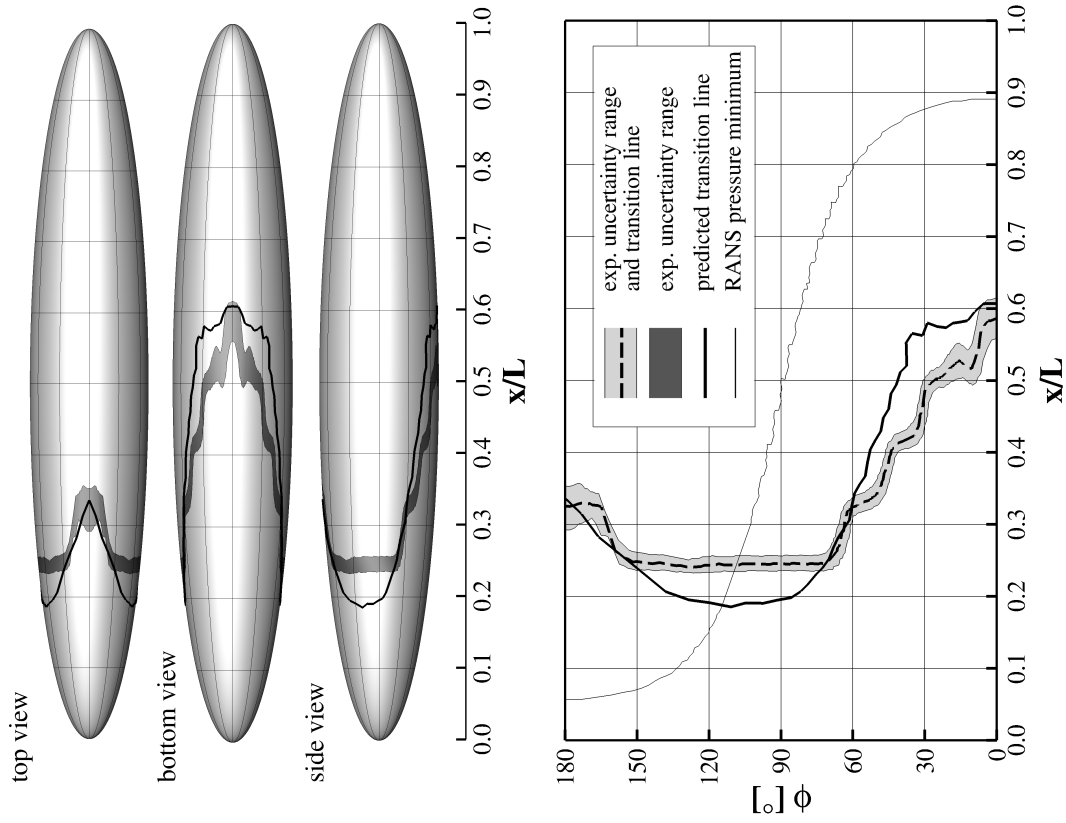


Figure 68: Predicted transition lines, DLR prolate spheroid,  $Re = 6.5 \times 10^6$ ,  $\alpha = 10.0^\circ$ .

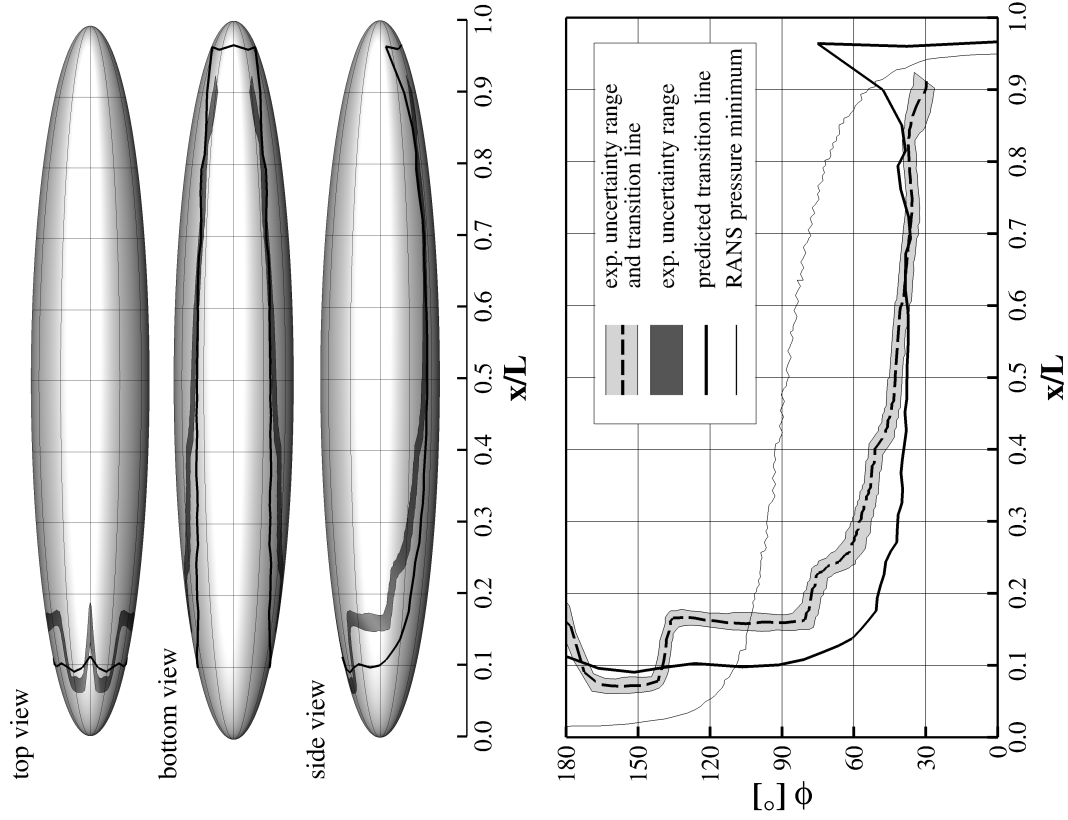


Figure 69: Predicted transition lines, DLR prolate spheroid,  $Re = 6.5 \times 10^6$ ,  $\alpha = 15.0^\circ$ .

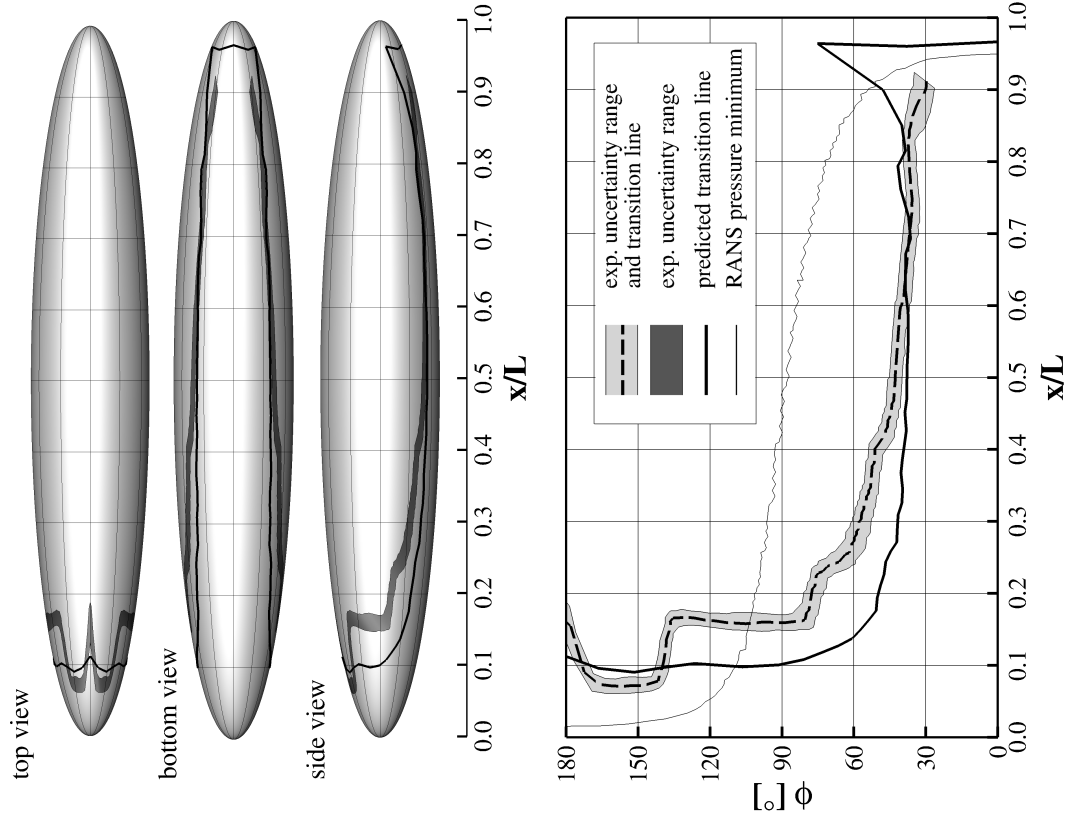


Figure 70: Predicted transition lines, DLR prolate spheroid,  $Re = 6.5 \times 10^6$ ,  $\alpha = 20.0^\circ$ .

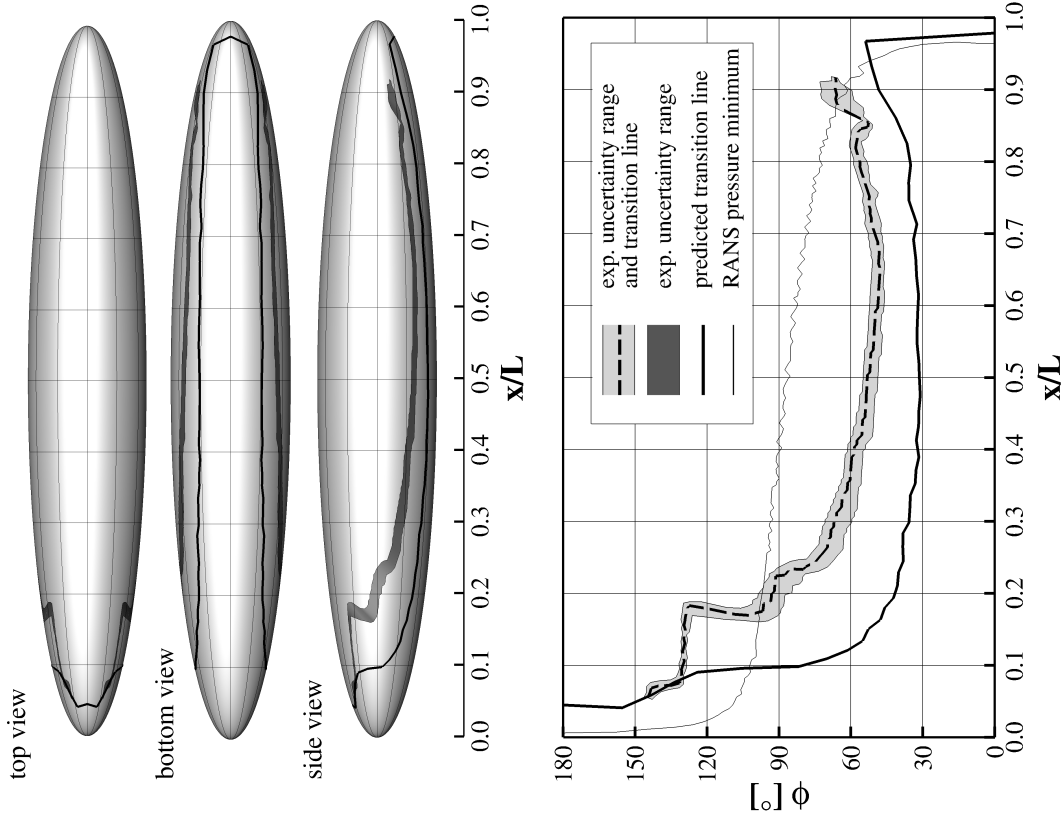


Figure 71: Predicted transition lines, DLR prolate spheroid,  $Re = 6.5 \times 10^6$ ,  $\alpha = 24.0^\circ$ .

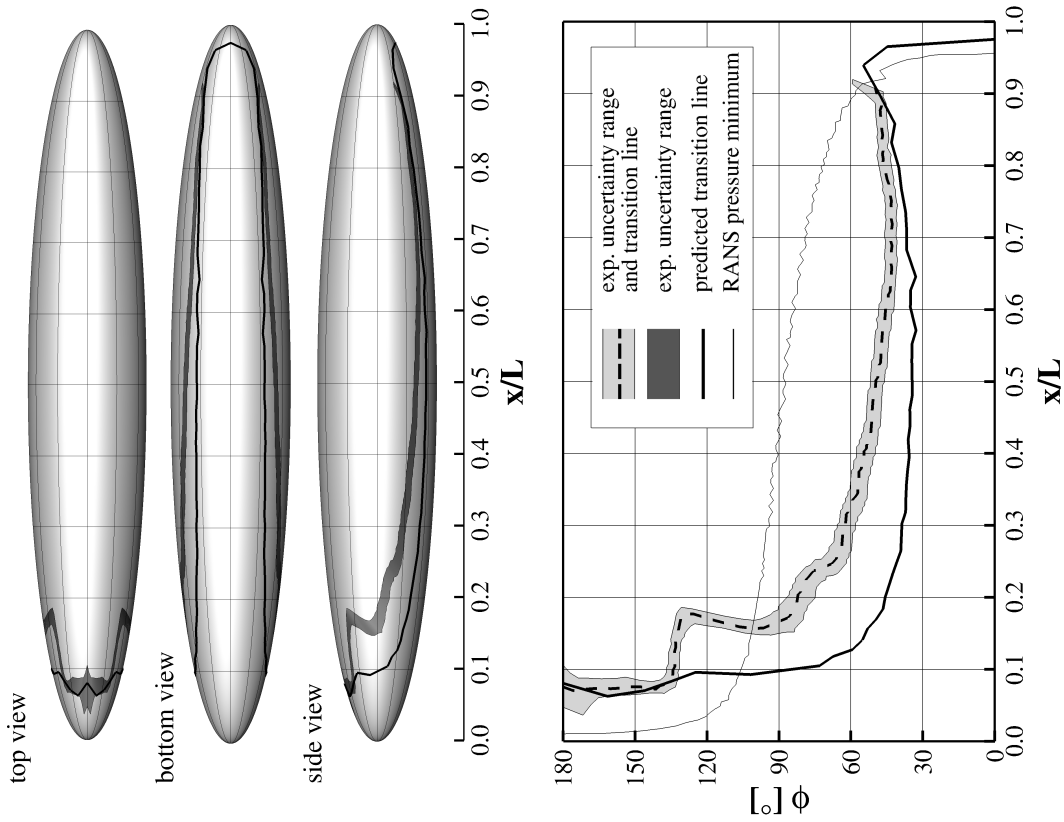


Figure 72: Predicted transition lines, DLR prolate spheroid,  $Re = 6.5 \times 10^6$ ,  $\alpha = 30.0^\circ$ .

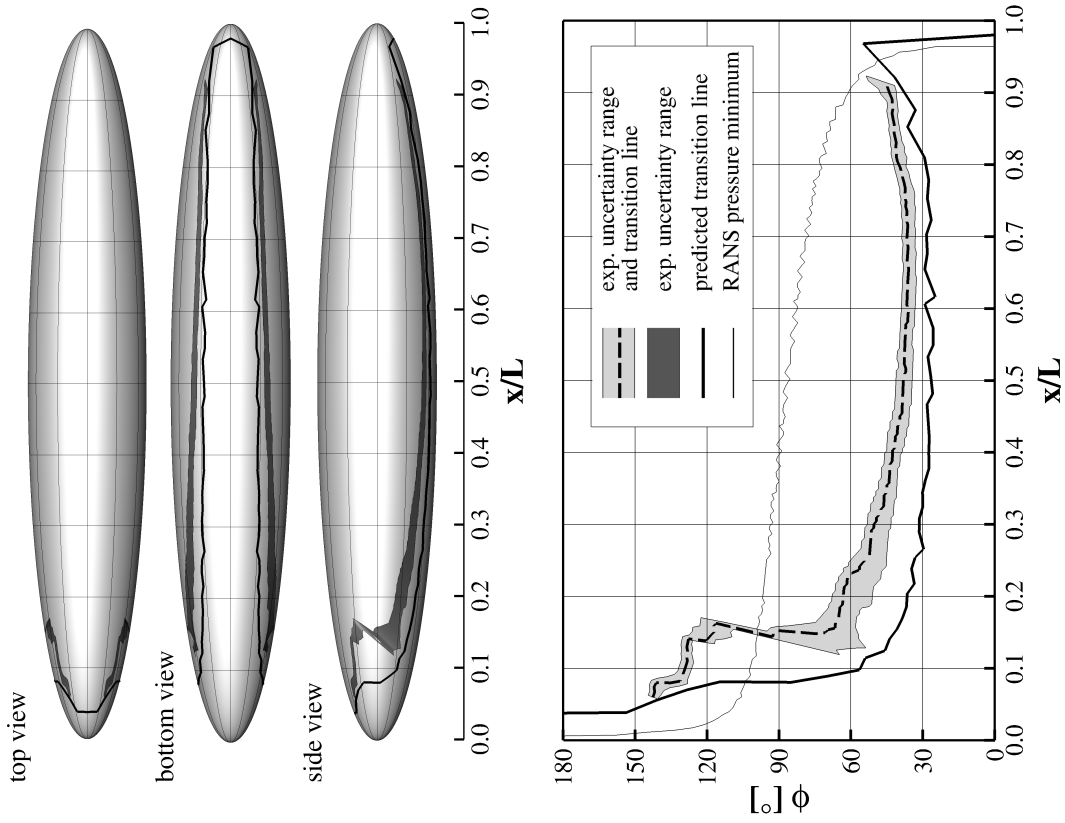


Figure 74: Predicted transition lines, DLR prolate spheroid,  $Re = 8.5 \times 10^6$ ,  $\alpha = 30.0^\circ$ .

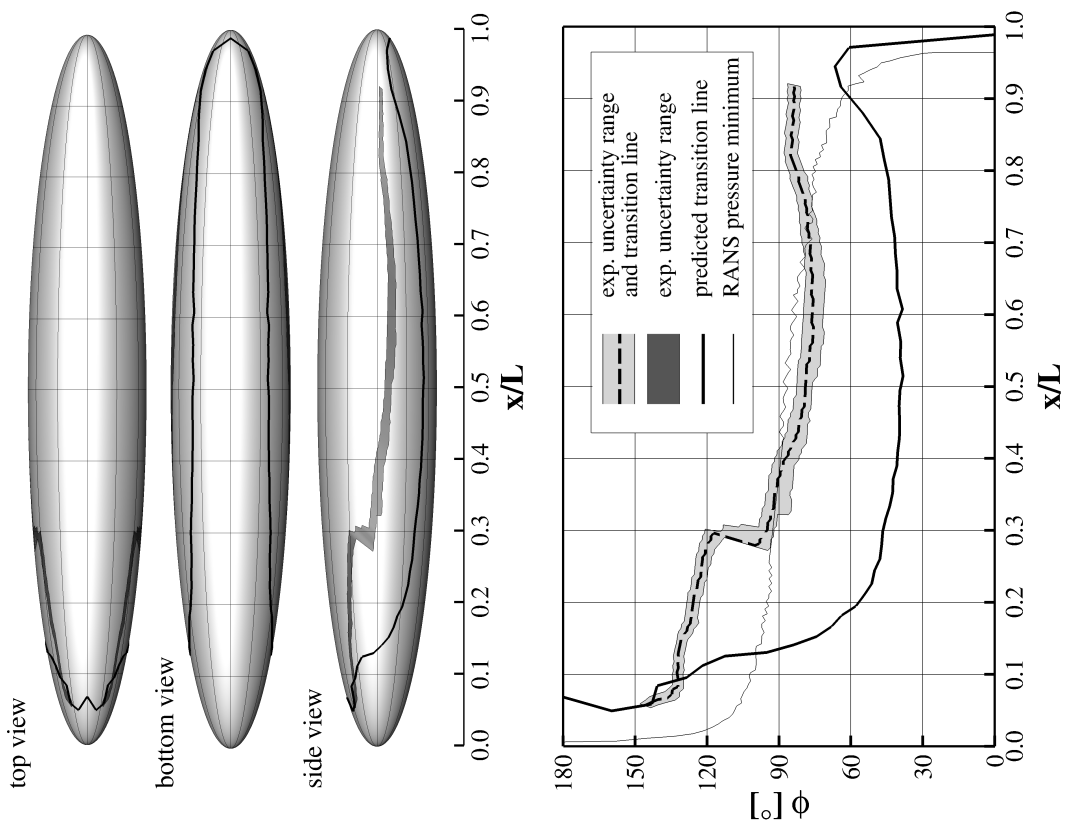


Figure 73: Predicted transition lines, DLR prolate spheroid,  $Re = 4.5 \times 10^6$ ,  $\alpha = 30.0^\circ$ .

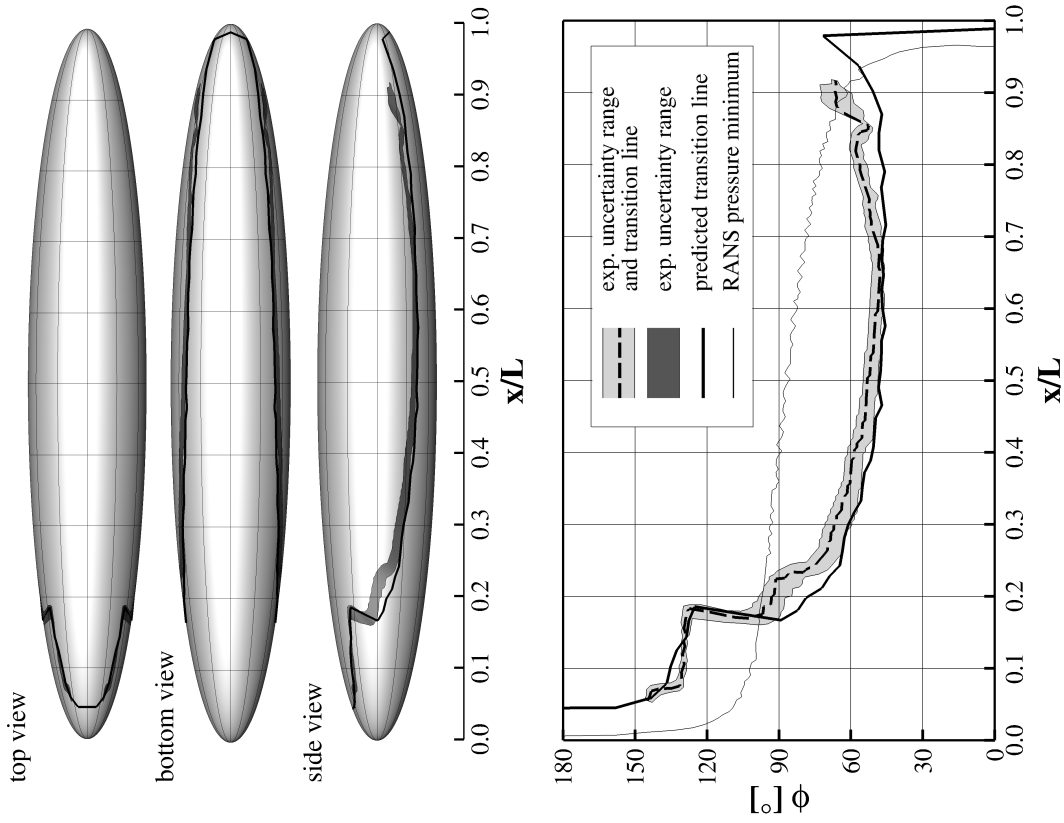


Figure 75: Predicted transition lines, DLR prolate spheroid,  $Re = 4.5 \times 10^6$ ,  $\alpha = 30.0^\circ$ , alternative prediction approach.

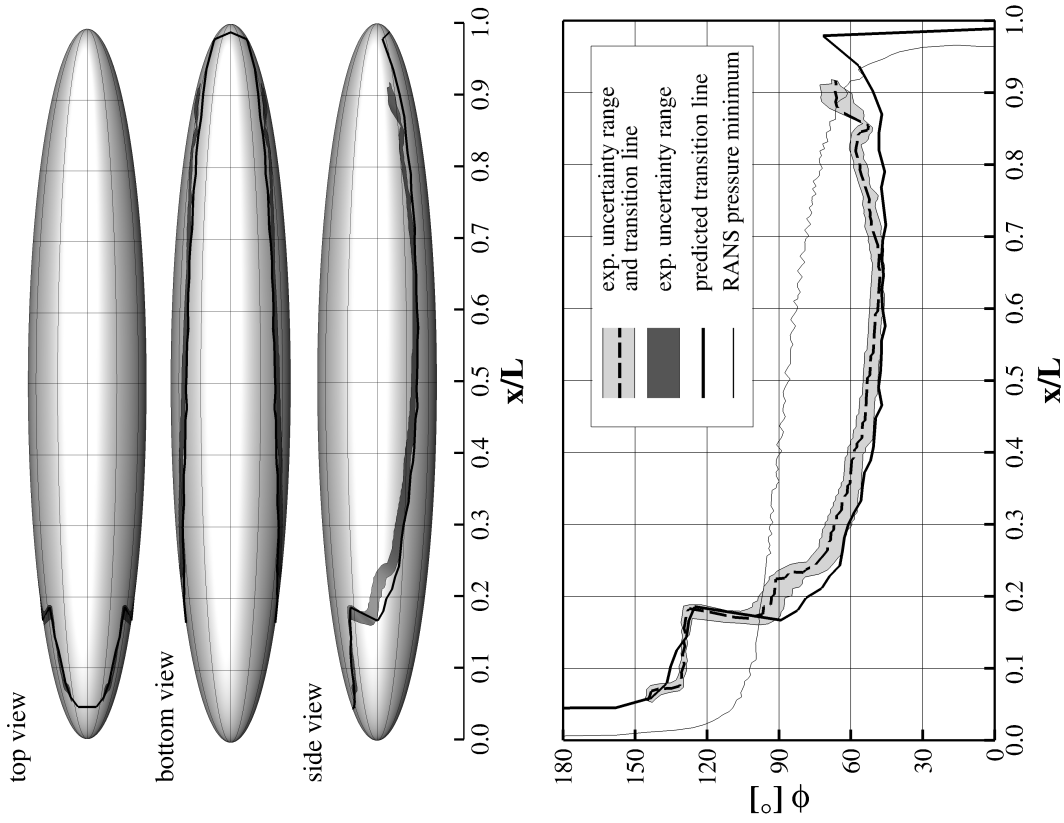


Figure 76: Predicted transition lines, DLR prolate spheroid,  $Re = 6.5 \times 10^6$ ,  $\alpha = 30.0^\circ$ , alternative prediction approach.



## A. Appendix

### A.1. Grid generation strategy

For the generation of computational grids for an unstructured RANS solver the near wall region covering the laminar and turbulent boundary layers is usually resolved with a region of prismatic or hexahedral grid cells. It is advantageous to adapt the size of this region to the extension of the boundary layer and to apply a proper resolution of the boundary layer, especially in close proximity to the wall. For this, an a priori estimation of the expected boundary layer thickness is usually made and the evolution of a turbulent boundary layer over a flat plate is used.

The thickness  $\delta_{turb}$  of a turbulent boundary layer over a flat plate of length  $L$  at a Reynolds number  $Re_L$  based on plate length  $L$  is approximated by [11]:

$$\delta_{turb} \approx 0.37 \cdot L \left( \frac{u_\infty L}{\nu} \right)^{-\frac{1}{5}} \quad (75)$$

If length  $L$  and Reynolds number  $Re_L$  correspond to the characteristic length and the respective Reynolds number of the actual problem, equation 75 gives a relatively accurate measure of the expected turbulent boundary layer thickness. To account for the approximate character of equation 75 with respect to the actual turbulent boundary layer, affected e.g. by pressure gradient etc., the extent of the prismatic or hexahedral region is usually adjusted by a factor  $f$ :

$$\delta_{prism} = f \cdot \delta_{turb} \quad (76)$$

For attached or mildly separated fully turbulent flows the factor  $f$  is typically set to  $f = 1.5$ . If a transitional boundary layer is considered, the approximation of a flat plate turbulent boundary layer does not take the laminar portion of the flow into account, where the boundary layer is considerably thinner. Since the laminar extent is not known a priori, the overall thinner boundary layer is accounted for by reducing the factor  $f$  and typically using, for example,  $f = 1.25$ .

For turbulent flows, the velocity gradient at the wall is much larger compared to laminar flows (Sec. 1). A certain resolution of this near wall area is needed with respect to the applied turbulence model to accurately predict the turbulent boundary layer. A definition of the near wall region follows from the introduction of the non-dimensional wall distance  $y^+$ :

$$y^+ = \frac{u_\tau y}{\nu} \quad (77)$$

The viscous sublayer, the region of the turbulent boundary layer in close vicinity to the wall, is characterized by the fact that the Reynolds shear stress can be neglected compared to the viscous stress [117]. The viscous sublayer is approximated to extent from the wall to  $y^+ \approx 5$ . To resolve this region sufficiently enough, a certain number of grid points needs to be placed in this region. To resolve the viscous sublayer with 3 to 5 grid points and by applying an algebraic stretching for the growth of the cells normal to the wall, the first grid point usually needs to be placed at  $y_0^+ \approx 1$ .

The desired distance  $y_0^+$  for the location of the first grid point directly determines the actual initial wall distance  $y_0$  for the grid generation:

$$y_0 = \frac{\nu y_0^+}{u_\tau} \quad (78)$$

This value can be determined from the friction velocity  $u_\tau$ , which in turn can be approximated with the skin friction coefficient  $c_f$ :

$$u_\tau = \sqrt{\frac{\tau_w}{\rho}} = \sqrt{\frac{c_f u^2}{2}} \quad (79)$$

For the turbulent flat plate boundary layer, the skin friction coefficient can be approximated, for example, as [11]:

$$c_f = \frac{0.455}{(\log Re_L)^{2.58}} \quad (80)$$

With equations 78 to 80 the first wall distance  $y_0$  for the prism mesh generation is determined and the overall extent  $\delta_{prism}$  of the prismatic region is given by equations 75 and 76. If, as last condition, the number  $n$  of prismatic layers inside the prismatic region is specified, the factor  $q$  for the algebraic stretching function can be determined from

$$\delta_{prism} = \frac{y_0 (q^n - 1)}{q - 1} \quad (81)$$

## A.2. Reynolds number based scaling of boundary layers

In section 4.2.4 a special approach is used for stability analyses based on RANS boundary layer profiles. For this, the initial boundary layer is computed for a certain Reynolds number with the RANS solver and then scaled to emulate the behaviour of the same boundary layer at a different Reynolds number. The approach borrows a general idea from boundary layer computations with a boundary layer code.

For boundary layer computations with a boundary layer code a similarity variable is often introduced, that scales the wall normal coordinate according to the boundary layer thickness. The normalized solution of the boundary layer equations is only dependent on the non-dimensional pressure distribution ( $c_p \neq f(Re)$ )<sup>26</sup> and independent of the Reynolds number. The Reynolds number effects on the boundary layer are subsequently considered by scaling the non-dimensional wall normal coordinate, that is the wall normal extent of the boundary layer, according to the similarity variable.

For incompressible flow, the relative laminar boundary layer thickness  $\delta(x)/L$  grows with the square root of the relative distance  $\sqrt{x/L}$  but is also proportional to the reciprocal of the square root of the Reynolds number  $1/\sqrt{Re_L}$ .<sup>27</sup> This also means, that the relative ratio of the thicknesses of two boundary layers for two different Reynolds numbers and for a fixed velocity distribution<sup>28</sup> is given by the reciprocal ratio of the square root of the two respective Reynolds numbers. That is, after the expressions is squared:

$$s_{Re} = \frac{Re_B}{Re_A} = \left( \frac{\delta_A}{\delta_B} \right)^2 \quad (82)$$

According to this theory, boundary layer characteristics based on a Reynolds number  $Re_B$  can be expressed by the same characteristics based on another Reynolds number  $Re_A$ . For the boundary layer thickness the scaling is:

$$\delta(Re_B) = \frac{\delta(Re_A)}{\sqrt{s_{Re}}} \quad (83)$$

If it is assumed, that the difference in the Reynolds numbers is solely based on a change of the onflow velocity  $u_\infty$  with viscosity (temperature) and size of the considered geometry unchanged, and since  $u_e$

---

<sup>26</sup>Applying the incompressible Bernoulli equation, the pressure coefficient  $c_p = (p - p_\infty)/(\frac{1}{2}\rho u_\infty^2)$  can be expressed as  $c_p = 1 - (u/u_\infty)^2$  for potential flow. Following potential flow theory, the flow around a geometry can be considered as the superposition of a translational flow with other elementary flows. Far away from the geometry, the flow is determined by the translational flow, for which  $u = u_\infty$ . If a change in Reynolds number is considered as a change in  $u_\infty$  by a factor  $f$  with otherwise constant flow quantities, the velocity induced by the other elementary flows needs to change by the same factor  $f$ , for the superpositioned flow to still describe the flow around the same geometry. Because of this, the ratio  $u/u_\infty$  does not change with changing Reynolds number for potential flow.

<sup>27</sup>"For a fixed velocity distribution along the body and a fixed point on the body, the non-dimensional thickness  $\delta/c$  of the boundary layer is inversely proportional to  $\sqrt{U_0 c/\nu}$ ." (TETERVIN [118], page 12),  $Re_L = u_\infty L/\nu \hat{=} U_0 c/\nu$

<sup>28</sup>i.e. the same non-dimensional pressure distribution,  $c_p = f(u_e/u_\infty) \neq f(Re_L)$

is proportional to  $u_\infty$ <sup>29</sup>, the boundary layer edge velocity can be simply scaled according to

$$u_e(Re_B) = s_{Re} \cdot u_e(Re_A) \quad (84)$$

With equations 83 and 84 the scaling for the Reynolds number based on displacement thickness is:

$$Re_{\delta_1}(Re_B) = \sqrt{s_{Re}} \cdot Re_{\delta_1}(Re_A) \quad (85)$$

For an unchanged pressure distribution,<sup>30</sup> the non-dimensional boundary layer profiles are unaffected by a change in Reynolds number for a considered geometry: *"For a fixed velocity distribution along the body and a fixed point on the body, the curve of  $u/U$  against  $y/\delta$  is invariable and is independent of the Reynolds number."* (TETERVIN [118], page 13).

Summarizing, the boundary layer (of a RANS solution) computed at a certain Reynolds number can be converted to a boundary layer corresponding to a different Reynolds number by a simple scaling of the thickness of the boundary layer and the boundary layer edge velocity. The theory presented here however neglects compressibility effects.

### A.3. NACA 64<sub>2</sub>-A-015 computation strategy

#### A.3.1. General computation strategy

To cover the large amount of data points needed to be investigated for the NACA 64<sub>2</sub>-A-015 wing test case (Sec. 4.2.4) in an effective way a special computational approach was developed.

The data points are defined by the sweep angle  $\Lambda$ , the angle of attack  $\alpha$  and the Reynolds number  $Re$ . If the experimental transition locations are considered, every transition point  $x_{tr}/c$  is related to a unique Reynolds number, resulting in  $\sim 500$   $\Lambda$ - $\alpha$ - $Re$ -combinations to be investigated. For the actual application of the transition prediction, the Reynolds number is determined from the Reynolds number range from the experiment. The number of Reynolds numbers to be investigated is determined by the resolution of the Reynolds number range in the computations, so that the number of  $\Lambda$ - $\alpha$ - $Re$ -combinations to be investigated is of the same order of magnitude as before.

To keep the computational effort as low as possible regarding the large amount of  $\Lambda$ - $\alpha$ - $Re$ -combinations to be investigated, only 42 basic computations have been carried out. The stability analysis is afterwards performed with a single transition prediction step. The input data for the stability analysis is taken from the basic solution corresponding to the considered  $\Lambda$ - $\alpha$ -pair. To account for the correct Reynolds number of the  $\Lambda$ - $\alpha$ - $Re$ -combination the input for the stability analysis is scaled according to the theory presented in section A.2. The theoretical considerations for the scaling are based on incompressible theory. Because of, that the scaling should preferably applied to an incompressible RANS computation ( $Ma \rightarrow 0$ ) so that compressibility effects can be neglected. However, the RANS solver used for the basic computation is a compressible solver. Using a low Mach number for the basic computations,  $Ma > 0$  and  $Ma \approx 0.1$ , is considered a good compromise.

With 6 sweep angles (from  $\Lambda = 0^\circ$  to  $50^\circ$ ) and 13 angles of attack (from  $\alpha = -3^\circ$  to  $3^\circ$ ) the initial  $\Lambda$ - $\alpha$  case matrix consists of 78 entries. Since the NACA 64<sub>2</sub>-A-015 wing is symmetrical, the  $\alpha$  range can be reduced to positive angles of attack. The analysis for any negative angle of attack is then performed on the lower surface of the wing at the corresponding positive angle of attack. This reduces the number of  $\Lambda$ - $\alpha$ -pairs to 42  $\Lambda$ - $|\alpha$ |-pairs for the basic computations..

The complete strategy for the stability analysis and transition prediction for the NACA 64<sub>2</sub>-A-015 wing test case can be summarized as follows:

<sup>29</sup>  $c_p \neq f(Re)$  and  $u_e = \sqrt{1 - c_p} \cdot u_\infty$  (incompressible flow)

<sup>30</sup> The velocity distribution at the boundary layer edge is determined by the pressure coefficient  $c_p \neq f(Re)$ . For incompressible flow, the velocity at the boundary layer edge is:  $u_e = \sqrt{1 - c_p} \cdot u_\infty$

- For all 42  $\Lambda$ - $|\alpha|$ -pairs basic solutions are created, with a Reynolds number of  $Re = 7.2 \times 10^6$  and a Mach number of  $Ma \approx 0.1$  for the RANS computations
- Transition is prescribed for the basic RANS computations at the approximate location of laminar separation<sup>31</sup>
  - for the fully three-dimensional geometry the laminar separation location is based on laminar separation points from a laminar boundary layer code analysis that in turn is based on the pressure distribution of a fully turbulent computation.
  - for the infinite swept wing computations laminar separation points are based on actual separation points of the RANS solution<sup>32</sup>
- For all  $\Lambda$ - $\alpha$ - $Re$ -combinations to be investigated with a stability analysis, a restart based on the basic solution for the matching  $\Lambda$ - $|\alpha|$ -combination is performed
  - for a negative angle of attack  $\alpha$ , data from the lower surface of the wing of the corresponding  $\Lambda$ - $|\alpha|$  basic solution is used as input for the stability analysis
  - for a positive angle of attack  $\alpha$ , data from the upper surface of the wing of the corresponding  $\Lambda$ - $|\alpha|$  basic solution is used as input for the stability analysis
  - for the analysis of the experimental transition locations the  $\Lambda$ - $\alpha$ - $Re$ -combination is determined by the Reynolds number from the respective  $\Lambda$ - $\alpha$ - $x_{tr}$ -data-point of the experiment
  - for a general transition prediction, the Reynolds number is prescribed based on the Reynolds number range to be investigated for a certain  $\Lambda$ - $\alpha$ -combination
- After the restart only one RANS iteration is executed and a stability analysis, respectively a transition prediction step, is performed at the end of this RANS iteration.
  - if the presented method is used for transition prediction no convergence of the transition locations is performed
- For the stability analysis the input for the stability code is scaled according to the theory that lead to equation 82, with  $Re_A$  the actual Reynolds number from the RANS computation and  $Re_B$  the target Reynolds number matching the value from the investigated  $\Lambda$ - $\alpha$ - $Re$ -combination
- The stability analysis is performed for the laminar part of the flow which extends up to the approximation of the laminar separation point
  - if an experimental transition location  $x_{tr} > x_{sep}$  is considered, values extrapolated to  $x_{tr}$  are used
  - for transition prediction, if the critical  $N$ -factor is not reached upstream of the separation point, the  $N$ -factor envelope is extrapolated in downstream direction

With  $n$  the number of data points to be investigated, this procedure reduces the overall computational extent to 42 basic RANS computations followed by  $n$  transition prediction steps, compared to  $(42 \times n)$  full RANS computations with transition prediction for the standard approach.

---

<sup>31</sup>”For a given velocity distribution over the body, the separation point is independent of the Reynolds number  $Re_c$ .” (Tetervin [118], page 13)

<sup>32</sup>A method typically used to improve the convergence of the transition prediction locations in two-dimensional flows is to start a computation fully laminar and check within short intervals of the RANS iterations the solution for laminar separation. If a laminar separation point is found this point is used as new transition location, otherwise the current transition location is not altered. With this, as much laminar flow as possible is created prior to the first actual transition prediction step, without exhibiting flow separation that may disturb the convergence of the RANS solution. This preliminary transition location can in turn be used as an approximation of the actual separation point in the RANS solution.

The validity of this approach has been tested for 6  $\Lambda$ - $|\alpha|$ -combinations (12  $\Lambda$ - $\alpha$ -combinations of the considered NACA 64<sub>2</sub>-A-015 wing test case using infinite swept wing computations. The results shown in figure 77 as dashed lines correspond to the computations discussed in section 4.2.4 and are based on the Reynolds number scaling approach presented in this section. The solid lines are based on transition prediction using the usual approach, that is a full convergence of flow solution and transition locations is achieved with multiple transition prediction steps during the RANS computation. The flow conditions in these computations correspond to the actual Reynolds number under consideration.

It can be seen from figure 77 that the differences in the predicted transition locations are vanishingly small. The two major discrepancies seen for  $\Lambda = 20^\circ$ ,  $\alpha = 0.5^\circ$  and  $\Lambda = 40^\circ$ ,  $\alpha = 1.5^\circ$  are a result of the resolution of the investigated Reynolds number range together with a change in transition scenario. The sudden upstream movement from one computed Reynolds number to the next is based on the change of streamwise instability to cross-flow instability as the critical stability that leads to transition. A finer resolution of the investigated Reynolds numbers in this area should reduce the visible differences in the predicted transition locations. Summarizing, with these results, the validity of the Reynolds number scaling approach is supported for flow conditions representative of the NACA 64<sub>2</sub>-A-015 wing experiment.

### A.3.2. Scaling for stability analysis

If a stability analysis is carried out based on boundary layer profiles from the RANS solution and if the stability analysis is to be based on a different Reynolds number  $Re_{target}$  compared to the Reynolds number  $Re$  used in the actual RANS computation (Sec. 4.2.4), a scaling of the input for the stability solver according to section A.2 has to be applied. The non-dimensional velocity profiles itself do not need any scaling (Sec. A.2) but for some boundary layer parameters a scaling is needed, using a scaling factor  $s_{Re}$  (Eq. 82) based on the two considered Reynolds numbers:

$$s_{Re} = \frac{Re_{target}}{Re} \quad (86)$$

The scaling for the non-dimensional velocity profiles is implicitly given by a scaling of the boundary layer thickness in form of the displacement thickness (Eq. 83)

$$\delta_{1,target} = \frac{\delta_1}{\sqrt{s_{Re}}} \quad (87)$$

and a scaling of the boundary layer edge velocity (Eq. 84)

$$u_{e,target} = s_{Re} \cdot u_e \quad (88)$$

Other input values required by the stability solver are the edge Mach number, directly determined according to equation 88, and the Reynolds number based on the displacement thickness (Eq. 85)

$$Re_{\delta_1,target} = \sqrt{s_{Re}} \cdot Re_{\delta_1} \quad (89)$$

### A.3.3. Attachment line analysis

For the analysis of experimental transition locations based on solution from RANS computations (Sec. 4.2.4) the flow state at and near the attachment line is of interest. The flow along the laminar attachment line is characterized by the Reynolds number based on the displacement thickness, which is defined for an infinite swept wing as [119]:

$$Re_{\theta_{AL}} \hat{=} Re_{\delta_{2,AL}} = 0.4 \frac{u_e}{\sqrt{\nu_e \cdot dv_e/dc}} \quad (90)$$

Equation 90 is formulated in the streamline coordinate system and the streamline corresponds in this context to the attachment line. The boundary layer edge velocity component along the attachment line (in streamline direction) is given by  $u_e$  and the cross-flow velocity component is  $v_e$  ( $v_e = 0$  at the attachment line, but  $dv_e/dc \neq 0$ ). For an infinite swept wing the cross-flow direction  $c$  at the attachment line corresponds to the direction normal to the leading edge along the surface of the geometry.

The attachment line Reynolds number can also be expressed in terms of the curvature of the potential lines (lines in direction of  $c$ ):

$$Re_{\delta_2,AL} = 0.4 \sqrt{\frac{-u_e}{\nu_e K_2}} \quad (91)$$

For converging streamlines (looked at in direction of the streamline) the curvature of the potential lines is positive ( $K_2 > 0$ ) and for diverging streamlines the curvature of the potential lines is negative ( $K_2 < 0$ ). At the attachment lines all streamlines are diverging and hence  $(-u_e/\nu_e K_2) > 0$ . The attachment line Reynolds number can thus be considered as a measure of the streamline divergence in the neighbourhood of the attachment line.

The attachment line Reynolds number can be used to determine the flow state (laminar/turbulent) of the attachment line [120]. For values of  $Re_{\delta_2,AL}$  approximately larger than 100, turbulent contamination of the attachment line can occur, resulting generally in turbulent flow spreading from the attachment line and eventually covering the whole wing. Attachment line contamination can occur for example for swept wing models attached to a turbulent (wind tunnel) wall. In reference [120] an uncertainty band for the critical attachment line Reynolds number of  $Re_{\delta_2,AL} = 80$  to 120 is given, reference [121] reports turbulent flow starting to develop for  $Re_{\delta_2,AL} = 104$  to 110.

Turbulent boundary layer flow, originating from a possibly turbulent attachment line, may undergo a laminarization process whereby the turbulent flow returns to a laminar state. This is considered to be possible, if the turbulent flow is sufficiently strong accelerated. The acceleration of the boundary layer can be characterized by the acceleration parameter  $K$  [122]:

$$K = \frac{\nu_e}{u_e^2} \frac{du_e}{ds} \quad (92)$$

Equation 92 is formulated in the streamline coordinate system, with  $s$  the arc length along the streamline and  $u_e$  the boundary layer edge velocity in streamline direction.

In reference [122] a lower limit for the acceleration is given, with laminarization to occur for values of  $K > 2.0 \times 10^{-6}$ . Reference [120] gives a range for the acceleration parameter of  $K = 2.0 \times 10^{-6}$  to  $K = 5.0 \times 10^{-6}$  that needs to be exceeded for the turbulent flow to return to a fully laminar state. Generally, it is also assumed, that the flow is accelerated over a sufficiently long distance to relaminarize.

In the context of the investigations of section 4.2.4, the values of the attachment line Reynolds number (Eq. 91) and the acceleration parameter (Eq. 92) are computed at a certain Reynolds number  $Re$  but need to be evaluated for a different Reynolds number  $Re_{target}$ . For this, a scaling of the attachment line values according to section A.2 has to be applied, using a scaling factor  $s_{Re}$  (Eq. 82) based on the two respective Reynolds numbers:

$$s_{Re} = \frac{Re_{target}}{Re} \quad (93)$$

The scaling of the attachment line Reynolds number follows from equation 85 and is:

$$Re_{\delta_2,target} = \sqrt{s_{Re}} \cdot Re_{\delta_2} \quad (94)$$

Since the acceleration parameter is proportional to the inverse of the Reynolds number, the scaling of the acceleration parameter is given by:

$$K_{target} = \frac{K}{sRe} \quad (95)$$

For the investigations presented in section 4.2.4, the limiting Reynolds number above which attachment line contamination occurs and the limiting Reynolds number below<sup>33</sup> which relaminarization occurs needs to be known. If limiting values for  $Re_{\delta_{2,AL}}$  and  $K$  are given, equations 93 to 95 can be re-arranged. The critical Reynolds number for attachment line contamination is then given by

$$Re(Re_{\delta_{2,target}}) = \left( \frac{Re_{\delta_{2,target}}}{Re_{\delta_2}} \right)^2 Re \quad (96)$$

and the critical Reynolds number for laminarization is

$$Re(K_{target}) = \frac{K}{K_{target}} Re \quad (97)$$

For the investigation of the flow around the NACA 64<sub>2</sub>-A-015 wing, presented in section 4.2.4, limiting values of  $Re_{\delta_{2,AL}} > 105$  for attachment line contamination and  $K > 2.8 \times 10^{-6}$  for relaminarization have been used. For these values the respective limiting Reynolds numbers for which attachment line contamination and relaminarization can occur have been determined. The strategy to determine the limiting Reynolds numbers is in principle given by the approach for the general stability analysis for this case, presented in section A.3.1. Computations have been carried out for the fully three-dimensional geometry and the infinite swept wing case, as specified in section 4.2.4, at a Reynolds number of  $Re = 7.2 \times 10^6$  and a Mach number of  $Ma \approx 0.1$ .

For the three-dimensional computations an average value of  $Re_{\delta_2}$  has been computed along the attachment line and the averaged value was used in equation 96. The acceleration parameter  $K$  was computed for several single streamlines and an average of  $K$  from these streamlines was taken and used in equation 97. For the infinite swept wing computations the respective values are directly used in equations 96 and 97.

Based on the limiting values,  $Re_{\delta_{2,AL}} = 105$  and  $K = 2.8 \times 10^{-6}$ , the flow conditions for which attachment line contamination and relaminarization can occur have been calculated and are shown in figure 78. The values of  $Re_{\delta_{2,AL}}$  are determined directly at the attachment line and since the airfoil defining the wing is symmetrical the attachment lines for two angles of attack of the same magnitude ( $\alpha$  and  $-\alpha$ ) are identical. This does not hold for the acceleration parameter  $K$ : for negative angles of attack, the streamlines, along which  $K$  is determined, originate at the attachment line and continue over the pressure side of the wing, for positive angles of attack the respective streamlines continue over the suction side of the wing. The acceleration parameter is defined by the pressure distribution along the streamline, and for angles of attack  $a \neq 0^\circ$ , the pressure distribution is not symmetrical. Because of that the acceleration parameters for angles of attack of the same magnitude  $|\alpha|$  but different sign differ. Only for  $a = 0^\circ$  the flow is symmetrical and the values of  $K$  of streamlines following the upper or the lower surface of the wing are the same.

In figure 78, for four sweep angles of the wing, the limiting Reynolds number  $s$  are plotted. The solid lines give the limit for attachment line contamination over the investigated angle of attack range. For Reynolds numbers larger than this limit the attachment line becomes turbulent if contaminated. Below the limit the attachment line is unaffected by contamination and stays laminar. The dashed lines in turn are the limit for relaminarization. For Reynolds numbers larger than the limit the acceleration is not strong enough to turn the possibly turbulent boundary layer to laminar. Below the limit relaminarization of a turbulent boundary layer is possible. Based on the opposing dependency

---

<sup>33</sup>The acceleration parameter  $K$  (Eq. 92) is inversely proportional to the Reynolds number.

on the onflow Reynolds number, the two limiting lines enclose a region that defines flow conditions for which attachment line transition followed by a relaminarization is possible. Outside of these regions, either the acceleration is too small to revert the turbulent boundary layer to a laminar state, or the attachment line is unaffected by contamination and the flow stays laminar.

It can be seen from figure 78, that the size of the region defining possible relaminarization increases with decreasing sweep angle for the NACA 64<sub>2</sub>-A-015 wing. For a sweep angle of  $\Lambda = 20^\circ$  relaminarization is possible for angles of attack larger than  $\alpha \approx -1.5^\circ$ , however at relatively high Reynolds numbers, beyond the maximum values achieved in the experiment for this sweep angle. With increasing sweep angle, the respective values of the Reynolds number at which relaminarization is possible decrease. For sweep angles  $\Lambda \leq 30^\circ$  they are in the range of Reynolds numbers that are covered in the experiment. However, the range for the critical angle of attack is also decreased, with the smallest range, still covered in the experiment, for  $\Lambda = 50^\circ$ , where laminarization is only possible for angles of attack larger than  $\alpha \approx 2.0^\circ$ .

B. Appendix figures

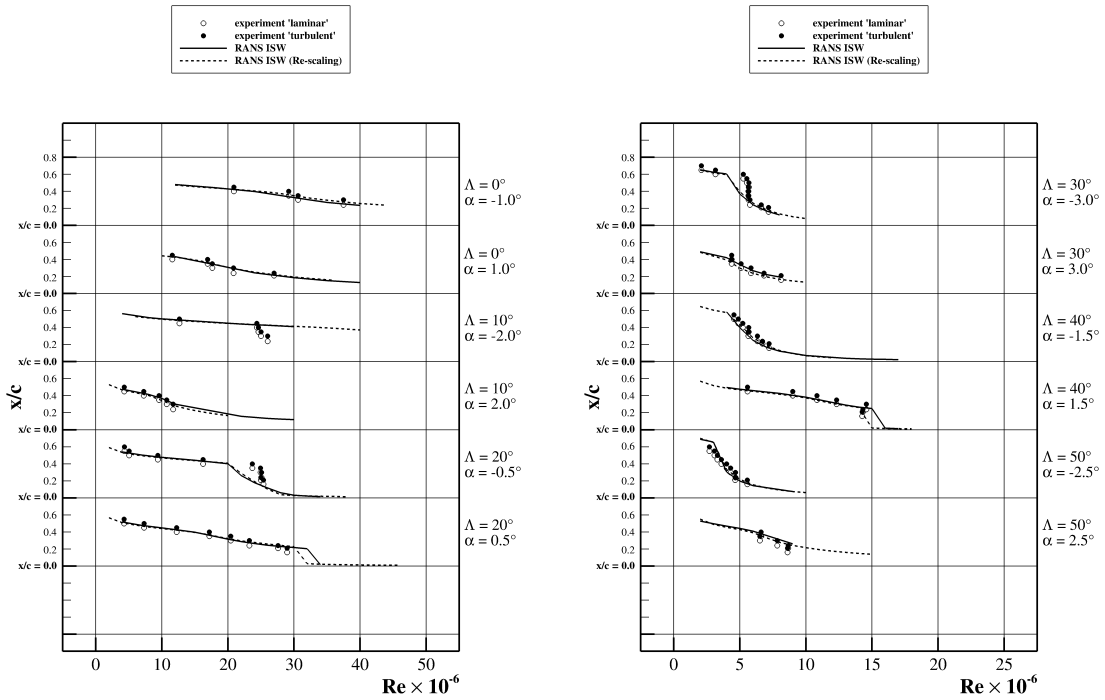


Figure 77: Validation of Reynolds number scaling, NACA 64<sub>2</sub>-A-015.

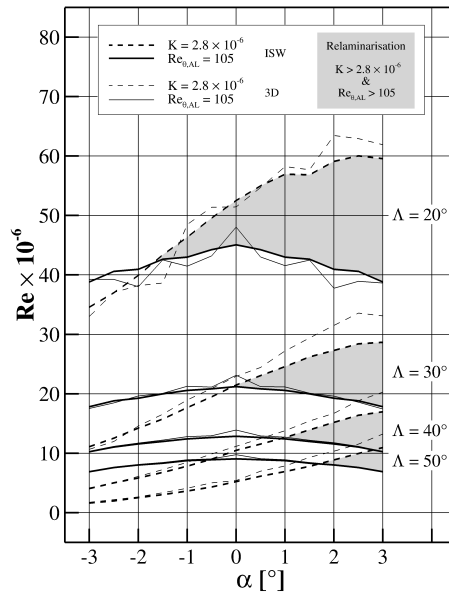


Figure 78: Attachment line transition and relaminarization criteria, NACA 64<sub>2</sub>-A-015.